Wideband and flat multibeam antenna solutions for ultrafast communications in millimeter band

Francesco Foglia Manzillo

To cite this version:

Francesco Foglia Manzillo. Wideband and flat multibeam antenna solutions for ultrafast communications in millimeter band. Networking and Internet Architecture [cs.NI]. Université de Rennes, 2017. English. NNT : 2017REN1S110 . tel-01766807

HAL Id: tel-01766807
https://theses.hal.science/tel-01766807

Submitted on 14 Apr 2018

ANNÉE 2017

THÈSE / UNIVERSITÉ DE RENNES 1
sous le sceau de l'Université Bretagne Loire

pour le grade de

DOCTEUR DE L'UNIVERSITÉ DE RENNES 1

Mention : Traitement du Signal et Télécommunications

Ecole doctorale Matisse

présentée par

Francesco FOGLIA MANZILLO

préparée à l'unité de recherche IETR – UMR 6164
Institut d'Electronique et de Télécommunications de Rennes
Université de Rennes 1

Wideband and flat multibeam antenna solutions for ultrafast communications in millimeter band

Thèse soutenue à Rennes
le 29 Mars 2017

devant le jury composé de :

Andrea NETO
Professeur, Delft University of Technology
Rapporteur

Thomas ZWICK
Professeur, Karlsruhe Institute of Technology
Rapporteur

Romain CZARNY
Docteur Ingénieur, Thales Research & Technology
Examinateur

Giovanni TOSO
Docteur Ingénieur, European Space Agency
Examinateur

Ronan SAULEAU
Professeur, Université de Rennes 1
Directeur de thèse

Mauro ETTORRE
Chercheur CNRS, HDR, IETR – UMR 6164
Co-directeur de thèse

This work was supported in part by the European Union Seventh Framework Programme (FP7/2007-2013) under grant agreement no. 619563 (MiWaveS).

Résumé

Dans quelques années, les technologies actuelles de télécommunications ne seront pas capables de soutenir la demande toujours croissante de connectivité et de trafic de données. De nouvelles techniques de communication et de systèmes antennaires à haute performance sont donc essentiels pour augmenter le débit de transmission et réduire les temps de latence. La congestion de bandes de fréquences traditionnellement utilisés pour les communications et la disponibilité de larges canaux à hautes fréquences a stimulé le développement de systèmes en ondes millimétriques. Parmi les applications émergentes dans ce contexte, nous nous concentrerons sur deux en particulier dans cette thèse: les réseaux mobiles de cinquième génération (5G), basés sur des point d'accès à 60 GHz, et les communications satellite en bande Ka. Ces applications exigent des antennes à bande large qui assurent une grande couverture angulaire sans substantielles pertes de balayage, tout en étant à la fois compactes et facilement intégrables avec les modules radios. La réalisation de l'ensemble de ces objectifs pose des défis considérables, soit au niveau conceptuel, soit au niveau technologique. Les antennes réseaux à commande de phase et les antennes à réflecteurs représentent actuellement les solutions les plus performantes. Néanmoins, l'utilisation d'antennes multifaisceaux plates est un vrai défi, l'enjeu étant de réduire les couts et la complexité des systèmes rayonnants. Il est donc clairement nécessaire d'inventer de nouvelles architectures d'antenne innovantes, des modèles numériques préciss pour en faciliter l'analyse et la conception, et de nouvelles solutions technologiques visant à la réalisation de modules rayonnantes à faible profil. Tous ces aspects sont développés dans cette thèse, qui porte sur l'étude et le développement de systèmes antennaires multifaisceaux large bande et à très grande couverture angulaire, souvent appelé «Continuous Transverse Stub Antenna» (CTS) dans la littérature. L'architecture de l'antenne comprend un réseau de fentes longues excitées par un réseau d'alimentation en chandelier, basé sur des guides d'onde à plans parallèles qui supportent la propagation d'un mode quasi-transverse électromagnétique (quasi-TEM). Cette structure est excitée par un formateur de faisceaux quasi-optique co-intégré, appelé système «pillbox». Il consiste en un réflecteur parabolique bidimensionnel excité par un cornet d'alimentation. Le réflecteur transforme l'onde cylindrique lancée par la source en une onde

quasi-plane qu'est dirigée, grâce à une transition spécifique, vers le réseau d'alimentation. La position de la source dans le plan focal détermine la direction de pointage du faisceau rayonné. Le balayage du faisceau, dans un plan, peut se faire soit électroniquement, en utilisant plusieurs sources contrôlées par un réseau de commutateurs, soit mécaniquement avec un seul cornet.

La bande d'adaptation de la partie rayonnante de ce système peut dépasser une octave, sur une plage angulaire supérieure à 60°. Ces performances remarquables sont dues à l'excitation des fentes par une onde quasi-TEM obtenu grâce au système «pillbox» et également au comportement quasi non-dispersif du réseau d'alimentation en guide d'onde à plans parallèles. Le formateur de faisceaux quasi-optique peut permettre un balayage de ±30° avec de faibles pertes, sur une très large bande. Dans cette thèse, nous présentons des modèles et des outils numériques qui permettent l'analyse des performances globales de ces antennes, soit en termes d'adaptation, soit en termes de diagrammes de rayonnement. En outre, ces outils facilitent la conception et l'optimisation de chaque sous-système de l'antenne. Ces outils sont exploités pour l'analyse et le développement des antennes CTS. Différentes technologies ont ainsi été explorées pour réaliser des antennes relativement fines en bande millimétrique, en vue de la grande requête de structures planaires avec un encombrement minimal. Une solution pour intégrer entièrement des antennes CTS dans des substrats multicouches basée sur l'utilisation de technologies planaires conventionnelles est présentée. Cette technique est exploitée pour la réalisation ds deux antennes intégrées en technologie LTCC («low temperature co-fired ceramic») pour des points d'accès 5G à 60 GHz. L'une des deux est à faisceau fixe, l'autre est à balayage électronique, avec un balayage de plus de 75° entre 57 GHz et 66 GHz. Les mesures démontrent l'efficacité des techniques d'analyse et de conception développées et valident les solutions technologiques proposées pour l'implémentation. Elles confirment les très bonnes performances des antennes CTS dépassant celles de solutions concurrentes. Enfin, nous proposons l'association de radomes polarisants planaires à faible profil aux antennes CTS, intrinsèquement à polarisation linéaire, pour réaliser des systèmes rayonnants en polarisation circulaire. Une méthodologie systématique pour la conception de polarisateurs à très large bande a été développée et validée numériquement. Un conception de polarisateur couvrant entièrement la bande Ka est présenté pour des applications satellite.

Plan de la thèse

Dans ce qui suit, nous proposons un bref résumé du contenu de chaque chapitre.

Au **Chapitre 1** nous commençons par expliquer la nécessité d'antennes à grande couverture et large bande dans des domaines d'applications bien spécifiés, c'est-à-dire les réseaux mobile 5G en bande millimétrique et les communications satellites en bande Ka. Le chapitre se poursuit avec un état de l'art.

Au **Chapitre 2** nous introduisons la structure de référence des antennes CTS qui sont étudiées et développées par la suite. En, particulier, nous présentons une antenne CTS multifaisceaux à haut-gain couvrant l'intégralité de la bande Ka, pour applications satellite.

Au **Chapitre 3** nous proposons des outils numériques pour l'analyse de la partie rayonnante des antennes CTS. L'impédance en balayage du réseau de fentes, éventuellement en présence d'un radôme diélectrique multicouche, est calculée, dans le cas d'un réseau infini, avec une méthode de « mode matching » dans le domaine spectral. Un circuit équivalent a été dérivé pour étudier ces réseaux. Nous présentons ainsi une approche pour évaluer les diagrammes de rayonnement qui repose sur l'évaluation de l'amplitude et de la phase du champ à la sortie du formateur de faisceaux, en utilisant une approche basée sur l'optique géométrique.

Enfin, nous analysons avec les outils développés, les relations entre les paramètres du réseau et le phénomène de directions aveugles qui provoque la presque totale annulation du faisceau pour certains angles de balayage. Un accent particulier est donné à l'impact de la périodicité du réseau. Une configuration utilisant une couche diélectrique placée sur l'ouverture a notamment étudiée

Au **Chapitre 4** nous proposons un outil pour l'analyse du réseau d'alimentation de l'antenne. Une approche modulaire est poursuivie dans la modélisation. Nous présentons les circuits équivalents et les modelés numériques utilisées pour les briques de bases du réseau. Nous proposons notamment une nouveau modèle numérique pour déterminer la matrice de diffusion d'un coude à 90° en guide d'onde à plans parallèles, essentiel pour atteindre une large bande de fonctionnement. Plusieurs topologies des diviseurs de puissance à bande large qui forment le réseau ont été considérés.

L'outil développé est enfin combiné à celui présenté au Chapitre 2, afin de déterminer le coefficient de réflexion à l'entrée du réseau d'alimentation. Les résultats présentent un très bon accord avec les simulations obtenues avec le logiciel commercial Ansys HFSS. Une réduction considérable du temps de calcul et de la mémoire allouée est réalisée.

Au **Chapitre 5** nous proposons de nouveaux systèmes antennaires CTS à 60 GHz, entièrement intégrés en technologies multicouches LTCC, et caractérisés expérimentalement. La réalisation des antennes CTS en technologie planaire favorise la miniaturisation et leur intégration «in-package» avec les autres composants du système radio. Nous introduisons un guide d'onde vertical entièrement intégrée dans le substrat qui supporte un mode quasi-TEM, en se rapprochant donc du fonctionnement d'un guide d'onde a plans parallèles. Nous présentons d'abord la conception et la réalisation d'une antenne CTS à faisceau fixe.

Les mesures présentent un très bon accord avec les simulations, et démontrent la validité de la conception et du processus de fabrication. La même plateforme technologique est donc exploitée pour réaliser un système antennaire multifaisceaux à balayage électronique, conçue pour des points d'accès haut-débit. Afin d'obtenir un fort recoupement entre les faisceaux et à la fois de faibles niveaux de lobes secondaires, la structure comporte deux antennes CTS qui rayonnent des faisceaux entrelacés et activés séparément en utilisant un réseau de commutateurs. La mesure et les résultats numériques confirment que les objectifs sont atteints pour un balayage de ±38° et pour des fréquences allant de 57 GHz à 66 GHz.

Au **Chapitre 6** nous proposons des radomes polarisants à faible profil et large bande pour réaliser des réseaux CTS en polarisation circulaire sans modifier l'architecture de l'antenne. Nous présentons une procédure de conception systématique reposant sur la manipulation des caractéristiques de dispersion des deux circuits équivalents qui modélisent le polariseur par des ondes incidentes en polarisation verticale et horizontale. Des cellules unitaires passe-haut ont été sélectionnées pour atteindre un fonctionnement large bande. Nous présentons la conception d'un polariseur qui comprend trois surfaces d'impédance anisotropes et deux substrats. Le polariseur vise à être intégré avec l'antenne CTS en bande Ka présentée au Chapitre 1, pour des applications Satcom. Les résultats numériques montrent que le polariseur possède une bande passante relative dépassant 48% pour une gamme d'incidence d'au moins ±30°.

Au **Chapitre 7** nous dressons un bilan global des principaux résultats de la thèse en soulignant aussi quelques questions ouvertes qui restent encore à résoudre et également de possibles développements futurs

Abstract

The ever-growing demand for fast and seamless connectivity shows the need of new communication paradigms and wideband radio technologies operating at millimeter-waves. Novel antenna concepts are essential to meet the specifications required in emerging applications in this frequency range, such as high-throughput 5G mobile networks and satellite communications. In this scenario, the antenna should achieve beam steering, low profile and an optimal trade-off among bandwidth, gain, efficiency, power consumption and fabrication complexity.

This work presents a promising antenna system to answer these needs: a parallel-fed continuous transverse stub (CTS) array fed by a quasi-optical beamformer. The antenna comprises an array of long slots, a corporate feed network based on parallel plate waveguides (PPWs) and an integrated quasi-optical system with a parabolic reflector illuminated by a focal array of horns. The non-dispersive behavior of the PPWs, operating in the transverse electromagnetic (TEM) mode, and the accurate design of the array provide wideband performance. The beamformer allows for passive beam steering in one plane, over a large scan range.

Efficient analysis tools are developed for each subsystem which enable a modular design of the antenna. A mode matching procedure is proposed to derive the active impedance of the array, in an infinite periodic environment. Based on this procedure, the scanning capabilities are assessed and a circuit representation of the array is derived. In particular, scan blindness phenomena are extensively investigated.

The main building blocks of the corporate feed network are modeled by means of equivalent circuits and ad-hoc numerical methods. The performance of the network are analyzed using a transmission matrix approach. The quasi-optical system dictates the characteristics of the radiated beams and is analyzed by means of geometrical and physical optics techniques.

These analysis methods are exploited in the design of low-profile 60-GHz antennas, fully-integrated in multilayer low temperature co-fired ceramic (LTCC) modules. Novel technological solutions to create substrate-integrated PPW-like structures are discussed.

First, the design and experimental characterization of a fixed-beam CTS array in LTCC is presented to validate the proposed technology. Then, a multibeam design, with a co-integrated switch network, is proposed. This antenna achieves wide scan range and high beam crossover levels, and is suitable for 5G wireless access points at 60 GHz.

Finally, the possibility to combine CTS arrays with linear-to-circular polarization converters to realize low-profile, wideband circularly-polarized antennas is discussed. A novel topology based on three anisotropic metasurfaces is presented. The dispersion properties of the device using a novel design procedure. High polarization purity and broadband operation are achieved with respect to standard meander-line polarizers.

Keywords: multibeam antennas, CTS antennas, wide-angle scanning antennas, braodband arrays, mode matching, LTCC technology.

Contents

List of Figures

List of Tables

Chapter 1

Introduction

In the new millennium, the huge demand for high data rate wireless services and ubiquitous connectivity showed the need for novel communication paradigms and radio technologies. The saturation of the spectrum currently exploited for civil telecommunications and the availability of larger channel bandwidths at higher frequencies boosted the development of communication systems at millimeter waves (mm-waves). Satellite systems will increasingly operate in the Ka-band (26.5 GHz - 40 GHz). Experimental programs for satellite communications (Satcom) between 40 GHz and 50 GHz have been already started [1]. Fifth-generation (5G) mobile networks will also exploit the mm-wave spectrum [2–4]. In particular, the use of large bandwidths in the V- and E-band have been proposed for enabling a high-speed, massive data transfer.

These applications require broadband antenna systems, with wide-angle scanning capabilities, and small form factors, tightly integrated with the transceivers. The simultaneous achievement of all these requirement poses design and technological challenges. Phased arrays and reflector antennas attain the highest performance among the present solutions. However, both these antenna systems are expensive and complex due to the electronics (phased array) or to mechanical and encumbrance issues (reflectors). Multiple beam antennas fed by passive beamformers are preferable to pursue costs reduction, but novel designs are needed to improve the performance.

In this scenario, there is a clear need for innovative scanning array architectures, accurate models for their analysis and design, and novel technological solutions for the realization of compact mm-wave antenna modules. These three research lines are developed in this thesis, that focuses on a particular broadband multibeam antenna solution: the continuous transverse stub (CTS) array.

1.1 Broadband, wide-angle scanning antennas for mm-wave applications

Broadband antennas with beam steering capabilities and large fields of view are required for a wide range of applications, from low-frequency radio astronomy [5] to sub-mm-wave instruments and imaging system [6]. In this section we highlight the need of novel antenna concepts for emerging applications at mm-waves. We will focus on the two specific applications that will be addressed in this thesis: new generation satellite communications and 5G networks.

1.1.1 Satellite communications in the Ka-band

The available capacity of existing Ku-band satellites is rapidly exhausting. Ka-band satellite communications receive increasing attention because of the availability of larger bandwidths, suitable for braodband services, and the size reduction of the terminal antennas. Several bands are allocated for different services and regulated by international standardization institutions, such as ETSI and ITU. The civil communications with geostationary satellites exploits the bands from 17.7 GHz to 20.2 GHz, for the downlink, and from 27.5 GHz to 30.0 GHz for the uplink. Moreover, the bands from 20.2 GHz to 21.2 GHz and from 30.0 GHz to 31.0 GHz are reserved for military applications. The use of the entire Ka-band and of even higher frequencies (40 GHz - 50 GHz) is currently being investigated in several research programs, e.g. in Paraboni experiment [1].

The possibility to cover both the downlink and uplink bands using the same hardware is definitely attractive in view of the reduction of costs and size that could be achieved. To this end, antennas with a fractional bandwidths exceeding 50% are needed.

Circular polarization is generally required to avoid the polarization mismatch due to the Faraday rotation experienced by a signal propagating in the atmosphere [7, 8].

High gain on-board satellite antennas are employed to achieve a multibeam spot coverage by using different frequency channels and orthogonal polarizations (left-handed and right-handed polarizations) for adjacent cells. Wideband or frequency agile terminal antennas, with a reconfigurable polarization, are then needed.

A robust mobile satellite communication link can be achieved only through a fast and accurate beam tracking. A line-of-sight connection between satellite and terminal can never be guaranteed during normal operation due to blockage effects. Conventional terminal antennas track the satellite using mechanical beam steering. The antenna is typically mounted on a two-axis positioner that adjusts its orientation so that it continuously points towards the satellite. The internal momentum of mechanically steered antennas can be a real issue

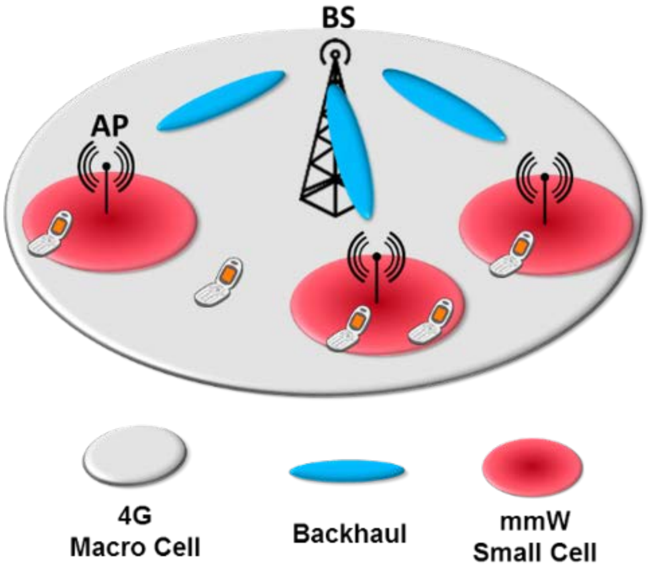

Figure 1.1: Basic scheme of a heterogeneous 5G wireless network, based on small cells with high-throughput access points at mm-waves.

for tracking accuracy. In many application scenarios, and especially for satellite communications on-the-move, ground terminals are deployed on highly dynamic platforms, e.g. vehicles and high-speed trains and low-profile, lightweight systems are needed. As a consequence, beam-switching antennas with large fields of views represent attractive solutions. They achieve an electronic scanning in the elevation plane with a reduced power consumption and a limited number of active devices, as compared to phased arrays. Hybrid electro-mechanical beam steering techniques can be employed to scan in the azimuth plane.

1.1.2 Millimeter-wave 5G mobile networks

The estimated mobile traffic in 2017 exceeds 11 exabytes per month. The data rate increase provided by every new generation of cellular networks is not sufficient to face the growth of the annual demand. Disruptive concepts in the design of the networks are currently being investigated. The first demonstrations of multi-Gb/s links at mm-waves [9, 10] and the advancements of radio technologies in this frequency range pushed operators and researchers to propose 5G network operating in the unlicensed 60-GHz-band (57-66 GHz) and in the light licensed E-band (71-76 GHz and 81-86 GHz). Networks based on a heterogeneous architecture are currently considered an effective solution that could be implemented in the next years. A scheme of a possible future 5G network is shown in Fig. 1.1. It includes small cells that operate at mm-waves, distributed in a standard macro-cell, and enable high data rate access points, e.g. 2-5 Gb/s near the access point and 250 Mb/s at the periphery of the cell. These small cells, with a radius in the order of 50 m, are connected to the base station of the macro-cell by mm-wave backhual links.

In this thesis, we will focus in particular on innovative antenna solutions for the access points. Antennas with high beam scanning performance and large field of views ($> 60°$ in the elevation plane [3]) are required to cope with the mobility of the users. Along with planar phased arrays, switched-beam antennas were proposed to realize the same function at lower costs. However, high beam overlap levels (≈ -3 dB), which are not easy to achieve using passive beamformers, are needed to provide a seamless and robust link with the user in the entire cell. The antennas should be suitable for highly-integrated system-in-package that represent the state-of-the-art solution for compact and efficient radio modules at mm-waves. The minimization of the losses, and in particular of those due to interconnect, is indeed a key requirement, since the attenuation at mm-waves is significantly higher than that observed in the microwave bands currently exploited for mobile communications. Low form factors and lightweight are also highly desirable characteristics that ease the installation on urban utility poles or street lamps and that minimize the environmental impact.

1.2 Limitations of present scanning antennas

Several antenna solutions have been proposed to achieve wide-angle scanning performance. Each solution is characterized by trade-offs and limitations. For instance, a large field of view is typical attained over moderate frequency bandwidths. Ultrawideband antennas, such as Vivaldi arrays [11, 12], often exhibit high cross-polarization levels. Advanced beam steering capabilities, such as simultaneous scanning in two planes (2-D scanning), and the effort to miniaturize the components drive up costs and increase the system complexity.

Table 1.1 provides a synthetic comparison of the performance of the most common wide-angle scanning antenna solutions at millimeter-waves. Reflector antennas [13, 14] ensure broadband operation and wide angular coverage and can be fabricated at low costs. However, the bulk and the weight of the reflectors restrict the domains of applications. Moreover, dedicated mechanical systems are required to steer the beam, which increase the size and the costs of the overall module. Even though more compact than reflectors, lens antennas [15–17] are bulky and are not usually considered for Satcom-on-the-move applications.

Phased arrays provide electronic 2-D scanning, with a fast and flexible beam steering control. This is a key advantage over the other antennas which require mechanical beam steering or hybrid electro-mechical systems. Standard phased arrays comprise resonant elements excited by planar feed networks which lower the antenna efficiency, especially for large arrays. Stacked [18, 19] and cavity-backed patches [20] are used as radiating elements

Table 1.1: Comparison of wide-angle scanning antennas. Figures of merit are rated with a scale from 1 to 5.

	Reflector antennas	**Lens antennas**	**Slotted planar arrays**	**Phased arrays of patches**	**Connected arrays**
Scan mechanism	1-D: electronic 2-D: hybrid	1-D: electronic 2-D: hybrid	1-D: electronic 2-D: hybrid	2-D electronic	2-D: electronic
Bandwidth	4	3	2	2	5
Scan coverage	5	4	4	4	5
Polarization purity	5	3	3	3	4
Number of active devices	4	4	4	2	2
Encumbrance	1	2	4	3	3
Cost	3	3	3	2	2

to enhance the operating bandwidth, which however rarely exceeds 25%. Moreover, these antennas are particularly sensitive to dimensional and material tolerances at mm-waves, due to their resonant behaviour.

Advanced phased array architectures have been proposed to overcome these limitations. Among them, connected arrays [21–24] exhibit broadband, wide-angle scanning performance and achieve low cross-polarization levels. They consist of arrays of dipoles or slots which are electrically connected and periodically fed. Their ultrawideband behaviour is due to the mutual coupling of the connected elements that results in smooth current distributions, nearly constant with frequency. However, like any phased array, connected arrays require several feeds in a double mesh grid with a periodicity lower than half wavelength at the highest operating frequency. A transmit/receive (TX/RX) module is associated to each feed, increasing the number of active devices, and related costs. Moreover, the design of the feed network of a connected array is not trivial and may significantly reduce the bandwidth [23]. Finally, most designs feature a backing ground reflector which increases the size of the system.

Switched-beam antennas represent attractive alternatives to phased arrays, especially for beam scanning in a single plane, that drastically reduce the number of active devices and the system complexity. Passive beamforming networks, either circuit-based, e.g. Butler matrices [25], or quasi-optical, e.g. Rotman lenses [26] and pillbox couplers [27], generate a discrete set of beams. The excitation of a specific beam is controlled by a switch network. Slotted planar arrays, based on rectangular, ridged or parallel plate waveguides, have been proposed for the realization of flat multibeam antenna panels, achieving high gain and high radiation efficiency. Several embodiments using standard hollow waveguides [28–30] or substrate integrated waveguides [31, 32] have been presented. However, these solutions are characterized by a narrowband behaviour, especially when they comprise slotted rectangular waveguide arrays. The bandwidth reduction can be mitigated by designing wideband, multilayer feed networks which complicate the stack-ups and the fabrication, in particular at millimeter-waves.

This thesis will focus on an antenna solution, the parallel-fed continuous transverse stub (CTS) array, that combines the advantages of passive multibeam antennas and the high performance of broadband phased arrays. CTS antennas are based on linear arrays of long slots, excited by a line source that can be generated by a passive beamformer, and achieve wide-angle electronic beam scanning in one plane. A review of CTS antennas and the specific antenna architecture that will be analyzed and developed in this work are presented in Chapter 2.

1.3 Outline of the thesis

This thesis is structured in three main parts. In the first, parallel-fed CTS antennas, excited by quasi-optical beamformer are presented. Original numerical models are proposed for their analysis and design. Particular emphasis is put on the study of the scanning performance. The second part presents novel designs and technological solutions for the integration of wide-angle scanning CTS antennas in flat modules, based on multilayer substrates and standard planar processes. The design and characterization of two antenna prototypes in LTCC technology are presented. In the third part, low-profile, ultra-wideband linear-to-circular polarization (LP-to-CP) converters are proposed to realize high performance circularly polarized CTS arrays and a novel approach for their design is outlined.

The first two parts were developed in the framework of the FP7 European project “MiWaveS", for the development of 5G heterogeneous mm-wave networks, and of two R&D projects with the French Space Agency (CNES), targeting novel antenna architectures for Ka-band satellite communications. The research leading to the results presented in the third part was carried out in collaboration with Prof. Anthony Grbic at the University of Michigan, Ann Arbor, USA.

More in details, this manuscript is organized as follows.

Chapter 2 provides an overview on CTS antennas, describing the principles of operation and the main antenna architectures proposed in the literature. The design, realization and characterization of a wideband, wide-angle scanning parallel-fed CTS antenna operating in the Ka-band are discussed in details. The architecture of this antenna will be the reference structure for the numerical models, technological developments and designs proposed in the thesis.

Chapter 3 focuses on the analysis of the array of long slots of the proposed CTS antenna. A mode matching method, based on a spectral Green's function approach, is developed to compute the active impedance of the radiating slots, in an infinite array environment, possibly loaded by a planar layered dielectric medium. A circuit representation of the array is derived from the expression of the active impedance.

An approach for the evaluation of the radiation pattern of a multibeam CTS antenna is presented.

Finally, the tools developed are employed to investigate the scanning performance of CTS arrays and to study possible scan blindness phenomena. The impact of the design parameters on the onset of blind spot is extensively discussed.

Chapter 4 presents a numerical tool for the analysis of the PPW corporate feed network of the CTS antenna. A modular approach is followed. The network is divided into building blocks that are studied using equivalent circuits and *ad-hoc* numerical models. A novel model for the analysis of a compensated right-angle bend is proposed. Several types of power dividers and the related models are presented. The numerical tools developed in Chapter 3 and in this chapter are combined to evaluate the reflection coefficient at the input of the corporate feed network. This approach is validated through comparisons with full-wave simulations and achieves a significant reduction of the computation time.

Chapter 5 proposes novel design and fabrication approaches for the realization of flat CTS antennas in multilayer dielectric substrates, suitable for highly-integrated mm-wave systems-in-package. A novel waveguide, based on parallel rows of vias, that supports the propagation of a quasi-TEM mode along the vertical axis of the substrate is proposed. The design and characterization of two V-band antennas, integrated in LTCC technology, are discussed. First, a fixed beam antenna is implemented to demonstrate the validity of the proposed technology. Then, a beam switching antenna module, with a field of view of ±38° and high beam overlap levels, is presented, with applications to 5G access points at 60 GHz. It comprises two CTS antennas that radiate interleaved beams and are controlled by a switch network, co-integrated in the same LTCC module.

Chapter 6 proposes the combination of low-profile, wideband LP-to-CP converters and standard CTS antennas to achieve circular polarization without modifying the basic antenna architecture. We propose a systematic procedure for the design of these polarizers. A configuration based on three anisotropic sheets and two dielectric slabs is investigated. A wideband, low-loss performance is achieved by engineering the dispersion relations of the polarizer, when shined by a vertically and a horizontally polarized field, respectively. A design for Ka-band Satcom applications is presented and numerically validated.

Chapter 7 reviews the main contributions of this thesis and provides an outlook on possible future developments.

Chapter 2

Continuous transverse stub antennas

The continuous transverse stub (CTS) has been originally proposed by Raytheon Systems Company in 1991 [33], as a high-performance solution that could offer a low-cost alternative to conventional phased arrays. In the last twenty-five years, many variants of the CTS array have been presented and successfully demonstrated using different technologies, in frequency ranges spanning from C-band [34, 35] to W-band [36]. All these embodiments share the unique characteristics of CTS systems: ultrawideband behavior, high efficiency, packaging and cost advantages as compared to competing approaches. Most CTS arrays are protected by patents and only a few journal papers are available in the open literature. This hinders a clear understanding of the physics at the basis of their operation, of the methods and technologies used for their analysis and design. These aspects will be covered from this chapter onwards.

The basic principles of operation of CTS arrays, the main antenna architectures and the performance they can offer are briefly reviewed and discussed in Section 2.1. A particular focus on the reference CTS structure, analyzed and further developed in this thesis, is given in Section 2.2. The latter presents the detailed design, realization and characterization of a parallel-fed multibeam CTS antenna, fed by a quasi-optical beamformer for Ka-band satellite communications.

2.1 Principle of operation and antenna architectures

The CTS array differs markedly from other planar antennas and electronically scanned arrays in terms of architecture, feeding system and radiation mechanism. Despite the variety of designs presented in the literature, all CTS antennas comprise broad, continuous radiating stubs that are connected to a parallel plate structure, excited by a primary line source. The structure is based on low-loss parallel plate waveguides (PPWs), truncated in

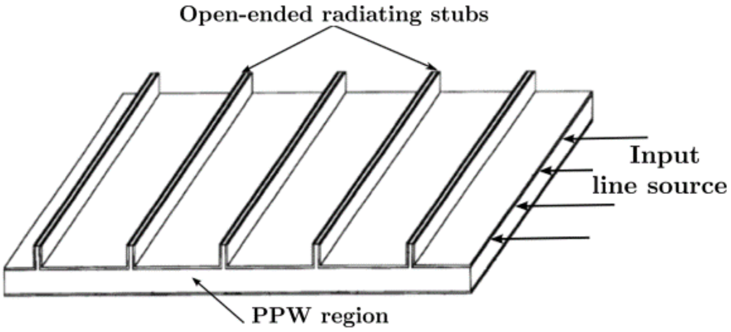

(a)

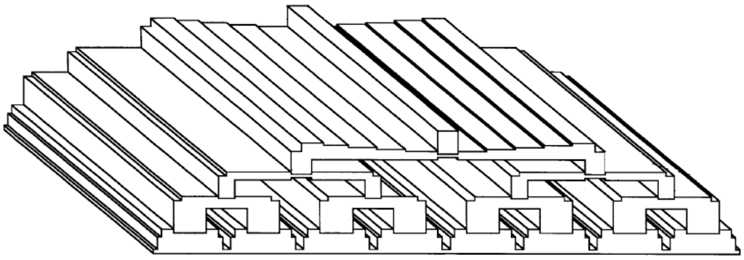

(b)

Figure 2.1: (a) Series-fed CTS architecture [34]. (b) Parallel-fed CTS architecture [38]. The radiating aperture is shown at the bottom of the figure.

the direction parallel to the broad edge of the stubs, or overmoded rectangular waveguides operating far from the cut-off frequency, if metallic edge walls are added. In both cases, a quasi-TEM mode propagates and a nearly non-dispersive operation is achieved. The presence of the transverse stubs interrupts the longitudinal currents within the PPWs. As a result, electromagnetic waves propagates through the stubs and are radiated at their open ends. Given the line source excitation and the continuous nature of the radiators, the radiated field is linearly-polarized. The cross-polarization levels are typically less than −30 dB and mainly depend on the purity of the excitation. The line source may be either a discrete linear array, such as a slotted waveguide or a phased array, or a continuous line source such as a pillbox system [27, 37] or a sectoral horn.

CTS can be subdivided into two main classes, based on series-fed and parallel-fed architecture, respectively. These configurations are illustrated in Fig. 2.1.

2.1.1 Series-fed architecture

A series-fed CTS antenna [33, 39] consists of an array of open-ended stubs, finite in height, extending from the upper conductive plate of a PPW. The antenna beam can be steered in the H-plane, i.e. along the broad edge of the stubs, by varying the angle of incidence of the wavefront launched in the PPW, as illustrated in Fig. 2.2. This can be achieved using

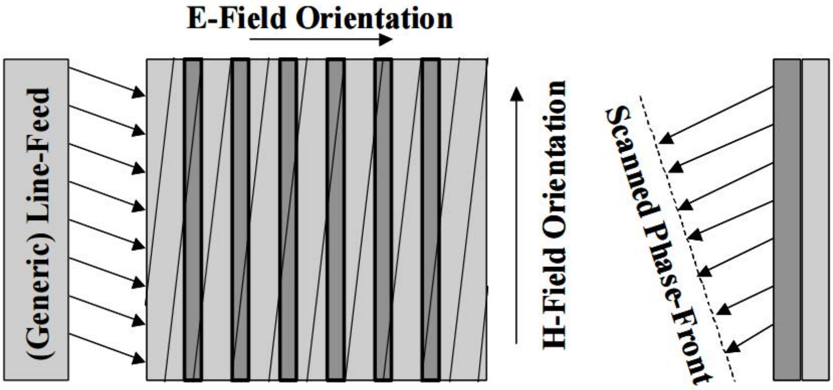

Figure 2.2: Scanning mechanism in the H-plane [35]. The beamformer generates a quasi-plane wave whose wavefront is tilted with respect to the direction of alignment of the stubs. The beam pointing direction is thus scanned in the H-plane.

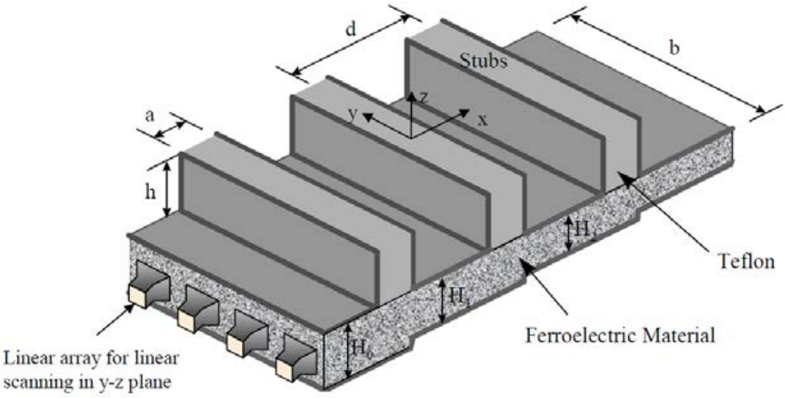

Figure 2.3: Possible technique to realize a series-fed CTS array with 2-D beam scanning capabilities [40]. The beam is steered in the E-plane by modulating along the x-direction the dielectric properties of the ferroelectric material inside the PPW. A linear array creates the line source, enabling the beam steering in the H-plane.

a mechanical system to control the position and the orientation of the primary line source. If the excitation is provided by a phased array, the wavefront can be electronically tilted. Alternatively, the phase velocity of the incident wave can be changed by modulating the constituent properties of the medium in the H-plane, e.g. using ferroelectric materials.

Being a traveling-wave structure [41], the series-fed CTS antenna exhibits a frequency-scanning behaviour in the E-plane, i.e. along the direction where the stubs are arrayed. High dielectric materials can be used to increase the variation of the beam pointing direction with frequency [33]. Beam scanning in the E-plane can be also attained by controlling the phase velocity of the wave propagating in the PPW [34]. To this end, several methods have been devised, such as the use of non-linear voltage variable dielectrics in the PPW structure

[40] and the direct implantation of varactor diodes in the parallel plate structure [35]. It is possible to simultaneously steer the beam in the two principal planes (2-D beam scanning) by combining the aforementioned beamforming techniques. A possible 2-D beam scanning architecture [40] is shown in Fig. 2.3. An electronic scanning line source (see Fig. 2.2) is employed to steer the beam in the H-plane. The control of the phase velocity along the propagation direction in the PPW, filled with a ferroelectric material, enables the E-plane scanning. This reveals a first advantage of CTS architectures over standard planar phased arrays. A CTS antenna allows for beam scanning in the H-plane or in both principal planes using a linear array of N stubs, whereas a phased array with an equivalent aperture generally comprises $N \times N$ elements, each connected to a dedicated phase shifter. Moreover, a CTS array has the same cross-section along the broad edge of the radiating elements, which significantly reduces fabrication costs, as compared to fully-populated planar arrays.

The active impedance [42] of the array can be made nearly real and almost frequency-independent over a wide range of frequencies (more than an octave) and of scan angles by properly selecting the periodicity and the height of stubs, the height of the PPW and the dielectrics filling the structure. The impedance bandwidth can benefit from the mutual coupling among the radiating stubs [33, 35], due to their close proximity and parallel orientation. This coupling can be exploited, through a proper design, to attain a non-resonant frequency response of the elements. A similar behaviour is observed in connected arrays [22, 43], whereas it is uncommon for standard planar phased array architectures based on resonant antenna elements, e.g. patches or slots. The scanning performance depends on the characteristics of the line source. Due to the continuous nature of the radiating elements, large fields of view can be covered in the H-plane, using an appropriate beamformer to generate scanned linear phase-fronts.

The low-dispersive parallel plate environment ensures wideband and low-loss operation. The theoretical dissipative losses for the PPW exciting a series-fed CTS array are about one-half of those associated with a rectangular waveguide of the same length, realized with identical materials and operating at the same frequency [34].

2.1.2 Parallel-fed architecture

Parallel-fed or true-time-delay (TTD) CTS arrays [38, 44–47] were later introduced to further enhance the active impedance bandwidth of the array. A schematic view of this configuration is shown in Fig. 2.1b. Unlike the series-fed variant, the field launched by the line source in the parallel plate structure is coupled to a PPW corporate feed network that excites long radiating slots (stubs of zero thickness) realized in a ground plane on the top of

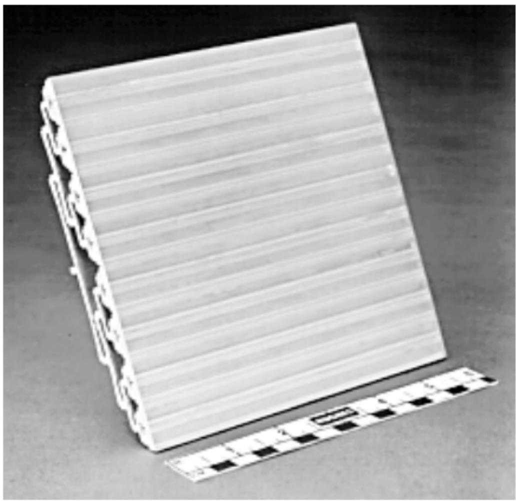

(a)

(b)

Figure 2.4: Two parallel-fed CTS arrays: (a) an antenna operating from 5 GHz to 20 GHz [35] (size: 15 cm × 15 cm); (b) a Ka-band antenna by Cobham [49] (size: 30 cm × 20 cm). The details of the corporate feed network can be recognized.

the structure. A similar antenna concept was previously presented in [48], based on coaxial transmission lines.

Due to the quasi-TEM propagation and to the parallel excitation of the slots, the parallel-fed architecture can achieve wider impedance bandwidths than the series-fed one, which is, instead, limited by the frequency variations of the electrical path between adjacent stubs. The active impedance of parallel-fed CTS arrays, seen at the radiating slots, is almost frequency independent over several octaves, as it will be clear from the analysis provided in Chapter 3. Parallel-fed CTS antennas can be fabricated in hollow PPW technology by means of computer numerical control (CNC) machining techniques or using extruded and injection molding. Multilayer printed circuit board (PCB) processes have been also employed [49], even though their complexity is generally high. A solution to ease the fabrication of parallel-fed CTS antennas in multilayer substrates, using planar processes, is

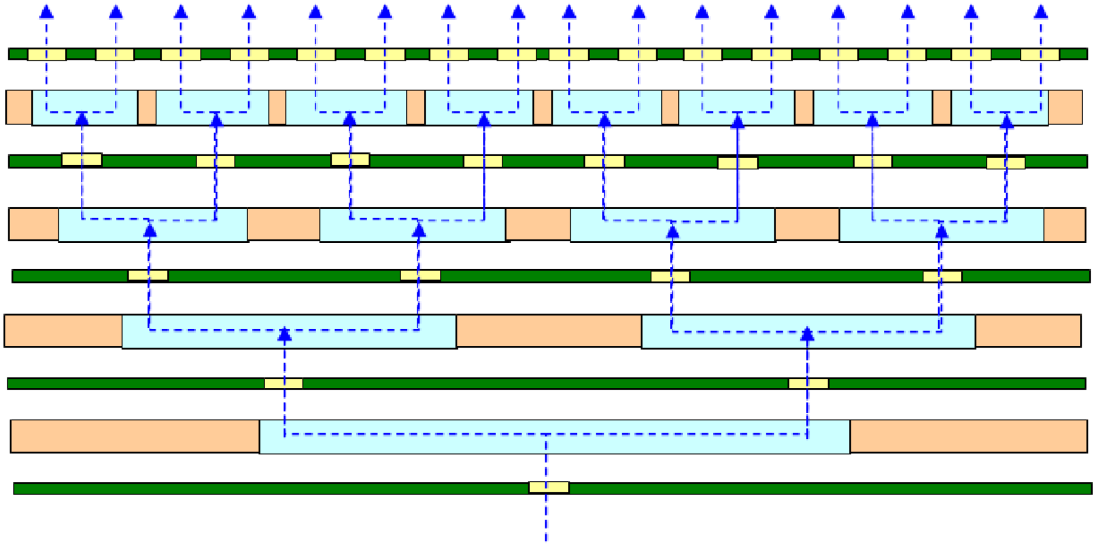

Figure 2.5: Stack-up and assembly of the multilayer parallel-fed CTS arrays of Fig. 2.4b. Conductive adhesive layers are used to bond the dielectric substrates. Coupling slots are employed to ensure the propagation in the vertical direction.

proposed in Chapter 5, with particular emphasis on LTCC technology.

Two different embodiments are shown in Fig. 2.4. The prototype of Fig. 2.4a comprises hollow PPWs and achieves an aperture efficiency greater than 70% from 5 GHz to 20 GHz. The multilayer antenna shown in Fig. 2.4b covers both the receiving and transmitting bands for Ka-band Satcom applications, with excellent radiation characteristics.

However, a challenging manufacturing process, illustrated in Fig. 2.5, and a large number of dielectric layers (about forty) were employed. The PPWs in the corporate feed network are implemented by realizing numerous cavities in the substrate layers, with metalized walls. Costly conductive adhesives were used to bond the substrates. The propagation along the vertical axis of the structure is enabled by aperture coupling slots etched in specific substrate layers. Several issues are associated to this procedure. The high-temperature bonding cycles may damage the profiles of the cavities, degrading the antenna performance. Moreover, the conductive adhesive layers introduce significant losses.

A method to connect PPW structures fabricated in stacked substrates using dielectric bonding layers, has been proposed in the framework of this Ph.D. work and is currently patent pending [50]. This technique and the implementation of vertical PPW structures by means of rows of vias, discussed in Chapter 5, pave new ways for integration of large, low-loss CTS arrays in multilayer dielectric substrates.

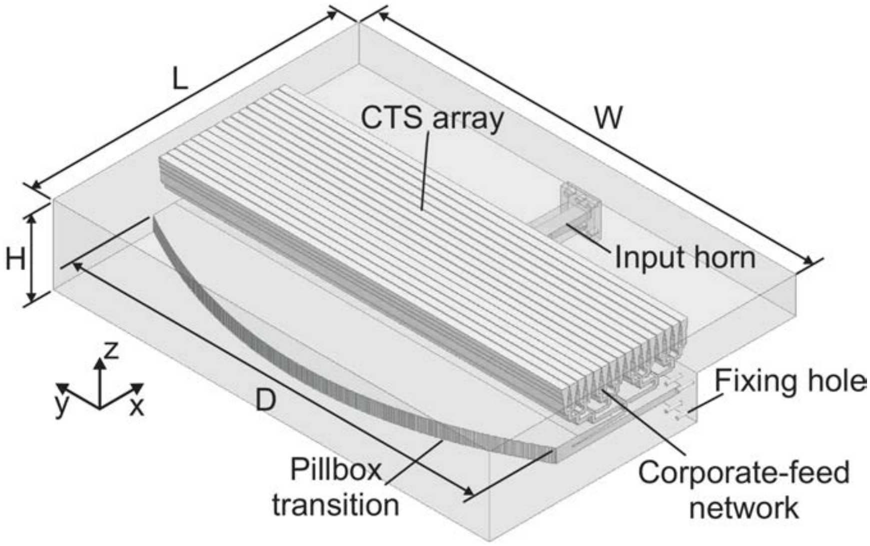

(a)

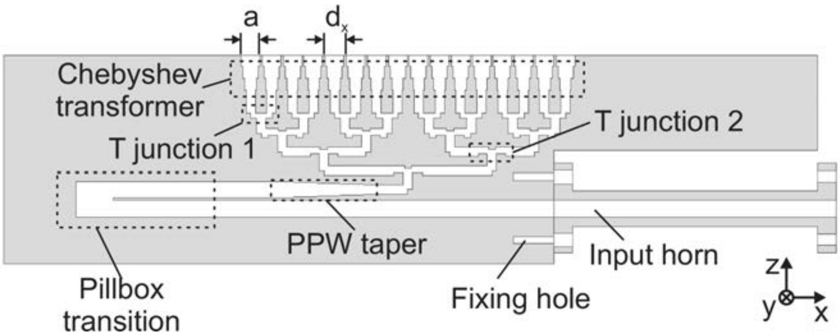

(b)

Figure 2.6: CTS array. (a) Perspective view. (b) Cross sectional view taken along the xz-plane. The various building blocks are highlighted. a and d_x denote the slot width and slot periodicity, respectively.

2.2 A CTS antenna fed by a quasi-optical system for Ka-band applications

This section describes the design, the realization and the experimental characterization of a flat, high-gain parallel-fed CTS array, suitable for Satcom applications in the Ka-band [47]. In particular, this antenna has been designed for operation between 27.5 GHz and 31 GHz, i.e. the band allocated for transmitting Satcom units. Nevertheless, high scanning performance are achieved over the entire Ka-band.

The parallel-fed architecture of this antenna will represent the reference structure for all the numerical models, the technological developments and the designs proposed in the next chapters. The perspective view and the cross-section of the system are shown in Fig. 2.6. The array comprises 16 slots, excited by a corporate feed network, realized with hollow

PPWs, that provides an equal power split. The generation of the line source that excites the CTS array is crucial for the scanning and bandwidth performance of the overall antenna. The quasi-optical beamformer employed in this design features a pillbox coupler [27], based on an integrated 2-D parabolic that is illuminated by a single input horn. This quasi-optical system typically attains broadband operation in a scan range wider than ±30° [37, 51, 52]. The antenna beam is mechanically steered in the H-plane (yz-plane in Fig. 2.6) by moving the feed horn.

The final structure has been fabricated in several aluminium parts, using standard milling and wire electric discharge machining (EDM) processes. These blocks are screwed together and the electrical contact is preserved without any bonding layer or electromagnetic choke. The antenna size is 17.5 cm × 27.0 cm × 4.5 cm.

2.2.1 Design of the slot array

The two array parameters that control the matching performance are the slot width a and the array periodicity d_x (see Fig. 2.6). For simplicity, we assume that slots are infinite along the y-direction. In actual CTS designs, the slot length is much greater than the free-space wavelength and has a small impact on the matching. Moreover, the edge effects along the y-direction are nearly negligible, given the field taper imposed by the quasi-optical system. Numerical models for the slot array and an extensive analysis of the impact of its parameters on the antenna performance are presented in Chapter 5. Here the main trade-offs and constraints encountered in the design are pointed out and some heuristic guidelines to maximize the bandwidth are given.

The upper bound for the slot width a is set by the highest operating frequency f_c. A single mode TEM excitation of the slots is achieved over the entire band if $a < a_{max} = c/2f_c$, being c the speed of light in free-space. By setting $f_c = 31$ GHz, the constraint $a < a_{max} = 4.84$ mm is obtained. On the other hand, as it will be demonstrated in Chapter 3, high d_x/a ratios, and thus small values of a, determine a severe mismatch between the impedance seen at each slot and the characteristic impedance of the PPWs that feed the slots. In addition, small slot widths result in larger ohmic losses [53].The value $a = 0.83\ a_{max} = 4$ mm is chosen for the slot width, so that the cut-off frequency of the first higher order mode is set to 37.5 GHz.

The constraints on the inter-element spacing d_x are less stringent. However, large array spacings results in poor matching characteristics, since a can not be increased beyond a_{max}, and may determine scan blindness (see Chapter 3). On the other hand, tightly spaced slots make harder the design of the corporate feed network along the x direction. As a good

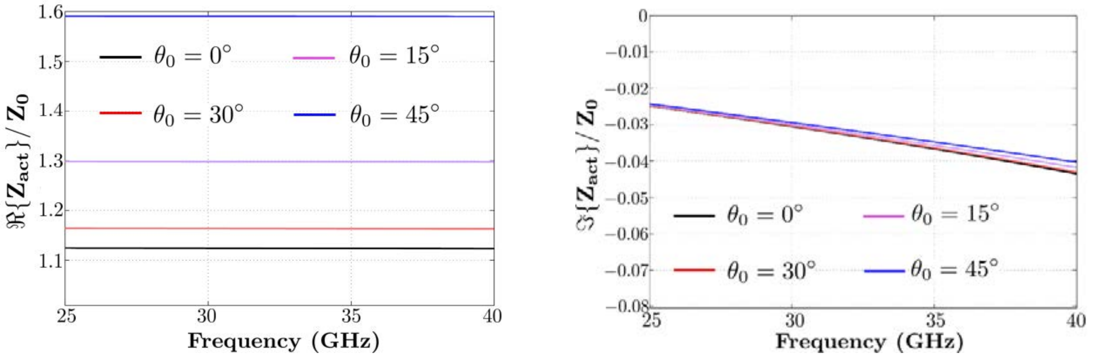

(a) (b)

Figure 2.7: Normalized active slot impedance of an infinite CTS array with $d_x = 4.5$ mm and $a = 4.0$ mm for different pointing directions in the H-plane, $\theta = (0°, 15°, 30°, 45°)$. (a) Real part of Z_{act}. (b) Imaginary part of Z_{act}. The active impedance is normalized to the characteristic impedance Z_0 of the feeding PPWs.

compromise between these two opposite exigences, the array periodicity has been fixed to $d_x = 4.5$ mm.

The active impedance Z_{act} of the array, simulated in an infinite environment for different scan angles in the H-plane, is plotted in Fig. 2.7. It represents the impedance seen at each slot when all elements are excited. The real part of Z_{act} is almost constant versus frequency, thus providing the broadband behaviour of the array. The imaginary part is much smaller than the characteristic impedance Z_0 of the feeding PPW line and can be compensated by the corporate feed network. The active impedance keeps quite stable even when the array beam is steered in the H-plane, enabling wide-angle scanning performance. The real part increases by only a factor 1.2 when the beam is tilted at ±30°.

2.2.2 Design of the corporate feed network

The structure of the corporate feed network and the design of the building blocks it comprises are here discussed. Equivalent circuits and numerical models for an efficient analysis and design of such PPW feed networks are proposed in Chapter 4.

The PPW network is based on E-plane power dividers, arranged in multiple stages. It provides an equal amplitude to all the radiating slots, therefore the power dividers employed in the same stage are identical. Two different power divider designs, namely T-junction 1 and T-junction 2, have been used. A multisection impedance transformer is added between the radiating slots and the power dividers in the stage closest to the slots, in order to enhance the matching. The network supports only the fundamental TEM mode. The design frequency is fixed to $f_0 = 29.25$ GHz with a free space wavelength of $\lambda_0 = 10.26$ mm.

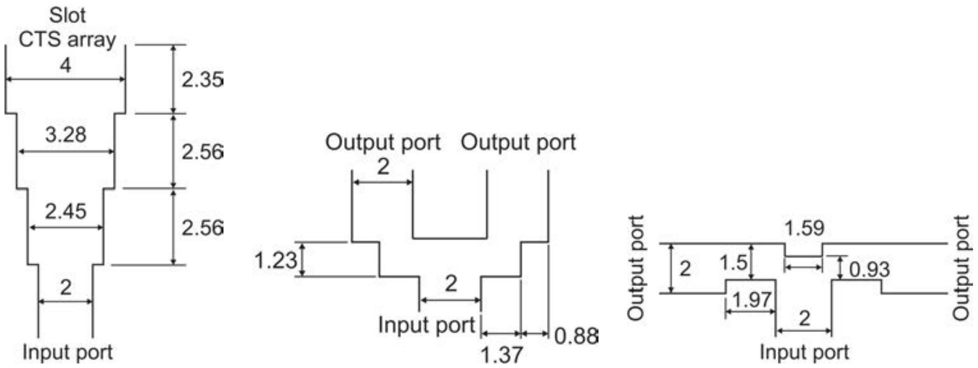

(a) (b) (c)

Figure 2.8: Cross sectional view along the xz-plane of the building blocks of the corporate-feed network. (a) Chebyshev transformer. (b) E-plane T-junction 1. (c) E-plane T-junction 2. All dimensions are given in millimeters.

Each component of the feed network is optimized to achieve an input reflection coefficient lower than −30 dB at its input port at the design frequency, for broadside radiation.

2.2.2.1 Chebyshev transformer

The two-section Chebyshev transformer shown in Fig. 2.8a has been used to match, over a wide band, the active impedance of the slots to a PPW line of height equal to 2 mm. This value is shared by all PPWs at the inputs and at the outputs of all power dividers. In particular, the height of the PPW at the input of the feed network is 2 mm. The procedure outlined in [54] has been used for designing the transformer. The design of the transformer assumes a single mode propagation. Higher order modes generated at the slot level are considered attenuated. The maximum reflection coefficient and the ratio between the load and characteristic impedances at the output and input ports have been chosen equal to 0.05 and 2, respectively. The final design parameters are shown in Fig. 2.8a.

2.2.2.2 E-plane T-junction 1

This E-plane T-junction (Fig. 2.8b) is used to match the input impedance of two consecutive slots seen at the output ports of the Chebyshev transformer to the input PPW feeding line of height 2.00 mm, as shown in Fig. 2.8b. The input and output ports present the same profile and thus the same characteristic impedance. A good matching is achieved by tuning the height of the PPW at the center part of the junction and by designing a reactive step in the 90° bends. The final design parameters are reported in Fig. 2.8b.

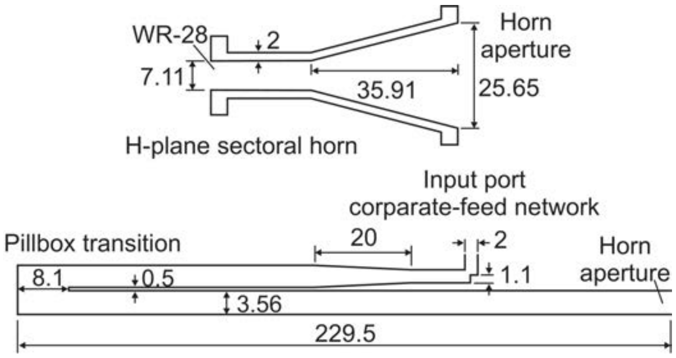

Figure 2.9: Cross sectional view along the xz-plane of the pillbox transition and of the input horn. Dimensions are given in millimeters.

2.2.2.3 E-plane T-junction 2

In this case (Fig. 2.8c), a classical power divider in PPW technology is associated to a quarter wavelength transformer for matching the output ports to the input one over a wide bandwidth [38,55]. The input and output ports have the same characteristic impedance and height (2.00 mm). The quarter wavelength transformer of height 1.50 mm is used to halve the impedance value at the output ports before joining the section with height 0.93 mm. A good matching is therefore achieved, since the output ports are seen in series by the input port. All geometrical parameters are reported in Fig. 2.8c.

2.2.2.4 Pillbox transition

The pillbox coupler, shown in Fig. 2.9, creates the line source needed to excite the CTS array. It is made by two stacked PPW lines coupled by a long slot of width 8.1 mm contouring a 2-D parabolic reflector. This coupling slot is realized in the metal plate, of thickness 0.5 mm, shared by the two PPWs. The quasi-optical system converts the cylindrical TEM mode launched by the H-plane sectoral horn in the lower PPW into a quasi-plane wave, that is coupled to the upper PPW and excites the corporate feed network. The guidelines provided in [27] and [52] have been followed for designing the pillbox transition. The parabolic reflector has a focal distance equal to $F = 10\,\lambda_0 = 102.6$ mm and a diameter of $D = 22.38\,\lambda_0 = 229.5$ mm. The system provides an edge tapering of about -30 dB. The horn aperture is equal to $2.5\,\lambda_0 = 25.65$ mm and is fed by a WR-28 waveguide, whose transverse section has size 7.11 mm × 3.56 mm. The horn is made in aluminium with a wall thickness of 2.00 mm. A smooth transition of length 20 mm is used to gradually reduce the height of the upper PPW in the region close to the corporate feed network. Finally, a 90° bend with a reactive step of height 1.10 mm connects the pillbox transition to the input port of the corporate feed network (see Fig. 2.8). The antenna main beam is steered in

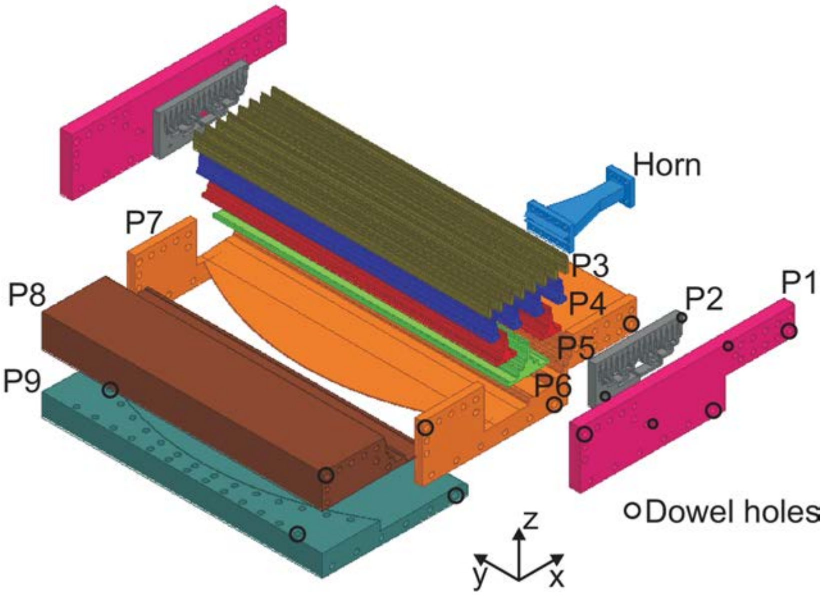

Figure 2.10: Manufacturing and assembling details. The various parts of the antenna are aligned with dowels and screwed together. Black circles indicate the positions of the dowels on one lateral side of the antenna. Dowel holes are present also on the other side.

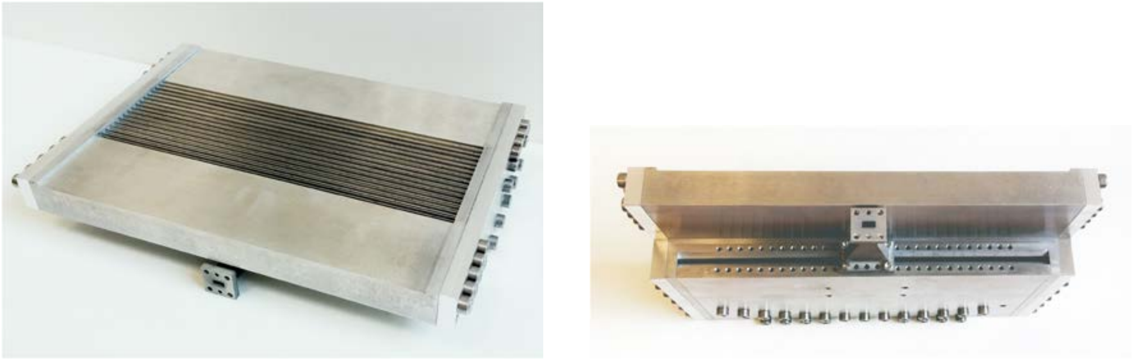

(a)

(b)

Figure 2.11: Antenna prototype. (a) 3D view. The CTS array and the input horn can be recognized. (b) Lateral view from the feeding side.

the H-plane by moving the input horn in the focal plane of the parabolic reflector. For this reason, the lower PPW is left open on the edge connected to the horn and several holes are made on this side of the antenna for fixing the horn, as shown in Fig. 2.11.

2.2.3 Prototype and measurements

An effective procedure based on the fabrication of separate modules and their assembly by means of screws has been employed to ease the realization of the antenna. As discussed in Section 2.1.2, the fabrication of parallel-fed CTS arrays may rely on costly bonding or

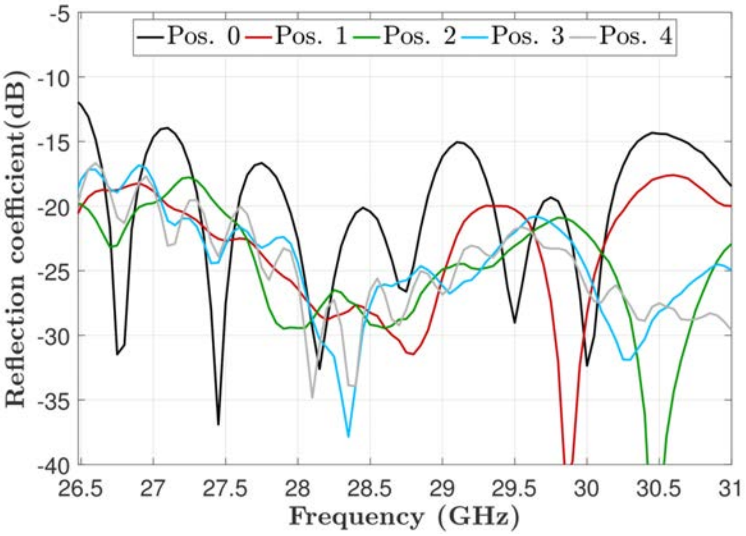

Figure 2.12: Measured input reflection coefficients of the CTS array for several positions of the input horn in the focal plane of the parabolic reflector.

brazing processes [56]. Corrugations and adhesive layers are used to ensure a good electric contact through the antenna structures, but they may introduce air-gaps, thus degrading the antenna performance.

In the present design, the corporate feed network and pillbox system have been divided in nine parts (P1 to P9), as shown in Fig. 2.10. Each part has been manufactured as a stand alone element using either a milling or an EDM process. The central part of the corporate feed network comprises parts P3-P6. These parts are assembled by sliding them in P2. The ensemble is fixed to P1 using dowels and then connected to P7. Parts P8 and P9 are joined together with dowels and slid into P7. Finally, screws are used on the lateral and bottom sides of the antenna to fix all sections. An alignment accuracy of about $10\,\mu$m is guaranteed by the dowels. A fabrication accuracy better than $50\,\mu$m is expected. The horn has been realized in a single piece by using an EDM process. The wedges on the horn aperture, as shown in Fig.2.10, are used for a better alignment with the lower PPW line of the antenna structure. Complementary wedges are made in P7 and P9. The final antenna prototype is shown in Fig. 2.11. The horn is fixed to the antenna by screws using the holes shown in Fig. 2.11, located in P7 and P9. The assembling solution does not employ any bonding process and does not require any electromagnetic choke among the various stages of the hollow corporate feed network, as opposed to previous CTS designs [56], thus reducing the complexity and cost of the overall structure.

The measurements have been repeated for different positions of the input horn in the focal plane of the reflector, in order to evaluate the scanning performance of the antenna. The step between two consecutive horn positions is equal to $1.25\,\lambda_0$, i.e. half the horn

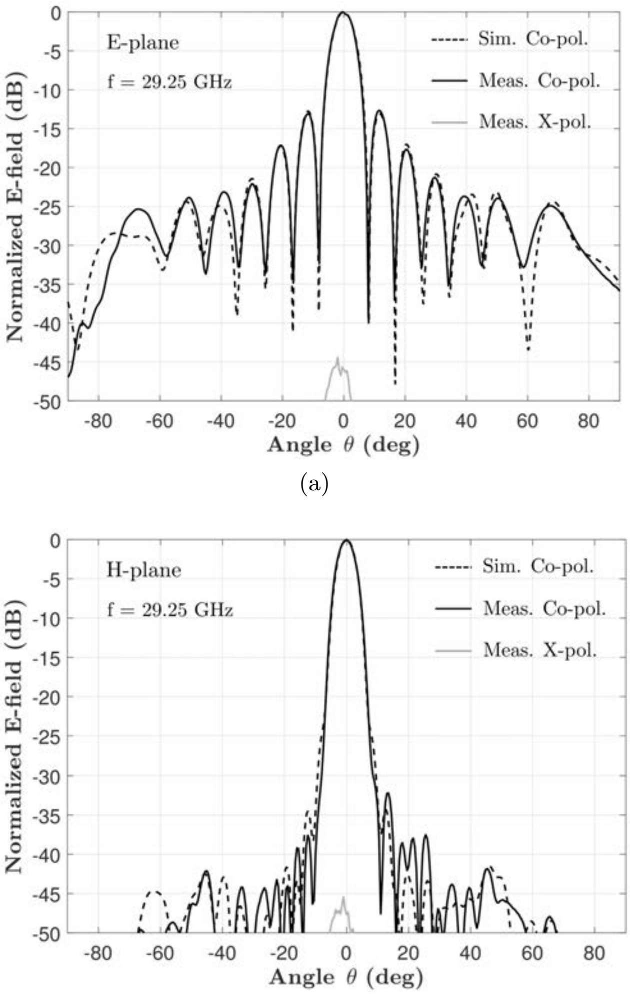

(a)

(b)

Figure 2.13: Normalized radiation patterns at the design frequency for broadside radiation. (a) E-plane. (b) H-plane.

aperture. The central position is denoted as Pos.0 and ascending numbers (Pos.1-Pos.6) are used for lateral positions along the positive y-axis. The antenna performance are reported only for positive displacements of the horn along the y direction. Indeed, similar results are obtained when the feed is placed in the negative y direction, since the design is symmetric. The antenna has been designed targeting a maximum scan angle in elevation of about 30° which corresponds to Pos.4.

The measured input reflection coefficients of the CTS array for various positions between 26.5 GHz and 31 GHz are shown in Fig. 2.12. The antenna is matched in the entire band. An input reflection coefficient better than -15 dB is obtained in the 27-31 GHz band for all scanning positions. For brevity, only experimental results are provided, but the measurements are in very good agreement with full-wave simulation results.

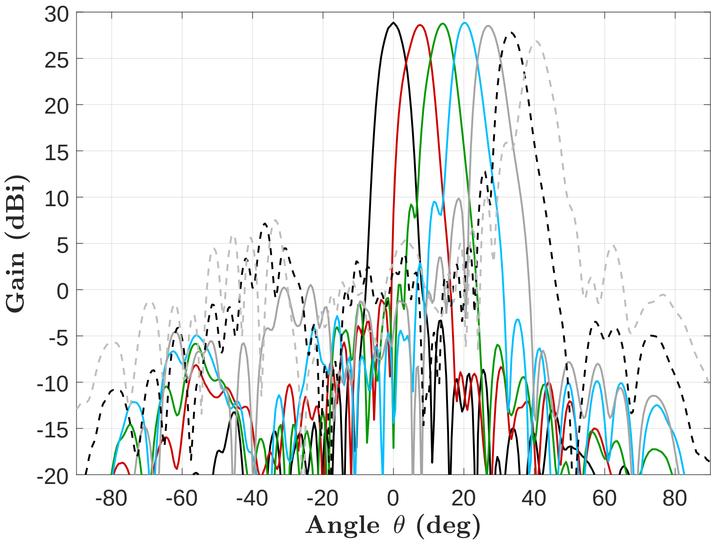

Figure 2.14: Measured radiation patterns at the design frequency for various scan angles in the H-plane.

Table 2.1: Measured radiation performance in the H-plane at the design frequency.

Pos.	θ_{max} (deg)	Gain (dBi)	SLL (dB)	$\lvert S_{11}\rvert$ (dB)
0	0	28.87	-32.20	-16.41
1	7.5	28.61	-29.72	-20.20
2	14	28.77	-19.56	-24.89
3	20	28.84	-19.33	-25.17
4	27	28.52	-18.66	-23.22
5	33	27.8	-15.03	-20.70
6	40.5	26.85	-10.95	-21.50

The normalized radiation patterns in the E- (xz-plane in Fig. 2.6) and H-plane (yz-plane in Fig. 2.6) at the design frequency for broadside radiation (Pos.0) are reported in Fig. 2.13. An excellent agreement between measurements and simulations is observed. The measured -3 dB beamwidths are about 7° and 6° in E- and H-plane, respectively. The SLLs in the E-plane are in the order of -13 dB, due to uniform illumination of the corporate feed network. Lower SLLs can be achieved by designing unbalanced power dividers in the corporate feed network. On the other hand, SLLs in the H-plane are lower than -30 dB thanks to the tapered illumination provided by quasi-optical system. The measured cross-polarization levels are less than -40 dB (peak-to-peak) in both planes.

The measured radiation patterns in the H-plane for different horn positions, at 29.25

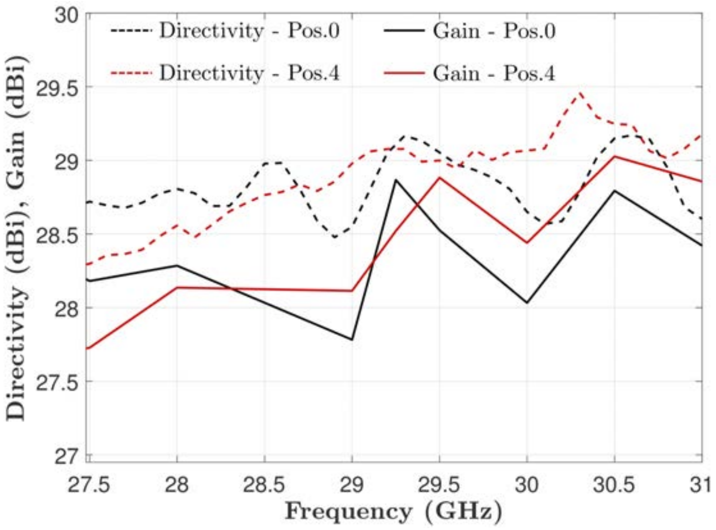

Figure 2.15: Measured gain and simulated directivity between 27.5 GHz and 31 GHz when the horn is placed in Pos.0 and in Pos.4, respectively.

GHz, are shown in Fig. 2.14. The radiation performance for each beam are summarized in Tab. 2.1. A scan range wider than the targeted one (±30°) has been considered to highlight the excellent scanning performance. The SLLs are lower than −18.6 dB within a ±27° field of view and the scan losses are lower than 0.35 dB. The SLLs and the scan losses reduce to about −11 dB and −2 dB, respectively, for $\theta = 40°$.

The measured gain is compared to the simulated directivity in Fig. 2.15 for Pos.0 ($\theta = 0°$) and Pos.4 ($\theta \approx 27°$) between 27.5 GHz and 31 GHz. At the design frequency, the gain is 28.87 dBi at broadside and 28.52 dBi at $\theta = 27°$. Moreover, the gain is greater than 27.6 dBi in the whole frequency band for both feed positions. Similar results are obtained for other pointing directions (Pos.1-Pos.3). The radiation efficiency has been evaluated as the ratio between the simulated directivity and the measured gain. At the the design frequency, it reaches a value of 93% for the broadside beam. Up to a scan angle of $\theta \approx 27°$, the estimated radiation efficiency is greater than 80% over the entire frequency band. This excellent performance is mainly due to the accurate design of the quasi-optical system and to the high edge tapering imposed by the parabolic reflector (see Section 2.2.2.4).

Finally, the radiation patterns in the H-plane are shown in Fig. 2.16 as functions of frequency and of elevation angle, in the entire Ka-band (26.5 – 40 GHz). The results are reported for four radiated beams, corresponding to the horn positions Pos.1-Pos.4. The pointing direction is preserved within the overall band for all considered positions and the −3 dB beamwidths have small variations, thus confirming the wideband, stable performance of the antenna.

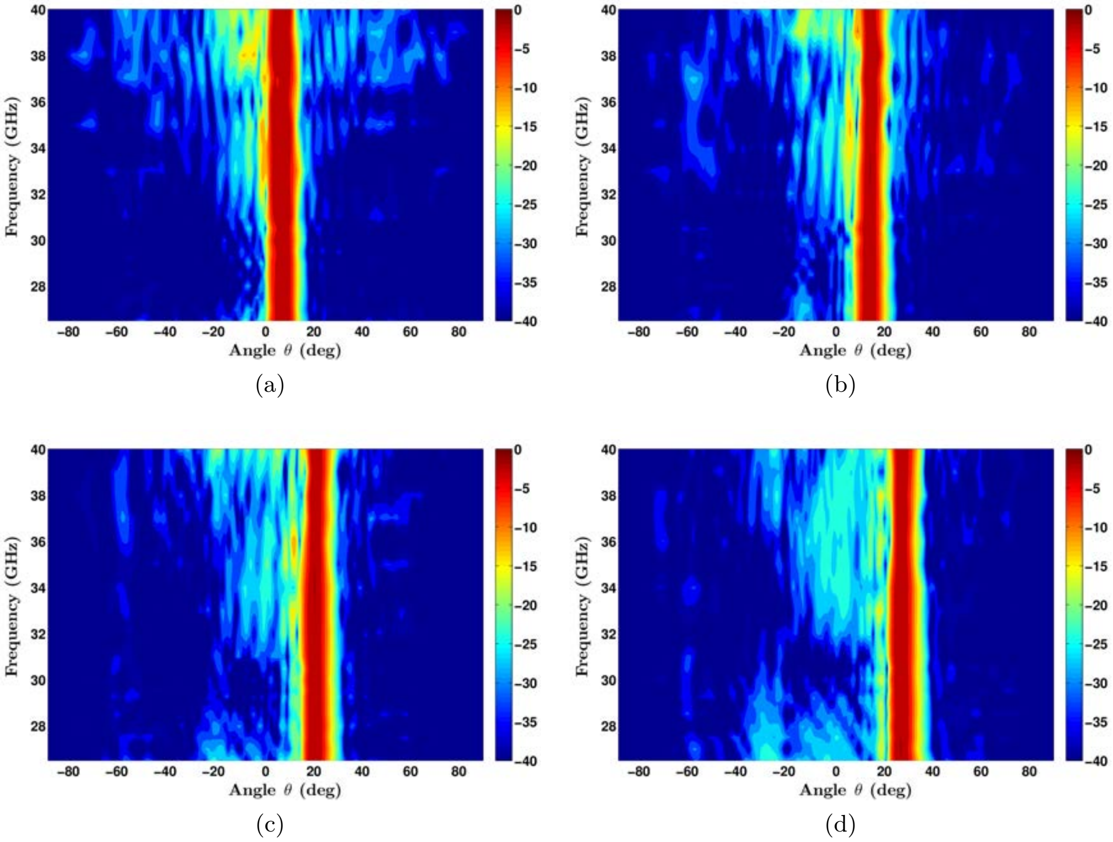

(a) (b)

(c) (d)

Figure 2.16: Measured radiation patterns, in the H-plane, for different horn positions in the Ka-band, as functions of frequency and elevation angle. Patterns are normalized and plotted in dB. (a) Pos.1, (b) Pos.2, (c) Pos.3, (d) Pos.4.

2.3 Conclusion

This chapter has introduced the continuous transverse stub antenna. The two main CTS architectures proposed in the literature, namely the series-fed and the parallel-fed CTS arrays, have been described, highlighting the principles of operation and the key characteristics that provide a wideband, wide-angle scanning performance. The beam steering mechanisms, the fabrication techniques and several designs have been reviewed, focusing mainly on CTS arrays at millimeter-waves. Particular emphasis has been put on parallel-fed CTS arrays, since the models and the designs presented in the next chapters are based on this antenna architecture. The reference parallel-fed CTS structure that will be considered in this thesis has been described by presenting an antenna designed for Satcom applications in the Ka-band. This antenna comprises 16 slots, parallel-fed by a corporate feed network based on hollow PPWs. A quasi-optical beamformer, comprising a pillbox coupler and a single input horn, excites the CTS array. The antenna beam is steered mechanically by moving the horn in the focal plane of the quasi-optical system. The design of each building block has been discussed. The antenna has been fabricated in separate parts, subsequently assembled with screws, without using any electromagnetic choke for the metallic junctions. Measurements results demonstrated the wide angular coverage of this antenna in the entire Ka-band operation. The scan loss for a beam pointing at $\pm 40^\circ$ is about 2 dB. In a scan range of $\pm 27^\circ$ the measured SLLs are lower than -18.6 dB at 29.25 GHz. The measured antenna gain is about 29 dBi at broadside with an efficiency of 93% at 29.25 GHz. The gain and efficiency are greater than 27.6 dBi and 80% in the 27.5-31 GHz band, respectively. The radiation performance achieved, the multibeam capability and the low-profile make this antenna architecture an attractive solution for the mm-wave applications targeted in this work.

Chapter 3

Analysis of the long slot array

Systematic methods of analysis are required to accomplish an effective and efficient design of complex antenna systems, such as CTS arrays. In this chapter and in the next one, we will present several models and numerical procedures developed for the analysis of parallel-fed CTS arrays, fed by quasi-optical systems in PPW technology. A modular approach will be followed in the analysis. First, the stand-alone array of slots is investigated in this chapter. The analysis of the PPW corporate feed network that excites the array is examined in Chapter 4.

Given the applications targeted in this work, the actual array will be modeled assuming an infinite periodic environment. This strategy provides an excellent approximation of the impedance behaviour of most of the elements in large arrays [57]. Moreover, since this approach exploits Floquet's theorem [58], it avoids the numerical issues arising in full-wave element-by-element analysis of finite arrays.

A numerical method to derive the active impedance of an infinite array of infinitely-extended slots excited by TEM modes with a progressive phase is presented in Section 3.1. It accounts for the presence of a planar multilayer dielectric medium above the antenna aperture, enabling the analysis of the effects of devices such as radomes, polarizers and matching layers, that may be associated to the array. This procedure provides a powerful tool to accurately evaluate the active impedance of the array of slots, as a function of frequency and scan angle, and analyze the impact of each array parameter. Design guidelines are proposed in view of different application cases, to achieve an active impedance stable over large bandwidths or on wide fields of view and to minimize the number of elements for a give aperture.

An equivalent circuit of the array is derived from the expression of the active admittance and discussed in Section 3.2. This network representation provides further physical insights and may be employed to analyze the array when it is associated with other circuit elements.

The developed numerical procedure is employed to study scan blindness phenomena, that are characterized, in infinite arrays, by unitary peaks of the active reflection coefficient.

The presence of blind spots may severely limit the scanning performance of the array. An extensive analysis of the relations between the onset of blind angles and the array parameters, with particular emphasis on the array periodicity, is provided in Section 3.2, considering several designs. Moreover, the appearance of radiation nulls is interpreted with the concurrent excitation of free resonance modes of the array.

An approximate method to compute the radiation pattern of a finite CTS array, using the results obtained with the model for the infinite structure, is presented in Section 3.4. The characteristics of the radiation patterns of a CTS array are mainly dictated by the beamforming system that excites the radiating section. Techniques of geometrical and physical optics (GO/PO) have been used to analyze the quasi-optical beamformer employed in this work, and to derive the field distribution that feeds each slot.

3.1 Modeling of the radiating section

In this section a rigorous and effective model for an infinite array of infinite longitudinal slots is presented. The array is uniformly excited by transverse electromagnetic (TEM) modes with progressive phases. Given the hypothesis of infinite environment, all conclusions that will be drawn do not account for finiteness. However, the characteristics predicted by the infinite model represent a useful approximation for large finite arrays of slots with a length much greater than the operating wavelength. The unknown equivalent currents over the slots are expanded in PPW modes, simplifying the mathematical treatment. A mode matching procedure, based on a spectral Green's function approach, enables the derivation of a compact expression for the active impedance of the array, when the antenna scans in the principal planes. The accuracy of this formula is demonstrated over a broad range of frequency and scan angles through comparisons with full-wave simulations. The impact of the geometrical parameters on the active impedance is investigated and provides physical insights to outline effective design strategies.

3.1.1 Active impedance of parallel-fed long slot arrays

The geometry of the problem is shown in Fig. 3.1. An infinite array of rectangular slots of width a and infinite length along the y-axis is placed along the x-direction in a metal plane. The inter-element spacing is d. The incident fields propagate along the z-direction in ideal PPWs. All metals are assumed to be perfect conductors. The model accounts for slots fed by dielectric-filled PPWs radiating into a plane-stratified dielectric half-space. For clarity, only one layer is shown in Fig. 3.1. Each dielectric layer is linear, isotropic, non-dispersive, homogeneous and lossless. The slots are parallel-fed by mono-modal PPWs. The incident fields have equal amplitudes and are progressively phased, steering the antenna beam in

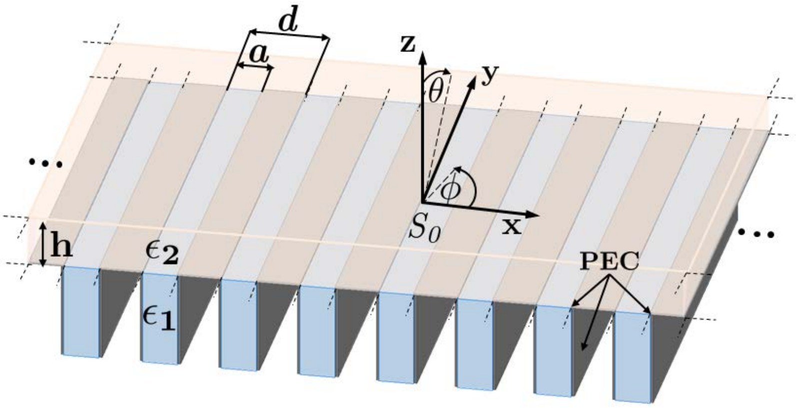

Figure 3.1: Geometry of a parallel-fed, infinite CTS array with slot width a and periodicity d. Dielectric-filled open-ended PPWs radiate into an arbitrary plane-stratified dielectric medium. Only one dielectric sheet of thickness h is shown for clarity.

the direction (θ, ϕ). The electromagnetic problem is solved by expanding the equivalent magnetic current over the aperture plane $z = 0$ in modes supported by a PPW. The scalar potentials ψ^{TE} and ϕ^{TM} for transverse electric (TE) and magnetic (TM) modes in a PPW, with respect to the z-axis, have the following expressions [59]

$$\psi_m^{TE}(x,y) = \sqrt{\frac{\nu_m}{a}} \cos\left(\frac{m\pi}{a}x\right) e^{-j\eta y}, \qquad m = 0,1,2,\ldots,\ -\infty < \eta < +\infty \tag{3.1}$$

$$\phi_m^{TM}(x,y) = \sqrt{\frac{2}{a}} \sin\left(\frac{m\pi}{a}x\right) e^{-j\eta y}, \qquad m = 1,2,3,\ldots,\ -\infty < \eta < +\infty \tag{3.2}$$

where $\nu_m = 1$ for $m = 0$ and $\nu_m = 2$ for $m \neq 0$. The transverse component of the vector wavenumber for both TE and TM modes is given by

$$k_{t,TE} = k_{t,TM} = \sqrt{(m\pi/a)^2 + \eta^2}. \tag{3.3}$$

We consider $\eta = k_{y0} = k_0 \sin\theta_0 \sin\phi_0$, where k_0 is the wavenumber in free space and (θ_0, ϕ_0) is the pointing direction of the array. From (3.1) and (3.2), the transverse fields $\mathbf{E_g}$, $\mathbf{H_g}$ guided in the PPW centered at $x = a/2$, are derived

$$\begin{aligned}\mathbf{E_g} = &\sum_{m=0}^{+\infty}\left(\frac{b_m^{TE}}{Y_m^{TE}}V_m^{TE} - \frac{b_m^{TM}}{Y_m^{TM}}V_m^{TM}\right)\cos\left(\frac{m\pi}{a}x\right)e^{-jk_{y0}y}\,\hat{x}\\ &+\sum_{m=1}^{+\infty}\left(\frac{c_m^{TM}}{Y_m^{TM}}V_m^{TM} - \frac{c_m^{TE}}{Y_m^{TE}}V_m^{TE}\right)\sin\left(\frac{m\pi}{a}x\right)e^{-jk_{y0}y}\,\hat{y}\end{aligned} \tag{3.4}$$

$$\begin{aligned}\mathbf{H_g} = &\sum_{m=1}^{+\infty}\left(c_m^{TE}\,V_m^{TE} - c_m^{TM}\,V_m^{TM}\right)\sin\left(\frac{m\pi}{a}x\right)e^{-jk_{y0}y}\,\hat{x}\\ &+\sum_{m=0}^{+\infty}\left(b_m^{TE}\,V_m^{TE} - b_m^{TM}\,V_m^{TM}\right)\cos\left(\frac{m\pi}{a}x\right)e^{-jk_{y0}y}\,\hat{y}\end{aligned} \tag{3.5}$$

The expressions of the coefficients b_m^{TE}, b_m^{TM}, c_m^{TE} and c_m^{TM}, for $m \in \mathbb{N}_0$ are given in Appendix A. The scalar modal functions for TE and TM modes $V_m^{TE,TM} = V_m^{TE,TM}(z)$ are measured in $V/\sqrt{m}$.

The modal admittances for TE and TM modes [59] are given by

$$Y_m^{TE} = \frac{\sqrt{k^2 - (m\pi/a)^2 - k_{y0}^2}}{\zeta\, k} \tag{3.6}$$

$$Y_m^{TM} = \frac{k}{\zeta\sqrt{k^2 - (m\pi/a)^2 - k_{y0}^2}} \tag{3.7}$$

where k and ζ are the wavenumber and the impedance of the medium in the PPW, respectively.

The incident fields are assumed to be pure TEM (TE_0) modes, equal in amplitude and progressively shifted in phase to steer the beam in (θ_0, ϕ_0). The incident magnetic field $\mathbf{H^i}$ on xy-plane ($z = 0$) has thus the following expression

$$\mathbf{H^i} = \frac{jY_0^{TE}\, V^i\, e^{-jk_{y0}y}}{\sqrt{a}} \sum_{n=-\infty}^{+\infty} \Pi_a\left(x - \frac{a}{2} - nd\right) e^{-jk_{x0}nd}\, \hat{y} \tag{3.8}$$

where $k_{x0} = k_0 \sin\theta_0 \cos\phi_0$, V^i is the known scalar modal function of the incident field, and the rectangular function $\Pi_a(\cdot)$ is given by

$$\Pi_a(x) = \begin{cases} 1 & x \in (-a/2, a/2) \\ 0 & x \le -a/2 \cup x \ge a/2 \end{cases} \tag{3.9}$$

The electromagnetic discontinuity at $z = 0$ gives rise to a second wave in the region $z < 0$, besides the incident field. It can be interpreted as the field reflected back from the slots into the PPWs and will be referred as reflected field. This field is a solution of Maxwell's equations in a PPW region. Therefore, it is analytically described by equations (3.4) and (3.5), except for a sign that accounts for the reversed direction of propagation (negative z semi-axis). Formally, the reflected magnetic field $\mathbf{H^r} = \mathbf{H^r}(x, y, 0)$ at the plane $z = 0$ is given by

$$\mathbf{H^r} = -\sum_{n=-\infty}^{\infty} \mathbf{H_g}\,(x - nd, y)\; \Pi_a\left(x - \frac{a}{2} - nd\right) e^{-jk_{x0}nd}\,. \tag{3.10}$$

The electric field scattered in the region $z > 0$ is derived from the equivalent magnetic current $\mathbf{M_n}$ over the aperture plane xy. This current is related by the equivalence theorem to the unknown aperture field $\mathbf{E_a}$. By expanding $\mathbf{E_a}$ in a series of PPW modes, as in (3.4), an effective expression for $\mathbf{M_n}$ is found

$$\mathbf{M_n}(x, y) = -\hat{z} \times \mathbf{E_a}|_{z=0}\,, \tag{3.11}$$

$$\mathbf{E_a} = \sum_{n=-\infty}^{\infty} \mathbf{E_g}(x-nd,y)\,\Pi_a\left(x-\frac{a}{2}-nd\right)e^{-jk_{x0}nd} \tag{3.12}$$

The tangential component of the transmitted magnetic field at $z=0$, denoted as $\mathbf{H^t} = \mathbf{H^t}(x,y,0)$, is given by the convolution of $\mathbf{M_n}$ with $\underline{\underline{G_t}}^{HM}$, the transverse dyadic Green's function of the upper half-space for the magnetic field, evaluated for $z=0$

$$\mathbf{H^t} = \int_{\mathbb{R}^2} \underline{\underline{G_t}}^{HM}(x-x',y-y')\mathbf{M_n}(x',y')dx'dy' \tag{3.13}$$

The computation of (3.13) is straightforward if performed in the spectral (k_x,k_y) domain. After some algebraic steps and an inverse Fourier transform (see Appendix A for more details), the x and y components of the transmitted magnetic field at $z=0$ are found

$$\begin{aligned} H_x^t = {}& \frac{e^{-jk_{y0}y}}{d}\sum_{m=1}^{+\infty}\left(\frac{c_m^{TM}}{Y_m^{TM}}V_m^{TM} - \frac{c_m^{TE}}{Y_m^{TE}}V_m^{TE}\right)\sum_{n=-\infty}^{+\infty}\Gamma_m(k_{xn})\tilde{G}_{xx}^{HM}(k_{xn},k_{y0})e^{-jk_{xn}x} \\ &+ \frac{e^{-jk_{y0}y}}{d}\sum_{m=0}^{+\infty}\left(\frac{b_m^{TM}}{Y_m^{TM}}V_m^{TM} - \frac{b_m^{TE}}{Y_m^{TE}}V_m^{TE}\right)\sum_{n=-\infty}^{+\infty}\Lambda_m(k_{xn})\tilde{G}_{xy}^{HM}(k_{xn},k_{y0})e^{-jk_{xn}x} \end{aligned} \tag{3.14}$$

$$\begin{aligned} H_y^t = {}& \frac{e^{-jk_{y0}y}}{d}\sum_{m=1}^{+\infty}\left(\frac{c_m^{TM}}{Y_m^{TM}}V_m^{TM} - \frac{c_m^{TE}}{Y_m^{TE}}V_m^{TE}\right)\sum_{n=-\infty}^{+\infty}\Gamma_m(k_{xn})\tilde{G}_{yx}^{HM}(k_{xn},k_{y0})e^{-jk_{xn}x} \\ &+ \frac{e^{-jk_{y0}y}}{d}\sum_{m=0}^{+\infty}\left(\frac{b_m^{TM}}{Y_m^{TM}}V_m^{TM} - \frac{b_m^{TE}}{Y_m^{TE}}V_m^{TE}\right)\sum_{n=-\infty}^{+\infty}\Lambda_m(k_{xn})\tilde{G}_{yy}^{HM}(k_{xn},k_{y0})e^{-jk_{xn}x} \end{aligned} \tag{3.15}$$

where $k_{xn} = k_{x0} - 2\pi n/d$, $\tilde{G}_{ij}^{HM}$ is the Fourier transform of the (i,j)-th element of $\underline{\underline{G_t}}^{HM}$ and can be derived, even in presence of layered media above the slots, using the equivalent transmission line technique [59]. The auxiliary functions $\Lambda_m(k_x)$ and $\Gamma_m(k_x)$ are defined as

$$\begin{aligned} \Lambda_m(k_x) = {}& \int_0^a \cos\left(\frac{m\pi}{a}x\right)e^{jk_x x}dx = \\ & \frac{a}{2}\,e^{j(k_x\frac{a}{2}+m\frac{\pi}{2})}\left[\operatorname{sinc}\left(k_x\frac{a}{2}+\frac{m\pi}{2}\right)+e^{-jm\pi}\operatorname{sinc}\left(k_x\frac{a}{2}-\frac{m\pi}{2}\right)\right] \end{aligned} \tag{3.16}$$

$$\begin{aligned} \Gamma_m(k_x) = {}& \int_0^a \sin\left(\frac{m\pi}{a}x\right)e^{jk_x x}dx = \\ & \frac{a}{2j}\,e^{j(k_x\frac{a}{2}+m\frac{\pi}{2})}\left[\operatorname{sinc}\left(k_x\frac{a}{2}+\frac{m\pi}{2}\right)-e^{-jm\pi}\operatorname{sinc}\left(k_x\frac{a}{2}-\frac{m\pi}{2}\right)\right] \end{aligned} \tag{3.17}$$

where $m = 0, 1, \ldots$, and the cardinal sine function $\operatorname{sinc}(\cdot)$ is given by

$$\operatorname{sinc}(x) = \begin{cases} \dfrac{\sin x}{x} & x \neq 0 \\ 1 & x = 0 \end{cases} \tag{3.18}$$

In order to find the unknown equivalent current, i.e. the coefficients V_m^{TE}, V_m^{TM}, the continuity of the tangential component of the magnetic field is enforced over the slot S_0

centered at $x = a/2$ (see Fig. 3.1). As the incident magnetic field has only a non-null component, along the y-axis, the equations to be solved are

$$\begin{cases} H_x^r(x,y,0)|_{S_0} = H_x^t(x,y,0)|_{S_0} & (3.19) \\ H_y^i(x,y,0)|_{S_0} + H_y^r(x,y,0)|_{S_0} = H_y^t(x,y,0)|_{S_0} & (3.20) \end{cases}$$

An approximate solution can be found by truncating the field expansions with $2M-1$ PPW modes (M TE modes and $M-1$ TM modes) and $2N_f+1$ Floquet modes. Both sides of (3.19) and (3.20) are then averaged with two different sets of basis functions in the domain $x \in [0,a]$. For (3.19) and (3.20) the basis functions are, respectively, ξ_p and χ_q, given by

$$\xi_p(x) = \sin\left(\frac{p\,\pi}{a}x\right), \qquad p = 1,2,\ldots,M-1 \tag{3.21}$$

$$\chi_p(x) = \cos\left(\frac{q\,\pi}{a}x\right), \qquad q = 0,1,\ldots,M-1 \tag{3.22}$$

The two sets of equations obtained after the test procedure can be rearranged in a standard block matrix form by grouping TE and TM components, yielding

$$\begin{bmatrix} \underline{\underline{Y}}^{TE,TE} & \underline{\underline{Y}}^{TE,TM} \\ \underline{\underline{Y}}^{TM,TE} & \underline{\underline{Y}}^{TM,TM} \end{bmatrix} \begin{bmatrix} \mathbf{V^{TE}} \\ \mathbf{V^{TM}} \end{bmatrix} = \begin{bmatrix} \mathbf{I_0} \\ \mathbf{0} \end{bmatrix} \tag{3.23}$$

where $\mathbf{I_0} = \left[jV^i\sqrt{a}Y_0^{TE}, 0, \ldots, 0\right]^T$ is the $M \times 1$ column vector of the excitations, all null except for the fundamental mode. The $M \times 1$ column vector $\mathbf{V}_{TE}$ and the $M-1 \times 1$ column vector $\mathbf{V}_{TM}$ contain the unknown coefficients of the current expansion and are given by

$$\mathbf{V}_{TE} = \left[V_0^{TE}, V_1^{TE}, \ldots, V_{M-1}^{TE}\right]^T \tag{3.24}$$

$$\mathbf{V}_{TM} = \left[V_1^{TM}, V_2^{TM}, \ldots, V_{M-1}^{TM}\right]^T \tag{3.25}$$

Explicit expressions for the elements of matrices $\underline{\underline{Y}}^{T\cdot,T\cdot}$ in (3.23) are given in Appendix A.

All fields can be completely determined after solving (3.23) for $\mathbf{V_{TE}}$, $\mathbf{V_{TM}}$. It is possible to compute the active input impedance at any element in the fully excited array, at any scan angle. In general, the active impedance depends on the particular fed element in the array. However, given the assumptions of infinite and uniformly periodic array, the active impedances will be identical for all elements in the array. In practice, if the array is finite but large, the active impedances seen at the central elements will be almost identical and equal to the value derived for the infinite array case [57, 60].

All elements are voltage-driven. We focus on the slot S_0 centered at $x = a/2$. The dominant component of the voltage excitation on S_0 is $V_{S_0} = V_0^{TE}\sqrt{a}$. The active admittance $\overline{Y}_{act}$ can be derived from the expression of the power on S_0. Let $\mathbf{H^a} = \mathbf{H^t}|_{S_0}$ and $\mathbf{I_{S_0}}$ be the total magnetic field and total current, respectively, on the slot S_0, that accounts for the effect of the simultaneous excitation of all ports. Moreover, the fundamental components of the electric field and of the magnetic current on S_0 are denoted with $\mathbf{E_0}$ and $\mathbf{M_0}$, respectively. The complex power flowing through S_0 is given by

$$\frac{1}{2} V_{S_0} I_{S_0}^* = \frac{1}{2} \int_{S_0} [(\mathbf{E_0} \times (\mathbf{H^a})^*)] \cdot \hat{z} \, dx \, dy \tag{3.26}$$

Therefore, the current I_{S_0} can be written as

$$\begin{aligned} I_{S_0} &= \frac{1}{V_{S_0}^*} \int_{S_0} (\mathbf{E_0^*} \times \mathbf{H^a}) \cdot \hat{z} \, dx \, dy = \frac{1}{V_{S_0}^*} \int_{S_0} \mathbf{H^a} \cdot (\hat{z} \times \mathbf{E_0^*}) \, dx \, dy \\ &= -\frac{1}{V_{S_0}^*} \int_{S_0} \mathbf{H^a} \cdot \mathbf{M_0^*} \, dx \, dy \end{aligned} \tag{3.27}$$

where the magnetic current $\mathbf{M_0}$ is given by

$$\mathbf{M_0} = -\frac{j \, V_0^{TE}}{\sqrt{a}} \Pi_a \left(x - a/2\right) e^{-jk_{y0}y} \, \hat{y} \tag{3.28}$$

The active impedance $\overline{Y}_{act}$ is computed as the ratio of the total current induced on the slot S_0 and the dominant mode of the voltage excitation, yielding

$$\overline{Y}_{act} = \frac{I_{S_0}}{V_{S_0}} = -\frac{1}{\left|V_0^{TE} \sqrt{a}\right|^2} \int_{S_0} \mathbf{H^a} \cdot \mathbf{M_0}^* \, dS \tag{3.29}$$

Since the array is infinite along the y-direction, the active admittance per unit length Y_{act} is introduced by reducing the double integral (3.29) to a linear integral in the domain $x \in [0, a]$. The final expression of Y_{act} can be decomposed in three different parts, as follows

$$Y_{act} = Y_{FM} + Y_{HM} + Y_{XPOL} \tag{3.30}$$

The admittance Y_{FM} is the component of Y_{act} due to the fundamental PPW mode (TE$_0$). It does not depend on the expansions coefficients and can be expressed with the following closed form

$$Y_{FM} = -\sum_{n=-N_f}^{N_f} \Lambda_m(k_{xn}) \Lambda_0(-k_{xn}) \frac{\tilde{G}_{yy}^{HM}\left(k_{xn}, k_{y0}\right)}{a^2 \, d} \tag{3.31}$$

The admittance Y_{HM} contains the contribution of higher order expansion modes related to the y-polarized component of the magnetic current.

$$\begin{aligned} Y_{HM} = &-\frac{j\sqrt{2}}{a^2 \, d} \sum_{m=1}^{M-1} \frac{(m\pi/a) V_m^{TM} - jk_{y0} V_m^{TE}}{V_0^{TE} \sqrt{k_{y0}^2 + (m\pi/a)^2}} \\ &\times \sum_{n=-N_f}^{N_f} \Lambda_m\left(k_{xn}\right) \Lambda_0(-k_{xn}) \cdot \tilde{G}_{yy}^{HM}\left(k_{xn}, k_{y0}\right) \end{aligned} \tag{3.32}$$

Finally, the cross-polarized component Y_{XPOL} is related to higher order expansion modes induced by the x-polarized component of the magnetic current.

$$
\begin{aligned}
Y_{XPOL} = -\frac{j\sqrt{2}}{a^2\, d} \sum_{m=1}^{M-1} \frac{j k_{y0} V_m^{TM} - (m\pi/a) V_m^{TE}}{V_0^{TE} \sqrt{k_{y0}^2 + (m\pi/a)^2}} \\
\sum_{n=-N_f}^{N_f} \Gamma_m\left(k_{xn}\right) \Lambda_0\left(-k_{xn}\right) \cdot \tilde{G}_{yx}^{HM}\left(k_{xn}, k_{y0}\right)
\end{aligned}
\tag{3.33}
$$

In (3.31) – (3.33), M TE, $M-1$ TM modes and $2N_f + 1$ Floquet modes are considered.

3.1.2 Numerical validation

In this section, the model described in Section 3.1.1 is validated through comparisons with full-wave results obtained with Ansys HFSS. In particular, the simulations are performed on the unit cell of the array, using periodic boundary conditions. The accuracy of the formula derived for the active admittance and its rate of convergence with respect to the number M of PPW modes have been analyzed for arrays with different parameters and for several scan angles in the principal planes. Eleven Floquet modes, corresponding to $N_f = 5$, have been used to derive the numerical results that are presented next. The number of PPW modes required in the field expansion for an accurate evaluation of the active impedance per unit length $Z_{act} = 1/Y_{act}$ is first investigated for arrays fed by hollow PPWs that radiate in air. Only one mode is generally needed for the computation of Z_{act} when the array scans in the H-plane (zy-plane in Fig. 3.1), up to large scan angles, unless scan blindness occurs. Conversely, for E-plane (zx-plane in Fig. 3.1) scanning, Z_{act} converges only when a proper value of M is considered. Significant differences between monomodal and multimodal computations are observed for $\mathrm{Im}(Z_{act})$. Moreover, larger slot widths a, close to the cut-off wavelength of higher order PPW modes, lead to larger discrepancies in the results for $M = 1$ and $M > 1$, even for $\mathrm{Re}(Z_{act})$.

Dielectrics in the PPWs and in the outer half-space have an impact on the number of modes required. With reference to Fig. 3.1, a slot array with $a = 0.5\, c/\left(f_{max}\sqrt{\epsilon_{r1}}\right)$, $\epsilon_{r1} = 2$, and $d = 1.07a$ is considered as a test case. A single-layer cover of relative permittivity ϵ_{r2} and thickness $h = c/(2 f_{max}\sqrt{\epsilon_{r2}})$ is placed above the slots. With these values, a single-mode propagation is guaranteed up to f_{max}. Fig. 3.2a shows Z_{act} versus scan angle in the E-plane at a frequency $\overline{f} = 0.5 f_{max}$, for three values of ϵ_{r2}. Discrepancies between results obtained for $M = 1$ (dashed lines) and $M = 3$ (solid lines) are observed for scan angles $> 15°$. The multimodal data are in very good agreement with HFSS simulations, shown with markers. High contrasts between inner and outer dielectric emphasize the discrepancies between simulations and results obtained for $M = 1$. In particular, the largest deviations

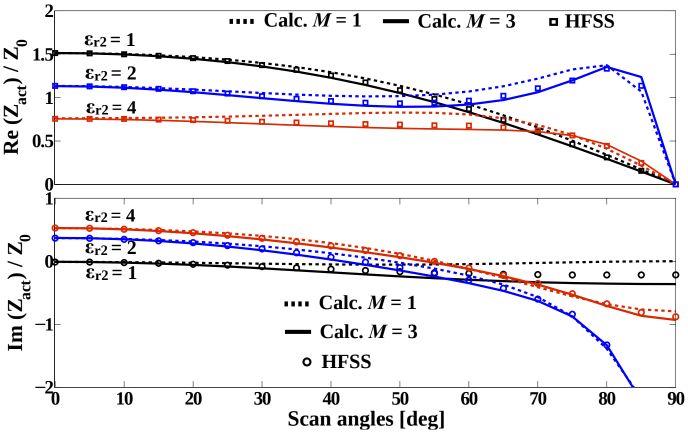

(a) Z_{act} versus scan angle at $\overline{f} = 0.5 f_{max}$

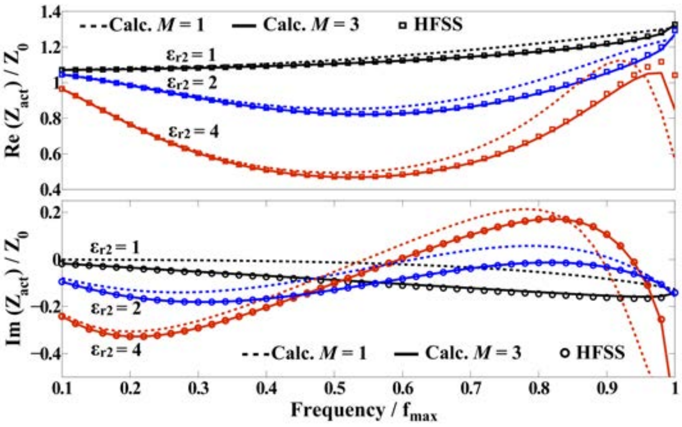

(b) Z_{act} versus frequency for $\theta = 45°$ in the E-plane

Figure 3.2: Active impedance for E-plane scanning. Numerical results for $M = 1$ and $M = 3$ in dashed and solid lines, respectively; HFSS results with markers. The array parameters are: $a = 0.5\,c/(f_{max}\sqrt{\epsilon_{r1}})$, $d = 1.07a$, $\epsilon_{r1} = 2$, $h = 0.5\,c/(f_{max}\sqrt{\epsilon_{r2}})$, $\epsilon_{r2} = \{1, 2, 4\}$. $Z_0 = \zeta_1\, a$, with ζ_1 impedance of medium 1.

from HFSS results are observed for $\mathrm{Im}\,(Z_{act})$ when the medium inside the PPWs is denser than the outer one ($\epsilon_{r1}/\epsilon_{r2} = 2$). By contrast, the computation of $\mathrm{Re}(Z_{act})$ with $M = 1$ is less accurate when $\epsilon_{r2} > \epsilon_{r1}$.

The active impedance of the same array is plotted against frequency in Fig. 3.2*b*, considering a beam steering angle $\theta = 45°$ in the E-plane. The results for $M = 1$ and $M = 3$ exhibit large discrepancies. The error for $\mathrm{Re}\,(Z_{act})$ is mainly observed when the frequency approaches f_{max}, while for $\mathrm{Im}\,(Z_{act})$ it is large over the whole band. This is physically due to the excitation of higher order modes at the aperture plane, that largely affect the array reactance.

The model is numerically validated for H-plane scanning as well. The test structure is the array analyzed in Fig. 3.2, with $\epsilon_{r2} = 4$. Figure 3.3 shows that Z_{act}, computed with

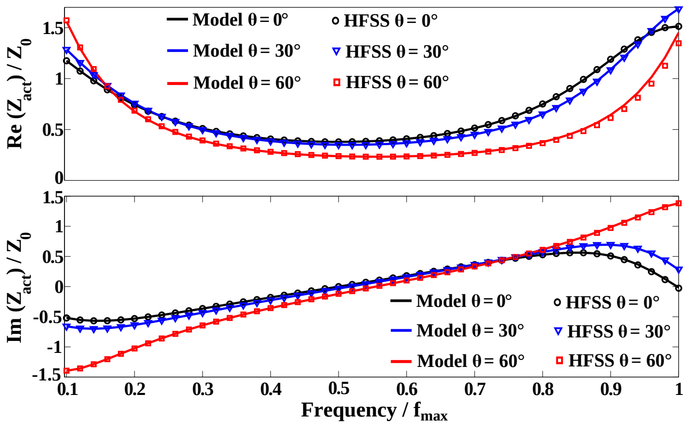

Figure 3.3: Active impedance for three scan angles θ in the H-plane. Z_{act} is normalized to $Z_0 = \zeta_1\, a$ (ζ_1 impedance of medium 1). The array has the same geometrical parameters of that in Fig. 3.2 with $\epsilon_{r2} = 4$. Numerical results are obtained with $M = 1$ and are shown in solid lines.

$M = 1$, is in excellent agreement with full-wave simulations, up to a scan angle of 60° in the H-plane.

In summary, for most cases analyzed, very accurate results are achieved, for both E- and H-plane scanning, by setting $N_f = 5$ and $M \geq 3$ in (3.30)-(3.33). Results computed by using $M < 3$ are generally inaccurate when the array scans in the E-plane, while they are still in good agreement with full-wave simulations for H-plane scanning. Larger values of M may be required for more complex structures, e.g. array that includes thick dielectric layers above the slots or several stratifications, or in presence of scan blindness phenomena.

3.1.3 Design guidelines

This section discusses the impact of the geometrical and electrical parameters of the array on the active reflection coefficient S_{act}, in order to outline some design guidelines. The active reflection coefficient is here normalized on the admittance per unit length Y_0^{TE}/a, relative to the dominant mode in the PPW feeds. Therefore, the expression for S_{act} is

$$S_{act} = \frac{Y_0^{TE}/a - Y_{act}}{Y_0^{TE}/a + Y_{act}} \tag{3.34}$$

First, the relations between S_{act} the fundamental array parameters, i.e. the width a of the slots and the element spacing d, are studied, in order to achieve broadband operation or to maximize the array spacing. Air-filled PPWs radiating in free-space are first considered, to avoid additional effects due to dielectrics. Then, the benefit of loading the array with dielectric sheets for wide angle impedance matching is demonstrated.

3.1.3.1 Optimal design for broadband operation

For standard applications, CTS arrays work in monomodal TEM regime. Thus, the slot width a must be smaller than the cut-off wavelength λ_c of the first higher order mode propagating in the PPWs, i.e. $\lambda_c = c/(2f_{max}\sqrt{\epsilon_{r1}})$, where f_{max} is the maximum frequency in the operating band. Given this constraint, a can be selected taking into account several design specifications. Here we focus on the input matching, that generally improves for larger apertures. The ratio between array spacing and slot width is crucial for the performance of the array. This parameter can be optimized using the fast procedure proposed for the computation of the active admittance. Indeed, S_{act} can be mapped for several values of d/a, within a given frequency range and for different scan angles in the E- and H-planes. Then the value of d/a that best fits the requirements on S_{act} in terms of bandwidth and scan range is selected. This process is illustrated for an array fed by hollow PPWs and radiating in air, with a slot width $a = 0.25\,c/f_{max}$. The contour plots of $|S_{act}|$ as a function of d/a and frequency are shown in Fig. 3.4, for different scan angles. For broadside operation, the flat contour lines indicate the great stability of S_{act} over the decade considered. The best input matching is achieved for $d \approx a$, i.e. this class of arrays exhibits the widest bandwidths when the elements are tightly coupled. The results in Fig. 3.4*b* - 3.4*e* highlight different behaviors when the antenna beam is steered in the principal planes. In the E-plane, the optimum ratio d/a for best matching varies with the scan angle. Moreover, the return loss and bandwidth reduce when the scan angle increase. By contrast, $|S_{act}|$ is almost frequency-independent and fairly affected by the H-plane scanning. This is the key physical reason behind the outstanding scanning performance achieved by CTS antenna systems [47]. Thus, the ratio d/a selected for broadside operation ensures a good impedance matching even large scan angles in the H-plane. With reference to the case discussed, a return loss > 15 dB within a $\pm 60^\circ$ scanning range in both planes is achieved up to $0.6f_{max}$ by choosing $d/a \approx 1.4$. The procedure can be iterated for different values of a, if wider bandwidths are targeted.

3.1.3.2 Largely spaced CTS arrays

The need for wide-angle scanning usually limits the element spacing and thus the size of the elements. In standard wide-scanning planar antennas, elements are arrayed in a double-meshed grid with periods close to half the wavelength at f_{max}, in order to avoid grating lobes. Such low inter-element spacings typically reduces the bandwidth of the array.

By contrast, the arrays of long slots considered in this chapter suffer from grating lobes when they scan in the E-plane but not in the H-plane. Indeed, the radiating elements along H-plane are continuous slots of infinite length, or much longer than the wavelength in real cases. The scan range in the H-plane can be limited by the scan blindness phenomena,

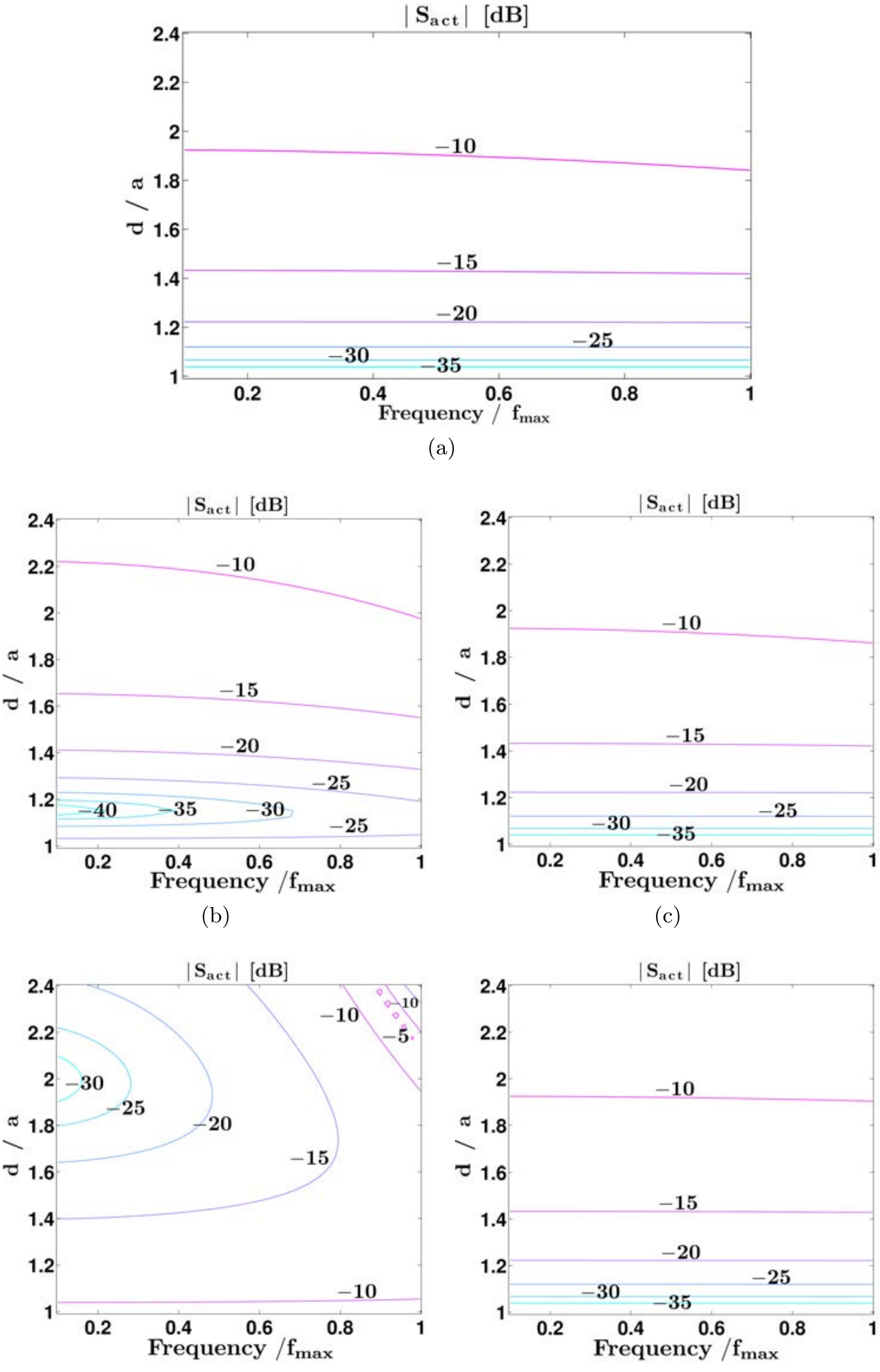

(a)

(b)

(c)

(d)

(e)

Figure 3.4: Contour plots of the amplitude of the active reflection coefficient, as a function of frequency and ratio d/a, for different scan angles in the E- and the H-plane. (a) Broadside. (b) E-plane, $\theta = 30°$. (c) H-plane, $\theta = 30°$. (d) E-plane, $\theta = 60°$. (e) H-plane, $\theta = 60°$.

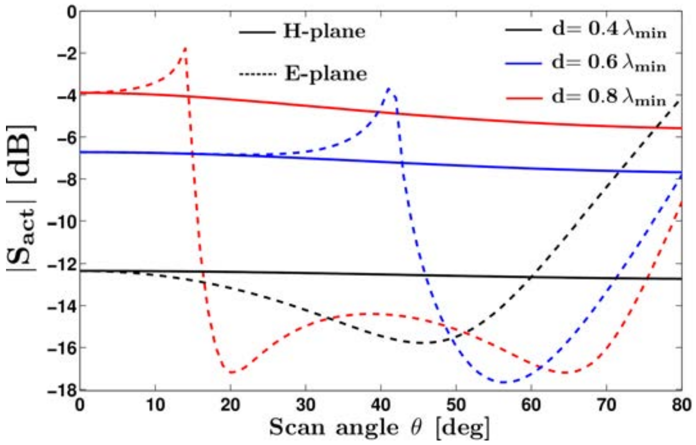

Figure 3.5: Active reflection coefficient versus scan angle in the H-plane (solid lines) and the E-plane (dashed lines) for several element spacings d. The slot width is $a = 0.25\lambda$, where λ is the free-space wavelength at the frequency considered. The array is fed by hollow PPWs and radiates in free-space.

that will be discussed in Section 3.3. The presence of grating lobes can be detected from peaks in the amplitude of the active reflection coefficient. Figure 3.5 reports $|S_{act}|$ at f_{max} as a function of scan angle, both in the E- and the H-plane, for the arrays studied in Section 3.1.3.1 ($a = 0.25\,\lambda_{min}$). Several array spacings d are considered. The sharp maxima in the E-plane for $d > 0.5\lambda_{min}$ indicate grating lobes centered at the corresponding angles. Conversely, S_{act} has small variations with the scan angle in the H-plane, even for large values of d. The low matching level, due to large d/a, is not a concern since the relevant paramer for broadband matching is the flatness of $|S_{act}|$ against the scan angle. These results demonstrate that arrays of long slots designed for H-plane scanning, as the CTS antennas examined in this work, can achieve active impedances almost frequency independent over a decade range, and slow-varying with the beam pointing direction. Since no grating lobes occur, a value of $d > 0.5\lambda_{min}$ can be chosen. An upper bound on the periodicity d to avoid the occurrence of blind spots will be discussed in Section 3.3. If the array spacing is increased, a given antenna aperture can be sampled with less elements. Thus, the number of transmitter/receiver (TX/RX) units can be reduced, lowering the costs and the complexity of the antenna system. The slot width a can be increased up to the cut-off wavelength of higher order PPW modes to maximize the return loss, as explained in Section 3.1.3.1, and the radiated power.

Few antenna arrays can ensure such broadband, wide-angle scanning performance. Among them, connected arrays [22,61] allow for 2-D scanning, but require element spacings $< 0.5\lambda_{min}$ [61]. Thus, the number of feeds in a CTS array of N slots is scaled down at least by a factor N, as compared to connected arrays of N elements, fed by a $N \times N$ network.

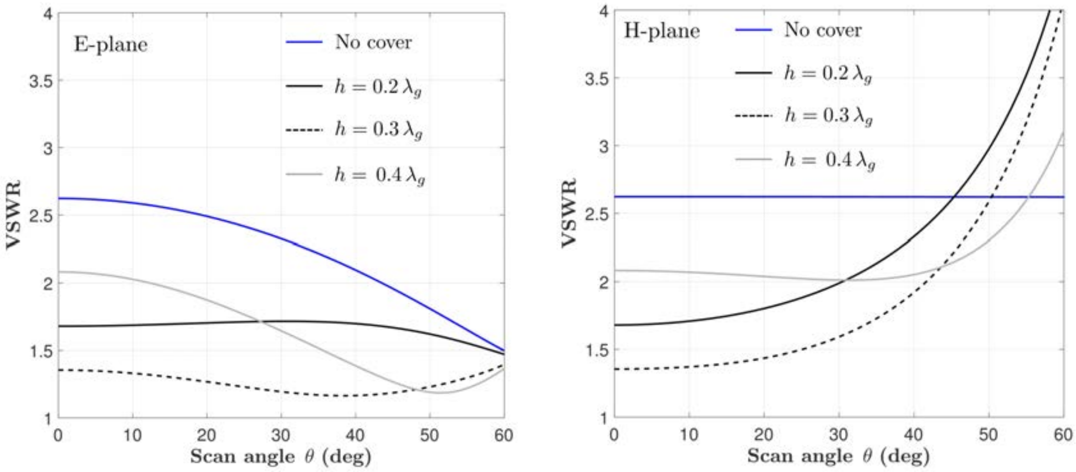

(a) (b)

Figure 3.6: VSWR at f_{max} for different thicknesses h of the dielectric cover, with $\epsilon_{r2} = 3.5$, $\lambda_g = c/(f_{max}\sqrt{\epsilon_{r2}})$. The other array parameters are $a = 0.42\,c/(f_{max}\sqrt{\epsilon_{r1}})$, $d = 1.40\,a$, $\epsilon_{r1} = 3.5$ (see Fig. 3.1). (a) E-plane and (b) H-plane scanning.

A further reduction may be achieved if the CTS antenna is designed with $d > 0.5\lambda_{min}$.

3.1.3.3 Dielectric cover for wide-angle matching

A permittivity step between the dielectric in the PPWs that feed the array and the medium in the half space above the slots may create a severe impedance mismatch. A common way to improve the impedance matching of phased arrays over wide scan and frequency ranges consists in adding dielectric layers over the radiating apertures [62]. An easy case is here discussed for a slot array whose PPW feeds are filled by a dielectric of relative permittivity $\epsilon_{r1} = 3.5$. The slot width is $a = 0.42\,c/(f_{max}\sqrt{\epsilon_{r1}})$ and $d = 1.4\,a$. A single-layer dielectric sheet of the same material used in the PPWs is placed just above the slots ($\epsilon_{r2} = 3.5$). Figure 3.6 shows the voltage standing wave ratio (VSWR) at f_{max}, as a function of scan angle, when the array is unloaded and when it is loaded by a dielectric cover of thickness h. The unloaded array is mismatched (VSWR>2) for every scan angle in the H-plane and up to an angle of 50° in the E-plane. With a $0.3\lambda_g$-thick cover, a good matching is achieved up to 50° in both E- and H-plane. Also the matching bandwidth is greatly improved. The unloaded array is mismatched in the band $(0.1f_{max}, f_{max})$ both in the E- and H-plane, when the scan angle is 30°. Using a $0.3\lambda_g$-thick cover, a VSWR < 2 is achieved in the bands $(0.4f_{max}, f_{max})$ and $(0.6f_{max}, f_{max})$ for E- and H-plane scanning, respectively.

Wide-angle impedance matching layers represent an effective solution for the design of CTS system fully-integrated in dielectric substrates, that are discussed in Chapter 5. However, electrically-thick radomes may cause scan blindness at certain frequencies. The numerical model presented in Section 3.1.1 can accurately predict their impact on the antenna performance. An exhaustive study on the relation between dielectric covers and radiation nulls is presented in Section 3.3.

3.2 Network representation of the array

In this section, a rigorous network representation of the infinite array of infinitely extended slots under analysis is derived by expanding the compact formulas for the active admittance per unit length. The contribution of all Floquet modes and expansion modes is isolated in different terms with a well defined physical meaning. It is clear from (3.30) – (3.33) that the active admittance per unit length Y_{act} can be expressed as a double summation over the Floquet modes and the PPW modes. The first step in the derivation of the network formalism is the decomposition of Y_{act} in two parts: one associated to the dominant PPW mode, the other due to the higher order PPW modes. Thus Y_{act} can be written as

$$Y_{act} = \sum_{n=-N_f}^{N_f} \sum_{m=0}^{M-1} Y_{m,n} = \sum_{n=-N_f}^{N_f} Y_n^{m=0} + \sum_{n=-N_f}^{N_f} Y_n^{m\neq 0} \tag{3.35}$$

where $Y_n^{m=0}$ is the component of the admittance related to the n-th Floquet mode and to the dominant PPW mode, given by

$$Y_n^{m=0} = -\frac{1}{d}\mathrm{sinc}^2\left(k_{xn}\frac{a}{2}\right) \tilde{G}_{yy}^{HM}\left(k_{xn}, k_{y0}\right), \tag{3.36}$$

while $Y_n^{m\neq 0}$ is associated to n-th Floquet mode and to all higher order expansion modes. The spectral Green's function $\tilde{G}_{yy}^{HM}$ of the stratified medium above the slots, relates the magnetic currents to magnetic fields on the aperture plane $z = 0$ and can be written as [59]

$$\tilde{G}_{yy}^{HM}(k_x, k_y, z = 0) = -\frac{I^{TM}\, k_x^2 + I^{TE}\, k_y^2}{k_x^2 + k_y^2} = -I^{TM}\,(\gamma_n^{TM})^2 - I^{TE}\,(\gamma_n^{TE})^2, \tag{3.37}$$

where I^{TM} and I^{TE} are the currents at $z = 0$, for unit series generator, in the equivalent transmission lines that represent the TE-TM decomposition of Maxwell's equations [59] in the half space $z \geq 0$. The expressions of the coefficients $\gamma_n^{TE}, \gamma_n^{TM}$, for $n = -N_f, \ldots, N_f$, are

$$\gamma_n^{TE} = \frac{k_0 \sin\theta \sin\phi}{\sqrt{(k_0 \sin\theta\cos\phi + n\,2\pi/d)^2 + (k_0 \sin\theta \sin\phi)^2}} \tag{3.38}$$

$$\gamma_n^{TM} = \frac{k_0 \sin\theta \cos\phi + n\,2\pi/d}{\sqrt{(k_0 \sin\theta\cos\phi + n\,2\pi/d)^2 + (k_0 \sin\theta \sin\phi)^2}} \tag{3.39}$$

The formula for Y_{act} has been recast in (3.35) in a sum of admittances due to each Floquet mode. Its network representation is illustrated in Fig. 3.7*a*. The first sum in

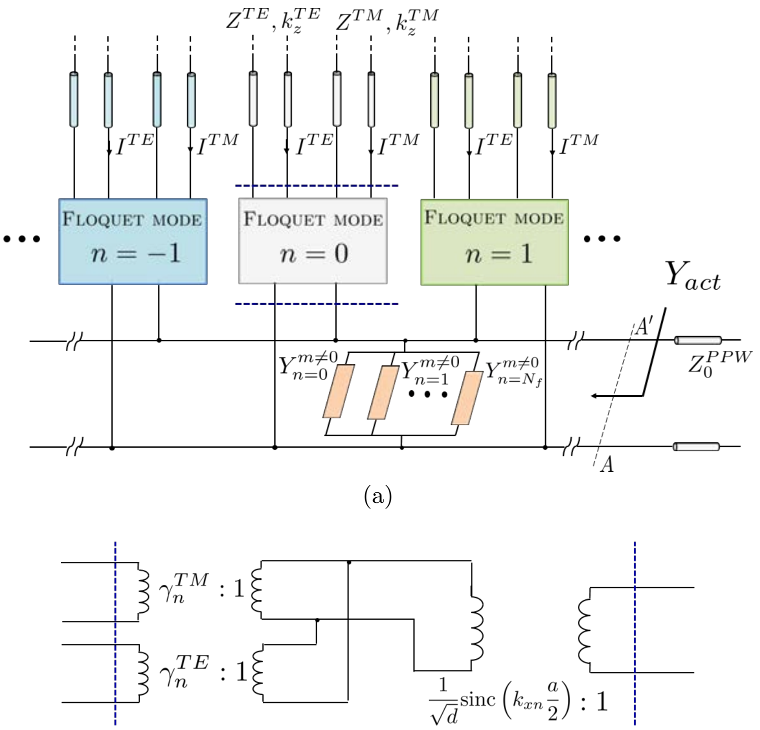

(a)

(b)

Figure 3.7: (a) Complete circuit representation for the unit cell of the infinite array of slots under analysis and (b) detail of the circuit block associated to the n-th Floquet mode.

(3.35), associated to the dominant PPW mode, is represented with parallel circuit blocks. The component of Y_{act} due to higher order PPW modes is expressed by the second sum in (3.35). It is represented with parallel shunt admittances ($Y_{n=-N_f}^{m\neq0}, \dots Y_{n=N_f}^{m\neq0}$) at the input section AA'. This term mainly contributes to the reactive part of the active admittance. It becomes more relevant and affects also the resistive part of Y_{act} as the array periodicity and the scan angle increase, or in presence of electrically thick covers, as discussed in Section 3.1.2.

For the component $Y_n^{m=0}$, each block related to a specific Floquet mode comprises equivalent TE and TM transmission lines (TLs) that account for the polarization and the direction of propagation of the radiated/received plane waves. For clarity, single transmission lines are shown for TE and TM waves. If the array is loaded by a stratified medium, several TL sections are needed. The lines corresponding to the i-th dielectric layer in the half space $z > 0$, with relative permittivity $\epsilon_{r,i}$ and wave impedance ζ_i, are characterized by propagation constant $k_{z,i} = \sqrt{k_0^2\,\epsilon_{r,i} - k_x^2 - k_y^2}$ and characteristic impedances $Z_0^{TE} = \zeta_i k_0 \sqrt{\epsilon_{r,i}}/k_{z,i}$ and $Z_0^{TM} = \zeta_i k_{z,i}/(k_0\sqrt{\epsilon_{r,i}})$, for TE and TM wave, respectively.

The expanded circuit representation of Fig. 3.7b is derived for the component $Y_n^{m=0}$, for each Floquet mode, using (3.36)-(3.39). Two transformers, with voltage ratios $\gamma_n^{TE}:1$

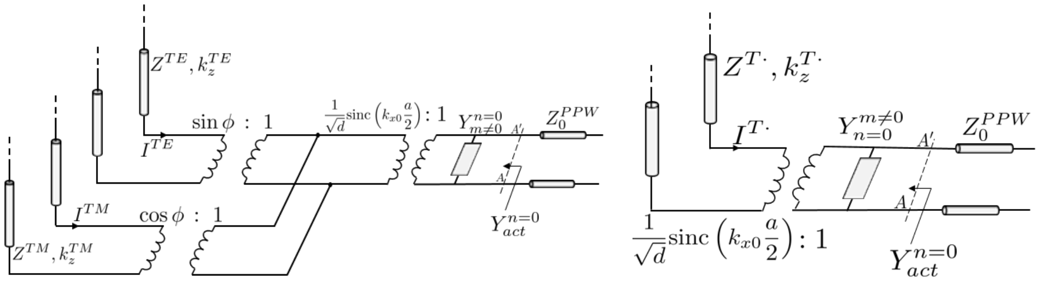

(a) (b)

Figure 3.8: (a) Circuit representation of the admittance term $Y_{act}^{n=0}$ related to the fundamental Floquet mode ($n = 0$). (b) Simplified circuit when the array scans in the principal planes. The symbol $T\cdot$ stands for TE and TM for E-plane ($\phi = 0°$) and H-plane scanning ($\phi = 90°$), respectively.

and γ_n^{TM} : 1, are connected to the transmission lines for TE and TM waves, respectively. Their secondary windings are connected in parallel. The transformer with voltage ratio $\frac{1}{d}\text{sinc}^2\left(k_{xn}\frac{a}{2}\right)$ accounts for the geometrical parameters of the unit cell.

In general, only a few Floquet modes give a significant contribution to the active admittance. Two important cases for the applications are here discussed. The general network presented in Fig. 3.7 is particularized using the fundamental ($n = 0$) and the first higher order ($n = \pm 1$) Floquet modes. The circuit representation of the admittance $Y_{act}^{n=0}$, that accounts only for the fundamental Floquet mode, is shown in Fig. 3.8a. This case corresponds to a quasi-static approximation of the behaviour of tightly spaced arrays [63]. The coupling of TE and TM waves is modeled by the two transformers of ratios $\sin\phi : 1$ and $\cos\phi : 1$, respectively, whose secondary windings are parallel connected. However, when the array scans in the principal planes, the TE and TM lines are completely uncoupled and the equivalent circuit reduces to the network of Fig. 3.8b. For E-plane scanning ($\sin\phi = 0$), the transformer connected to the TE line is shorted. Conversely, when the array scans in the H-plane ($\cos\phi = 0$) only TE waves propagate.

It is easy to show from (3.38) that the transformation ratio γ_n^{TE} vanishes for $\phi = 0°$, for all Floquet modes. Therefore, only TM waves can be radiated or received when the array scans in the E-plane. By contrast, both TE and TM waves can be excited for H-plane scanning, since both γ_n^{TE} and γ_n^{TM} assume, in general, finite, non-null values for $n \neq 0$. Indeed, for $n \neq 0$ and $\phi = 90°$, the transformation ratios γ_n^{TE} and γ_n^{TM} assume finite, non-null values. The equivalent circuit relative to the Floquet modes $n = \pm 1$ is shown in Fig. 3.9. This representation is particularly useful in the analysis of scan blindness phenomena since the first higher order Floquet modes can determine the onset of radiation nulls, as discussed in Section 3.3.

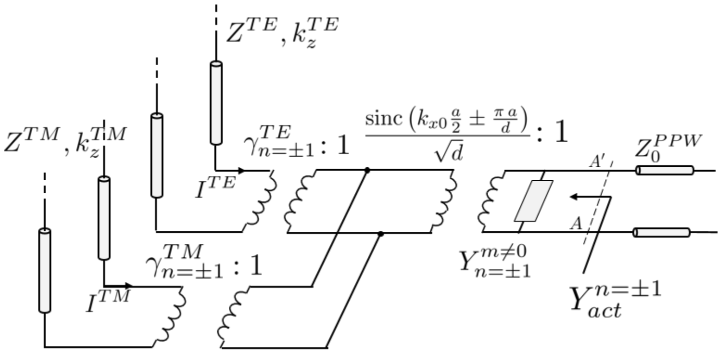

Figure 3.9: Circuit representation of the admittance term $Y_{act}^{n=\pm1}$ related to the first higher order Floquet modes ($n = \pm1$).

3.3 Scan blindness phenomena

The wideband properties of arrays of long slots, parallel-fed by progressively phased TEM modes, have been demonstrated in Section 3.1.2. In this section, the scanning capabilities in the principal planes are investigated to determine possible physical limitations and provide design criteria for maximizing the scan range. The factors limiting the scan range of an antenna array are the onset of grating lobes [64] and blind spots [57, 60, 65]. The first ones are purely due to the array lattice. Blindness phenomena are, instead, related to the mutual coupling [57] and to eigenmodes of the structure [65] that destructively interfere with the radiated space wave [65, 66] at certain frequencies, and determine dips in the radiation pattern. In practical cases, a near-unity active reflection coefficient is observed at a blind angle, at most elements of the array [57]. In infinite arrays, with equal current distributions at each element, scan blindness causes a zero in the radiation pattern and a unitary active reflection coefficient, i.e. all incident energy is back reflected in the feeding lines. The blind angles experimentally observed for a real array are generally close to those numerically predicted for the related infinite periodic array model [57, 65]. Therefore, the procedure for the computation of the active impedance of the infinite structure associated to the array under analysis (see Section 3.1.1) will be employed to predict the radiation nulls. In this context, the active reflection coefficient Γ_{act} is defined using the characteristic admittance Y_0^{PPW} of the PPWs as normalization admittance, as follows

$$\Gamma_{act} = \frac{Y_0^{PPW} - \overline{Y}_{act}}{Y_0^{PPW} + \overline{Y}_{act}} = \frac{\frac{1}{\zeta a} - Y_{act}}{\frac{1}{\zeta a} + Y_{act}} \tag{3.40}$$

where we recall that $\overline{Y}_{act}$ and Y_{act} are, respectively, the active admittance and the active admittance per unit length (along the y-direction) of the array. The blind spots are then defined as the angles θ_{blind} such that $|\Gamma_{act}(\theta_{blind})| = 1$.

The relations between the dimensions of the array lattice and the presence of radiation nulls in the principal planes are studied in Section 3.3.1. Particular emphasis is placed on the analysis of scan blindness in the H-plane, that is the plane where the CTS antennas considered in this work scan the beam. Moreover, this study has not been comprehensively addressed in the technical literature for this class of arrays. A novel condition on the element spacing for the onset of blind angles in the H-plane is derived for slot arrays in absence of dielectric.

The effects of dielectrics and, in particular, of a slab placed above the array aperture, are investigated in Section 3.3.1. This slab model dielectric layers for matching [62] and gain [67] enhancement that may be employed in conjunction with the antenna. Heuristic conditions that relates the geometrical and electrical features of the array and the blind angles are derived through parametric studies. It is shown that arrays loaded by a dielectric cover are prone to scan blindness in the H-plane if the element spacing is larger than half a wavelength.

3.3.1 Impact of the array lattice

The array lattice dimensions play a key role in determining the onset of grating lobes and radiation nulls [57]. These artifacts of the radiation pattern are particularly critical for largely spaced arrays. We focus on long slot arrays in absence of dielectrics, in order to define the maximum array periodicity d that can be employed without limiting the field of view in the principal planes.

As seen from the E-plane, the array is an infinite periodic structure of period d. Therefore, a grating lobe at an angle θ appears in the E-plane, at a frequency f when the array spacing is

$$d = \frac{\lambda_0}{1 + |\sin\theta|}, \tag{3.41}$$

where λ_0 is the free-space wavelength at f. Therefore, the array spacing should be less than half an operating wavelength in order to avoid grating lobes overall the field of view. It has been already shown in Fig. 3.5 that grating lobes are manifested by peaks in the amplitude of the active reflection coefficient. From (3.41), it can be noted that, for a given d, the grating lobe enter the visible region at $\theta = \pm 90^\circ$ and moves towards boresight as the frequency increases. However, blind angles can appear even for $d < \lambda_0/2$, in presence of dielectrics, and further reduce the scan range, as it will be discussed in Section 3.3.2.

The array does not feature any periodic structure along the H-plane. The antenna elements are continuous slots (along y-direction in Fig. 3.1) with uniform section. Therefore, no grating lobes can occur in the H-plane, disregarding the array spacing. Thus, the scan range of the array in the H-plane can only be limited by the scan blindness.

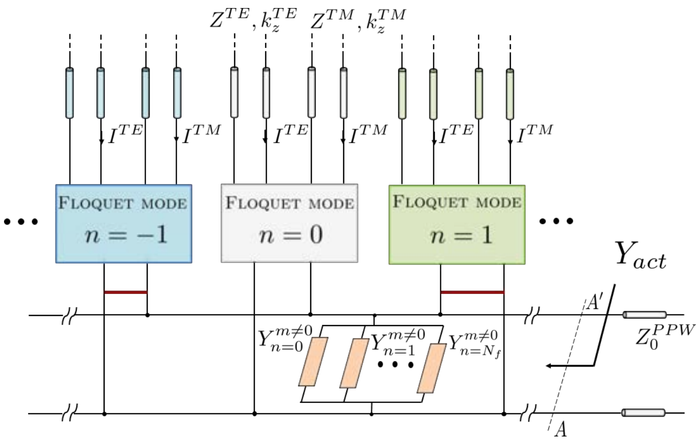

Figure 3.10: Equivalent circuit of the array when condition (3.11) holds for $n = \pm 1$.

It is has been stated in [65] and [68], without providing an exhaustive study, that blind spots can occur in the H-plane only when electrically thick radomes cover the radiating elements. A simple reasoning is here presented to show that radiation nulls can actually appear in the H-plane, even for arrays fed by hollow TEM waveguides and radiating in free space, provided that the period $d \geq \lambda_0$. The following relation of proportionality for the active admittance per unit length Y_{act} is inferred from (3.31) and (3.32)

$$Y_{act} \propto \tilde{G}_{yy}^{HM}\left(k_{xn}, k_{y0}, z = 0\right) \propto \frac{1}{\sqrt{k_0^2 - k_{xn}^2 - k_{y0}^2}}. \tag{3.42}$$

since the expression of the free-space Green's function $\tilde{G}_{yy}^{HM}$ is

$$\tilde{G}_{yy}^{HM}\left(k_x, k_y, z\right) = -\frac{1}{k\zeta_0}\frac{k_0^2 - k_y^2}{\sqrt{k_0^2 - k_x^2 - k_y^2}}. \tag{3.43}$$

When the array scans in the H-plane, $k_{xn} = 2n\pi/d$, with $n = -N_f, \dots N_f$ and $k_{y0} = k_0 \sin\theta_0$. The active admittance goes to infinity as the denominator in (3.42) vanishes. In this case, the array is virtually shorted and the incident energy cannot be radiated. The denominator is non-null for $n = 0$, except at grazing angle. By fixing the frequency and the scan angle θ_0, a zero of the denominator is found if the array period d fulfills the condition below

$$\sqrt{\left(\frac{2\pi}{\lambda_0}\cos\theta\right)^2 - \left(\frac{n}{2\pi}d\right)^2} = 0 \iff d = |n|\frac{\lambda_0}{\cos\theta} \tag{3.44}$$

In Section 3.1.3 it has been observed that the largely spaced slot array can reduce complexity and costs of CTS antennas. Condition (3.44) reveals that a blind spot appears in the H-plane pattern if the array spacing is greater than λ_0. This radiation null is related to the transition of the n-th Floquet modes from the evanescent to the propagating regime. In particular, the first higher order Floquet modes ($n = \pm 1$) determines the first observable

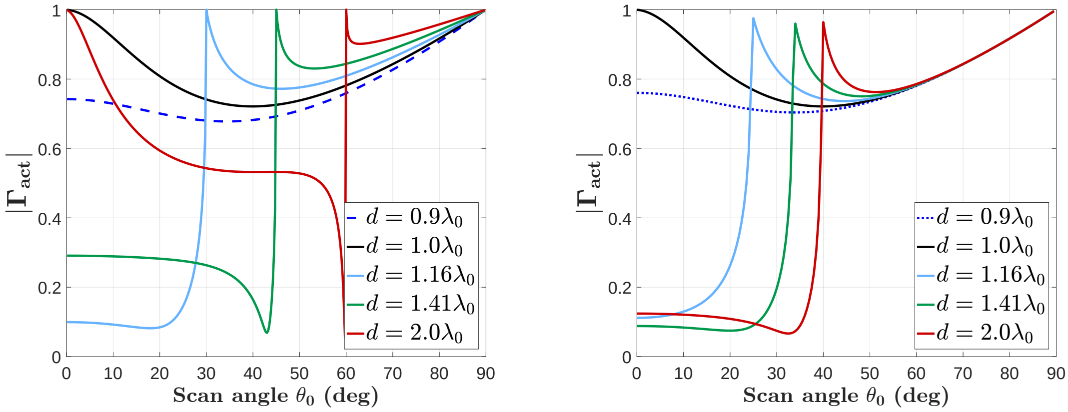

(a) (b)

Figure 3.11: Active reflection coefficient as a function of scan angle in the H-plane for an array fed by hollow PPWs that radiates in free space. The slot width is $a = 0.25\lambda_0$, where λ_0 is the free-space wavelength at $f_0 = 30$ GHz. Results for: (a) several values of d at f_0 and (b) $d = \lambda_0$ at different frequencies.

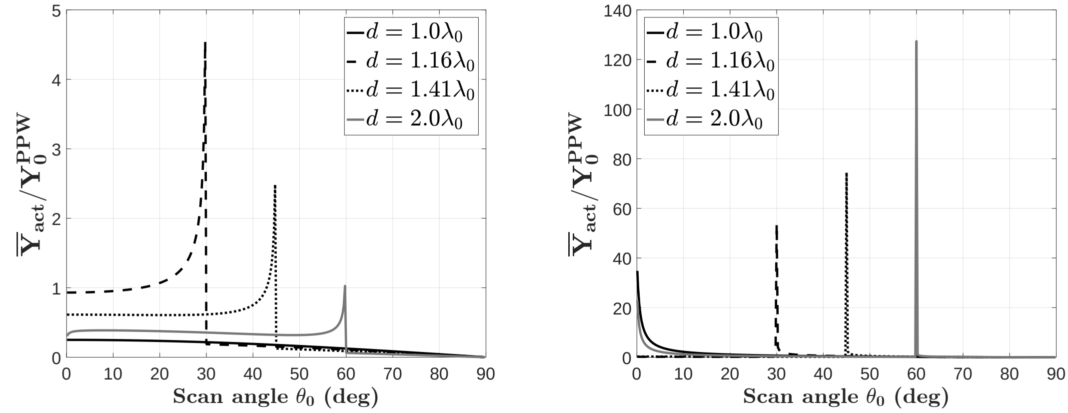

(a) (b)

Figure 3.12: (a) Real and (b) imaginary part of the normalized active admittance of the array of Fig 3.11 as a function the scan angle in the H-plane at $f_0 = 30$ GHz. Several array spacings are considered.

blind spot with the minimum array spacing ($d = \lambda_0$). When (3.44) holds for $n = \pm 1$, the equivalent network of Fig. 3.7 changes as shown in Fig. 3.10. The circuit blocks related to the first higher order Floquet modes are shorted, determining an infinite admittance at the input of the array. Figure 3.11a shows the active reflection coefficient as a function of scan angle, for several array spacings d, at $f_0 = 30$ GHz. The slots are narrow ($a = 0.25\lambda_0$) so that the higher order PPW modes have a small impact. Results are obtained running a Matlab code based on the procedure of Section 3.1.1. The parameters related to expansion and Floquet modes are set to $M = 5$ and $N_f = 5$, respectively, to get accurate results even in the neighborhood of resonances, so that blind angles can be precisely evaluated. For $d < \lambda_0$, no peaks are observed. A blind spot appears at broadside for $d = \lambda_0$ and it shifts towards end-fire as the array period increases. The corresponding active reflection coefficient is unitary. The onset of a blind spots at $\theta = 0°$ represents a severe issue. A careful choice of the array period is necessary even though the targeted field of view is narrow. When the array period is $d = 2\lambda_0$, two blind angles can be recognized: the first at $\theta = 60°$ is due to the first higher order Floquet mode, while the second one appears at boresight and is caused by the propagation of the Floquet modes $n = \pm 2$. In Figure 3.11b, $|\Gamma_{act}|$ is plotted for an array with $a = 0.25\lambda_0, d = \lambda_0$ at several frequencies. The blind spots moves from $\theta = 0°$ to $90°$ for increasing frequencies.

In order to get more insight on the onset of blind angles, the array active admittance, normalized to the characteristic admittance Y_0^{PPW} of the PPW feeds, is plotted in Fig. 3.12. Both the conductance and the susceptance diverge when a blind angle appears, except for the array with $d = \lambda_0$ that exhibits a finite real part of the active admittance.

3.3.2 Blindness in arrays loaded by a dielectric slab

Dielectric layers are commonly employed to improve the scanning performance of phased arrays, in terms of input matching [62] and realized gain [67]. Moreover, dielectric covers are often used to protect the array aperture [68]. In these configurations, the dielectric material is placed in the near field of the array and perturbs the aperture distribution. The spectral Green's function formulation presented in Section 3.1.1 accounts for these effects. In this section, the analysis tool is exploited to extensively investigate the occurrence of blind angles in the principal planes. In particular, we consider an array covered by a single dielectric slab of thickness t and relative permittivity ϵ_{r2}, as shown in Fig. 3.13. Though specific, this configuration can be used to model most cases encountered in common applications. Moreover, the individual influence of each parameter, e.g. the array period, the permittivity and thickness of the slab, on the onset and on the location of blind spots can be easily recognized considering a single slab.

The correlation between scan blindness and the presence of a dielectric cover on the antenna aperture has been first studied in [60,69] for phased arrays of rectangular waveguide and in [65] for arrays of open-ended PPWs. The latter work deals with an array configuration similar to that analyzed in this chapter. However, it focuses on the behaviour of the array for E-plane scanning and does not discuss the scan blindness in the H-plane. A systematic investigation on the relations among the array parameters and the blind spots, is presented

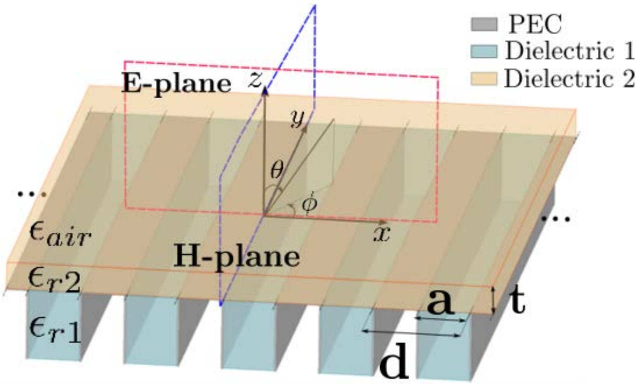

Figure 3.13: Infinite array of slots covered by a single dielectric slab of thickness t and relative permittivity ϵ_{r2}

for E-plane scanning in Section 3.3.2.1, yielding conclusions similar to those in [65]. Novel results relative to the scan in the H-plane are discussed in Section 3.3.2.2.

3.3.2.1 E-plane

When the array periodicity d is less than half the free-space operating wavelength, its radiation pattern does not exhibit grating lobes in the E-plane. However, an array loaded by a dielectric slab can present radiation nulls even if $d < \lambda_0/2$. Figure 3.14a shows the active reflection coefficient versus scan angle for an array fed by hollow PPWs that is loaded by a quarter wavelength slab ($t = 0.25\lambda_0/\sqrt{\epsilon_{r2}}$), with relative permittivity $\epsilon_{r2} = 4$. These values of thickness and dielectric constant are relatively small and are likely to occur in practical applications. Unitary peaks appear close to end-fire for arrays spacings less than half a wavelength. In particular, a blind spot is observed at about 57° when $d = 0.50\lambda_0$. Increasing the array spacing, the peaks of $|\Gamma_{act}|$ move toward the broadside direction and become sharper. This blind angle moves from 90° to 0° as d increases from $0.46\lambda_0$ to $0.77\lambda_0$. A further increase in the array spacing causes the onset of additional blind angles. The angular position θ_{blind} of the radiation null that first appears in the visible range is plotted in Fig. 3.14b as a function of d/λ_0, for different values of the permittivity of the slab. For all cases, the electrical thickness of the sheet is a quarter wavelength in the dielectric ($t = 0.25\lambda_0/\epsilon_{r2}$). The onset of the blind angles slightly shifts to smaller values of d as the dielectric constant of the slab increases. Moreover, the blind angles move faster from 90° to 0° when the permittivity of the slab is higher. This complicates the exact identification of the radiation nulls for practical designs.

A study on the impact of the slab thickness on the scan blindness is proposed in Fig. 3.15. The array considered has a small periodicity $d = 0.38\lambda_0$ and narrow radiating slots ($a = 0.25\lambda_0/\sqrt{\epsilon_{r1}}$). The effect of different dielectric contrasts between the permittivity of the

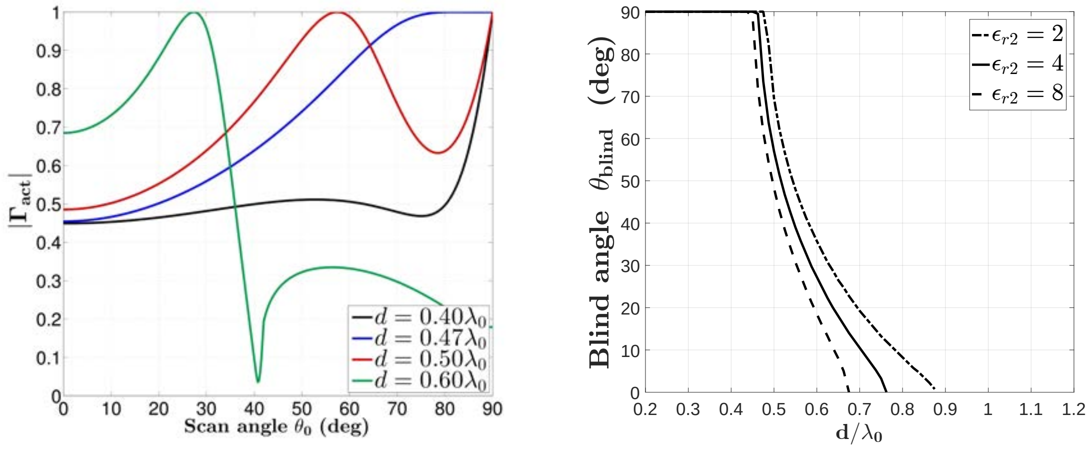

(a) (b)

Figure 3.14: (a) Active reflection coefficient of the array of Fig 3.13, with $a = 0.25\lambda_0$, $\epsilon_{r1} = 1$, $\epsilon_{r2} = 4$ and $t = \lambda_0/(4\sqrt{\epsilon_{r2}})$, as a function the scan angle in the E-plane, at $f_0 = c/\lambda_0 = 30$ GHz. (b) Blind angle as a function of array spacing d, for several values of ϵ_{r2}.

medium in the PPWs and that of the slab is illustrated as well. Figure 3.15a shows the blind angle as a function of layer thickness, normalized to the wavelength in the slab, for different values of ϵ_{r2}, with $\epsilon_{r2} > \epsilon_{r1}$ and $\epsilon_{r1} = 2$. No radiation nulls are observed for electrically thin slab. When t is increased beyond a critical value, a blind angle appears at 90° and moves toward the broadside direction for thicker slabs. This critical value of t reduces when the ratio $\epsilon_{r2}/\epsilon_{r1}$ increases. The onset of the blind angle is observed for $t > 0.49\lambda_0/\sqrt{\epsilon_{r2}}$ when $\epsilon_{r2} = 2\epsilon_{r1}$, and for $t > 0.31\lambda_0/\sqrt{\epsilon_{r2}}$ when $\epsilon_{r2} = 3\epsilon_{r1}$.

When the dielectric material in the PPWs is denser than the slab ($\epsilon_{r2} < \epsilon_{r1}$), the behaviour of the blind angle as a function of t is similar to that discussed for the previous case ($\epsilon_{r2} > \epsilon_{r1}$). However, an opposite trend is observed with respect to the dielectric contrast, i.e. to the ratio $\epsilon_{r2}/\epsilon_{r1}$. The blind angles are plotted against t in Fig. 3.15b, for $\epsilon_{r1} = 6$. It can be seen that the onset of the blind angles occurs for thinner slabs when ϵ_{r2} approaches ϵ_{r1}.

3.3.2.2 H-plane

The onset of radiation nulls in the H-plane pattern for element spacing $d \geq \lambda_0$ has been demonstrated in Section 3.3.1. When the array is loaded by a dielectric slab, scan blindness can occur in the H-plane even if the array spacing is less than half a wavelength. In particular, if d is in the range $(0.5\lambda_0, 1.0\lambda_0)$ blind angles are observed when the loading effect of the slab is moderate, i.e. for a slab thickness of about a quarter-wavelength and for

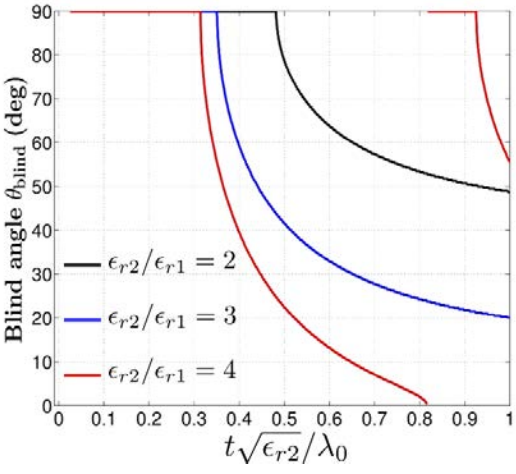

(a)

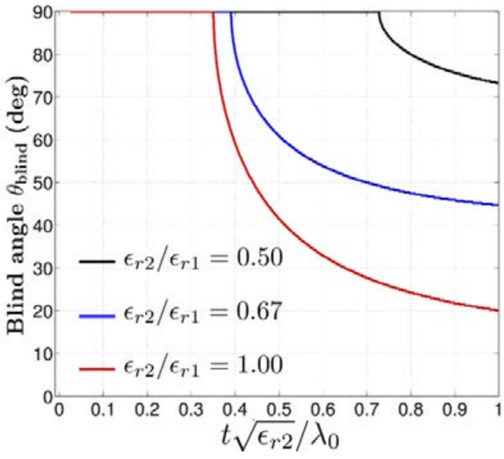

(b)

Figure 3.15: Blind angles in the E-plane, at $f_0 = 24.5$ GHz, as a function of slab thickness t for the array of Fig 3.13 with $a = 0.25\lambda_0/\sqrt{\epsilon_{r1}}$, $d = 0.38\lambda_0$. Two different sets of values are considered for the dielectrics: (a) $\epsilon_{r1} = 2$, $\epsilon_{r2} = \{4, 6, 8\}$; (b) $\epsilon_{r1} = 6$, $\epsilon_{r2} = \{3, 4, 6\}$.

small differences between ϵ_{r1} and ϵ_{r2}. Therefore, when the array periodicity is in this range of values, blindness is a relevant issue to handle in the design of CTS antennas. Figure 3.16a shows the active reflection coefficient against scan angle in the H-plane, at 30 GHz, for the structure analyzed in Fig. 3.14. The radiation null first appears at 0°, for $d \geq 0.75\lambda_0$. For larger element spacings, the unitary peak of $|\Gamma_{act}|$ moves toward 90° and becomes narrower. The threshold value of d for the onset of blind angles is greater than the one observed in the analysis of the E-plane scan.

The blind angle is an increasing function of the array spacing, as shown in Fig. 3.16b, that is the opposite of what has been observed for the scan blindness in the E-plane (see Section 3.3.2.2). The evidence that the radiation nulls first occur at boresight imposes a

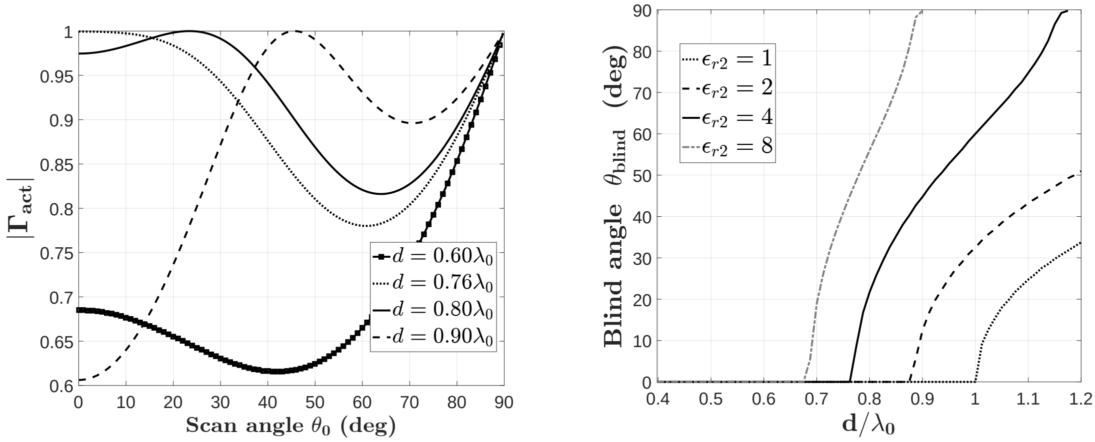

(a) (b)

Figure 3.16: (a) Active reflection coefficient of the array of Fig 3.13, with $a = 0.25\lambda_0$, $\epsilon_{r1} = 1$, $\epsilon_{r2} = 4$ and $t = \lambda_0/(4\sqrt{\epsilon_{r2}})$, as a function of scan angle in the H-plane at $f_0 = c/\lambda_0 = 30$ GHz. (b) Blind angle as a function of d/λ_0, for different values of ϵ_{r2}.

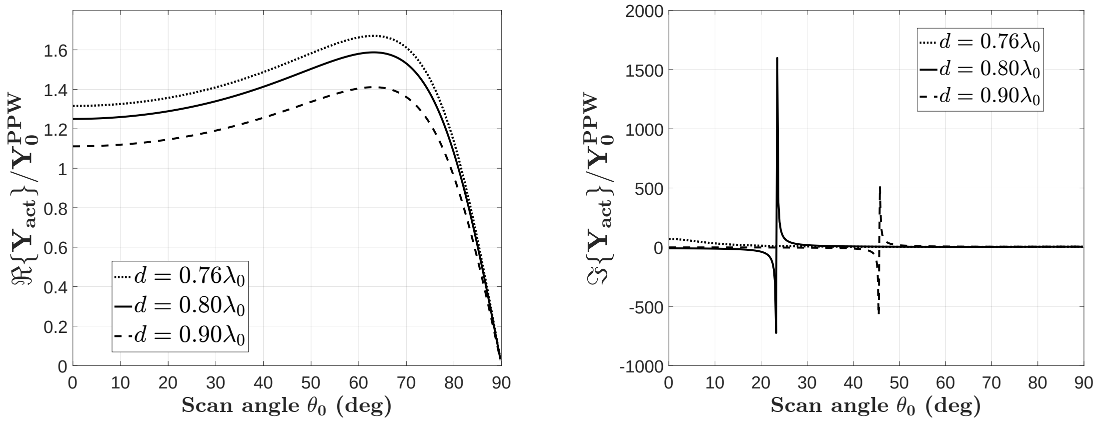

(a) (b)

Figure 3.17: (a) Real and (b) imaginary part of the normalized active admittance of the array of Fig 3.16 at $f_0 = 30$ GHz as a function of scan angle in the H-plane for several values of d that produce blind angles.

careful choice of the array spacing, since the antenna operation can be compromised even if a small scan range is targeted. Therefore, a conservative approach based on the design tightly spaced arrays may be followed to avoid scan blindness. For a robust design of largely spaced arrays, the value of d should guarantee that the blind angles are far enough from the limits of the desired scan range, at the operating frequency.

The active admittance of the array, normalized to the characteristic admittance of the PPW feeds, is plotted in Fig. 3.17 as a function of scan angle, for several values of d that

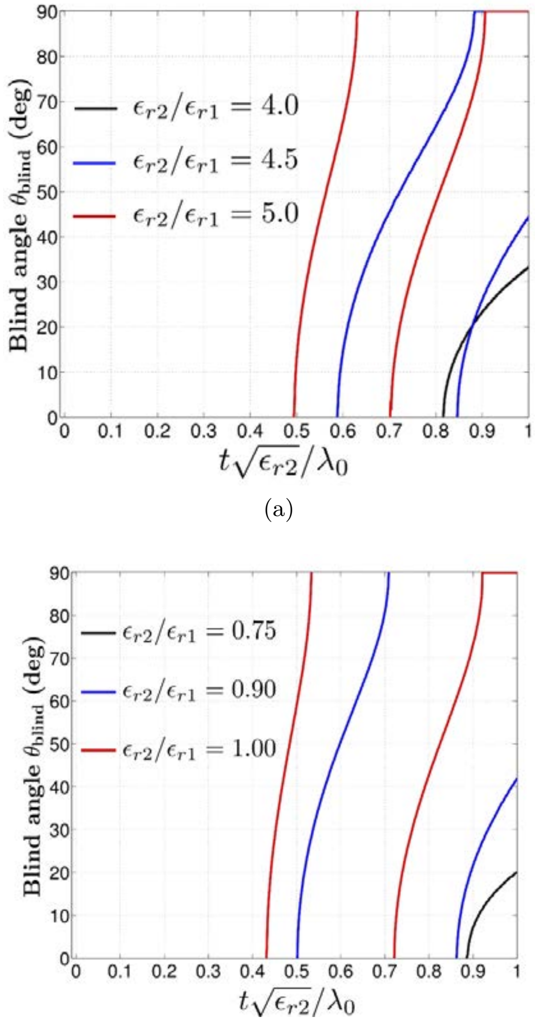

(a)

(b)

Figure 3.18: Blind angles in the H-plane, at $f_0 = 24.5$ GHz, as a function of slab thickness t for the array of Fig 3.13 with $a = 0.25\lambda_0/\sqrt{\epsilon_{r1}}$, $d = 0.40\lambda_0$. Two different sets of values are considered for the dielectrics: (a) $\epsilon_{r1} = 2$, $\epsilon_{r2} = \{8, 9, 10\}$; (b) $\epsilon_{r1} = 10$, $\epsilon_{r2} = \{7.5, 9, 10\}$.

determine blind angles. The real part, shown in Fig. 3.17a, is finite and does not exhibit discontinuities, whereas the active susceptance (Fig. 3.17b) diverges at the scan angles where the peaks of the active reflection coefficient are observed (see Fig. 3.16a). It is worth pointing out that this behaviour is different from that observed for arrays in absence of dielectrics. Indeed, both the active conductance and susceptance of the arrays considered in Section 3.3.1 exhibit singularities at the blind angle.

If the loading effect of the dielectric slab is emphasized, e.g. by increasing its permittivity, the radiation nulls appear for smaller element spacings. This trend is illustrated in Fig. 3.16b, for the same structure analyzed in Fig. 3.17. The critical value of d, that causes scan blindness, shifts from $d = \lambda_0$ to $d = 0.68\,\lambda_0$ when the relative permittivity ϵ_{r2} is increased from 1 (i.e. the case of an array radiating in free-space, discussed in Section 3.3.1) to 8. Moreover, the rate of increase of the blind angle with d is higher for high values of ϵ_{r2}.

Nulls in the H-plane pattern were observed also for tightly spaced arrays, with periodicity $d < 0.5\,\lambda_0$. However, thick dielectric slabs and a high contrast between the permittivity of the cover and that of the medium filling the PPWs are necessary. As a test case, an array with the following parameters is considered: $d = 0.38\,\lambda_0$, $a = 0.25\,\lambda_0/\sqrt{\epsilon_{r1}}$, $\lambda_0 = c/f_0$, with $f_0 = 24.5$ GHz. The angular position θ_{blind} of the radiation nulls are plotted in Fig. 3.18a as a function of slab thickness, normalized to the dielectric wavelength, for $\epsilon_{r1} = 2$ and several values of ϵ_{r2}. The slab is assumed electrically denser than the medium in the PPW ($\epsilon_{r2} > \epsilon_{r1}$). The values of slab thickness that cause scan blindness are higher than those observed when the array scans in the E-plane. In this example, they are greater than half a dielectric wavelength, even when a high dielectric contrast ($\epsilon_{r2} = 5\epsilon_{r1}$) is assumed. Blind angles move from boresight to the end-fire direction with increasing thickness. Multiple blind angles may appear for larger values of t.

Similar results for an array with $\epsilon_{r2} \leq \epsilon_{r1}$ are presented in Fig. 3.18b. The array geometry is the same considered in Fig. 3.18a, but here a relative permittivity $\epsilon_{r1} = 10$ is assumed for the material in the PPWs. Such a high value is necessary to observe radiation nulls with a cover thinner than a dielectric wavelength. As opposed to the case previously discussed, scan blindness phenomena are more relevant when the dielectric discontinuity is small, i.e. for $\epsilon_{r2} \approx \epsilon_{r1}$. This is an important information for the design of CTS antennas fully-embedded in a dielectric substrate [70], that is discussed in Chapter 5. Indeed, in order to ease the fabrication, the same material is employed for the antenna and for the slab above the aperture, that is typicall needed to improve the matching.

3.3.3 Physical interpretation of scan blindness

Since the first experimental observations of scan blindness phenomena [71–73], the interpretation of their physical origins has been controversial. The presence of blind spot was first attributed to surface-wave-like modes [71], supported by waveguide arrays, seen as a corrugated structure. Pozar and Schaubert [66] expalained scan blindness in arrays of printed elements as the matching of the phase velocities of the first Floquet mode and of the dominant surface wave supported by the substrate. However, pure surface waves cannot be supported by waveguide arrays, since the feeding waveguides are not reactively terminated. Knittel *et al.* [65] demonstrated a correlation between blind angles and the radiation angles of leaky modes supported by the array. They concluded that the scan blindness is due to the interaction of the space wave with a free resonance mode of the array. Following

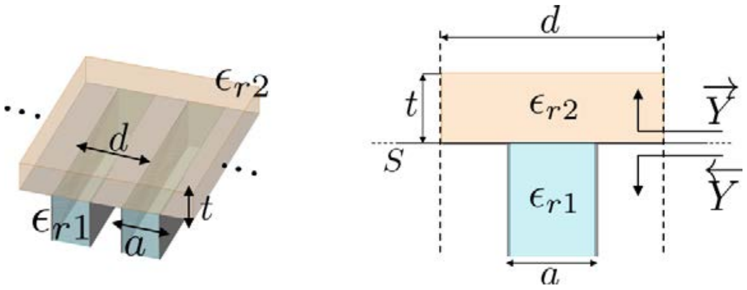

Figure 3.19: Illustration of the transverse resonance method applied to the unit cell of the array under analysis.

this explanation, we will determine the eigenmodes of the structure of Fig. 3.13 by deriving and solving the dispersion equation for its unit-cell, shown in Fig. 3.19. To this end, the transverse resonance method [41,59] is applied. The aperture plane S is chosen as reference section and the following dispersion equation is obtained

$$\overrightarrow{Y}(k_x, k_y) + \overleftarrow{Y}(k_x, k_y) = 0 \tag{3.45}$$

where $k_x = k_0 \sin\theta \cos\phi, k_y = k_0 \sin\theta \sin\phi$. $\overrightarrow{Y}$ and $\overleftarrow{Y}$ are, respectively, the admittances seen looking out from the PPW feed, and looking into the PPW. Therefore, $\overrightarrow{Y}$ is the active admittance of the array and $\overleftarrow{Y}$ is the characteristic impedance of the PPW feed. Equation (3.45) can be rewritten as

$$Y_{act}(k_x, k_y) + Y_0^{PPW} = 0 \tag{3.46}$$

The solutions of (3.46) are poles of the active reflection coefficient of the array, as it is clear from (3.40). When the array scans in the principal planes, the active admittance in (3.46) is a function of only one component of the transverse wavenumber, i.e. k_x in the E-plane and k_y in the H-plane.

The complex wavenumbers that solve (3.46) are numerically found using a Padé procedure [74]. Among the solutions, we focus on leaky modes [41,75], that propagate along the array aperture but also carry power away from it in the z-direction.

The relations between these free resonances of the structure and the blind angles are first studied for E-plane scanning. Figure 3.20 shows the active reflection coefficients against the scan angle at different frequencies for an array with periodicity $d = 0.405\ \lambda_0$. The parameters of the structure are reported in the caption of Fig. 3.20. The blind angles, that fulfill the condition $|\Gamma_{act}| = 1$, move from 90° to 0° for increasing frequency. The position of the radiation null is compared to the direction of maximum of the θ_{lw}^E of the beam radiated by the leaky mode supported by the structure. An approximate expression for θ_{lw}^E is found

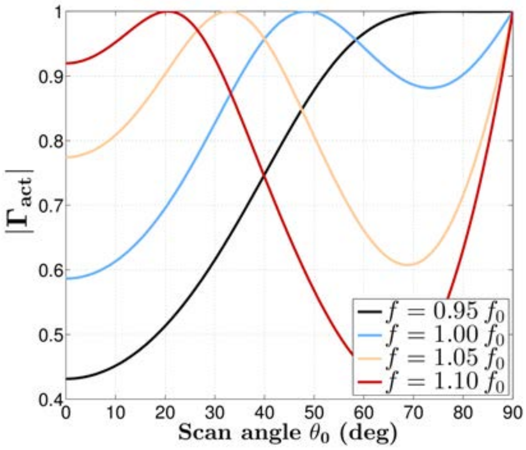

Figure 3.20: Amplitude of the active reflection coefficient as a function of scan angle in the E-plane at several frequencies for an array with the following parameters (refer to Fig. 3.13): $\epsilon_{r1} = 4, \epsilon_{r2} = 8$, $d = 0.405\lambda_0$, $a = 0.25\lambda_0/\sqrt{\epsilon_{r1}}$, $t = 0.3\lambda_0/\sqrt{\epsilon_{r2}}$, $\lambda_0 = c/f_0$ and $f_0 = 24.5$ GHz.

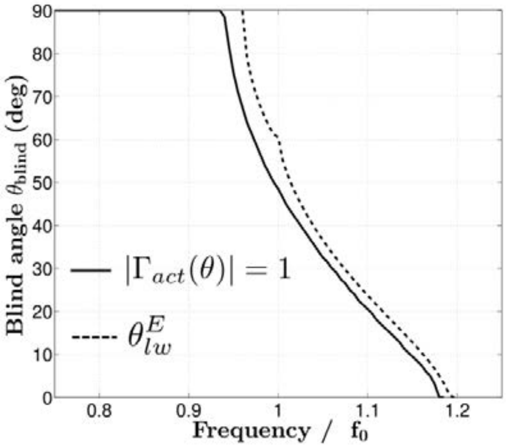

Figure 3.21: Blind angle in the E-plane and direction of propagation of the leaky mode supported by the array analyzed in Fig. 3.20, as functions of frequency ($f_0 = 24.5$ GHz).

using the following formula [41, 76]

$$\theta_{lw}^E = \arcsin\left(\frac{\Re\{\overline{k}_x\}}{k_0}\right) \tag{3.47}$$

where $\overline{k}_x$ is the pertinent complex wavenumber that solves the dispersion equation (3.46) in the E-plane, i.e. $\overline{Y}_{act}(\overline{k}_x) + Y_0^{PPW} = 0$. A correlation between the actual blind angle and θ_W is observed overall the frequency range (see Fig. 3.21).

The free resonances when the array scans in the H-plane are studied using the same rationale. A structure similar to that of Fig. 3.20, but with a thicker slab ($t = 0.7\lambda_0/\sqrt{\epsilon_{r2}}$), is considered. All parameters are reported in the caption of Fig. 3.22 that shows the

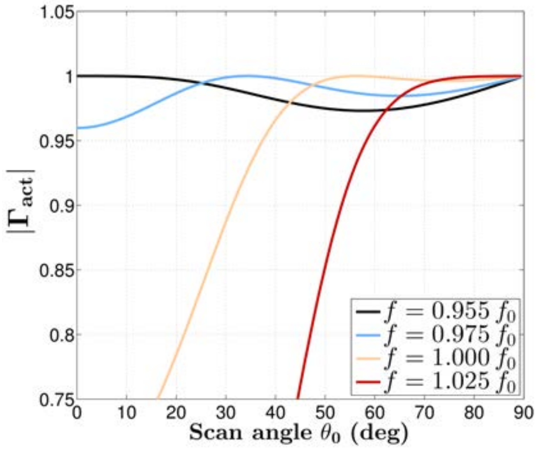

Figure 3.22: Amplitude of the active reflection coefficient as a function of scan angle in the H-plane at several frequencies for an array with the following parameters (refer to Fig. 3.13): $\epsilon_{r1} = 4, \epsilon_{r2} = 8$, $d = 0.40\lambda_0$, $a = 0.25\lambda_0/\sqrt{\epsilon_{r1}}$, $t = 0.7\lambda_0/\sqrt{\epsilon_{r2}}$, $\lambda_0 = c/f_0$ and $f_0 = 24.5$ GHz.

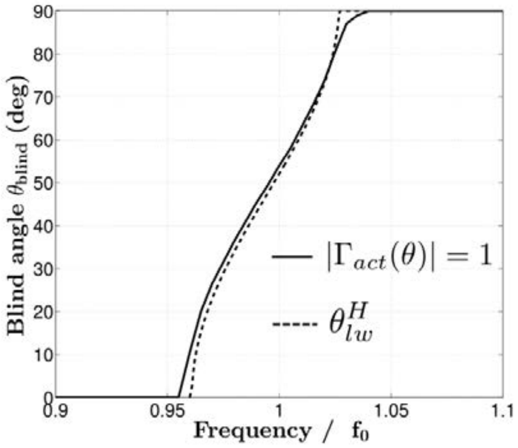

Figure 3.23: Blind angle in the H-plane and direction of propagation of the leaky mode supported by the array analyzed in Fig. 3.22, as functions of frequency ($f_0 = 24.5$ GHz).

computed active reflection coefficient as a function of scan angle. The blind spot moves from 0° to 90° when the frequency increases. Due to the significant loading effect of the slab, the rate of increase of the blind angle is high. This null is in the visible range only in a fractional band of 7%.

The radiation angle θ_W of the leaky mode that fulfills the dispersion equation for H-plane scanning is found as

$$\theta^H_{lw} = \arcsin\left(\frac{\Re\{\overline{k}_y\}}{k_0}\right) \tag{3.48}$$

where $\overline{k}_y$ is the complex transverse wavenumber such that $\overline{Y}_{act}(\overline{k}_y) + Y_0^{PPW} = 0$. Figure 3.23

demonstrates that the leaky mode radiates at about the same direction from broadside as the angle for which $|\Gamma_{act}| = 1$.

In summary, scan blindness in an array of long slots, loaded by a dielectric slab, can be interpreted as a destructive interaction between the radiated space wave and the beam radiated by a leaky mode that is a free resonance of the structure and, when excited, propagates in the slab along the array aperture.

3.4 Radiation patterns in the principal planes

Results and considerations discussed so far have been based on the active impedance of the array. The active element pattern, defined as the radiation pattern of the array when a radiating element is driven and all others are terminated with matched loads [57], can be calculated from the active reflection coefficient following the approach in [42, 77]. However, the expressions for the active admittance have been derived assuming an infinite array of slots of infinite length along the y-direction (see Section 3.1). This section presents an approximate method for the evaluation of the radiation patterns, in the principal planes, of a finite arrays of long slots, fed by a pillbox beamformer [52]. The model developed for the infinite array in Section 3.1 is combined with a windowing approach [78] to approximate the equivalent current distribution in a finite array. Due to finiteness and edge effects, the validity of this approach is restricted to large arrays, of eight or more elements, which are typically required for the applications targeted in this work [2, 8].

The computation of the patterns radiated by real CTS antennas must be based on a proper evaluation of the field distribution that excites the slots. Indeed, the beamforming system plays a fundamental role in the definition of the pattern characteristics. Here we focus on the CTS architecture presented in Section 2.2. The E-plane pattern of this antenna is mainly determined by the array lattice and by the corporate feed network. In the analysis, we assume that the corporate feed network excites each element with the same field distribution. The H-plane pattern is, instead, mainly dictated by the amplitude and the phase distributions along each slot, that are determined by the quasi-optical system. Since CTS arrays are generally designed to scan the beam in the H-plane, *ad-hoc* routines have been developed to analyze the pillbox beamformer. These procedures are based on geometrical optics (GO) [79] and on physical optics (PO) techniques previously proposed in the literature [80].

Some mathematical details relative to the computation of the normalized radiation patterns are given in Section 3.4.1. Numerical results are presented in Section 3.4.2 and compared with measured data.

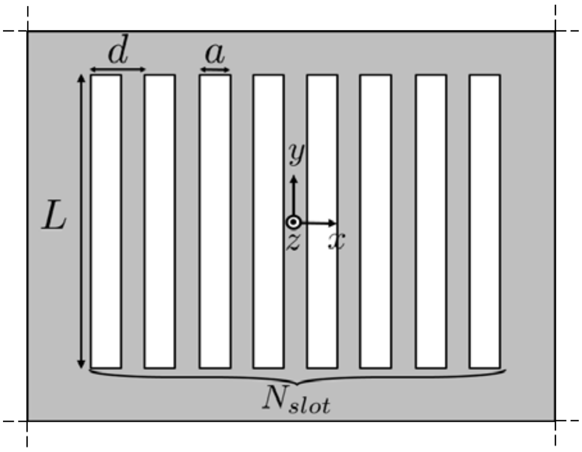

Figure 3.24: Top view of a finite array of slots in an infinite ground plane.

3.4.1 Approximate computation of the normalized radiation patterns

The geometry of an array of N_e slots in an infinite ground plane, with length L along the y-direction, is shown in Fig. 3.24. The slots are fed by PPWs and may be loaded by a planar multilayer dielectric cover, as shown in the general configuration of Fig. 3.1. The electric field $\mathbf{E}(x, y, z)$ radiated in the half-space $z > 0$ can be expressed using the plane wave spectrum representation [64]

$$\mathbf{E}(x, y, z) = \frac{1}{4\pi^2} \int_{\mathbb{R}^2} \mathbf{f}(k_x, k_y) e^{-jk_z z} e^{-j\mathbf{k}_\rho \cdot \boldsymbol{\rho}} dk_x dk_y \tag{3.49}$$

where $\mathbf{k}_\rho = k_x\hat{x} + k_y\hat{y}$, $\boldsymbol{\rho} = x\hat{x} + y\hat{y}$ and $\mathbf{f}(k_x, k_y) = f_x(k_x, k_y)\hat{x} + f_y(k_x, k_y)\hat{y}$. An alternative expression for the electric field is found by introducing the spectral Green's dyadic function $\tilde{\underline{\underline{G}}}^{EM}$ of the region $z > 0$, that relates the magnetic current on the aperture to the radiated electric field as follows

$$\mathbf{E}(x, y, z) = \frac{1}{4\pi^2} \int_{\mathbb{R}^2} \tilde{\underline{\underline{G}}}^{EM}(k_x, k_y, z)\, \tilde{\mathbf{M}}(k_x, k_y) e^{-j\mathbf{k}_\rho \cdot \boldsymbol{\rho}} dk_x dk_y \tag{3.50}$$

where $\tilde{M}$ is the Fourier transform of the magnetic current at $z = 0$. From (3.49) and (3.50), the vector $\mathbf{f}(k_x, k_y)$ can be written as

$$\mathbf{f}(k_x, k_y) = e^{jk_z z} \underline{\underline{G}}^{EM}(k_x, k_y, z)\, \tilde{\mathbf{M}}(k_x, k_y) \tag{3.51}$$

In the far-field approximation, the integrals (3.49) and (3.50) can be asymptotically evaluated, considering a stationary point $(k_{xs}, k_{ys}, k_{zs}) = (k_0 \sin\theta \cos\phi, k_0 \sin\theta \sin\phi, k_0 \cos\theta)$. Under this assumption, equation (3.51) can be rewritten as

$$\mathbf{f}(\theta, \phi) = e^{jk\cos\theta\,\overline{z}}\, \tilde{\underline{\underline{G}}}^{EM}(k\sin\theta\cos\phi, k\sin\theta\sin\phi, \overline{z})\, \tilde{\mathbf{M}}(k\sin\theta\cos\phi, k\sin\theta\sin\phi) \tag{3.52}$$

where a specific value $z = \overline{z}$ has been considered. It is convenient to choose $\overline{z}$ as the z-coordinate of the interface between the uppermost dielectric layer of the cover and the free-space.

In the far-field region, the polar components of the electric field are given by

$$E_\theta(r,\theta,\phi) = \frac{jke^{-jkr}}{2\pi r}\left[f_x(\theta,\phi)\cos\phi + f_y(\theta,\phi)\sin\phi\right] \tag{3.53}$$

$$E_\phi(r,\theta,\phi) = \frac{jke^{-jkr}}{2\pi r}\cos\theta\left[-f_x(\theta,\phi)\sin\phi + f_y(\theta,\phi)\cos\phi\right] \tag{3.54}$$

The Green's function in (3.52) can be easily evaluated using the equivalent transmission lines [59] for the region $z > 0$. Therefore, once an explicit expression for the magnetic current on the array aperture is found, the radiated far field can be calculated using (3.53) and (3.54). The magnetic current is found by preliminarily assuming that the array is infinite. The finiteness of the array is accounted for by truncating the magnetic current over a proper number of cells, with finite size along the y-direction. Thus, the magnetic current $\mathbf{M}(x,y)$ can be expressed as

$$\mathbf{M}(x,y) = \mathbf{M}_\infty(x,y)\,w(x,y) \tag{3.55}$$

where $\mathbf{M}_\infty(x,y)$ is the magnetic current at $z = 0$, computed in the infinite array environment, assuming an infinite length of the slots along the y direction, as in Section 3.1. The window function $w(x,y)$ can be factorized as follows

$$w(x,y) = w_E(x)\cdot w_H(y) \tag{3.56}$$

$$w_E(x) = \Pi_{N_e d}\left(x - \frac{a}{2}\right) = \begin{cases} 1 & \text{for} \quad |x - a/2| < N_e\, d/2 \\ 0 & \text{elsewhere} \end{cases} \tag{3.57}$$

$$w_H(y) = \Pi_L\,(y)\cdot E_{taper}(y) = \begin{cases} E_{taper}(y) & \text{for} \quad |x| < L/2 \\ 0 & \text{elsewhere} \end{cases} \tag{3.58}$$

where N_e is the number of elements, L is the length of the radiating slots in the y-direction and $E_{taper}(y)$ is introduced to account for the field distribution impressed by the beamforming system, e.g. by the pillbox coupler [47, 52]. Note that the functions $w_E(x)$ and $w_y(y)$ affect, respectively, the E- and H-plane cut of the radiation pattern.The Fourier transform $\tilde{\mathbf{M}}$ of the truncated magnetic current is found as the convolution of $\tilde{\mathbf{M}}_\infty$, whose expression is given in Appendix A, and $\mathcal{F}\{w_H(y)\}$, i.e. the Fourier transform of $w_H(y)$. Once $\tilde{\mathbf{M}}$ is computed, the polar components of the far field are derived by substituting (3.52) in (3.53) and (3.54). According to the third Ludwig's definition [81], the co-polar component of the far field in the E-plane is E_θ, for which the following relation holds

$$E_\theta(\theta,\phi = 0^\circ) \propto \sum_{n=-\infty}^{+\infty} \Lambda(k_{xn},m)\,\mathrm{sinc}\left(k_x - k_{xn}\right)\underline{\underline{\tilde{G}}}^{EM}\left(k_{xn},\overline{z}\right) \tag{3.59}$$

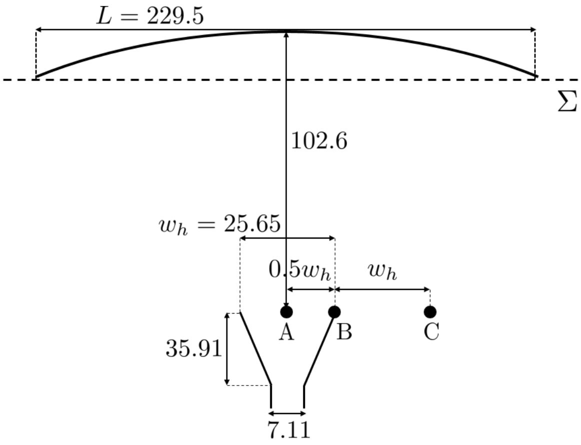

Figure 3.25: Geometry of the quasi-optical system of the CTS antenna in [47]. The positions of the input feed corresponding to scan angles of $0°, 7.5°$ and $20°$ are shown. Dimensions are given in millimeters.

The uniform illumination of the array elements results in a sinc-like pattern. The co-polar of the far field for H-plane scanning is instead E_ϕ. The follow proportionality is derived

$$E_\phi(\theta, \phi = 90°) \propto \mathcal{F}\{w_H(y)\}\, \underline{\underline{\tilde{G}}}^{EM}(k_y, \overline{z}) \tag{3.60}$$

This relation demonstrates that the radiation pattern in the H-plane of the analyzed CTS array mainly depends on $w_H(y)$ and thus on the excitation provided by the beamformer.

3.4.2 Numerical results

The accuracy of the proposed approximate approach, in its validity range, is discussed in this section considering, as a test case, the Ka-band CTS antenna [47] presented in Chapter 2.

A schematic view of the quasi-optical system is shown in Fig. 3.25. Three positions of the input horn in the focal plane of the parabolic reflector are considered, that corresponds to three beams in the H-plane, pointing at $\theta = 0°$ (position A), $\theta = 7.5°$ (position B) and $\theta = 20°$ (position C).

The window function $w_H(y)$ in (3.56) mathematically expresses the distribution of the field scattered by the parabola at the input of the corporate feed network of the CTS antenna. In order to evaluate this field, two numerical procedures for the analysis of the quasi-optical system have been developed. The first is a ray tracing routine [79], based on GO approximations. The second tool exploits the PO assumptions [80]. It computes the scattered field as a convolution of the electric current on the reflector with the 2-D Green's function of the output PPW of the pillbox coupler, assumed laterally unbounded. In both models, the actual radiation pattern of the input horn is considered as excitation source. Figure 3.26 shows the electric fields computed using the GO and PO procedures at the

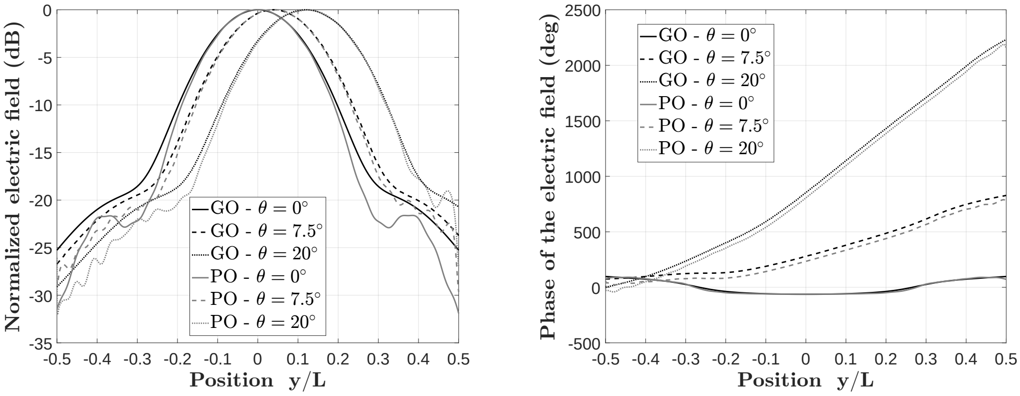

(a) (b)

Figure 3.26: (a) Normalized amplitude distribution and (b) phase distribution of the electric field at 29.25 GHz, at section Σ in the beamformer of Fig. 3.25, for several positions of the input feed. Results obtained with GO and PO methods are compared.

plane Σ (see Fig. 3.25) in the beamformer under analysis. For all positions of the input horn, the results are in good agreement. The numerical results reported in what follows are computed based on a PO analysis. Nevertheless, the GO procedure achieves a good accuracy with a lower computational effort.

Figure 3.27 shows the normalized far-field patterns in the principal planes, at 29.25 GHz for the broadside beam. An excellent agreement between measured and calculated data is observed. It is worth to stress that the proposed analysis does not account for the corporate feed network. Nevertheless, this has only a small impact on the amplitude of the side lobes at large angles.

Measured and calculated radiation patterns for scan angles of 7.5° and 20° in the H-plane are shown in Fig. 3.28. The beam pointing directions, the main lobe and the positions and the amplitudes of the first SLLs are accurately predicted. These parameters are very sensitive to the phase of the field scattered by the parabola that excites the array. Thus, these results prove the high accuracy of the PO procedure. Minor differences with measurements arise for amplitude levels lower than -30 dB that can be attributed to the corporate feed network.

The array considered in this test-case has sixteen elements and a slot length that is large as compared to the operating wavelength ($L = 22.38\lambda_0$ at 29.25 GHz). With these parameters, the errors introduced by the windowing approach are small and accurate results are achieved. As a rule of thumb, the formulation proposed to derive the far-field patterns provide good results for CTS arrays comprising more than 8 slots, each with a length $L > 5\lambda_0$.

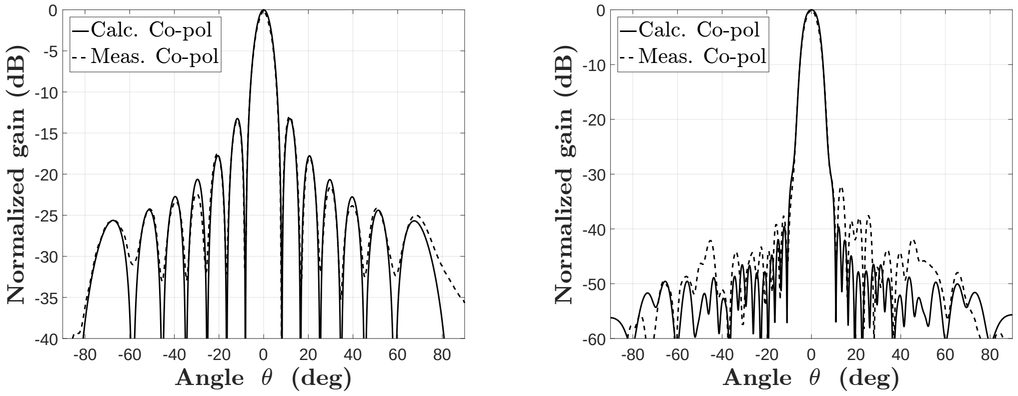

(a) (b)

Figure 3.27: Computed and measured normalized far-field patterns (broadside beam) at 29.25 GHz of the CTS antenna presented in [47]: (a) E-plane; (b) H-plane.

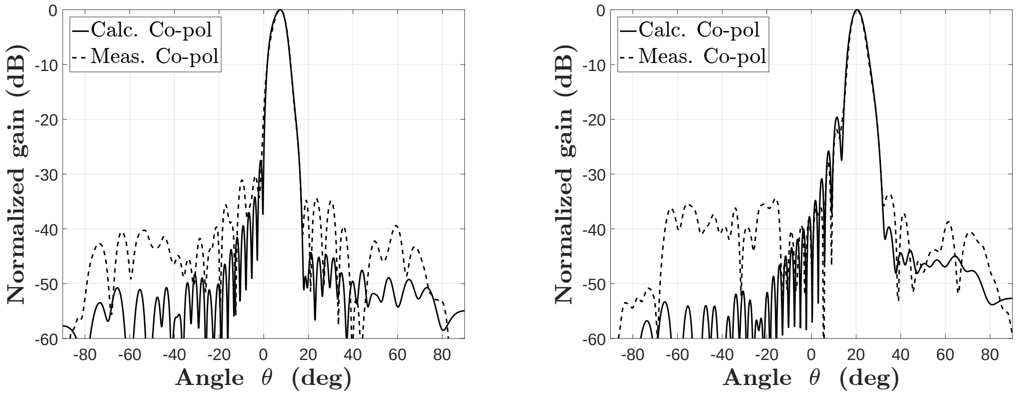

(a) (b)

Figure 3.28: Computed and measured normalized far-field patterns in the H-plane at 29.25 GHz of the CTS antenna presented in [47]. (a) Beam pointing at $\theta = 7.5°$. (b) Beam pointing at $\theta = 20°$.

3.5 Conclusion

Numerical models for the analysis of the slot array of parallel-fed CTS antennas have been presented. An accurate expression of the active admittance of an infinite array of infinitely-extended slots, loaded by a multilayer planar medium, has been derived using a spectral mode matching procedure. This procedure is based on the expansion in PPW modes of the magnetic current on the slots. This approach provides results in excellent agreement with full-wave simulations, using a few expansion modes, even for large scan angles in the principal planes. A circuit representation of the array has been derived from the formula of the active admittance, that reveals the specific contribution of Floquet and expansion modes.

The impact on the bandwidth of the array parameters have been discussed. Some design guidelines have been provided to achieve an almost frequency-independent impedance, over an octave bandwidth, and wide-angle operation.
The scanning performance of the array have been discussed, with emphasis on scan blindness phenomena. It has been observed that radiation nulls appear in the H-plane when the element spacing is greater than λ_0, if the array is fed by hollow PPWs and radiates in free-space. The impact on the scan blindness of a dielectric slab on the array aperture has been investigated. Blind spots are more likely to occur in the E-plane rather than in the H-plane. However, it has been shown that for $\lambda_0/2 < d < \lambda_0$ and for a slab thickness in the order of a quarter dielectric wavelength, blind spots may appear in the H-plane. The radiation nulls in the H-plane appear at boresight and move towards the end-fire direction when the frequency increases. When the slab is electrically denser than the dielectric in the PPWs that feed the slots ($\epsilon_{r2} > \epsilon_{r1}$), the onset of blind spots is favoured by large differences of the dielectric constants of the two media. Conversely, when $\epsilon_{r2} < \epsilon_{r1}$, the scan blindness is more critical when $\epsilon_{r2} \approx \epsilon_{r1}$. A dispersion analysis on the unit cell of the array revealed a correlation between the blind angles and the radiation angles of leaky modes supported by the structure.

Finally, an approximate approach to compute the normalized radiation patterns in the principal planes of finite arrays has been presented. The equivalent magnetic currents on the slots are assumed equal and are calculated in an infinite environment. Then, they are truncated using proper window functions. A simple rectangular window is used in the direction of the array, while along the longitudinal direction of the slots, a function that accounts for the field distribution introduced by the beamformer is employed. In order to predict the field distribution that excites each radiating slot in a CTS antenna fed by a quasi-optical system, *ad-hoc* GO and PO procedures have been developed and validated. The proposed windowing approach provides a good accuracy for CTS arrays with eight or more elements.

Chapter 4

Analysis of the corporate feed network

This chapter presented an effective, modular approach for the analysis of corporate feed networks of parallel-fed CTS antennas. The reference architecture that is here modeled has been implemented in several broadband designs [38, 47]. It consists of equal-split power dividers that are arranged in multiple stages to form the feed network.

The general structure and the modeling approach are detailed in Section 4.1. The network is subdivided into several building blocks that are separately modeled, using equivalent circuits and *ad-hoc* numerical procedures. The circuit models of basic PPW components, such as E-plane T-junctions and step discontinuities, are reviewed in Section 4.1. More complex subsystems, e.g. two designs of power dividers, are modeled in Section 4.2. Moreover, a compensated E-plane 90° bend is proposed to achieve a broadband matching, and a mode matching procedure for its analysis is described.

Different designs of the corporate feed network can be built and analyzed by cascading the blocks presented and the related models. This lends wide applicability to the proposed analysis method, that can be employed in the design to tackle different specifications, such as the maximization of the bandwidth or the minimization of the thickness of the structure. The accuracy of the results and the low computation time of the proposed method are demonstrated in Section 4.3 for full-corporate feed networks. This analysis technique can be combined with the procedure for the computation of the active impedance of the slot array, described in Chapter 3, to evaluate the reflection coefficient at the input of the feed network of a CTS antenna, as discussed in Section 4.4.

4.1 General structure and modeling strategy

The general structure of the radiating section of a CTS array is shown in Fig. 4.1. An array of N long slots in a ground plane is excited by a PPW corporate feed network. In order to

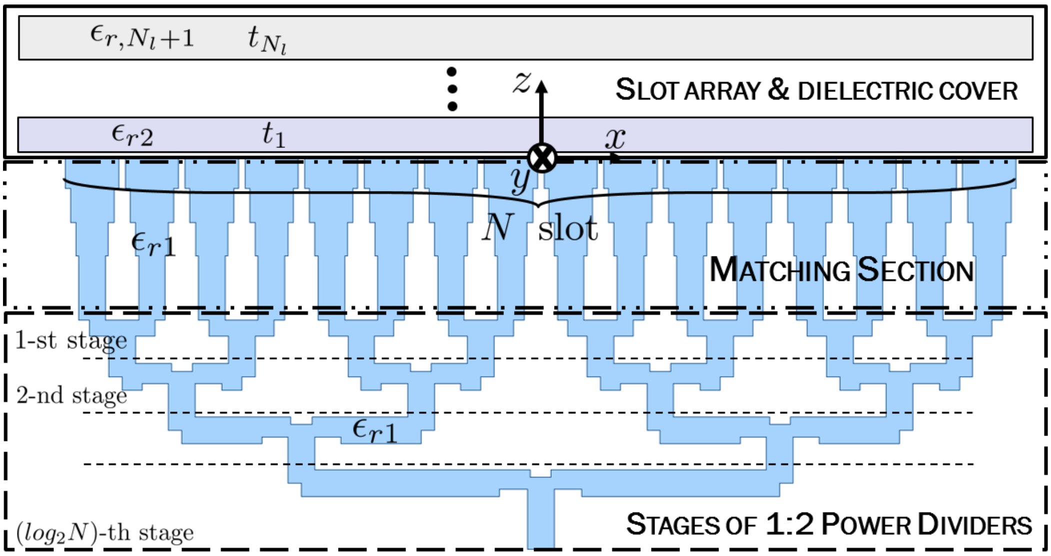

Figure 4.1: General architecture of the parallel-fed CTS array under analysis, with N radiating elements. Three main sections are highlighted: the slot array, the matching section and the log_2N stages of 1:2 power dividers.

ease the analysis, this architecture is subdivided into three functional blocks, highlighted in Fig. 4.1:

1. the array of rectangular slots, of length $L \gg \lambda_0$ along the y-axis, possibly loaded by a planar stratified cover with N_l layers. The i-th layer has permittivity $\epsilon_{r\ (i+1)}$ and thickness t_i, for $i = 1, \ldots, N_l$.

2. A matching section that features multistage or tapered impedance transformers, each connected to one of the N radiating slots.

3. $\log_2 N$ cascaded stages of E-plane, 1-to-2 way, equal split power dividers. A uniform excitation of the array is assumed. Therefore, the power dividers in a given division stage of the networks are assumed identical. This sub-network can be analyzed as a $N+1$-port component.

The arrays that we intend to study comprise a large number of elements. Therefore, they can be analyzed using the model presented in Section 3.1. The infinite array of infinitely-extended slots associated to the actual one and a pure TEM excitation is considered. All elements are assumed to exhibit the same active impedance and the edge effects are neglected.

We assume that the matching section and the network of power dividers feature ideal PPWs, unbounded along the y-direction. This hypothesis is justified by the large width of the waveguides ($L \gg \lambda_0$) and by the high amplitude taper introduced by the quasi-optical system in real CTS antennas [47]. All PPWs are filled by a linear, non-dispersive, homogeneous and isotropic material of relative permittivity ϵ_{r1} and guide a single TEM mode. Therefore, it is assumed that the height of each PPW is less than $0.5\lambda_{d1}$, being λ_{d1} the minimum wavelength in the dielectric.

The scattering parameters of each building block of the corporate feed network are determined using *ad-hoc* numerical procedures or equivalent circuits available in the literature [82] for basic components, such as E-plane T-junctions, step discontinuities and 90° bends. The scattering matrix of the feed network is computed by properly cascading the transmission matrices of the various subsystems. The input reflection coefficient of the overall structure, at the antenna boresight, is calculated by assuming that the N outputs are all terminated on the active impedance of the broadside infinite array.

4.2 Building blocks and related models

Different corporate feed networks can be analyzed using the modular approach outlined in Section 4.1. In this section, we introduce basic components and building blocks that are commonly used in the feed network of CTS antennas and we present equivalent circuits and numerical procedures for their modeling. We mainly focus on the designs proposed in [38] and [47]. Nevertheless, different designs can be built up and analyzed from the set of building blocks and models here presented.

4.2.1 Basic E-plane T-junctions, steps and right-angle bends

The performance of E-plane bends, E-plane T-junctions and E-plane step transformers in conventional rectangular waveguide operating in the dominant TE_{10} mode is described extensively in the literature [54, 82]. The fractional matching bandwidth that these components can achieve is generally much less than 40%, due to the inherent dispersive characteristics of the TE_{10} mode. In contrast to rectangular waveguide implementations, E-plane circuits that are realized with PPWs operating in the TEM mode can exhibit multi-octave frequency ranges. Their non-dispersive nature is essential for the design of wideband PPW corporate feed network.

It is straightforward to derive the equivalent circuits of basic PPW bends, T-junctions and steps from those presented in [82] for rectangular waveguide E-plane components. Figure 4.2 shows a PPW T-junction and its circuit model at the reference planes T and T'. The distance of the plates of the PPW fed at Port 3 is b' and its characteristic admittance is $Y_0' = \sqrt{\epsilon_{r1} w/(\zeta_0 b')}$, where ϵ_{r1} is the relative permittivity of the dielectric material in the component. The height of the other two PPWs is b and their characteristic admittance is $Y_0 = \sqrt{\epsilon_{r1} w/(\zeta_0 b)}$. We assume a single mode TEM propagation in the component, therefore

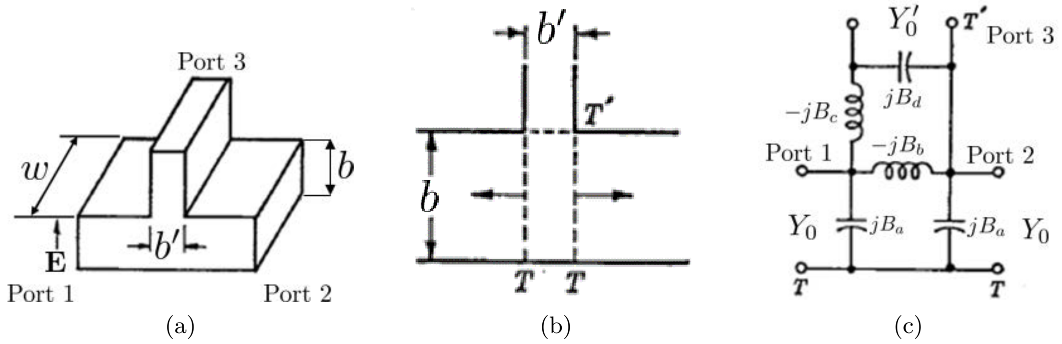

Figure 4.2: Basic PPW T-junction. (a) 3-D view. (b) Side view and location of the reference planes T, T' considered in the equivalent circuit. (c) Equivalent circuit. Pictures are taken from [82].

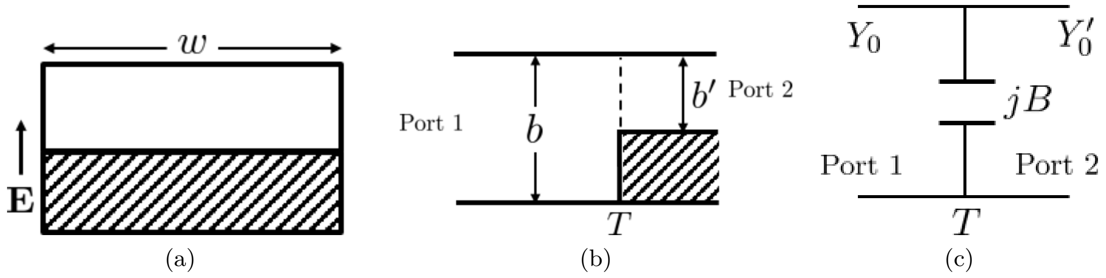

Figure 4.3: PPW step discontinuity. (a) Cross section. (b) Side view and location of the reference plane T considered in the equivalent circuit. (c) Equivalent circuit.

$b, b' < \lambda_g$ where $\lambda_g = \lambda_0/\sqrt{\epsilon_{r1}}$ and λ_0 is the free-space operating wavelength. The width of all PPWs along the longitudinal direction is $w \gg b, b', \lambda_g$. The circuit parameters in Fig. 4.2c are given in [82, p. 337]. The relative error in the computation of the elements admittance matrix from the equivalent circuit is in the order of 5% for $b'/b < 1$ and $b < 0.8\ \lambda_g$.
It can be shown that, in the quasi-static regime, the reflection coefficient seen at Port 3 is null when $Y_0 = 2Y'_0$, that is for $b' = 2\ b$. This observation will be exploited to design the power dividers in order to get the best matching performance.

Figure 4.3 shows the geometry and the equivalent circuit of a step discontinuity between two PPWs of height b (Port 1) and b' (Port 2), respectively. The circuit model at the plane of the step consists of a shunt capacitor. The expression of its capacitance can be found in [82, pp. 307-308]. Different characteristic admittance are seen on the two sides of the discontinuity: $Y_0 = \sqrt{\epsilon_{r1}}w/(\zeta_0 b)$ at Port 1 and $Y'_0 = \sqrt{\epsilon_{r1}}w/(\zeta_0 b')$ at Port 2. The equivalent circuit is valid for $b, b' < 0.5\ \lambda_g$ and provides results that agree within a few percent with the measured admittance parameters.

Right-angle bends play a key role in the design of the PPW true-time delay network.

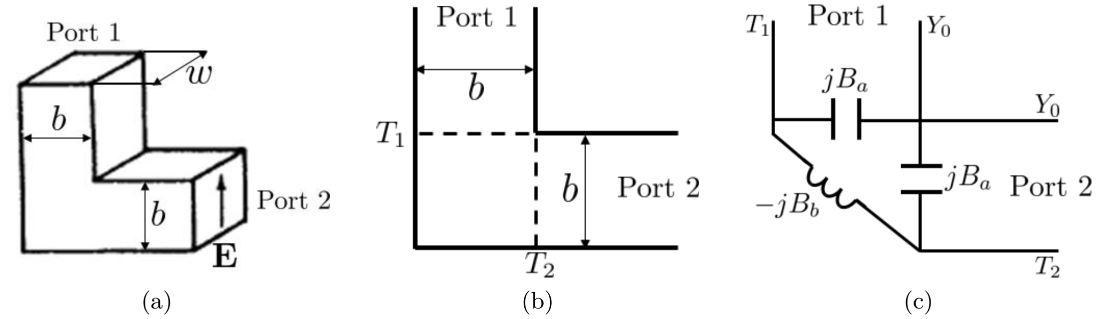

Figure 4.4: Basic PPW right-angle bend. (a) 3-D view. (b) Side view and location of the reference planes T_1, T_2 considered in the equivalent circuit. (c) Equivalent circuit. Pictures are taken from [82].

They are also employed to connect the PPW at the output of the pillbox coupler to the input of the corporate feed network, as in [47]. The structure and the circuit model of a simple 90° bend is shown in Fig. 4.4. The bend connects two orthogonal PPWs, with the same dimensions, (distance between the plates b, width w), and characteristic admittance $Y_0 = \sqrt{\epsilon_{r1}}w/(\zeta_0 b)$. The equivalent circuit is derived from the model of an E-plane waveguide bend and is valid for $b < \lambda_g$. The values of the reactances are reported in [82, p. 313].

4.2.2 Matching section: multistage impedance transformers

In the design of CTS antennas, the width of the radiating slots is typically maximized to enhance gain and input matching, whereas the waveguides in the corporate feed network are narrow, due to the limited inter-element spacing and the need to implement several components along the x-direction (see Fig. 4.1). Therefore, multistage impedance transformers may be required to gradually match the active impedance of the elements of the array to the characteristic impedance of the output lines of the first stage of power dividers (see Fig. 4.1). Figure 4.5 shows the cross section and the circuit model of the two-stage PPW impedance transformer of the CTS array described in Section 2.2. The geometrical details are given in the caption.

In general, an N-stage impedance transformer can be modeled using $N+1$ symmetric step discontinuities [82] and N transmission lines. The circuit model of symmetric steps is the same shown in Fig. 4.3c for asymmetric steps, but with a different value of the shunt capacitance, that is given in [82, p. 307-308]. The complete equivalent circuit for the structure under analysis is shown in Fig. 4.5b and is valid for $a_j < 0.5\ \lambda_g$, with $j = 1, 2, \ldots, N+2$.

The S-parameters calculated using the circuit model are in excellent agreement with full-wave simulations, as shown in Fig. 4.6. Finally, we observe that a tapered matching section

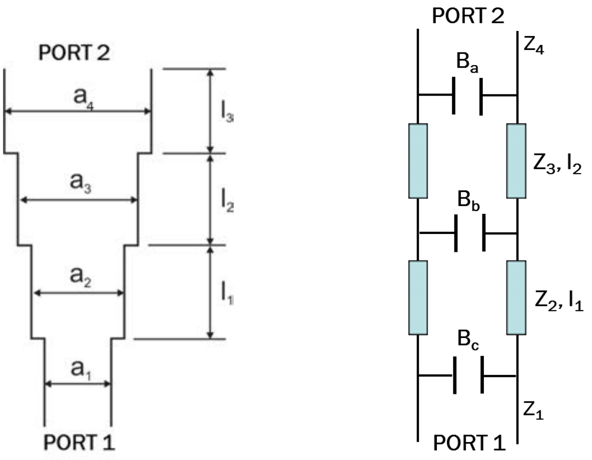

(a) (b)

Figure 4.5: Two-stage impedance transformer, based on hollow PPWs, of the CTS antenna presented in Section 2.2. (a) Cross section. (b) Equivalent circuit. The geometrical parameters are: $a_1 = 2.00$ mm, $a_2 = 2.45$ mm, $a_3 = 3.28$ mm, $a_4 = 2.00$ mm, $l_1 = l_2 = 2.56$ mm, $l_3 = 2.35$ mm.

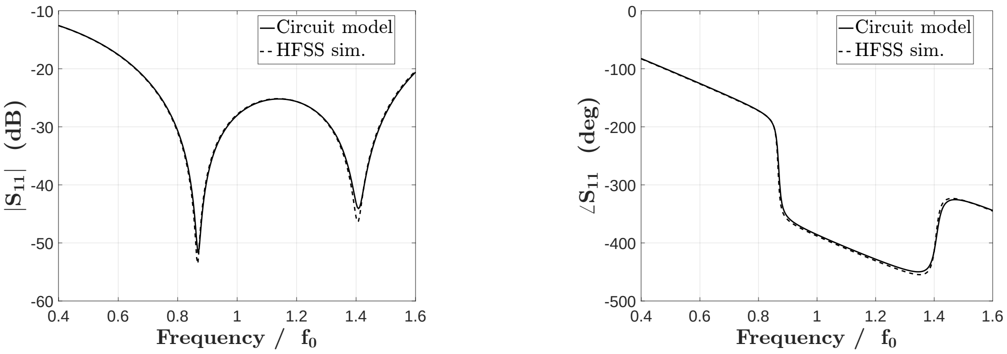

(a) (b)

Figure 4.6: (a) Amplitude and (b) phase of the S-parameters of the impedance transformer shown in Fig. 4.5. Results obtained from the circuit model are compared to HFSS simulations.

can be modeled as well, by using a stepped impedance transformer with a large number of electrically short stages [53].

4.2.3 Broadband E-plane power divider

The design of broadband E-plane power dividers is essential for the performance of CTS antennas. Conventional linear, passive, lossless E-plane T-junctions, as those presented in Section 4.2.1, are dispersive even if implemented with PPWs, due to their reactive char-

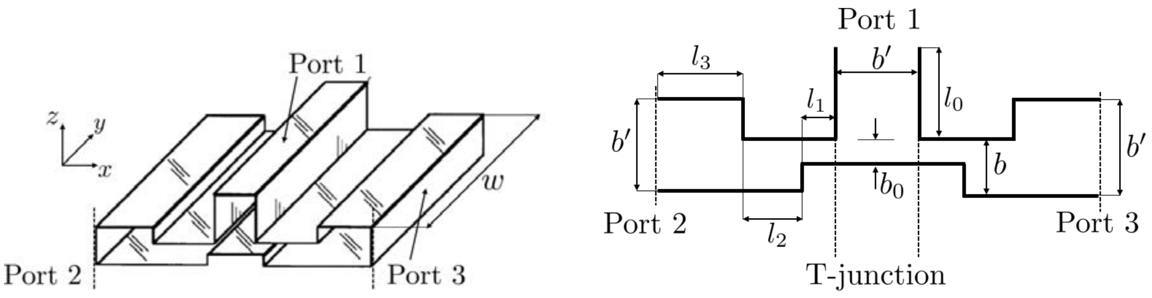

(a) (b)

Figure 4.7: Broadband E-plane PPW power divider presented in [55]. (a) 3-D view. (b) Cross section. Pictures are taken from [55].

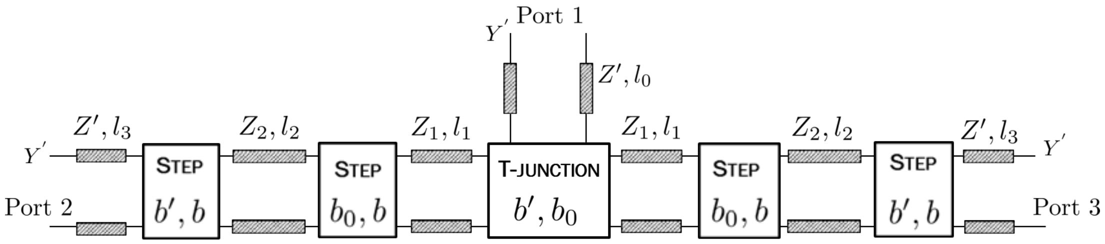

Figure 4.8: Circuit model of the power divider of Fig. 4.7. The boxes represent the equivalent circuits for the T-junction and the asymmetric step presented in Section 4.2.1.

acteristics. Tuning elements such as posts or irises are commonly used to match these junctions, but they achieve narrowband operation. Milroy proposed in [55] a design, based on E-plane stepped impedance transformers, that has been successfully employed in true-time delay feed networks for CTS antennas [38, 47]. The geometry of the E-plane power divider under analysis is shown in Fig. 4.7. It comprises a basic E-plane T-junction and an E-plane multistage transformer with asymmetric steps. The T-junction is formed by the PPW at Port 1, of height b', and the PPWs of height b_0. For clarity, an impedance transformer with a single section is shown. This transformer can be designed to cancel out the junction reactance and minimize the overall phase slope of the power divider over a wide frequency range. By doing that, a wideband matching can be achieved at one port, e.g. at Port 1. Note that the PPW lines at the three ports of the power divider have equal height b' and characteristics impedance $Y' = \sqrt{\epsilon_{r1}} w/(\zeta_0 b')$. This feature simplifies the design of full-corporate feed networks, that can be based on a repetitive scheme, by using modules with same impedances at the input and output ports.

The circuit model of the power divider is shown in Fig. 4.8. It has been built by cascading the equivalent circuits for the basic T-junction, the asymmetric steps and transmission line sections. The width of the inset ($w = b' + l_1$) is assumed larger than the height b' of the PPW at Port 1. The proposed circuit is valid for $\max\{b', b, b_0\} < 0.5\ \lambda_g$. The expected

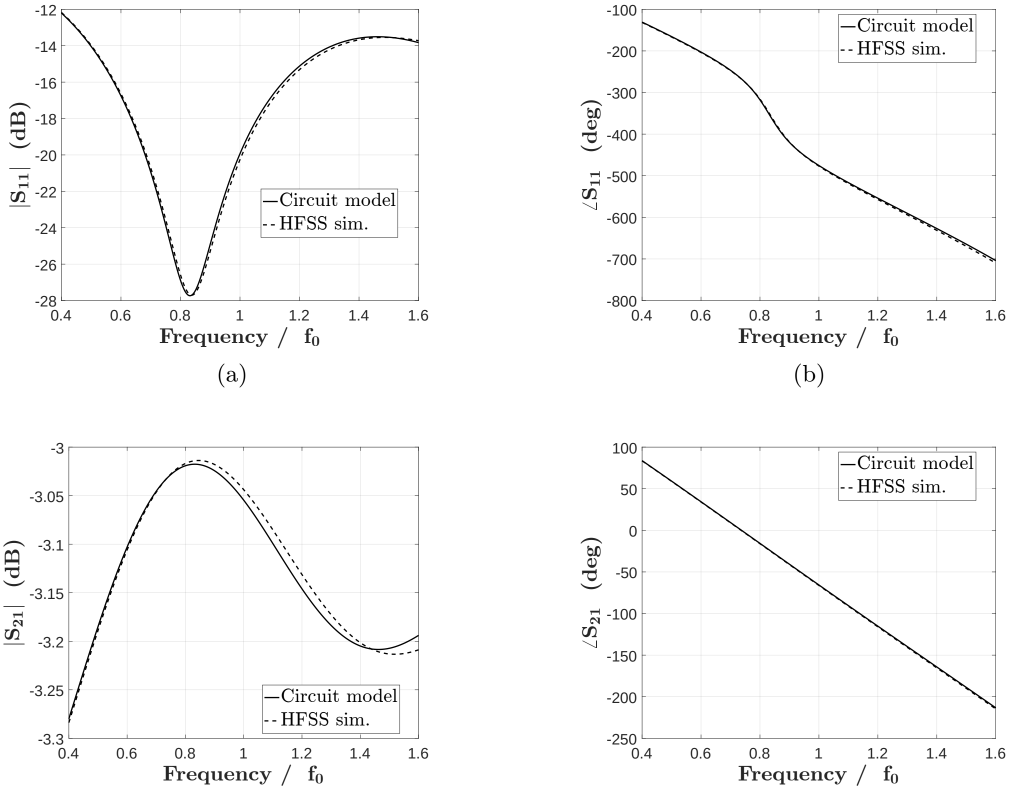

(a) (b)

(c) (d)

Figure 4.9: Calculated and simulated S-parameters of the power divider in Fig. 4.7, with $b' = 1.50$ mm, $b_0 = 0.5\ b'$, $b = b'/\sqrt{2}$, $l_1 = 0.45$ mm, $l_0 = l_2 = 3.00$ mm, $l_3 = 1.05$ mm. (a) $|S_{11}|$. (b) $\angle S_{11}$. (c) $|S_{21}|$. (d) $\angle S_{21}$. The central frequency is $f_0 = 25$ GHz.

relative error on the computed admittance parameters is within 5%, as for the model of the T-junction discussed in Section 4.2.1.

Figure 4.9 compares the S-parameters of a test structure, computed by using the circuit model, to full-wave simulated data. The geometrical parameters of the power divider are listed in the caption of the same figure. The circuit parameters of the T-junction are calculated using the formulas obtained in [82] with the equivalent static method. A very good agreement is observed for both amplitude and phase, in the entire frequency range. The results highlight the broadband performance of the power divider. The -15 dB matching bandwidth spans from 0.55 f_0 to 1.20 f_0 (about 75%), even though this design has not been optimized and comprises only a single-stage impedance transformer. The transmission coefficient form Port 1 to Port 2 (or Port 3) is greater than -3.3 dB in the considered band.

In the corporate feed network of a CTS antenna, the two outputs of each power divider are connected to E-plane right-angle bends (see Fig.4.1). Thus, it is interesting to study the performance of the power divider analyzed in Fig.4.10, when two square 90° bends are

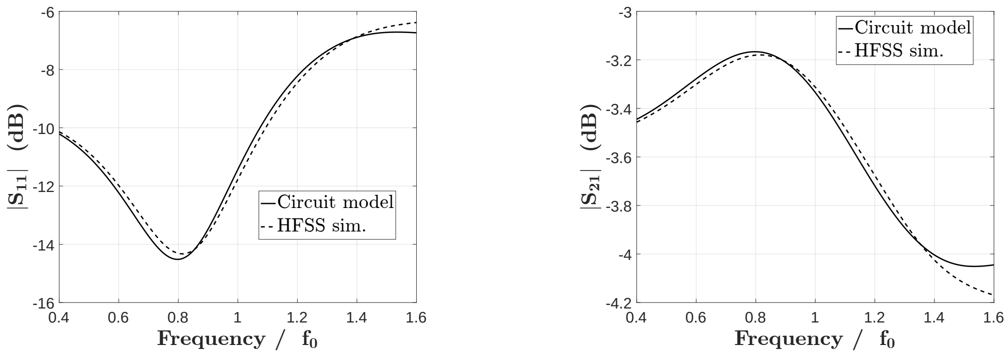

(a) (b)

Figure 4.10: Calculated and simulated S-parameters of the power divider analyzed in Fig. 4.9 with right-angle bends at Port 2 and Port 3. (a) $|S_{11}|$ and (b) $|S_{21}|$. The central frequency is $f_0 = 25$ GHz.

cascaded to Port 2 and Port 3, respectively. The input reflection coefficient at Port 1 and the insertion loss from Port 1 to one of the two output of the device so obtained are shown in Fig. 4.10.

A significant degradation in the input matching is observed and the broadband behaviour of the original power divider is lost. This is due to the dispersive nature of the 90° bend. Compensated designs, such as mitered and stepped bends, are required to preserve the wideband features of the feed network. A bend design that comprises a square step and enables a broadband matching performance is presented and modeled in Section 4.2.5.

4.2.4 Compact E-plane power divider

The power divider [55] described in Section 4.2.3 provides wideband performance but its implementation in tightly spaced arrays is impossible and inconvenient when the design is driven by factors other than bandwidth maximization. The power divider comprises at least two single-section impedance transformers and each of them typically has a length of about a quarter guided wavelength. Therefore, the center-to-center distance of the output ports of the device (Port 2 and Port 3 in Fig. 4.7) generally exceeds half a guided wavelength. The array spacing may be smaller than the distance between the output ports. In this case, the power dividers that are near the slots cannot be realized with this design. A different design has been implemented for the power dividers that feed the slots in the CTS antenna presented in [47].

The fabrication of several steps in the cross section of the broadband power divider design may be challenging and expensive, especially at high frequency. If this component

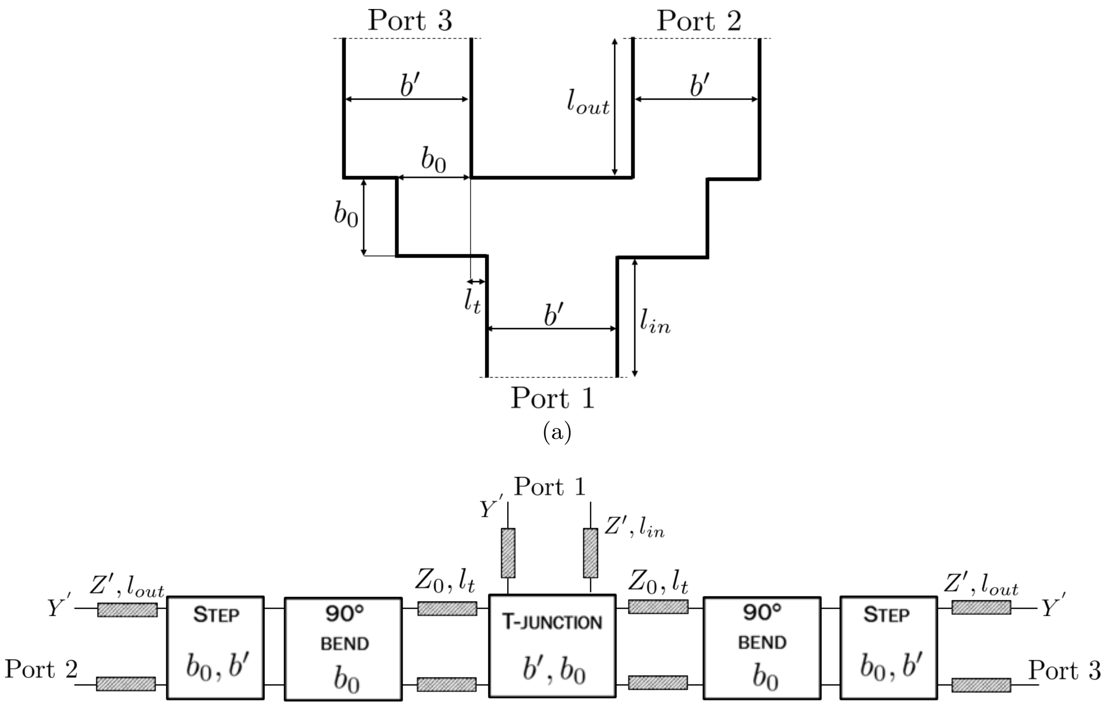

(a)

(b)

Figure 4.11: (a) Cross section and (b) circuit model of the proposed compact E-plane power divider. The dimensions of the design analyzed in this section are: $b' = 2.0$ mm, $b_0 = 1.2$ mm, $l_t = 0.35$ mm, $l_{in} = 2.1$ mm, $l_{out} = 2.1$ mm.

is integrated in a dielectric substrate, each step may require an additional layer to be implemented, as it will be explained in Chapter 5.

A compact and simple power divider is here presented and modeled, that achieves large bandwidth operation even for a small distance of the output ports. The design is shown in Fig 4.11a. It consists of a basic T-junction, whose outputs are connected to square right-angle bends. An asymmetric step discontinuity is employed at the output of each bend to enhance the input matching. All these components are individually mismatched, but can be jointly designed to minimize the reactance seen at the input of the power divider. The equivalent network in Fig. 4.11b can be easily derived. It is based on the circuit models described in Section 4.2.1 and is valid for $\max\{b', b_0\} < 0.5\ \lambda_g$.

The reflection coefficient at Port 1 and the transmission coefficient (from Port 1 to Port 2) are shown in Fig. 4.12. The values computed using the circuit model are in good agreement with the results obtained from HFSS simulations. The circuit parameters of the T-junction (see Fig. 4.2c) have been calculated using the asymptotic formulas in [82]. The input is well-matched over a broad band, in particular $|S_{11}| < -15$ dB from 22 GHz to 40 GHz, i.e. over a fractional bandwidth of about 70%. The transmission loss due to the mismatch is less than 0.42 dB overall the frequency range.

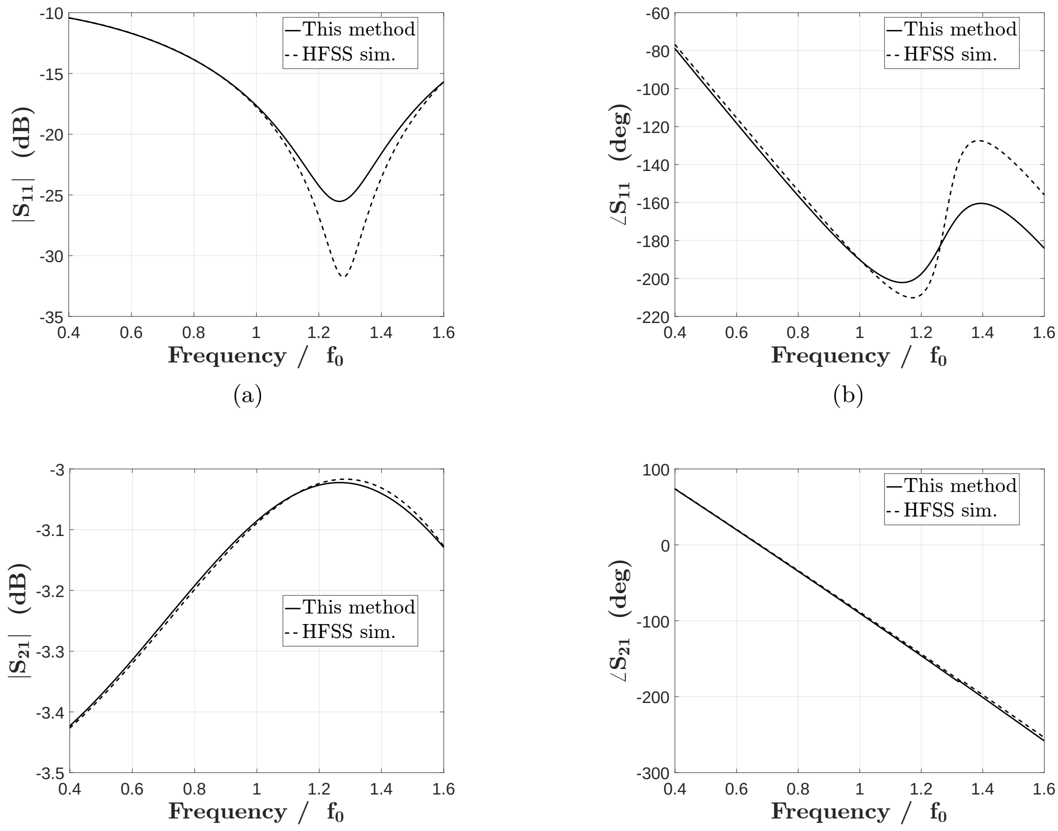

(a)

(b)

(c)

(d)

Figure 4.12: Calculated and simulated S-parameters of the power divider in Fig. 4.11a. (a) $|S_{11}|$. (b) $\angle S_{11}$. (c) $|S_{21}|$. (d) $\angle S_{21}$. The central frequency is $f_0 = 25$ GHz.

4.2.5 Mode matching analysis of a compensated 90° bend

The basic E-plane 90° bend presented in Section 4.2.1 exhibits a narrowband, dispersive behaviour that degrades the matching performance of the corporate feed network (see Section 4.2.3). Several compensated waveguide bends, e.g. curved [83], mitered [84, 85] and stepped [86], were proposed and variously modeled in the literature. In this section, we analyze a bend that is suitable for broadband PPW components and true-time delay feed networks [38, 55] for CTS antenna systems, operating in the transverse electromagnetic (TEM) mode. A square step is introduced in the corner to cancel out the reactive component of the bend and achieve broadband matching. As opposed to other compensated bends, this design can be realized in multilayer printed circuit boards [50, 70] (see Chapter 5), as well as in hollow waveguides.

The analysis methods for waveguide bends are generally based on mode matching techniques and on field expansions in fictitious cavities [85, 86], created by introducing shorting

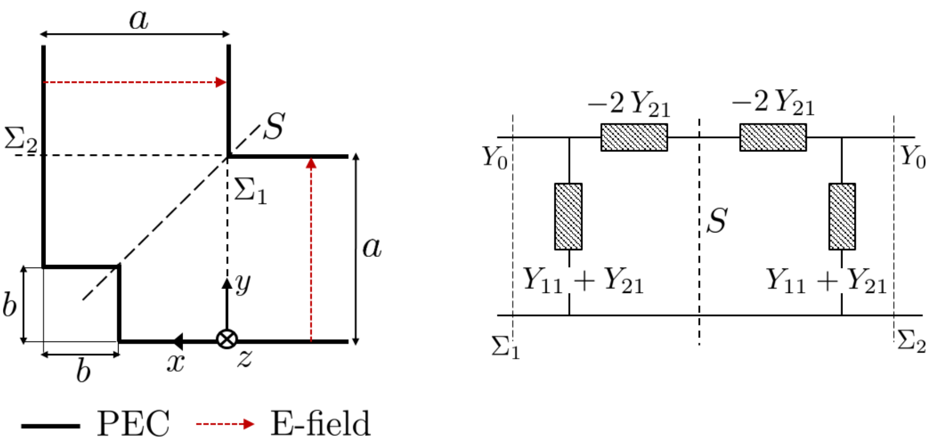

Figure 4.13: Geometry and equivalent circuit of the E-plane 90° PPW bend.

planes at the border of the bend. These models cannot be employed in the analysis of a bend directly connected to other components, since they do not account for higher-order mode interactions.

We present an efficient numerical procedure that overcomes this issue. The symmetry of the bend with respect to the bisecting plane is exploited to perform an even and odd mode analysis, following the approach in [84]. The unknown fields are computed using a mode matching method, that is discussed in the following sections, and the admittance matrix of the bend is determined.

4.2.5.1 Electromagnetic analysis

The reference system, the geometry of the bend and its equivalent circuit at the reference planes Σ_1 and Σ_2 are shown in Fig. 4.13. The structure includes two PPWs of height a and an E-plane 90° bend that presents a square step of width b. We assume that the PPWs support only the TEM mode, i.e. $a < \lambda/2$, where λ is the operating wavelength. The bend is symmetric with respect to the plane S. The admittance matrix is derived by separately solving two auxiliary problems. In the first one (Fig. 4.14a), the plane S is considered as a PEC, whereas in the second one (Fig. 4.14b) a PMC boundary is applied on S. The quantities relative to the first and second problem are denoted with superscripts “I” and “II”, respectively.

Given the symmetry and the TEM excitation, the transverse components of the fields in Region 1 of Fig. 4.14 are superpositions of TEM and transverse magnetic (TM) PPW modes.

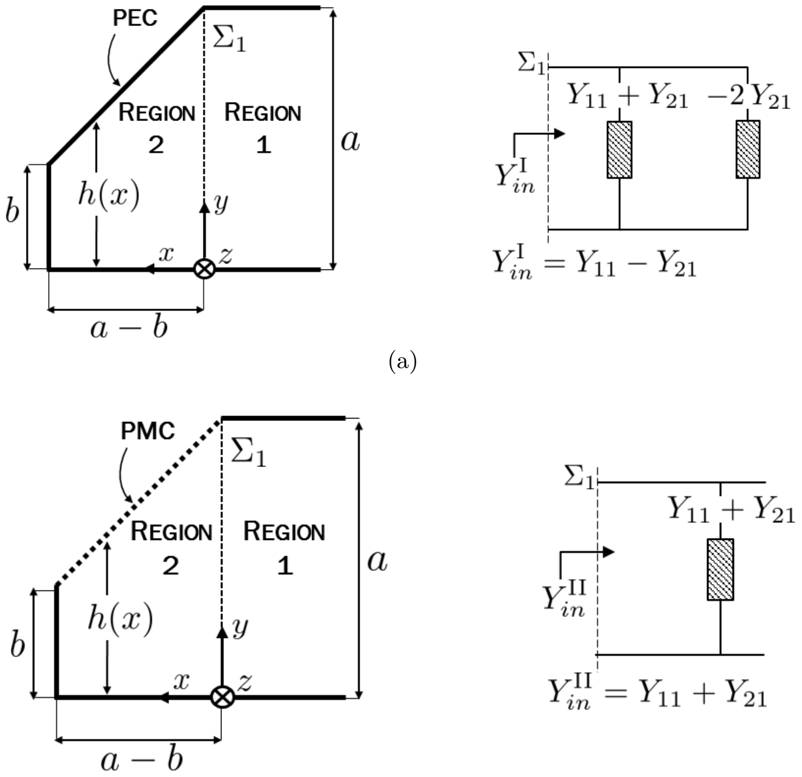

(a)

(b)

Figure 4.14: Geometry and equivalent circuit of the bend, bisected on the plane S by: (a) a PEC (case I); (b) a PMC (case II).

They can be written, omitting an amplitude factor 1 A/m, as

$$E^{\mathrm{I,II}}_{1y} = e^{-jkx} + \Gamma^{\mathrm{I,II}}_0 e^{jkx} + \sum_{n=1}^{+\infty} \Gamma^{\mathrm{I,II}}_n \cos\left(\frac{n\pi}{a}y\right) e^{jk_{xn}x} \tag{4.1}$$

$$H^{\mathrm{I,II}}_{1z} = Y_0\left(e^{-jkx} - \Gamma^{\mathrm{I,II}}_0 e^{jkx}\right) - \sum_{n=1}^{+\infty} Y_n \Gamma^{\mathrm{I,II}}_n \cos\left(\frac{n\pi}{a}y\right) e^{jk_{xn}x} \tag{4.2}$$

where Γ_n is the unknown reflection coefficient relative to the n-th mode. The expression of the modal admittance of the n-th mode is

$$Y_n = \frac{k_{xn}}{\zeta\, k} \tag{4.3}$$

where the propagation constant is $k_{xn} = \sqrt{k^2 - (n\pi/a)^2}$, being $\eta = \sqrt{\mu/\epsilon}$ the wave impedance in the medium that fills the bend, $k = \omega\sqrt{\mu\epsilon}$ is the wavenumber, and ω is the angular frequency.

The unknown fields in Region 2 fulfill Maxwell's equations

$$\frac{\partial E_{2y}^{\mathrm{I,II}}}{\partial x} = -j\omega\mu H_{2z}^{\mathrm{I,II}} + \frac{\partial E_{2x}^{\mathrm{I,II}}}{\partial y} \tag{4.4}$$

$$\frac{\partial H_{2z}^{\mathrm{I,II}}}{\partial x} = -j\omega\epsilon E_{2y}^{\mathrm{I,II}} \tag{4.5}$$

$$E_{2x}^{\mathrm{I,II}} = \frac{1}{j\omega\epsilon}\frac{\partial H_{2z}^{\mathrm{I,II}}}{\partial y} \tag{4.6}$$

subject to the following boundary conditions

$$E_{2x}^{\mathrm{I,II}}(x, y = 0) = 0 \tag{4.7}$$

$$E_{2y}^{\mathrm{I,II}}(x = a - b, y) = 0 \tag{4.8}$$

$$E_{2y}^{\mathrm{I}}\Big|_S = E_{2x}^{\mathrm{I}}\Big|_S \tag{4.9}$$

$$E_{2y}^{\mathrm{II}}\Big|_S = -E_{2x}^{\mathrm{II}}\Big|_S \tag{4.10}$$

Equations (4.9) and (4.10) account for the PEC and PMC on S, respectively, in the problems of Fig. 4.14a and Fig. 4.14b. The continuity of the fields across Σ_1 can be enforced using the equations below

$$E_{1y}^{\mathrm{I,II}}(x = 0, y, z) = E_{2y}^{\mathrm{I,II}}(x = 0, y, z) \tag{4.11}$$

$$H_{1z}^{\mathrm{I,II}}(x = 0, y, z) = H_{2z}^{\mathrm{I,II}}(x = 0, y, z) \tag{4.12}$$

In order to solve the differential problem defined by (4.4)−(4.6), with the pertinent boundary conditions, the transverse components of the unknown electric and magnetic fields in Region 2 are locally expanded in orthogonal modes. In the structure in Fig. 4.14a, the bend region can be seen, for each x, as PPW of height $h(x) = a - x$. Therefore, in this case a TEM and TM modes supported by a PPW of height $h(x)$ represent a convenient choice of the basis functions, yielding

$$E_{2y}^{\mathrm{I}} = V_0^{\mathrm{I}}(x) + \sum_{n=1}^{+\infty} V_n^{\mathrm{I}}(x)\cos\left[\frac{n\,\pi}{h(x)}y\right] \tag{4.13}$$

$$H_{2z}^{\mathrm{I}} = I_0^{\mathrm{I}}(x) + \sum_{n=1}^{+\infty} I_n^{\mathrm{I}}(x)\cos\left[\frac{n\,\pi}{h(x)}y\right] \tag{4.14}$$

For the case in Fig. 4.14b, the selected basis functions are TM modes in a region bounded by a PMC and PEC plane, spaced apart at a distance $h(x)$. The derivation of the mathematical expressions of these eigenmodes is presented in Appendix B. The transverse electric and magnetic fields in Region 2 can be then written as

$$E_{2y}^{\mathrm{II}} = \sum_{n=0}^{+\infty} V_n^{\mathrm{II}}(x)\cos\left[\frac{(2n+1)\,\pi}{2h(x)}y\right] \tag{4.15}$$

$$H_{2z}^{\mathrm{II}} = \sum_{n=0}^{+\infty} I_n^{\mathrm{II}}(x)\cos\left[\frac{(2n+1)\,\pi}{2h(x)}y\right] \tag{4.16}$$

Note that these expressions fulfill (4.7) and (4.10).

Approximate solutions are found by applying Galerkin method. The field expansions are truncated to N_1 and N_2 modes, for case I and case II, respectively, and are substituted into (4.4)-(4.6). Then, the L^2-inner products, in the domain $0 \leq y \leq h(x)$, of both sides of (4.4) and (4.5) are computed with the sets of test functions w_m^{I} (for case I) and w_m^{II} (for case II), yielding

$$\left\langle \frac{\partial E_{2y}^{\mathrm{I,II}}}{\partial x}, w_m^{\mathrm{I,II}} \right\rangle = -j\omega\mu \left\langle H_{2z}^{\mathrm{I,II}}, w_m^{\mathrm{I,II}} \right\rangle + \left\langle \frac{\partial E_{2x}^{\mathrm{I,II}}}{\partial y}, w_m^{\mathrm{I,II}} \right\rangle \tag{4.17}$$

$$\left\langle \frac{\partial H_{2z}^{\mathrm{I,II}}}{\partial x}, w_m^{\mathrm{I,II}} \right\rangle = -j\omega\epsilon \left\langle E_{2y}^{\mathrm{I,II}}, w_m^{\mathrm{I,II}} \right\rangle \tag{4.18}$$

where

$$w_m^{\mathrm{I}}(x,y) = \cos\left[\frac{m\pi}{h(x)}\, y\right], \; m = 0, \ldots, N_1 - 1 \tag{4.19}$$

$$w_m^{\mathrm{II}}(x,y) = \cos\left[\frac{(2m+1)\pi}{2h(x)}\, y\right], \; m = 0, \ldots, N_2 - 1 \tag{4.20}$$

The inner products are calculated integrating by parts and using (4.6) and (4.9) − (4.10). The original continuous problems are finally reduced to finite linear systems.

For case I, the following $2\,N_1$ equations are derived from (4.17)-(4.18), for $m = 0, 1, \ldots N_1 - 1$

$$\begin{aligned} \frac{dV_m^{\mathrm{I}}}{dx} = {} & \frac{h^2(x)k^2 - m^2\pi^2}{jh^2(x)\omega\epsilon} I_m^{\mathrm{I}}(x) - 2 \sum_{\substack{n=1,\\ n\neq m}}^{N_1-1} \frac{(-1)^{n+m}\, n^2}{(n^2 - m^2)\, h(x)} V_n^{\mathrm{I}}(x) - \frac{(1+\delta_m)}{2h(x)} V_m^{\mathrm{I}}(x) \\ & + \sum_{n=0}^{N_1-1} \frac{2\,(-1)^{n+m}}{(n^2-m^2)\, h(x)} V_n^{\mathrm{I}}(x) \end{aligned} \tag{4.21}$$

$$\frac{dI_m^{\mathrm{I}}}{dx} = -j\omega\epsilon V_m^{\mathrm{I}}(x) - \frac{I_m^{\mathrm{I}}(x)}{2h(x)}(1-\delta_m) - 2 \sum_{\substack{n=1,\\ n\neq m}}^{N_1-1} \frac{(-1)^{n+m}\, n^2}{h(x)} I_n^{\mathrm{I}}(x) \left(1 - \frac{\delta_m}{2}\right) \tag{4.22}$$

where $\delta_m = 1$ if $m = 0$ and is null otherwise.

For case II (Fig. 4.14b), $2N_2$ equations are found from (4.17)-(4.18), for $m = 0, 1, \ldots, N_2 - 1$

$$\begin{aligned} \frac{dV_m^{\mathrm{II}}}{dx} = & -j\omega\mu I_m^{\mathrm{II}}(x) + j\frac{(2m+1)^2\pi^2}{4\omega\epsilon h^2(x)} I_m^{\mathrm{II}}(x) - \sum_{\substack{n=0,\\ n\neq m}}^{N_2-1} \frac{(-1)^{n-m}(2n+1)}{2(n-m)h(x)} V_n^{\mathrm{II}}(x) \\ & - \sum_{n=0}^{N_2-1} \frac{(-1)^{m+n+1}(2n+1)}{2(m+n+1)\, h(x)} V_n^{\mathrm{II}}(x) \end{aligned} \tag{4.23}$$

$$\begin{aligned} \frac{dI_m^{\mathrm{II}}}{dx} = & -j\omega\epsilon V_m^{\mathrm{II}}(x) - \sum_{n=0}^{N_2-1} I_n^{\mathrm{II}}(x) \frac{(-1)^{n+m+1}(2n+1)}{2(m+n+1)\, h(x)} \\ & - \sum_{\substack{n=0,\\ n\neq m}}^{N_2-1} \frac{2n+1}{2(n-m)} \frac{(-1)^{n-m}}{h(x)} I_n^{\mathrm{II}}(x) \end{aligned} \tag{4.24}$$

Equations (4.21)-(4.22) and (4.23)-(4.24) are recasted in two systems of matrix differential equations, one for each problem in Fig. 4.14, that can be synthetically written as

$$\frac{d}{dx}\begin{pmatrix}\mathbf{v}^{\mathrm{I,\,II}}\\ \mathbf{i}^{\mathrm{I,\,II}}\end{pmatrix} = \underline{\underline{M}}^{\mathrm{I,\,II}}\begin{pmatrix}\mathbf{v}^{\mathrm{I,\,II}}\\ \mathbf{i}^{\mathrm{I,\,II}}\end{pmatrix} \tag{4.25}$$

where $\underline{\underline{M}}^{\mathrm{I}}$ and $\underline{\underline{M}}^{\mathrm{II}}$ are a $2N_1 \times 2N_1$ matrix and a $2N_2 \times 2N_2$ one, respectively. Their expressions are found from (4.21)-(4.22) and (4.23)-(4.24), respectively, and are given in Appendix B. The $N_1 \times 1$ column vectors $\mathbf{v}^{\mathrm{I}}$, $\mathbf{i}^{\mathrm{I}}$ are

$$\mathbf{v}^{\mathrm{I}} = \left(V_0^{\mathrm{I}}(x), V_1^{\mathrm{I}}(x), \dots, V_{N_1-1}^{\mathrm{I}}(x)\right)^T \tag{4.26}$$

$$\mathbf{i}^{\mathrm{I}} = \left(I_0^{\mathrm{I}}(x), I_1^{\mathrm{I}}(x), \dots, I_{N_1-1}^{\mathrm{I}}(x)\right)^T \tag{4.27}$$

Similarly, the elements of the $N_2 \times 1$ vectors $\mathbf{v}^{\mathrm{II}}$ and $\mathbf{i}^{\mathrm{II}}$ are given by

$$\mathbf{v}^{\mathrm{II}} = \left(V_0^{\mathrm{II}}(x), V_1^{\mathrm{II}}(x), \dots, V_{N_2-1}^{\mathrm{II}}(x)\right)^T \tag{4.28}$$

$$\mathbf{i}^{\mathrm{II}} = \left(I_0^{\mathrm{II}}(x), I_1^{\mathrm{II}}(x), \dots, I_{N_2-1}^{\mathrm{II}}(x)\right)^T \tag{4.29}$$

The fundamental matrix $\underline{\underline{F}}^{\mathrm{I}}$(x) for the system of differential equations (4.25), relative to case I, is determined by solving $2N_1$ initial value problems consisting of (4.25) subject to the following $2N_1$ orthogonal initial conditions on $\mathbf{v}^{\mathrm{I}}$ and $\mathbf{i}^{\mathrm{I}}$, obtained for $l = 1, 2, \dots, 2N_1$

$$\mathbf{v}^{\mathrm{I}}(0) = (\delta_{1,l}, \delta_{2,l}, \dots, \delta_{N_1,l}) \tag{4.30}$$

$$\mathbf{i}^{\mathrm{I}}(0) = (\delta_{N_1+1,l}, \delta_{N_1+1,l}, \dots, \delta_{2N_1,l}) \tag{4.31}$$

The solutions can be numerically found, e.g. by means of Euler or Runge-Kutta methods. Similarly, a fundamental matrix for the differential system (4.25), relative to the problem of Fig. 4.14b is built using the following $2N_2$ initial conditions, for $m = 1, 2, \dots, 2N_2$

$$\mathbf{v}^{\mathrm{II}}(0) = (\delta_{1,m}, \delta_{2,m}, \dots, \delta_{N_2,m}) \tag{4.32}$$

$$\mathbf{i}^{\mathrm{II}}(0) = (\delta_{N_2+1,m}, \delta_{N_2+1,m}, \dots, \delta_{2N_2,m}) \tag{4.33}$$

The boundary condition (4.8) yields

$$\mathbf{v}^{\mathrm{I,\,II}}(a-b) = \mathbf{0} \tag{4.34}$$

The solution in $x = 0$ of the final boundary value problems defined by (4.25) subject to (4.34) can be found by means of the fundamental matrices, as follows

$$\begin{pmatrix}\mathbf{v}^{\mathrm{I,II}}(0)\\ \mathbf{i}^{\mathrm{I,II}}(0)\end{pmatrix} = \underline{\underline{F}}^{\mathrm{I,II}}(0)\begin{pmatrix}\mathbf{v}^{\mathrm{I,II}}(a-b)\\ \\ \mathbf{i}^{\mathrm{I,II}}(a-b)\end{pmatrix}\left(\begin{array}{c|c}\underline{\underline{F_1}}^{\mathrm{I,II}}(0) & \underline{\underline{F_2}}^{\mathrm{I,II}}(0)\\ \hline \underline{\underline{F_3}}^{\mathrm{I,II}}(0) & \underline{\underline{F_4}}^{\mathrm{I,II}}(0)\end{array}\right)\begin{pmatrix}\mathbf{v}^{\mathrm{I,II}}(a-b)\\ \\ \mathbf{i}^{\mathrm{I,II}}(a-b)\end{pmatrix} \tag{4.35}$$

Equations (4.34) and (4.35) yield the following relations between the vectors $\mathbf{v}^{\mathrm{I,II}}(0)$ and $\mathbf{i}^{\mathrm{I,II}}(0)$

$$\mathbf{v}^{\mathrm{I,II}}(0) = \underline{\underline{F_2}}^{\mathrm{I,II}}(0) \left(\underline{\underline{F_4}}^{\mathrm{I,II}}\right)^{-1}(0)\, \mathbf{i}^{\mathrm{I,II}}(0) \tag{4.36}$$

The continuity of the fields must be stipulated for both the auxiliary problems.
For the first one (Fig. 4.14a), equations (4.11), (4.12) yield

$$\mathbf{i}^{\mathrm{I}}(0) = \mathbf{c}^{\mathrm{I}} - \underline{\underline{G}}^{\mathrm{I}}\, \mathbf{v}^{\mathrm{I}}(0) \tag{4.37}$$

where the $N_1 \times 1$-column vector $\mathbf{c}^{\mathrm{I}} = (2Y_0, 0, \ldots, 0)$ and $\underline{\underline{G}}^{\mathrm{I}}$ is a $N_1 \times N_1$ diagonal matrix, with $G^{\mathrm{I}}_{mm} = Y_{m-1}$, for $m = 1, \ldots, N_1$.
The expansion coefficients in $x = 0$ can be then calculated combining (4.36) and (4.37). The reflection coefficient Γ^{I}_0 is found from (4.11) and is given by

$$\Gamma^{\mathrm{I}}_0 = V^{\mathrm{I}}_0(0) - 1 \tag{4.38}$$

A weighted average method is applied in order to enforce the continuity of the fields in case II. This is necessary since the fields (4.1)-(4.2) in Region 1 have TEM components, as opposed to the field expansions (4.15)-(4.16) in Region 2. First, the latter expansions are inserted in (4.11) and (4.12). Both sides of each equation are multiplied by the set of N_2 test functions

$$\varphi_{(}y) = \cos\left(\frac{m\pi}{a}y\right), \qquad\qquad m = 0, 1, \ldots N_2 - 1 \tag{4.39}$$

and integrated in the domain $0 < y < a$. The equations so obtained can be recast in the following matrix equation

$$\underline{\underline{\Lambda}}\, \mathbf{i}^{\mathrm{II}}(0) + \underline{\underline{G}}^{\mathrm{II}}\, \underline{\underline{\Lambda}}\, \mathbf{v}^{\mathrm{II}}(0) = \mathbf{c}^{\mathrm{II}} \tag{4.40}$$

where the $N_2 \times 1$-column vector $\mathbf{c}^{\mathrm{II}} = (2Y_0, 0, \ldots, 0)^T$, $\underline{\underline{G}}^{\mathrm{II}}$ is a $N_2 \times N_2$ diagonal matrix, whose non-null elements are $G^{\mathrm{II}}_{rr} = Y_{r-1}$, for $r = 1, \ldots, N_2$, and the elements of $\underline{\underline{\Lambda}}$ are

$$\Lambda_{pq} = \frac{\cos\left[\pi\left(p + q - 2\right)\right]}{\pi\left[2\left(p + q - 2\right) + 1\right]} + \frac{\cos\left[\pi\left(q - p\right)\right]}{\pi\left[2\left(q - p\right) + 1\right]} \tag{4.41}$$

with $p, q = 1, 2, \ldots, N_2$. The expansion coefficients $\mathbf{v}^{\mathrm{II}}$ and $\mathbf{i}^{\mathrm{II}}$ are then determined using (4.36) and (4.40). From (4.40) the reflection coefficient Γ^{II}_0 can be expressed as

$$\Gamma^{\mathrm{II}}_0 = -1 + \sum_{l=1}^{N_2} \Lambda_{1l} V^{\mathrm{II}}_{l-1}(0) \tag{4.42}$$

The input admittances $Y^{\mathrm{I,II}}_{in}$ of the two structures in Fig. 4.14 are found using the TEM reflection coefficients (4.38), (4.42), yielding

$$Y^{\mathrm{I,II}}_{in} = Y_0 \frac{1 - \Gamma^{\mathrm{I,II}}_0}{1 + \Gamma^{\mathrm{I,II}}_0} \tag{4.43}$$

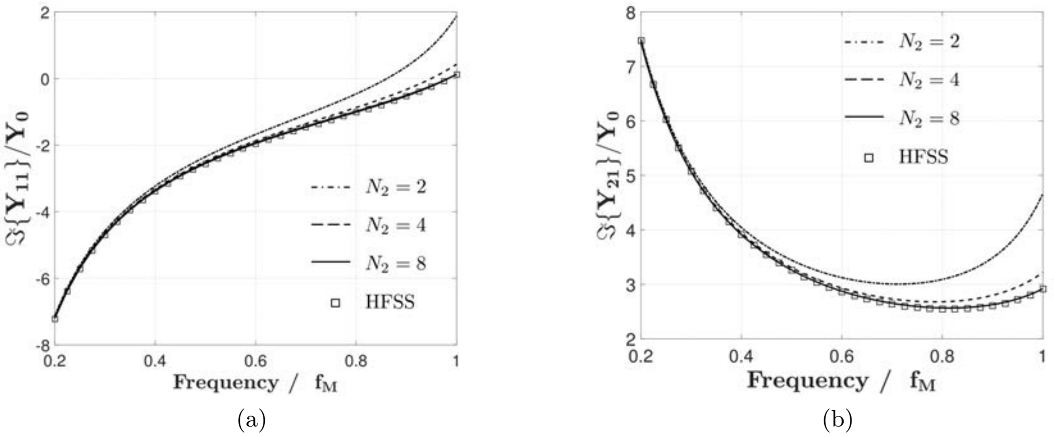

(a) (b)

Figure 4.15: Normalized admittances for a bend with $a = 0.3\,c/f_M$, $b = 0.8\,a$, $\epsilon_r = 1$ and $f_M = 40$ GHz. (a) $\Im\{Y_{11}\}/Y_0$; (b) $\Im\{Y_{21}\}/Y_0$. Results computed with $N_1 = 4$, for several values of N_2.

Finally, the two independent Y-parameters of the bend are derived with the aid of the circuit models of Fig. 4.14, as follows

$$Y_{11} = \frac{1}{2}\left(Y_{in}^{\mathrm{I}} + Y_{in}^{\mathrm{II}}\right) \tag{4.44}$$

$$Y_{21} = \frac{1}{2}\left(Y_{in}^{\mathrm{II}} - Y_{in}^{\mathrm{I}}\right) \tag{4.45}$$

4.2.5.2 Numerical validation

Four expansion modes ($N_1 = 4$) are generally required to solve the problem in Fig. 4.14a and accurately determine Y_{in}^{I}. More expansion modes are needed for the problem of Fig. 4.14b. The sensitivity to N_2 of the Y-parameters of the bend, computed for $N_1 = 4$, is studied in Fig. 4.15, for a structure with $\epsilon_r = 1$, $b = 0.8\,a$ and $a = 0.3\lambda_M$, being λ_M the wavelength at the maximum frequency f_M. The numerical results converge for $N_2 = 8$ and are in excellent agreement with full-wave simulations, performed with Ansys HFSS.

The developed code can quickly determine the optimal b/a ratio to match the bend. Figure 4.16a shows the voltage standing wave ratio (VSWR) at f_M as a function of b/a, for several values of a. The bend is filled with a dielectric of relative permittivity $\epsilon_r = 4$. For all a, the best matching is achieved for $b \approx 0.5a$. The reflection coefficient of a bend with $a = 0.5\lambda_m/\sqrt{\epsilon_r}$ and $\epsilon_r = 4$ is plotted against frequency in Fig. 4.16b, for several values of b. The -20 dB fractional bandwidth exceeds 150% when the step is half the height of the PPWs.

The computation (CPU) time needed to obtain the results of Fig. 4.16b, for $b/a = 0.5$ and 65 frequency points, is 24.7 s (0.38 s per point), using a workstation Intel Xeon 2.6

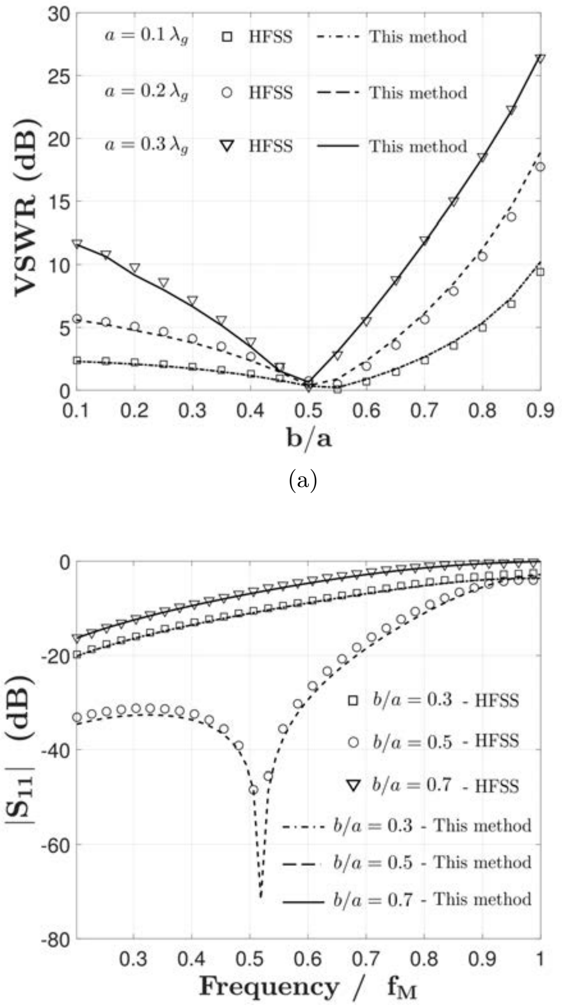

(a)

(b)

Figure 4.16: (a) VSWR at frequency $f_M = 40$ GHz as a function of b/a for a bend with $\epsilon_r = 4$. (b) $|S_{11}|$ against frequency for a bend with $a = 0.5\,\lambda_g$, with $\lambda_g = c/(\sqrt{\epsilon_r} f_M)$. Numerical results are computed with $N_1 = 4$, $N_2 = 8$.

GHz, 128 Gb RAM, whereas full-wave simulations require 74 s (11 s for the mesh and 0.93 s per frequency point). A further reduction of the CPU time can be achieved by accelerating the computation of the fundamental matrices $\underline{\underline{F}}^{\mathrm{I,II}}(\mathrm{x})$.

4.3 Numerical results for the feed network

A typical design of corporate feed network for parallel-fed CTS arrays is here analyzed by combining the numerical models developed for its building blocks (see Section 4.2). The reference structure, proposed by Milroy in [38], is shown Fig. 4.17. It comprises cascaded stages of broadband power dividers, as those discussed in Section 4.2.3, connected by transmission

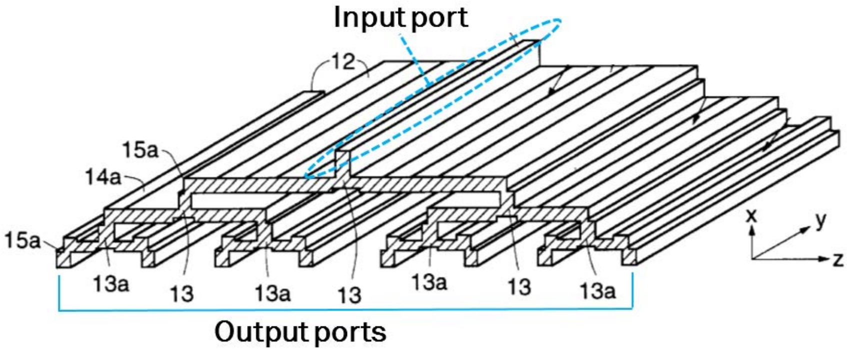

Figure 4.17: Scheme of the true-time delay feed network presented in [38].

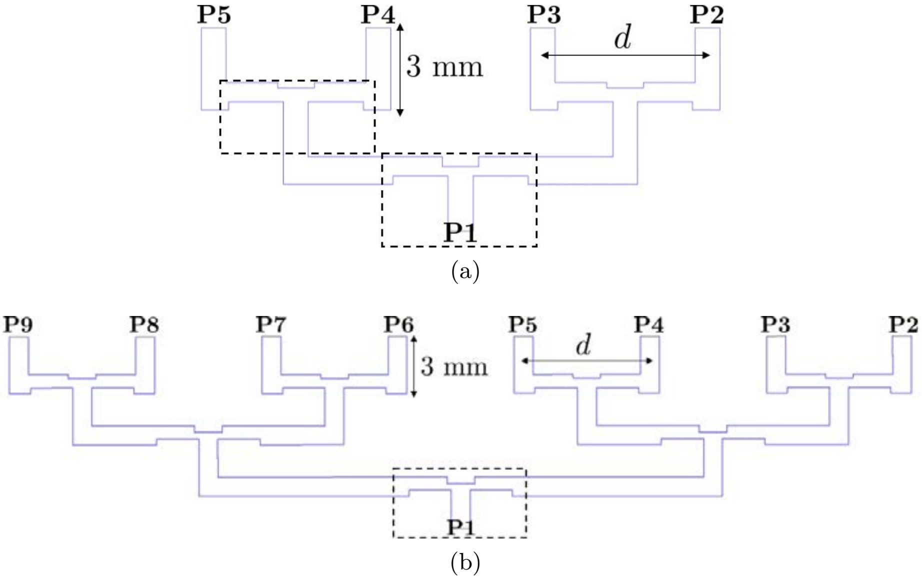

Figure 4.18: Cross sections of the corporate feed networks under analysis: (a) 1-to-4 way network; (b) 1-to-8 way network. The distance of adjacent output ports is $d = 10$ mm. All power dividers are equal (replicas of the one highlighted). With reference to the notation of the Fig. 4.9, the geometrical parameters of the power divider are $b' = 1.5\text{ mm}, b_0 = 0.5\,b', b = b'/\sqrt{2}, l_2 = l_{in} = 3\text{ mm}, w = 2.2\text{ mm}$.

lines and E-plane right-angle bends. The building blocks are not necessarily matched as stand-alone components. However, they are designed so that, once interconnected, their reactive parts cancel, and only real impedance steps remain. In such a way, the entire network can be viewed as a folded multistage transformer that can achieve wideband operation, due to the non-dispersive characteristics of PPWs. The accuracy of the proposed analysis approach for this network is evaluated with reference to two test cases: a 1-to-4-way network and a 1-to-8 way one. Their cross sections are shown in Fig 4.18. Both the networks are built by replicating the power divider design of Fig. 4.9. Therefore, all power dividers are equal. Their geometrical parameters are reported in the caption of Fig 4.18. Hollow PPWs

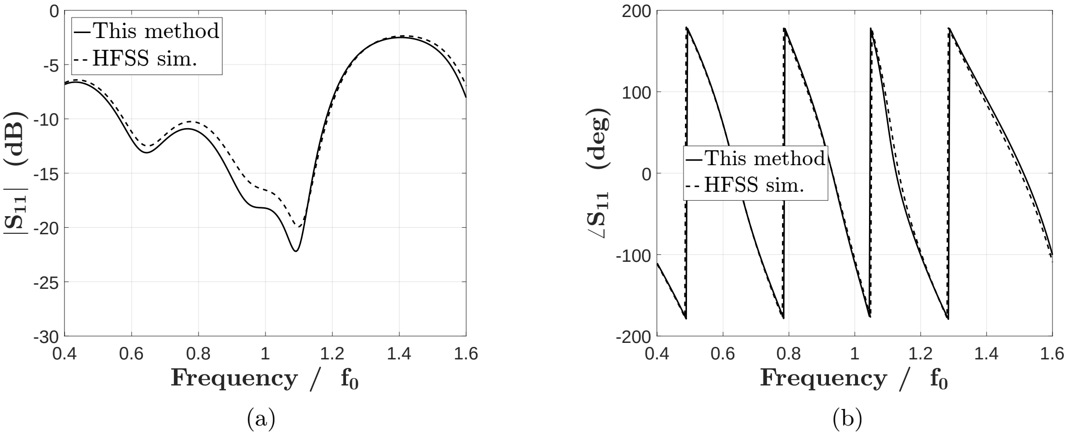

Figure 4.19: (a) $|S_{11}|$ and (b) $\angle S_{11}$ for the 1-to-4-way feed network in Fig. 4.18a. The central frequency is $f_0 = 25$ GHz.

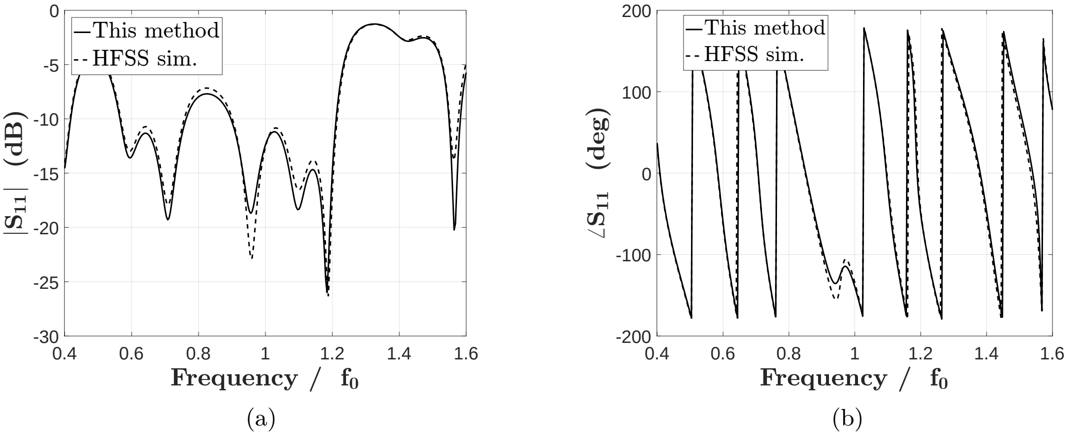

Figure 4.20: (a) $|S_{11}|$ and (b) $\angle S_{11}$ for the 1-to-8-way feed network in Fig. 4.18b. The central frequency is $f_0 = 25$ GHz.

($\epsilon_{r1} = 1$) are considered. The distance of the outputs d has been chosen larger than half the free-space wavelength so that the design of Fig. 4.9 can be used also for the power dividers directly connected to the output ports. The network comprises basic E-plane 90° bends. For both structures, the input and output lines of each power divider have the same height b' and characteristic impedance.

Figure 4.19 shows the reflection coefficient at Port 1 of the 1-to-4 way network (see Fig. 4.18a). The results computed using the proposed method closely agree with full-wave simulations. The shift between calculated and simulated resonant frequency is less than 3%. A similar accuracy is achieved for all other S-parameters.

The reflection coefficient at Port 1 of the 1-to-8 way network is shown in Figure 4.20, in amplitude and phase. The agreement between the results obtained using our analysis and HFSS simulations is improved, with respect to that observed for the 1-to-4 way network (see Fig. 4.19). This suggests that the accuracy of the proposed method improves with the number of cascaded stages of power dividers.

The computation time of the numerical tool developed is significantly lower than those required by full-wave simulations. The speed-up factor increases with the size of the structure analyzed. As an example, the computation of the S-parameters of the 1-to-8 way feed network requires 3.67 s for 301 frequency points, i.e. 0.012 s per point, using a workstation Intel Xeon 2.6 GHz with 128 Gb of RAM. The simulation of the same structure, on the same machine, is completed in 13 minutes and 3 s (192 s for the mesh and 2.06 s per frequency point). A similar quantity of RAM is used (about 900 Mb).

The test structures considered in this section have not been optimized for broadband performance. A wideband operation can be achieved by tuning the dimensions of each power divider and by replacing the basic 90° bends with the compensated design presented in Section 4.2.5. The wideband capabilities of the architecture here discussed are demonstrated in the next section, where a high-performance CTS design is analyzed using the numerical methods developed for the slot array and the corporate feed network.

4.4 Joint analysis of the array and the feed network

This section presents some numerical simulations obtained by jointly using the numerical tools developed for the analysis of the slot array and the corporate feed network of a CTS antenna. The modular analysis approach outlined in Section 4.1 is followed. The active impedance of the infinite array and the S-parameters of the true-time delay network are separately calculated. Then, each output of the network is terminated on the active impedance and the input reflection coefficient is evaluated.

The 16-element CTS antenna shown in Fig 4.21 is analyzed. This is a slightly modified version of the design presented in [47] and reviewed in Section 2.2. The antenna comprises hollow PPWs ($\epsilon_{r1} = 1$) and radiates in free-space ($\epsilon_{r2} = 1$). The structure is assumed infinite along the y-direction, i.e. the slots have infinite length and the feed network is realized with ideal PPWs. Moreover, the metal plate that contain the sixteen slots is assumed infinite, along both x- and y-direction.

From top (slot array) to bottom (Port 1), the corporate feed network comprises a matching section, a division stage based on the compact power dividers presented in Section 4.2.4 and three stages that comprises broadband power dividers (see Section 4.2.4). The compensated design discussed in Section 4.2.5 is employed for all right-angle bends in the structure.

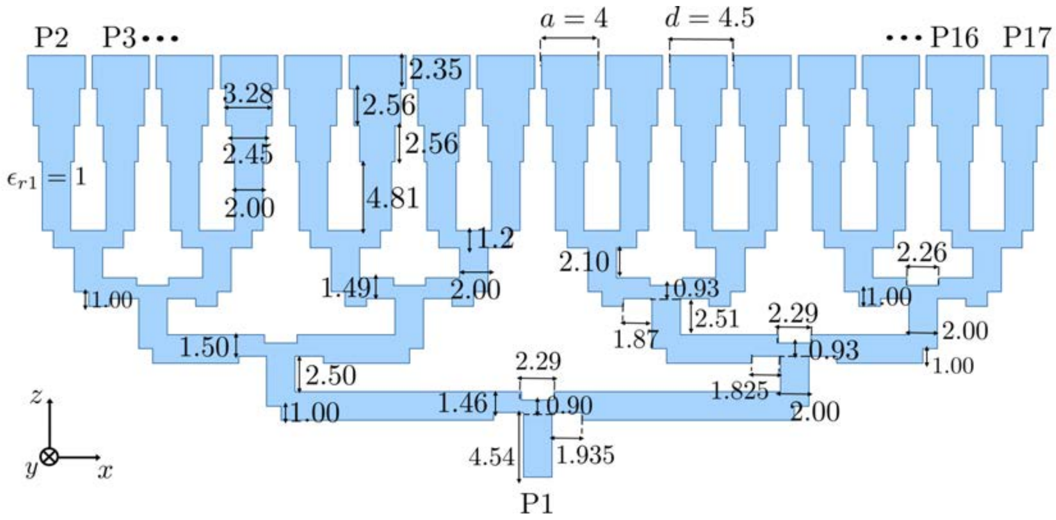

Figure 4.21: Cross section of the 16-element CTS array under analysis. The antenna is realized with hollow PPWs ($\epsilon_{r1} = 1$) and radiates in free-space. All dimensions are given in millimeters.

In order to analyze the 1-to-16 way corporate feed network, the S-matrices of its basic building blocks are computed using the circuital and numerical models presented in this chapter. A MATLAB routine has been implemented to properly cascade the transmission matrices of each component and to compute the 17×17 scattering matrix of the overall network. The network is assumed perfectly symmetric and achieves a uniform power division. Therefore, the transmission coefficient from the input to each of the sixteen output ports is the same. The computed input reflection coefficient and the transmission coefficient are shown in Fig 4.22. The results were obtained using quasi-static [82] formulas for the circuit models of the basic T-junctions (see Section 4.2.1) and by setting $N_1 = 4$ and $N_2 = 8$ for the analysis of the compensated 90° bends (see Section 4.2.5).

The numerical results are in excellent agreement with HFSS simulations. This confirms the validity of the modular approach and the accuracy of the models for the building blocks. The computation time depends on the accuracy requested for the S-parameters of the single-step 90° bends, but it is always significantly lower than the time required by HFSS simulations. The computation time needed to get the results in Fig. 4.22 is 28.1 s (0.46 seconds per frequency point), and the total RAM used is 985 Mb. The HFSS simulation performed on the same machine (Intel Xeon 2.6 GHz, 2 processors, 128 Gb of RAM) requires about 8 minutes (1.25 for meshing and 6.24 s per frequency point) and 1.45 Gb of RAM consumption, when a 1% accuracy on S-parameters and two converged passes are requested.

The active reflection coefficient of the infinite broadside array associated to the one

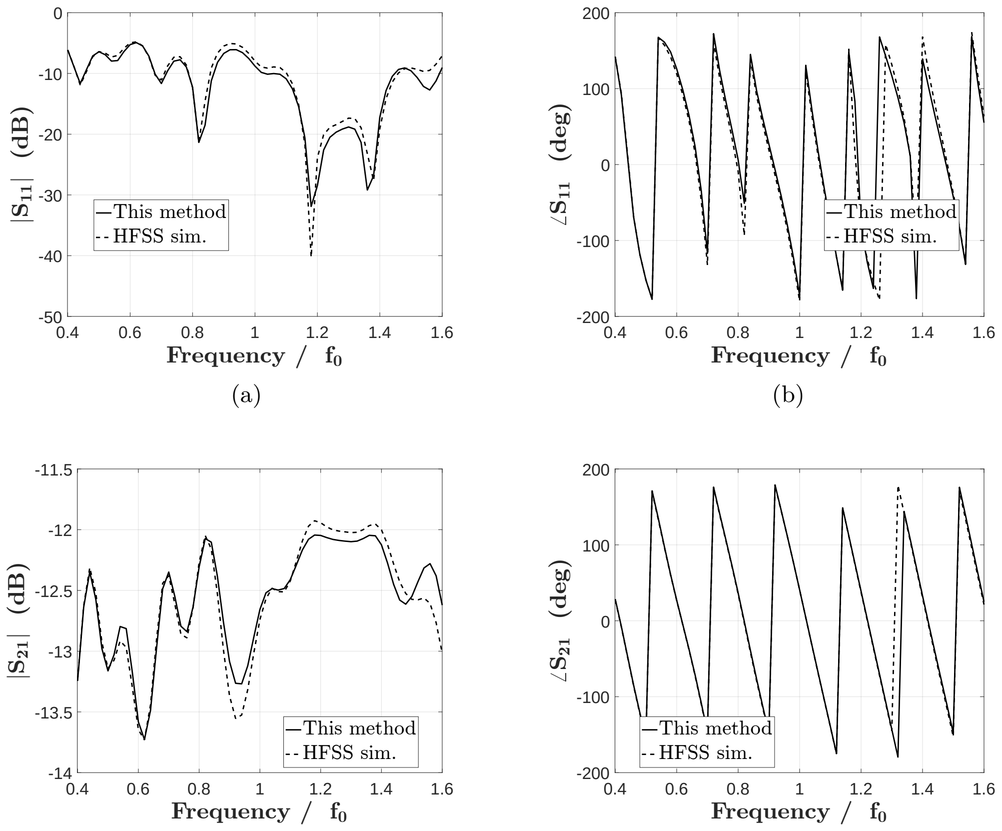

(a) (b)

(c) (d)

Figure 4.22: S-parameters of the corporate feed network of the CTS antenna in Fig. 4.21. Results obtained using the circuit model are compared to HFSS simulations. (a) $|S_{11}|$. (b) $\angle S_{11}$. (c) $|S_{21}|$. (d) $\angle S_{21}$. The central frequency is $f_0 = 25$ GHz.

analyzed here is found using the procedure discussed in Section 3.1. In order to evaluate the impact of the finiteness of the array, the actual active impedances at each element have been obtained from HFSS simulations. In the simulation setup, the slots and the PPW feeds were assumed infinite along the y-direction, and an infinite ground plane was considered. All 16 elements were fed simultaneously and the active impedances were evaluated on the radiating slot, for each element. Simulated results are compared to the computed active reflection coefficient in Fig 4.23. Given the symmetry with respect to the center of the array, only the first 8 elements are considered. The antennas are numbered from 1 to 8, moving from the edge element to the central one. Except for the edge elements, the active impedance computed for the infinite array is very close to the simulated values relative to the finite array, that exhibit limited variation across the elements. Therefore, the proposed modeling approach is expected to provide accurate results for the reflection coefficient at the input port of the antenna.

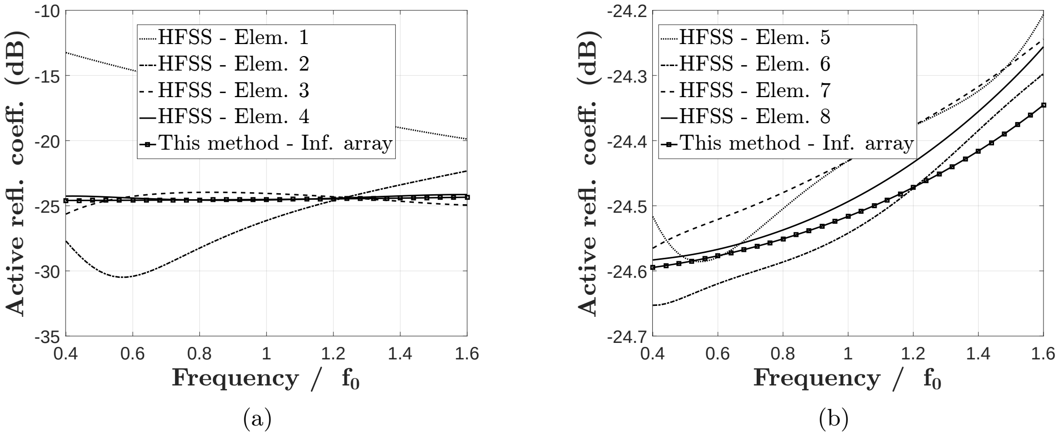

(a) (b)

Figure 4.23: Active reflection coefficients, simulated at each slot of the 16-element CTS array shown in Fig. 4.21, and computed for the infinite array. Results obtained using the circuit model are compared to HFSS simulations. By virtue of symmetry, only 8 antenna elements are considered. (a) Element 1 (edge element) to element 4; (b) elements 5 to 8 (central element). The central frequency is $f_0 = 25$ GHz.

A full-wave simulation of the overall structure in Fig. 4.21 has been performed. Periodic boundary conditions were applied to account for the infinite extension of the structure along the y-direction. Radiation boundaries were considered on the top of an air-box placed above the slots. The simulated input reflection coefficient is compared in Fig. 4.24 to that computed with the proposed approach. A good agreement is achieved, that demonstrates the effectiveness of the tools developed for the design of CTS antennas. Some differences arise in the upper edge of the frequency range, near the resonances. These can be attributed to the impact of higher order modes at the plane of the slots, that is the interface between the two modeled subsystems. Indeed, the model for the feed network assumes a single TEM mode propagation and does not account for back-reflected evanescent modes excited at the slots.

The joint use of the analysis tools developed for the slot array and the feed network enables a fast and reliable first-pass design of parallel-fed CTS arrays. Further comparisons with full-wave simulations will be presented in Chapter 5 to discuss the design of a substrate-integrated CTS antenna comprising eight slots.

4.5 Conclusion

A modular analysis method for PPW corporate feed networks of CTS antennas has been presented. A set of building blocks useful for the design of different feed networks has been individuated. The components have been modeled using equivalent circuits and *ad-hoc*

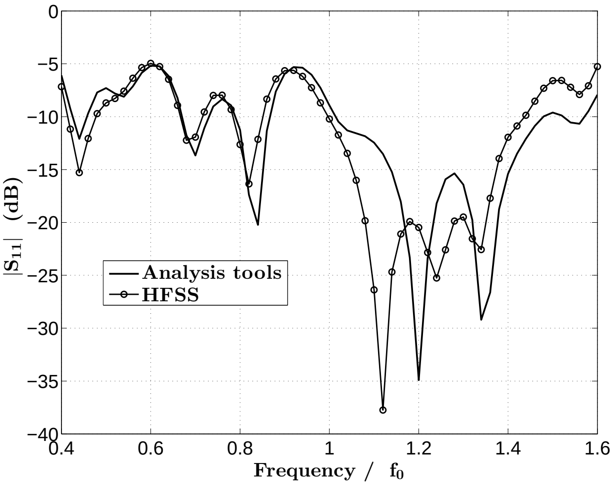

Figure 4.24: Input reflection coefficient (at Port 1) of the 16-element CTS array in Fig. 4.21. Results obtained using the proposed numerical procedure are compared to HFSS simulations.

numerical techniques in order to compute their scattering matrices. The subsystems that form the network and their scattering matrices are properly cascaded to characterize the structure under analysis.

Specific designs of power dividers for wideband operation have been discussed and modeled. A compensated E-plane right-angle bend that significantly improves the matching performance and an efficient mode matching procedure for its analysis have been presented.

The high accuracy of the proposed analysis has been demonstrated through comparisons with full-wave simulations. The computation time is significantly lower than that required by commercial solvers. The speed-up factor increases with the size of the network.

It has been shown that the numerical tools developed for the analysis of the corporate feed network and of the slot array can be combined to predict the reflection coefficient seen at the input port of the feed network of a CTS array, for broadside radiation. All output ports of the feed network have been terminated on the active reflection impedance of the infinite slot array. The results so obtained agree with full-wave simulations and confirms the effectiveness of the tools developed for the analysis of CTS antennas. It has been noted that the finiteness of the array has a small impact on the accuracy of the proposed procedure if the antenna comprises eight or more elements.

Chapter 5

CTS antennas in LTCC technology for 60-GHz communications

The demonstration of multi-Gb/s links in the 60-GHz band [4, 10] paved new ways for 5G mobile communications. Phased antenna arrays integrated with BiCMOS transceivers are currently considered as the most effective solution to achieve high gain and flexible beam steering control. These two features are essential to enable long-range non-line-of-sight (NLOS) links at mm-waves. However, significant challenges still remain in terms of power consumption, costs, thermal management and interconnects. CTS antennas achieve broadband scanning performance using a passive beamformer. Therefore, systems-in-package (SiPs) co-integrating CTS antennas and transceivers could attain high gain and wide fields of view, while reducing the losses of the interconnects, the power consumption and the system complexity. This chapter presents a novel technological implementation of CTS antennas, completely embedded in a multilayer substrate and suitable for compact, high-performance SiPs. Among the various packaging technologies, low temperature co-fired ceramic (LTCC) is employed since it provides the highest reliability in realizing multilayer, three-dimensional (3-D) structures, such as those of CTS antennas. Advantages and shortcomings of LTCC technology for the design of mm-wave antennas and SiPs are discussed in Section 5.1.

The fabrication of vertical PPWs with solid metal plates is not feasible in LTCC. The solid plates are thus replaced by multilayer rows of vias. This technological solution enables the realization of a new transmission line, discussed in Section 5.2, that supports a quasi-TEM mode, which is an essential requirement for CTS systems.

The design, fabrication and characterization of two LTCC prototypes are presented in order to validate the concept of integrated CTS antennas. The analysis tools presented in Chapter 3 and in Chapter 4 are employed for a preliminary design of the antennas, assuming ideal PPWs in the feed networks. Based on these models, the final structures comprising via-fences are fine-tuned using full-wave simulations. In Section 5.3, a fixed-beam antenna comprising four radiating slots [70] is described. It is shown how to mitigate, with a proper design, the impact of the technological limitations and of the high dielectric constant of LTCC tapes. The realization and characterization of this first prototype allow us to identify the fabrication challenges, the most sensitive design features, and the impact of tolerances. Based on the successful implementation of the fixed-beam antenna, a switched-beam LTCC module is proposed in Section 5.4, with applications to ultrafast access point (AP) links in V-band. Two CTS antennas are co-integrated with a switch-network that controls the radiated beam, by exciting only one of them. The beams exhibit high overlap levels and limited SLLs. Both these characteristics are required to track the mobile user within the cell associated to the AP. The antenna design is optimized, exploiting the analysis tools described in the previous chapters, to make an efficient use of the LTCC tapes. The beam switching functionality is experimentally demonstrated.

5.1 LTCC as a technological enabler for antennas-in-package

Antennas-in-package (AiPs) currently represent the most promising solution for highly-integrated mm-wave systems to achieve high gain and broadband operation [87]. A key benefit of AiP technology is the possibility to realize multi-functional SiPs [88–90] in integrated multilayer structures, with vertically stacked modules and low form factors. The integrated circuits (ICs) can be allocated in cavities within the same substrate and connected to the AiP using flip-chip bumps, vias or electromagnetic coupling. In this way, the losses of the interconnects from the transceiver to the antenna are minimized.

Several materials have been investigated for the implementation of AiPs, e.g. Teflon [91, 92], fused silica [93], liquid crystal polymer (LCP) [94, 95] and LTCC [96, 97]. Among them, LCP and LTCC have been recognized as the most promising technologies. LCP substrates [87, 98] and related processes are particularly attractive due to their low-cost, low relative permittivity ($\epsilon_r \approx 3$, $\tan\delta \approx 3 \cdot 10^{-3}$) and the small design features that can be realized, such as a substrate thickness of $25\,\mu$m and a conductor width of few micrometers [87]. Furthermore, the low lamination temperature (about 285 °C) potentially enables the simultaneous packaging of ICs and passive components. However, the low thermal conductivity of LCP materials and their softness, that increases with the temperature, can give rise to detuned antenna performance and mechanical instability.

By contrast, LTCC materials are good thermal conductors and their coefficients of thermal expansions are close to those of silicon and gallium arsenide [98, 99]. Moreover, LTCC technology is the most mature and versatile for advanced, hybrid 3-D integration and packaging. Due to the high lamination temperature (about 850 °C [87]), passive devices and ICs are integrated after co-firing the LTCC tapes. Despite this additional step in the fabrication, highly-dense SiPs, with low-loss interconnects, can be achieved. The LTCC process offers unparalleled flexibility for multilayer structures. The maximum number of dielectric and metal layers that can be stacked (more than twenty [100]) is higher than that provided by PCB or LCP technologies, which require also adhesive layers. Stacked and staggered vias can be densely distributed in the LTCC tapes. The dielectric constants of most popular LTCC materials are quite high, while their losses are generally less than those exhibited by LCP materials. For instance, Ferro A6M tapes, that were used for the CTS antenna presented in Section 5.3, have relative permittivity of about 5.74 and a tangent loss of 2.3×10^{-3}. The high dielectric constant eases the system miniaturization but penalizes the antenna performance and the operation bandwidth. An accurate design of LTCC AiPs is required to overcome these issues. Most LTCC and substrate integrated antennas are based on planar printed arrays [101, 102] that are very popular since they are low-cost and easy to design. However, they achieve low radiation efficiency, due to the lossy feed networks and to the excitation of surface-waves. Slotted waveguide and open cavity arrays [103–105], based on SIW structures, achieve relatively high gain values. However, they usually require large full-corporate feed networks, implemented on stacked layers. The signal propagation along the vertical axis of these modules is enabled by coupling elements, e.g. small apertures, that shrink the bandwidth and increase the losses of the overall system. The bandwidth reduction is made more severe by the dispersive behavior of the rectangular SIW components that are designed to guide quasi-TE modes, and in particular the fundamental quasi-TE_{10} mode. Moreover, the coupling elements in the network are sensitive to fabrication tolerances that degrade the performance of the overall AiP.

The implementation of a CTS system fully-integrated in LTCC can overcome most issues that have been pointed out for other LTCC antenna designs at 60 GHz. The non-dispersive operation of the PPW network and the broadband characteristics of the slot array ensure an operational bandwidth suitable for multi-Gb/s communications in V-band. A low insertion loss of the corporate feed network is expected, since the fields propagate on relatively short paths in the PPWs, without any coupling elements. Moreover, the intrinsic robustness to tolerances of CTS architectures [33] makes CTS-based AiPs suitable for mass-production and operation at high frequencies in the mm-wave range.

The first step to realize a CTS AiP, fully integrated in an LTCC substrate, is the implementation of PPW-like structure that supports a quasi-TEM mode. Some techniques to realize simple solid walls on a few LTCC tapes, using cavities, were recently proposed in [106, 107]. However, the fabrication of vertical, solid metallic walls in a complex multilayer LTCC module is prohibitive. Therefore, it is not possible to embed vertical PPWs. The

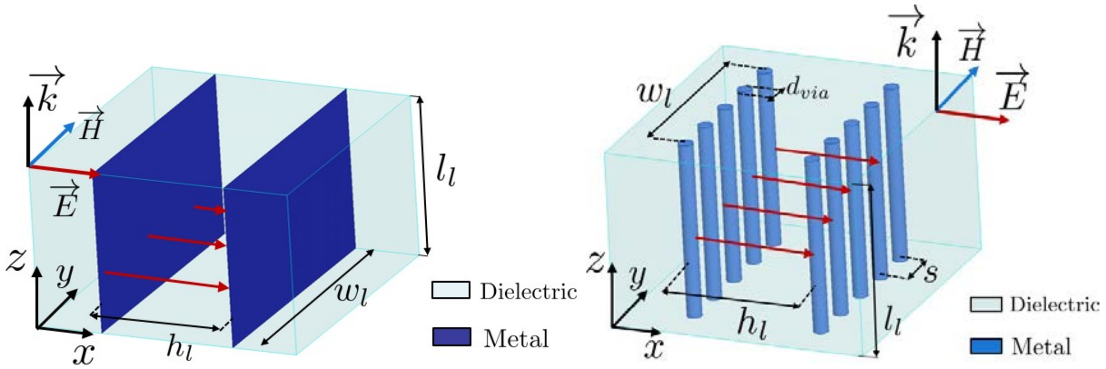

(a) (b)

Figure 5.1: Comparison of the structures of: (a) a PPW, with solid metal walls in a dielectric substrate; (b) a SI-PPW, whose guiding section is delimited by two parallel rows of vias. The geometrical parameters, the directions and orientations of electric and magnetic fields are reported.

solution consists in replacing the continuous metal walls with parallel rows of vias, stacked and aligned on several layers. The transmission line so obtained is suited for a quasi-TEM mode propagation. It will be next referred to as substrate integrated parallel plate waveguide (SI-PPW) and is extensively discussed in the next section.

5.2 Vertical substrate integrated parallel plate waveguides

The wideband characteristics of the proposed integrated CTS antenna rely on the proper operation of vertical PPW lines. A possible way to embed vertical PPW-like structures in dielectric substrates using planar processes is here presented. Via-rows are used to approximate the continuous metallic plates of ideal PPWs. The structure of a SI-PPW is illustrated in Fig. 5.1 and compared to a standard PPW in a dielectric medium. Two via-rows of length l_l along the propagation direction (z-axis) are spaced apart at a distance $h_l < 0.5\ \lambda_d$, where λ_d is the operating wavelength in the dielectric material. The width of a finite SI-PPW in the y-direction is $w_l \gg \lambda_d$, l_l, as for a highly-overmoded rectangular waveguide designed to approach the behavior of an ideal PPW. The via-rows act as the metal plates of a standard PPW, shown in Fig. 5.1a. If the spacing between adjacent vias is electrically small, the electric field is well confined between the two via-rows and polarized along a direction orthogonal to the vias (positive x-semi-axis in Fig. 5.1). A SI-PPW guides a quasi-TEM mode along the vertical direction (z-axis). Thus the field distribution and polarization in a SI-PPW are different from those observed for a quasi-TE$_{10}$ mode in a conventional SIW. The electric field in a SIW is parallel to the vias, i.e. to the vertical axis of the substrate, confined between two horizontal metal plates, with a sinusoidal amplitude

Table 5.1: Simulated insertion losses at 60 GHz for a PPW and a SI-PPW, with the following parameters (see Fig. 5.1): $h_l = 0.48$ mm, $w_l = 0.48$ mm, $l_l = 1$ mm, $d_{via} = 0.15$ mm, $s = 0.30$ mm.

	Ohmic (dB/mm)	Dielectric (dB/mm)	Leakage (dB/mm)	Total (dB/mm)
PPW	0.021	0.023	0	0.044
SI-PPW	0.039	0.023	10^{-4}	0.062

distribution in the transverse section of the SIW.

The length of a SI-PPW along the z-axis, in the corporate feed network of a CTS antenna, may exceed the thickness of a substrate layer. In this case, the rows of vias relative to the same SI-PPW are fabricated in several layers, that are eventually aligned and stacked.

The attenuation characteristics of a SI-PPW, infinitely extended along the y-axis ($w_l \rightarrow \infty$), are evaluated and compared to those of an equivalent ideal PPW, embedded in the same medium. Ferro A6M [108] is considered as dielectric material ($\epsilon_r = 5.74, \tan\,\delta = 2.3 \times 10^{-3}$) and a golden paste of conductivity $\sigma = 7 \times 10^6$ S/m is assumed for vias and conductors. The vias of the SI-PPW line have diameter $d_{via} = 0.15$ mm and center-to-center pitch $s = 0.30$ mm. This set of technological values are employed in the design of the fixed-beam CTS antenna in LTCC, described in Section 5.3.

The insertion loss of the vias-made structure are extracted from full-wave simulations performed with Ansys HFSS. The two ports of the SI-PPW are excited by waveports. Perfect magnetic conductor boundaries were applied at the edges of the structure along the y-direction, in order to study the behavior of non-truncated SI-PPW lines. The leakage loss, due to the energy that flows away from the region between the via-rows, is evaluated by neglecting material losses and assuming perfect conductors in the simulation. The computed attenuation at 60 GHz, for $h_l = 0.48$ mm is very low, about 3.3×10^{-6} Np/mm^2, i.e. per unit of length of propagation (along z-axis) and unit of length along the y-axis of the vias-made structure. For example, if $w_l = 30$ mm, the attenuation along the z-direction is about 0.1 dB/m. This value is comparable to typical attenuation values in low-loss standard SIW [109]. Table 5.1 reports the attenuation values for the SI-PPW and for the corresponding PPW, computed at 60 GHz, for $w_l = 30$ mm. The contribution of each dissipation mechanism is illustrated. The overall attenuation of the SI-PPW line under analysis is 0.062 dB/mm, which is very close to the value estimated for the PPW. The ohmic losses are the most relevant ones.

The low-loss performance observed for SI-PPWs proves that they can be effectively used to guide a quasi-TEM mode along the vertical axis of the substrate and to form corporate feed networks. The only example of vertical propagation in a SIW structure was presented in [110], for a corrugated horn. However, the field confinement is realized by using three parallel via-fences for each side of the rectangular SIW. The solution of multiple vias-fences is too bulky for the design of substrate integrated feed networks at mm-waves. By contrast, the proposed vertical SI-PPW can be implemented using a single via-row for each plate of the equivalent PPW. It enables the design of quasi-TEM corporate feed networks, fully embedded in a LTCC module, that are almost dispersion-free.

5.3 A broadband fixed-beam CTS module

The proposed concept of substrate integrated CTS antenna, based on novel SI-PPW structures, is demonstrated with the design and experimental characterization of a fixed-beam module in LTCC technology. The antenna module, shown in Fig. 5.2, is fed on the bottom face by a V-band end-launch connector [111]. A SIW H-plane sectoral horn is fed through a GCPW-to-SIW transition and excites a quasi-optical beamformer, that an integrated parabolic reflector, realized with vias. The signal is coupled to the corporate feed network using a broadband multi-slot pillbox transition [52, 112] in the pillbox. The array comprises four long slots, covered by a matching layer. The final size is $32.5 \times 34.0 \times 3.4$ mm^3. The radiating aperture occupies only a small part of the total area (8.4×34.0 mm^2), since this test CTS structure features only four elements. Therefore, the focal length of the parabola is much greater than the length of the array along the x-direction. Since the present design primarily aims at the validation of the antenna concept and LTCC process, it has not been optimized to reduce the number of layers and features 18 Ferro A6M [108] tapes. Two tape thicknesses are employed. Their nominal values after co-firing [100], i.e. 0.10 mm and 0.20 mm, are assumed in the design. Each subsystem is described in the next subsections. The full-wave simulations that will be presented are obtained using Ansys HFSS.

5.3.1 Input section

A coaxial end-launch connector [111] feeds a $50\,\Omega$ GCPW line printed in the bottom metal layer of the module. A GCPW-to-SIW transition guides the signal from the input line to the horn feeding the beamformer. The details of the transition are given in Fig. 5.3a. The width of the strip and gaps of the GCPW are 0.40 mm and 0.20 mm, respectively. The GCPW is gradually matched to a SIW line of width 1.70 mm (center-to-center distance of the via-rows), that ensures a single mode propagation in the $37-75$ GHz band. A thickness of 0.40 mm $\approx 0.2\lambda_d$, where λ_d is the wavelength in the dielectric at 60 GHz, is chosen for the SIW line in order to reduce its losses. The GCPW line has the same height, i.e. the distance between signal plane and reference ground, so that the input section occupies two

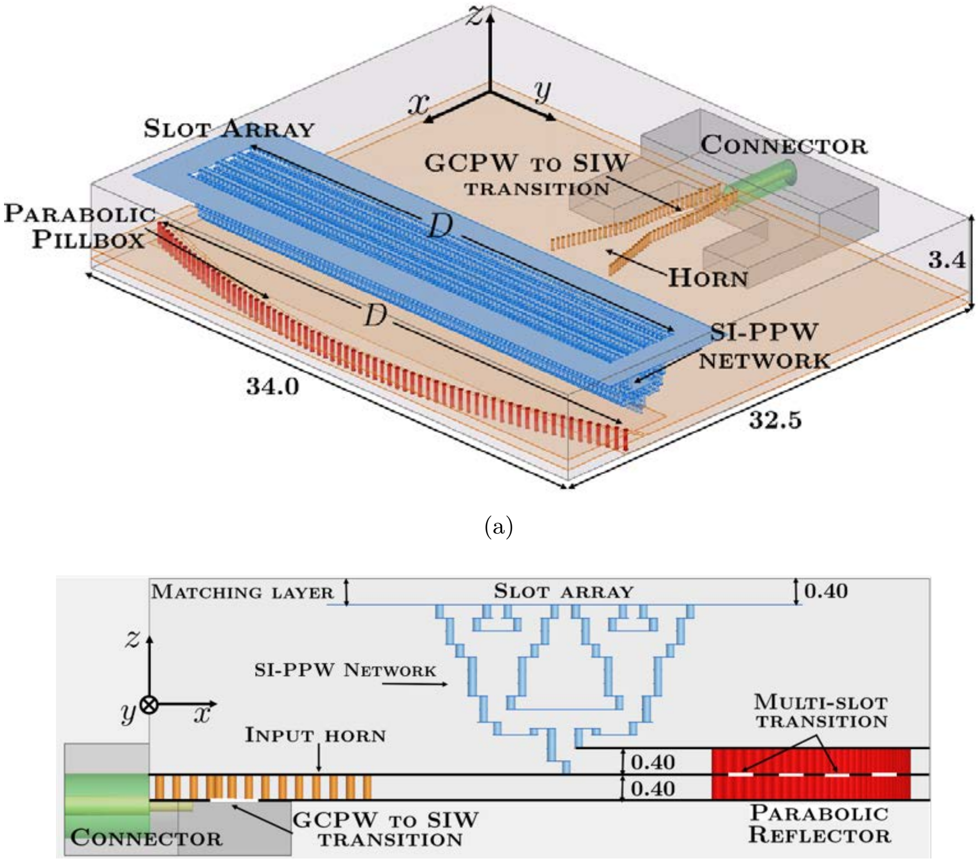

(a)

(b)

Figure 5.2: (a) 3-D view and (b) cross section in the xz-plane of the fixed-beam CTS antenna. The basic subsystems of the module are indicated. Dimensions are given in millimeters.

LTCC tapes of thickness 0.20 mm. The design is based on a tapered section of length 2 mm $\approx \lambda_d$. An impedance step in the GCPW line at the interface with the SIW and two $\lambda_d/4$-long coupling stubs ensure both impedance and field matching. The width of the coupling slots is tuned to maximize the field transfer to the SIW line. The via-fences surrounding the GCPW are designed to suppress surface waves. The minimum diameter (0.15 mm) and pitch (0.30 mm) allowed by the process are chosen to minimize leakages in the SIW line [109]. The simulated performances of the transitions are reported in Fig. 5.3b. The model of the end-launch connector has been included in the simulations and Port 1 refers to the input of the coaxial connector. The reflection coefficient is less than −10 dB between 50 and 70 GHz, and less than −18 dB in the design band (57 GHz - 66 GHz). Within this range the insertion loss is about 0.65 dB.

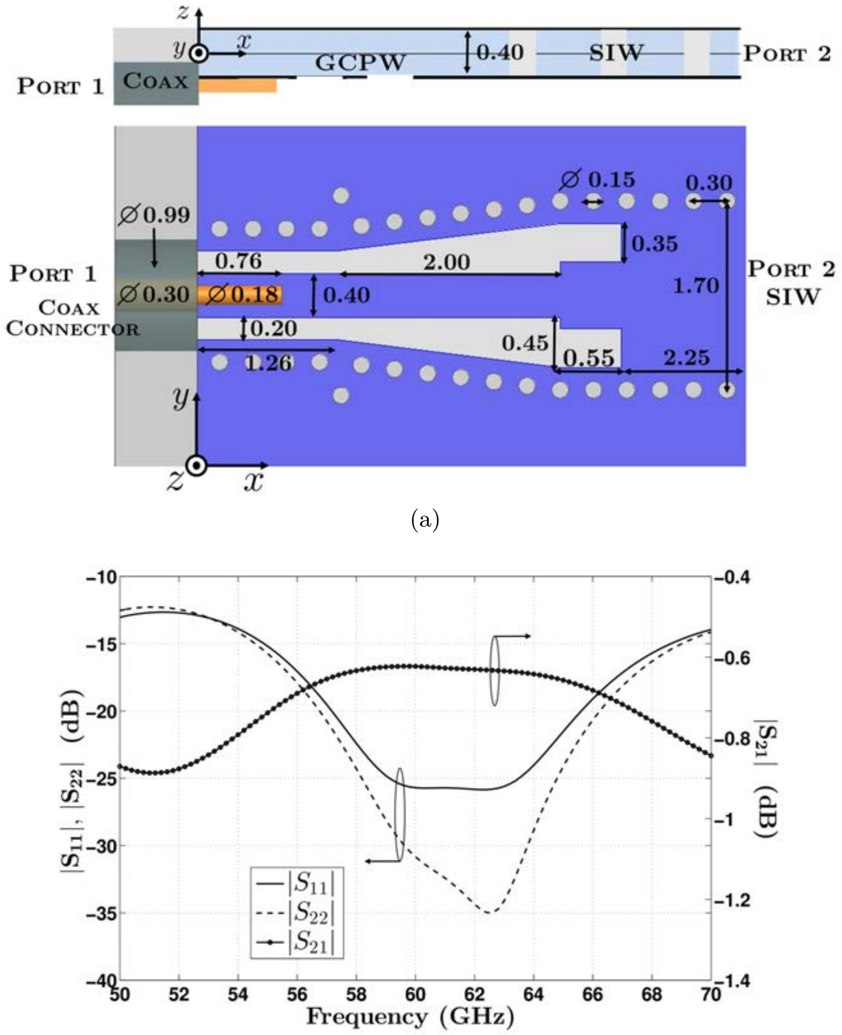

(a)

(b)

Figure 5.3: Input transition: (a) geometry and stack-up (shown in the top inset). Dimensions are in millimeters. (b) Simulated results when the transition is fed by the V-band end-launch connector.

5.3.2 Quasi-optical system

The quasi-optical system is sketched in Fig. 5.4. The phase center of the H-plane sectoral horn is placed in the focus of a 2-D vias-made parabolic reflector. The horn aperture is $w = 4.13$ mm $\approx 2\lambda_d$, the flaring length is $l_t = 2\lambda_d$. These parameters minimize the phase aberrations at the aperture plane in the operating band [113].

The input section is embedded in a PPW structure, of height 0.40 mm. A second PPW, of the same height, is stacked on the first one, as shown in Fig. 5.2b. The common ground shields input and radiating sections. A pillbox transition [52, 112] connects the two PPW regions. It consists of a 180° PPW bend with a parabolic profile and of a series of thin slots

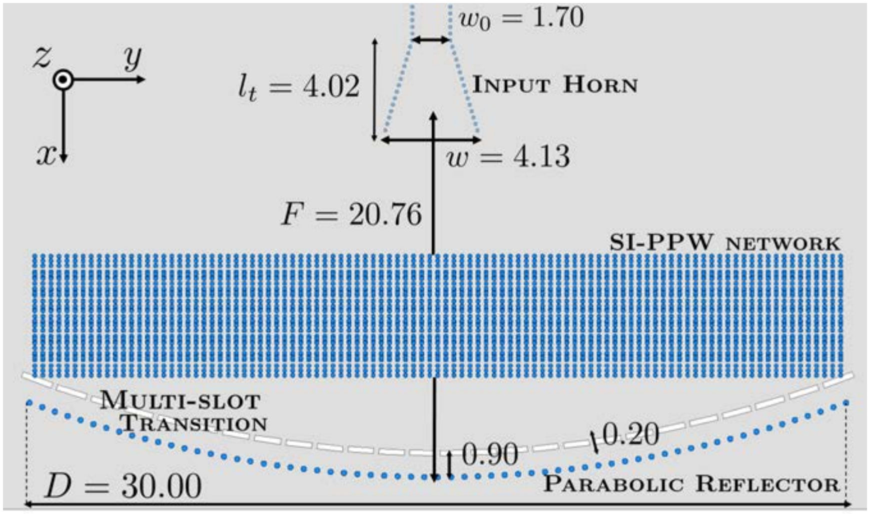

Figure 5.4: Top view of the quasi-optical system. Dimensions are in millimeters.

contouring the reflector, in the common ground of the PPWs. The slots are placed at a distance of about $\lambda_d/2$ (0.90 mm) from the reflector and have a width of $\lambda_d/10 = 0.20$ mm. Their lengths are designed so that they subtend the same angle ($\approx 2.5°$), as seen from the focus of the parabola. The cylindrical wave launched by the horn is transformed into a quasi-plane wave in the upper PPW by the parabola.

The design of the reflector determines the radiation characteristics of the array in the H-plane (yz-plane in Fig. 5.4). The diameter D of the reflector, equal to the length of the radiating slots, is set to 30 mm. The focal-to-length ratio of the reflector is $F/D = 0.67$, so that the system has an edge-tapering (ET) of about -16.5 dB. This value ensures at the same time a good illumination of the reflector, high spill-over efficiency and low SLLs of the radiation patterns in the H-plane. The diameter of the vias used for the reflector is 0.20 mm. The via spacing (0.40 mm) ensures negligible leakage. The overall quasi-optical system has a thickness of 0.80 mm, i.e. four 0.20 mm-thick LTCC tapes.

5.3.3 Antenna and corporate feed network

An accurate design of the array is essential to achieve broadband operation [114], given the high permittivity of the LTCC tapes. The array comprises four slots in a metal plane, as shown in Fig. 5.5. Each slot is fed along the z-axis by a SI-PPW. The distance between the parallel via-rows of each line is equal to the slot width. It can be thus seen as an open-ended waveguide integrated in LTCC and radiating in the upper half-space. If this structure radiated in air, it would suffer from strong reflections at the air-dielectric interface. The real part of the active impedances can be several times greater than the characteristic

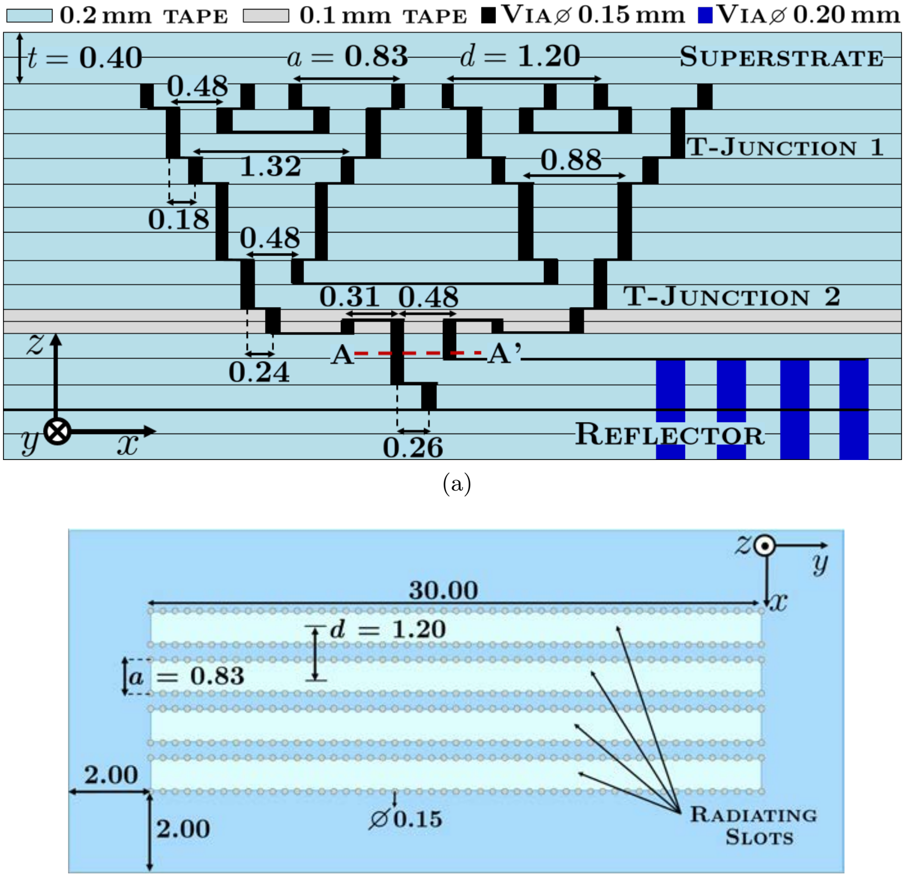

(a)

(b)

Figure 5.5: Radiating part of the integrated CTS antenna: (a) cross section and (b) top view of the array. Dimensions are in millimeters.

impedance of the feed lines. To overcome this issue, the array can be loaded by a matching dielectric cover, made of several LTCC tapes, without any metallic pattern. Such a cover can be placed right above the radiating slots and integrated in the same fabrication process. Its thickness can be tuned to enhance the bandwidth.

The slot width a, the array period d and the thickness t of the cover have been jointly optimized to minimize the active reflection coefficient in the design band. Values of $a \leq 0.9$ mm have been considered, so that only the fundamental mode propagates in the SI-PPWs that feed the slots. The optimization has been constrained to values of $d \leq \lambda_0/2$, where λ_0 is the free-space wavelength at 66 GHz, in order to avoid grating lobes and scan blindness (see Chapter 3). The final values are $a = 0.83$ mm, $d = 1.20$ mm, and $t = 0.40$ mm. The length of the slots is equal to the diameter of the parabola $D = 30$ mm $\approx 15\lambda_d$. Figure 5.6a shows that without the matching layer ($t = 0$ mm) the real part of the active impedance Z_{act} seen at the edge elements would be more than three times greater than the characteristic impedance of the SI-PPW feed line. The latter is approximated with the impedance of

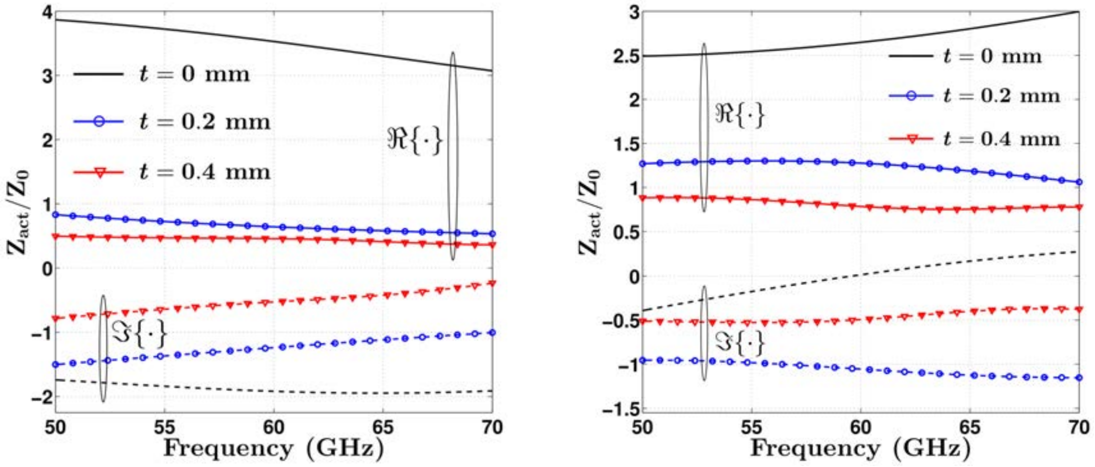

(a) (b)

Figure 5.6: Active impedance Z_{act} seen at (a) the edge elements and (b) at the central elements of the 4-elements array, for different thicknesses t of the cover. The array spacing is $d = 1.20$ mm and the slot width is $a = 0.83$ mm. Values are normalized to the characteristic impedance Z_0 of the feed PPW, which has a length of 30 mm along the y-axis (see Fig. 5.5).

an ideal PPW of height a, that is $Z_0 = \eta_d a/D$, where η_d is the wave impedance in the dielectric. For such an impedance ratio, a good matching cannot be practically achieved without using overmoded SI-PPWs in the feed network. By contrast, for $t = 0.40$ mm, corresponding to two LTCC tapes, $\Re\{Z_{act}\} < Z_0$ when seen both from edge and central elements of the array (see Fig. 5.6b). Moreover, $\Im\{Z_{act}\}$ is very low and constant against frequency and can be easily compensated.

The corporate feed network matches, over a wide band, the active impedances of the array, seen at the radiating slots, to the impedance of the input SI-PPW line. First, ideal PPW components were assumed in order to exploit their equivalent circuits for a systematic design of the network. Only single-mode PPW lines, i.e. with height lower than 0.9 mm, were considered.Then, the PPWs were replaced by the SI-PPWs and the design was optimized using full-wave simulations. Vias of minimum diameter (0.15 mm) were chosen to realize the SI-PPW structures. Vertical multistage transformers were avoided to reduce the number of LTCC tapes. The reactive parts of the active impedances of the array were compensated using an E-plane step in series with the feed lines of the slots and a 90° stepped bend. A basic T-junction (see T-junction 1 in Fig. 5.5a) and a vertical quarter-wavelength transformer that occupies 3 layers, match the active impedances to the characteristic impedance of the SI-PPW lines at the outputs of the input power divider. The latter, namely T-junction 2 in Fig. 5.5a, comprises two quarter-wavelength transformers to achieve a broadband input matching [38]. Note that two thinner tapes, each of thickness

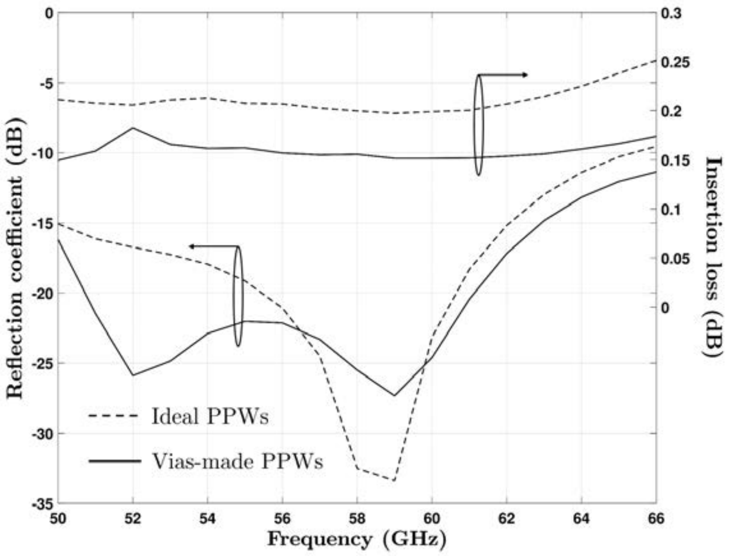

Figure 5.7: Simulated reflection coefficient and losses of the corporate feed network, considering ideal PPWs (dashed lines) and the actual vias-made structure (solid lines). The input port is placed at section AA' in Fig. 5.5a.

0.10 mm, were used to realize the impedance transformers (see Fig. 5.5a).

The impact of the via-rows on the performance of the feed network has been investigated in simulations. Two simulation setups have been considered. In the first one, ideal PPWs with continuous metal plates have been used, while in the second one, the actual vias-made structure has been introduced. Dielectric and conductive losses have been included in both the setups. The results are shown in Fig. 5.7. The reflection coefficient at the input of the feed network (section AA' in Fig. 5.5a) is not significantly affected by the vias. The -10 dB impedance matching bandwidth exceeds the frequency range considered in simulations (50 GHz - 66 GHz). The simulated insertion loss from the input port to the plane of the radiating slots is also reported in Fig. 5.7. The difference between the values obtained from the two simulation setups are due to additional losses introduced by the SI-PPWs, i.e. the ohmic losses of the vias and the leakage through the via-rows. The increase of the loss observed for the vias-made structures is about 0.05 dB at 60 GHz. Similar values are obtained in the entire band of interest. These results confirm the broadband, low-loss behaviour of the SI-PPW feed network.

5.3.4 Fabrication

Among commercially available LTCC materials, Ferro A6M tape system [100] was selected because its dielectric loss and permittivity are the most suitable to achieve good antenna

Table 5.2: Some design rules of the LTCC process

Parameter	**Typical value**
Minimum linewidth (μm)	50
Tolerance of linewidths (μm)	±5
Layer-to-layer positioning accuracy (μm)	15
Minimum diameter of vias (μm)	80
Minimum via pitch (μm)	160
Number of layers	4-20

performance. The values assumed in the design for the relative permittivity ($\epsilon_r = 5.74$) and loss tangent ($\tan\delta = 2.3 \times 10^{-3}$) were obtained from measurement on test structures at 60 GHz. Gold conductors, with a conductivity $\sigma = 7.0 \times 10^6$ S/m, were scree-printed. The antenna prototypes were fabricated by the Technical Research Centre of Finland (VTT) . Some of the processing parameters are shown in Table 5.2. The overall substrate consists of 18 tapes, two of which are blank layers on the top surface, used for the matching cover. The thickness of 16 tapes is 10 mils ($\approx$ 0.20 mm after co-firing). The remaining two tapes have a thickness of 5 mil, corresponding to $\approx$ 0.10 mm after co-firing, and are used to realize the input power divider (T-junction 2 in Fig. 5.5a). Particular effort was put in the process so that the two different tape thicknesses have a close shrinkage match, avoiding any delamination or warpage issues.

The SI-PPW network does not comprise narrow conductor lines. Thus, the requirements on the resolution and accuracy of the metal patterns can be relaxed, as compared to those commonly requested for the fabrication of mm-wave passive components. While the realization of SIW feed networks requires a precise control of conductor-to-conductor distances and fine design features for the coupling slots, the proposed SI-PPW network consists of rows of vias. Thus, the correct alignment of stacked vias in different layers is the only feature that the process must guarantee.

Via holes were punched and filled with Au paste using stencils. Conductor patterns were carefully aligned to the vias by proper scaling of the screen pattern and by printer adjustments. Cavity holes were punched to the tape layers to realize through holes in the substrate for mounting the connector with screws. Tape layers were stacked in a mechanical fixture, and the stack was laminated iso-statically. The laminate was cut into modules, each of size 70 mm × 70 mm, eventually co-fired at 850° C. The fired substrates were then diced to the final antenna dimensions.

Figure 5.8 reports some photos of the fabricated antennas. The alignment of vias achieved by the process is good, as demonstrated in Fig. 5.8b and in the cross section

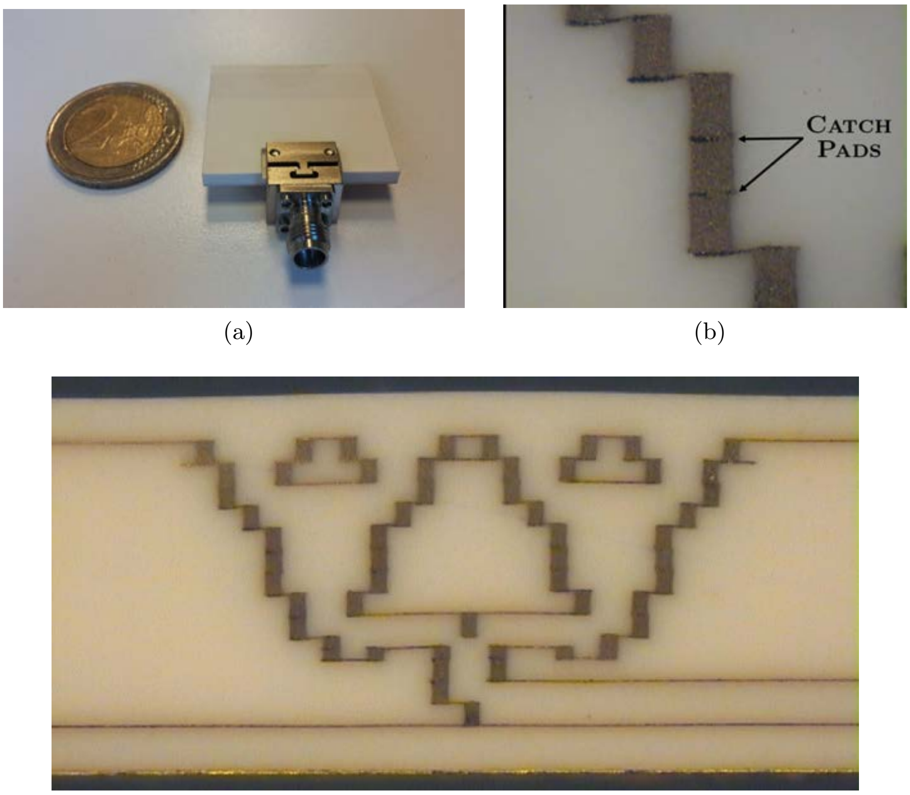

(a) (b)

(c)

Figure 5.8: (a) Photo of the antenna prototype. Microscope photos of one of the fabricated antenna: (b) detail of the CFN and (c) cross section.

view (Fig. 5.8c) for an antenna design slightly different from the one described and tested. Metallic catch pads (see Fig. 5.8b) were used to improve the electrical contact of via-rows stacked on different layers that are relative to the same SI-PPW. The measured thickness of the each prototype varies between 3.135 mm and 3.185 mm along the y-axis (see Fig. 5.2), from the edges to the center. This is due to the fact that vias filled with Au, that are mainly concentrated in the middle, do not shrink as much as the surrounding ceramic.

5.3.5 Experimental results

Measured and simulated reflection coefficients at the input connector are compared in Fig. 5.9. They are in very good agreement, thus confirming the reliability of the proposed design and fabrication process. Except for a peak of -9.2 dB at 51.2 GHz, the reflection coefficient is lower than -10 dB over the entire frequency range, i.e. the relative impedance bandwidth exceeds 26%.

The H-plane cuts (yz-plane in Fig. 5.2) of the normalized patterns are reported in Fig. 5.10 at several frequencies. Well shaped patterns, with low SLLs are observed over the

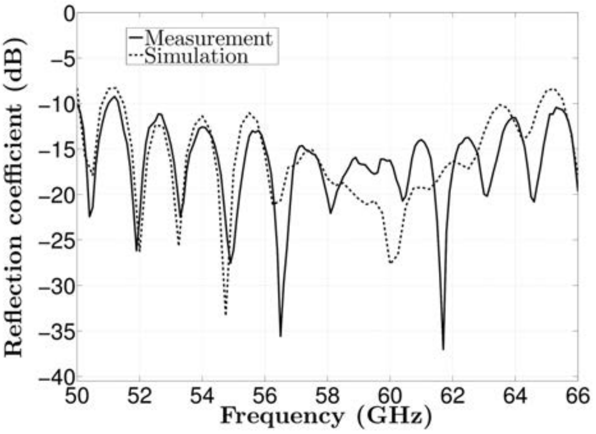

Figure 5.9: Measured and simulated reflection coefficients at the input connector of the antenna.

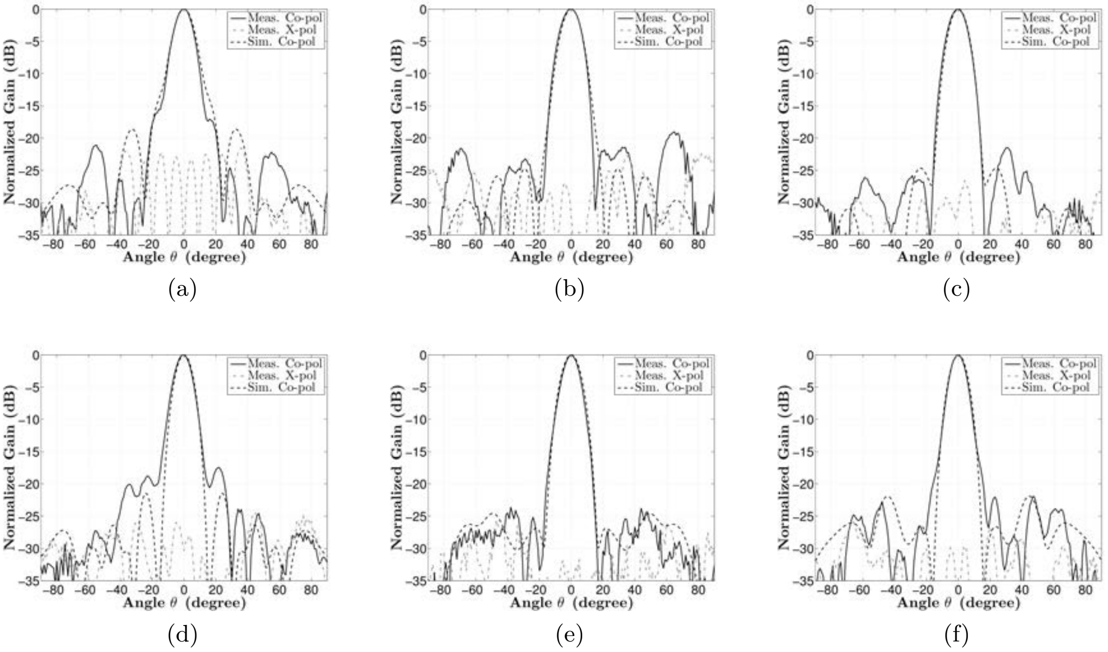

(a)

(b)

(c)

(d)

(e)

(f)

Figure 5.10: Normalized radiation patterns in the H-plane at: (a) 52 GHz, (b) 54 GHz, (c) 58 GHz, (d) 60 GHz, (e) 63 GHz, (f) 66 GHz.

entire measurement band. A good agreement with simulations is observed, in particular for the main lobe, despite the complexity of the fabrication process. The differences in the positions of the first nulls at some frequencies may be due to fabrication errors. The measured radiation characteristics are stable between 50 GHz and 66 GHz band. The angular tilt of the main beam is lower than 0.6°. The peak-to-peak cross-polarization level is less than −23 dB. The full half power beamwidth (HPBW) varies between 9.0° and 12.6°, while the first SLLs are less than −17.5 dB, with an average value of −20.6 dB, as shown

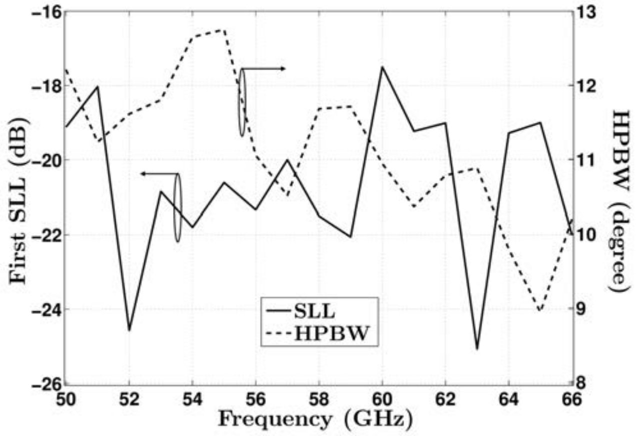

Figure 5.11: Measured first SLLs and HPBW of the patterns in the H-plane.

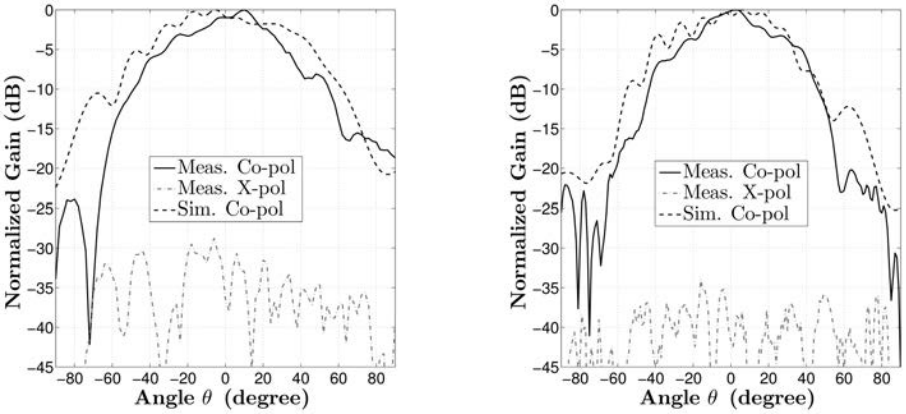

(a)

(b)

Figure 5.12: Radiation patterns in the E-plane at: (a) 57 GHz, (b) 66 GHz.

in Fig. 5.11. The radiation patterns in the E-plane, at two different frequencies, are shown in Fig. 5.12. The asymmetries are due to the off-center position of the array along x-axis, while the ripples are mainly due to the limited size of the ground plane of the slots.

The measured realized gain is compared to simulated values and directivity in Fig. 5.13 between 50 GHz and 66 GHz. The maximum measured value is 14.25 dBi at 62.7 GHz. The measured -3 dB gain bandwidth spans from 54 GHz and 66 GHz, which corresponds to a relative bandwidth of 20%. The average difference between simulated and measured realized gain is 0.68 dB in the $50-66$-GHz band.

The radiation efficiency is estimated as the ratio of measured gain and simulated directivity. Its mean value in the measurement band is 46%, and it is always greater than 33%. Despite the large volume of the system and related material losses, these values are in line

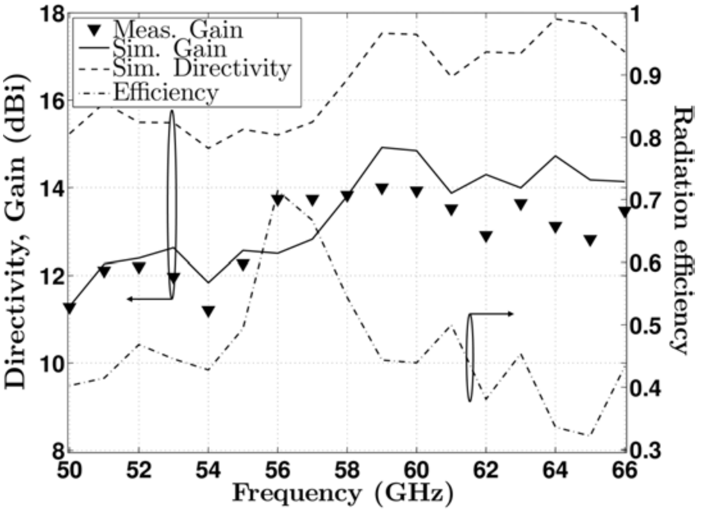

Figure 5.13: Realized gain, directivity and radiation efficiency against frequency.

Table 5.3: Losses at 60 GHz, estimated from full-wave simulations.

Simulation setup	Directivity (dBi)	Gain (dBi)	Losses (dB)
Sim. lossy dielectric Perfect conductors	17.49	16.51	Dielectric: 0.98
Sim. lossless dielectric Lossy conductors	17.41	15.66	Conductive: 1.75
Sim. lossy dielectric Lossy conductors	17.50	14.85	Total: 2.65
Measurements	-	14.03	-

with the efficiency achieved by more compact state-of-the-art LTCC antennas at mm-waves.

5.3.6 Discussion and comparison with the state of the art

The antenna gain and radiation efficiency are mainly limited by dielectric and ohmic losses. An estimation of their separate impact at 60 GHz is proposed in Table 5.3. The simulated results presented in this section account for the effect of the input connector. First, the overall module is simulated assuming lossy dielectrics and perfect conductors. The dielectric losses are evaluated as the difference between simulated directivity and gain. The ohmic losses are computed by considering the finite conductivity of the metals and lossless dielectric. It is found that the ohmic losses represent the dominant dissipation mechanism. The most relevant component of the losses is due to the quasi-optical system ($\approx$ 1.9 dB at 60 GHz), because of its large size. The insertion loss of the input transition at 60 GHz is about 0.6 dB. By subtracting these values from the total loss in Table 5.3, a loss of $\approx$ 0.15 dB is evaluated for the corporate feed network.

Table 5.4: Comparison of state-of-art 60-GHz antennas in LTCC technology.

Ref.	**Type**	**No. elements**	**Size (mm^3)**	**-10 dB Impedance bandwidth (GHz)**	**-3 dB Gain bandwidth (GHz)**	**Max. gain (dBi)**	**First SLLs (dB)**	**Radiation efficiency**
[96]	Patch array	64	35.4× 43.8× 0.7	56.2 – 67 (17.5%)	56.3 – 65.7 (15.4%)	24.2	E-plane: – 13.6 H-plane: – 11.0 (60 GHz)	> 41%, up to 55.1%
[97]	Patch with soft surface	16	14.4× 14.4× 1.0	> 51.5 – 67 (> 26.1%)	54.5 – 65.5 (18.3%)	17.5	n.a.	n.a.
[101]	Patch with air-cavities	16	18.6× 18.6× 0.6	57.3 – 64.0 (11.0%)	n.a.	18.2	E-plane: ≈ -12 H-plane: ≈ -12 (61 GHz)	n.a.
[102]	Microstrip grid array	60	15 × 15 × 0.6	57.5 – 63.3 (9.6%)	56.5 – 66.5 (16.3%)	17.6	E-plane: ≈ -15 H-plane: ≈ -14 (61.5 GHz)	n.a.
[115]	Open-ended cavity	64	47.0× 31.0× 2.0	54.86–65.12 (17.1%)	> 56.3–65.7 (> 17.1%)	22.1	E-plane: – 13.0 H-plane: – 13.0 (60 GHz)	44.4%
This work	Slot array	4	32.5× 34.0× 3.4	> 51.2 – 66.0 (> 25.2%)	54.0 – 66.0 (20%)	14.25	H-plane: < – 17.5 (50.0 – 66.0 GHz)	44% at 60 GHz

This analysis demonstrates that the limited gain is the main drawback of the proposed antenna solution. The reasons of this limitation are twofold: the losses of the quasi-optical system, that are inherently related to the antenna architecture, and the small number of radiating slots due to technological constraints on the number of LTCC tapes (see Table 5.2). Even though the quasi-optical beamformer is responsible for the largest part of the losses of the entire system, it provides multibeam capabilities and high scanning performances [52, 112]. The losses of the quasi-optical system are proportional to the focal length F and to the diameter D of the reflector. The definition of these quantities is related to the trade-off among SLLs, beam overlap level in a multibeam system [112] and antenna directivity. A fixed-beam design, such as the one presented in this paper, may benefit from small values of F that lower the losses and ensure low SLLs. However, this choice generally penalizes the scanning performances in multibeam architectures [112]. The implementation of a larger array ensures a higher gain but requires additional LTCC tapes and thicker stack-ups. Furthermore, fabrication costs and risks increase.

The key characteristic and the performance achieved by the antenna here presented are compared in Table 5.4 with state-of-the-art 60-GHz antennas in LTCC technology. It emerges that microstrip arrays [101, 102] are compact and require a few LTCC tapes, but they are limited in bandwidth and efficiency. Arrays of braodband elements, such as metamaterial-enhanced patches [96], L-probe fed [97] or cavity antennas [115], achieve the widest bandwidths and the best antenna performance. They are typically fed by SIW feed networks that lead to larger sizes and higher losses, thus requiring more radiating elements to achieve a given gain value. Thanks to the SI-PPW true-time delay network, the proposed CTS antenna attains significant improvements in impedance and gain bandwidth, while preserving a good radiation efficiency. The maximum gain and the E-plane pattern are penalized by the small number of radiating slots implemented. The architecture and the integration concept are very attractive for the realization of flat, multibeam antennas achieving wideband, wide-angle scanning performance, as it will shown in Section 5.4.

5.4 A switched-beam antenna for 5G wireless access points

The successful implementation of the fixed-beam 4-slot array described in the previous section demonstrated the feasibility of CTS AiPs in LTCC technology. The tolerances and the performance limitation dictated by the technology have been preliminarily assessed. In particular, the maximum achievable gain is limited by the maximum number of LTCC tapes and the maximum thickness allowed for the entire module. Moreover, the bandwidth is related to the minimum geometrical features that can be realized. In this section, we present a wide-angle scanning switched beam CTS design, based on the LTCC integration approach described in Section 5.3. The design aims at demonstrating the effectiveness of the proposed solution for novel, flat, multibeam antennas for 5G wireless access points. These systems should ensure a continuous and robust link with the user terminal, within the coverage area. Thus, stringent requirements in terms of beam overlap level and antenna gain are set. Realistic specifications, derived from possible application scenarios, were considered. They are discussed in Section 5.4.1. The system-level design of the antenna and the physical design of the beamformers are discussed in Section 5.4.2 and Section 5.4.3. Particular effort was put in increasing the array directivity and realized gain, as compared to the fixed-beam design, and into the simultaneous reduction of the number of LTCC tapes used. These goals are pursued by pushing the technology, using smaller geometrical features, at the expenses of an increased sensitivity to tolerances. The design of the radiating section of the CTS antenna is described in Section 5.4.4 . Another objective of the present design is the co-integration of the antenna and of the switch network, based on single-pole-three-throw (SP3T) switches, in the same compact module. Few switches operating at 60 GHz are commercially available. Moreover, they are barely matched in this frequency range. The switch network, presented in Section 5.4.5, is designed to overcome this issue and achieve the best input matching. The fabrication and assembly of the prototypes are described in

Table 5.5: Specifications for the switched-beam CTS antenna.

Parameter	**Specification**
Realized gain	17 dBi
-3 dB gain bandwidth	57 GHz - 66 GHz
- 10 dB impedance bandwidth	57 GHz - 66 GHz
Scan range	$> 70°$ in the H-plane
Scan loss	< 3 dB
Beam overlap level	-3 dB
Half-power beamwidth	8°
Maximum module size	10 cm × 10 cm × 5 cm

Section 5.4.6. Full-wave simulations and preliminary experimental results are presented in Section 5.4.7.

5.4.1 Specifications

The antenna specifications were formulated considering the requirements for a V-band access point link, defined in the framework of the European project MiWaveS [3]. They are summarized in Table 5.5. A scan range in elevation of about 70°, i.e. ±35° is required to cover a small cell having a radius between 10 m and 50 m. The expected beam overlap level, i.e. the amplitude of the intersection between the normalized radiation patterns of two adjacent beams, is -3 dB. A minimum down-link data rate of 3 Gb/s in a range of 10 m is expected. In order to achieve this performance, the antenna must be matched between 57 GHz and 66 GHz, and must have a realized gain greater than 17 dBi. For all beams, the gain drop in the frequency range cannot exceed 3 dB. The value of the expected realized gain is given for the bare radiating part of the module, neglecting the losses of the switch network. Indeed, the nominal insertion loss of each SP3T (Qorvo TGS4305-FC [116]) is 2.8 dB at 60 GHz. The losses of the switch network are neglected. Amplifiers are needed to compensate them in practical systems. Low cross-polarization and side-lobe suppression are requested, as well. Finally, the design should be compact, low-profile and easily integrable with RF and control electronics.

5.4.2 Architecture of the module

The first step in the design of the antenna is the definition of its general architecture and of the beamforming scheme, in order to fulfill the specifications shown in Table 5.5. It has been demonstrated [71, 117, 118] that is impossible to independently control the SLLs and the overlap level of the beams radiated by a passive and lossless multibeam antenna with

a single radiating aperture. This conclusion holds for both circuit-based and quasi-optical scanning systems, like a pillbox beamformer. The multibeam pillbox antenna presented in [52] achieves low first SLLs (about -26 dB) and low beam overlap levels (-19 dB). The latter parameter can be improved by reducing the amplitude taper of the field due to the reflector and by reducing the distance between adjacent feeds. In a single feed per beam (SFB) configuration, both these solutions increase the SLLs. If a radiating aperture is excited by a uniform amplitude distribution, a pillbox antenna achieves high SLLs (about -13.3 dB) and high beam overlap level (-4 dB). Similarly, in a SFB scheme, a reduction of the spacing between two adjacent feeds leads to narrower feed apertures and thus to higher SLLs of the radiated beams and reduced spillover efficiency.
The reduction of the beam overlap level is emphasized in a substrate-integrated CTS antenna, excited by a pillbox system. Indeed, as a result of the refraction at the air-dielectric interface, the scan angle θ_0 in the H-plane is magnified with respect to the angle of incidence θ_i of the wavefront impinging on the radiating aperture. The relation between these angles can be approximately expressed using Snell's law

$$\sin\theta_0 = \sqrt{\epsilon_r}\,\sin\theta_i \tag{5.1}$$

where ϵ_r is the relative dielectric constant of the substrate. The LTCC tapes (Ferro A6M-E [108]) employed in this design have a nominal relative permittivity $\epsilon_r = 5.8$.

An antenna with a single radiating aperture can achieve low SLLs and high beam overlap levels if it radiates non-orthogonal beams. As demonstrated in [118], this is possible only when lossy devices, such as resistive terminations, or, instead, active devices are introduced in the system. Multiple feed per beam (MFB) systems [119,120] can be employed to generate orthogonal beams. However, they require complex beamforming networks to control the clusters of feeds associated to each beam.

A SFB solution that eases the fabrication and does not require additional components is based on the split aperture decoupling method [32, 117]. It consists in interleaving the beams radiated by two separate apertures, each fed by a dedicated beamformer.
A schematic view of the proposed CTS system is shown in Fig. 5.14. It includes two identical CTS radiating sections that are fed by two separate pillbox beamformers. The two quasi-optical systems differ only for the positions of the feed horns in the focal plane of the respective parabolic reflector. The two sets of horns are displaced along the y-axis (see Fig. 5.14). Their relative shift is designed so that adjacent beams, in the H-plane, are radiated by different CTS apertures. Therefore, the overall system, seen as the union of the two CTS subsystems, can attain high beam overlap level. At the same time, for

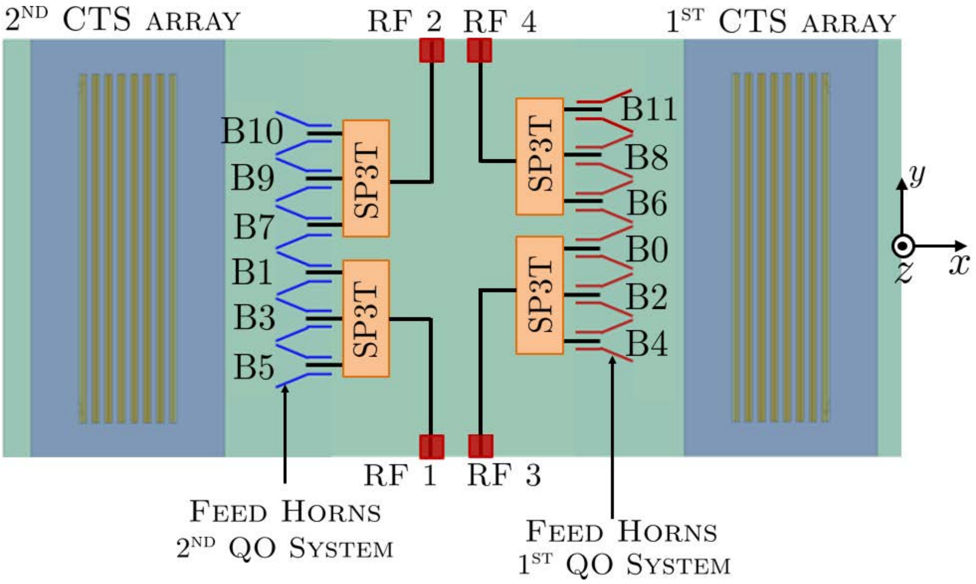

Figure 5.14: Schematic view of the proposed switched-beam CTS antenna.

each beamformer, the horn spacing can be increased and thus the horn apertures can be enlarged, so that the SLLs of the radiated beams are lowered.

A switch network is designed to select one of the available beams, by exciting only one of the feed horns. A preliminary analysis of the quasi-optical system, proposed in Section 5.4.3, reveals that eleven beams, including the broadside one, are necessary to cover a scan range larger than 70° and to meet all other specifications (see Section 5.4.1). Thus each beamformer includes six feeds that are controlled by four SP3T switches. Note that a dummy horn is added in one beamformer so that the loads at the outputs of the switches are equal.

In order to simplify the design and the control logic, each SP3T switch is fed by a dedicated RF connector. This choice does not affect the validity of the present proof of concept. In future implementations, the inputs of the four switches could be controlled by a SP4T, fed by a single RF connector. The details of the design of the switch network are discussed in Section 5.4.5.

Each radiating section of the system comprises an array of 8 slots, since a minimum realized gain of 17 dBi is targeted and the 4-slot fixed-beam design achieved a gain of about 14 dBi. A further increase of the directivity, with respect to the previous design, is achieved through an improved design of the quasi-optical beamformer.

5.4.3 System level design and quasi-optical beamformers

The system level design of the antenna is based on the GO analysis of the quasi-optical beamformers. The characteristics of the radiated beams are evaluated using the methods

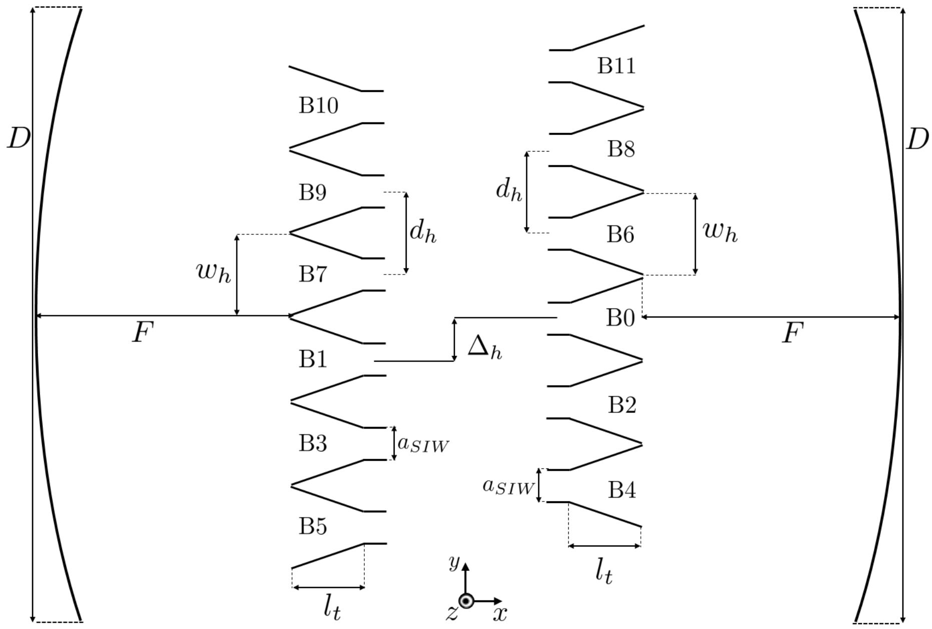

Figure 5.15: Geometry of the two beamformers of the switched-beam antenna.

Table 5.6: Geometrical parameters of the quasi-optical systems, obtained from a system level design.

D (mm)	F/D	w_h (mm)	d_h (mm)	Δ_h (mm)	a_{SIW} (mm)	l_t
40.30	0.68	2.80	3.02	1.51	1.57	3.57

discussed in Section 3.4.2, for different configurations of the beamformers. Their design is slightly modified until the specifications are met. The achievement of low first SLLs and high beam crossing level, in the entire scan range, is complicated by the high permittivity of the LTCC tapes, as discussed in Section 5.4.2. A good trade-off is found by using eleven beams. A schematic view of the system is shown in Fig 5.15. The main parameters to be designed are the diameter D of the parabolic reflectors that is also equal to the length of the radiating slots, the focal length F, the aperture w_h of the horn, the distance d_h between two adjacent horns. The values of all these parameters are the same for the both beamformers. The shift Δ_h between the sets of horns of the two quasi-optical systems must be chosen. The width a_{SIW} of the input SIW lines of the horns and the length l_t of their tapered sections have a minor impact on the radiation performance. In order to increase the directivity, values of D and F greater than those used in the fixed-beam design are considered. The parameters chosen for a preliminary design of the quasi-optical systems are listed in Table 5.6.

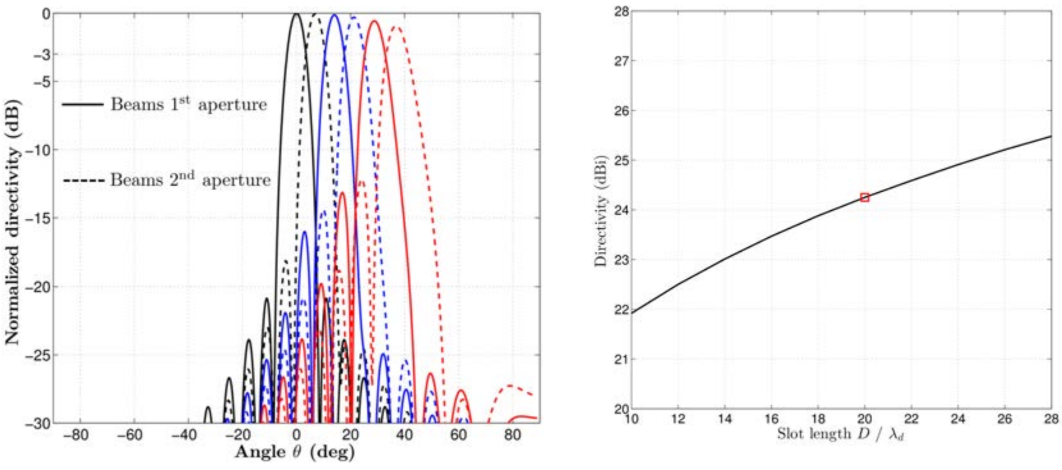

(a) (b)

Figure 5.16: Numerical results, based on the proposed GO approach, relative to preliminary design of the antenna (see Table 5.6). (a) Normalized radiation patterns in the H-plane and (b) directivity at 61.5 GHz as a function of D, for $F/D = 0.68$.

The radiation patterns in the H-plane at $f_0 = 61.5$ GHz are computed using the proposed GO approach and are shown in Fig 5.16. By virtue of symmetry, only the beams that points at non-negative angles θ are plotted. The impact of the D on the directivity for a focal-to-length ratio $F/D = 0.68$ is illustrated in Fig. 5.16b. Eight radiating slots of width $a = 0.85$ mm, length D, and an array spacing $d = 1.50$ mm were assumed. The expected directivity for the selected value of D is 24.2 dBi, that is high enough to ensure the required gain, assuming that the radiation efficiency is in the order of 40%, as for the fixed-beam antenna.

The antenna performance between 57 GHz and 66 GHz was evaluated by iterating the GO analysis at several frequencies. For the broadside beam, the SLLs in this band are less than -19.7 dB, the beam overlap level is higher than -3.2 dB and the HPBW is between 6.7° and 7.4°.

The beam pointing directions are stable in frequency. The largest variation over the $57 - 66$-GHz band is observed for the beams B5 and B10 and is about 1.3° in absolute value. Moreover, as the scan angle increases, the beams broaden and the SLLs increases, up to -11 dB. In the design band, the maximum scan loss, i.e. the difference between the gain of the broadside beam and that of the beam closest to end-fire, is 1.2 dB. However, this value is underestimated since this analysis does not take into account material losses which lower the gain of the scanned beams more than that of the broadside beam.

The physical implementation of the beamformers is based on the designs presented in Section 5.3 and in [52, 112]. The design features are optimized by means of full-wave simulations, using the results of the GO analysis as starting values. As illustrated in Fig. 5.17b,

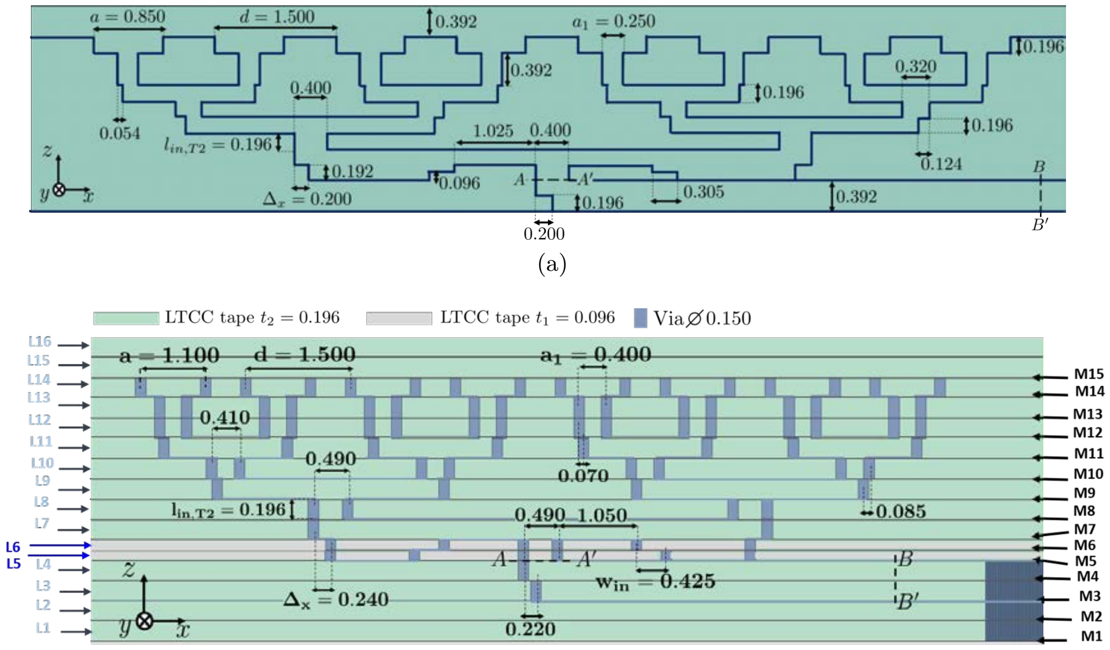

(a)

(b)

Figure 5.17: Cross section of the two CTS arrays of the switched-beam antenna. (a) Preliminary design based on ideal PPW components. (b) Final design, based on SI-PPW components. All dimensions are in millimeters.

four LTCC tapes of thickness $t_2 = 0.196$ mm are employed for the quasi-optical system. This limits the number of tapes that can be used for the corporate feed network. However, full-wave simulations demonstrated that if the height of each PPW is halved, i.e. if only two LTCC tapes are used, the insertion loss increases of 1.3 dB. Given this significant loss and the required gain, the design with four tapes was preferred.

5.4.4 Design of the radiating section

Specific objectives in the design of the 8-slot array and of the corporate feed network are the minimization of the input reflection coefficient and of the number of LTCC tapes used. In order to achieve these goals, the numerical tools developed for the analysis of CTS arrays (see Chapter 3 and Chapter 4) were extensively employed in the design. Indeed, a preliminary design was performed considering ideal PPW components, i.e. structures with perfect electric conductive parallel plates, infinite along the y-direction. The geometrical details of this structure are shown in Fig. 5.17a. The thickness of the corporate feed network and the number of LTCC tapes are reduced by using, in two division stages, the compact power divider presented in Section 4.2.4. The input power divider, instead, features is based on the broadband design discussed in Section 4.2.3.

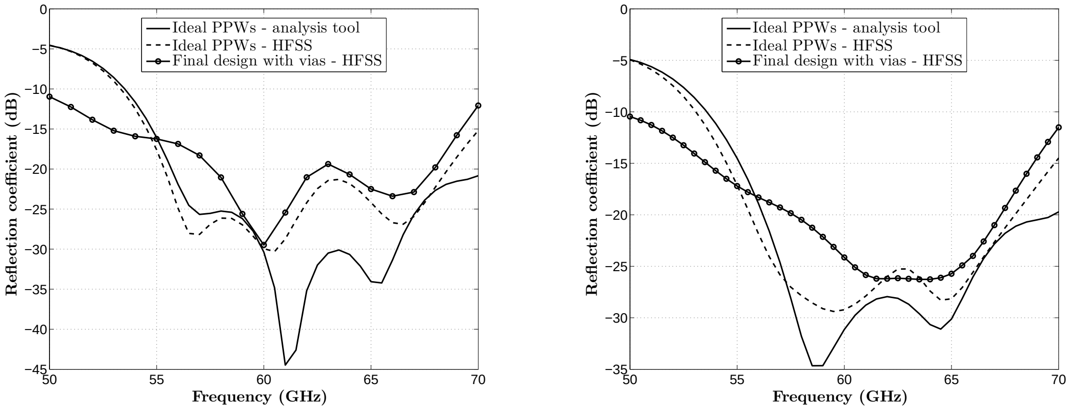

(a)

(b)

Figure 5.18: Reflection coefficient computed at the reference planes (a) AA’ and (b) BB’ of the CTS antenna shown in Fig. 5.17, relative to beam B0. For the structure of Fig. 5.17a, results computed using the analysis tool and HFSS simulations are shown. For the final design (see Fig. 5.17b), HFSS data are presented.

As in the fixed-beam design, a dielectric cover of thickness 0.392 mm is added on the radiating aperture to enhance the matching.

The reflection coefficients at the reference planes AA' and BB' (see Fig. 5.17), computed using the analysis tools,are in tight agreement with full-wave simulations, as shown in Fig. 5.18. The input port was excited with a uniform amplitude. The structure is assumed infinite along the y-axis and periodic boundaries were used in simulations. Note the finiteness of the array, that comprises only eight slots, does not affect the accuracy of the analysis procedure, thus confirming the conclusions of Section 4.4.

Once the first-pass design had been finalized, the actual structure was defined by replacing the ideal PPWs with SI-PPWs. The rows of vias were designed so that the final structure achieves a similar performance, in terms of reflection coefficient and radiated patterns. The minimum diameter (0.15 mm) and centre-to-centre spacing (0.30 mm) allowed by the technology were used. The distance between the two parallel via-rows of each SI-PPW component were optimized by means of full-wave simulations. The cross section of the final design, based on SI-PPWs, is shown in Fig. 5.17b. The overall stack-up comprises sixteen LTCC tapes. Fourteen of them have nominal thickness $t_2 = 0.196$ mm, whereas the remaining two have thickness $t_1 = 0.096$ mm, that are used for the design of the broadband power divider. The simulated input matching of the final design is in line with that computed for the preliminary structure, as shown in Fig. 5.18. The reflection coefficients at section AA' and at section BB' are both less than −18.3 dB between 57 GHz and 66 GHz.

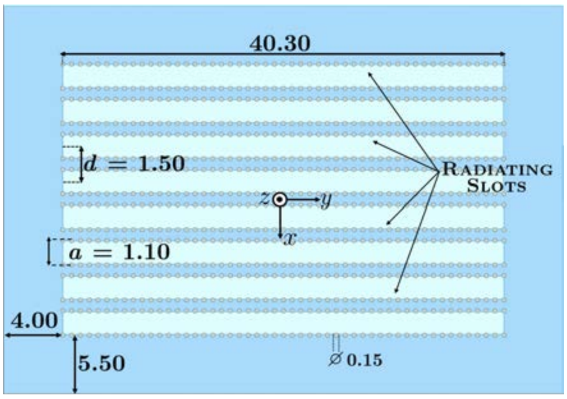

Figure 5.19: Top view of the eight-slot array of each of the two CTS antennas in the switched-beam module. All dimensions are in millimeters.

The structures considered so far are infinite along the y-direction. As a result of the analysis presented in Section 5.4.3, the length of the slots and of the feed network along the y-axis is $D = 40.30$ mm. The top view of the slot array is illustrated in Fig. 5.19. As per simulations, the differences in terms of input reflection coefficient between the finite and the infinite structure are negligible. With respect to the fixed-beam design, the number of slots was doubled and two LTCC tapes were saved. This was achieved by scaling down some design features in the corporate feed network. Therefore, the sensitivity of the design to fabrication tolerances must be assessed. To this end, full-wave simulations were performed on the antenna structure of Fig. 5.17b, assumed infinite along the y-direction and excited by a normal incident TEM mode with uniform amplitude. First, two key technological parameters are investigated. The variations of the reflection coefficient at section AA', due to deviations of the tape thicknesses from their nominal values ($t_1 = 0.096$ mm, $t_2 = 0.196$ mm) are shown in Fig. 5.20a.

Relative variations up to 8% for t_2 and up to 17% for t_1 are considered. Even if the uncertainty on the shrinkage of a single tape is less than 1% [108], significant reduction may occur in a complex multilayer stack-up, with a large number of vias, such as the one shown in Fig. 5.17b. The results demonstrate that the matching bandwidth is penalized by the tape shrinkage and broadens for thicker tapes. The reflection coefficient is less than -10 dB in the band of interest, provided that t_1 and t_2 vary less than 8%. For simplicity, in each step of this analysis, the same thickness was assumed for all tapes having the same nominal value. Nevertheless, these results prove a good robustness of the design to tolerances on the thicknesses of the tapes.

The value of permittivity assumed in the design is $\epsilon_r = 5.8$, based on past measurements on test structures. However, a higher value, i.e $\epsilon_r = 5.9$, has been retrieved from more recent measurements. The impact of ϵ_r on the reflection coefficient is illustrated in Fig. 5.20b.

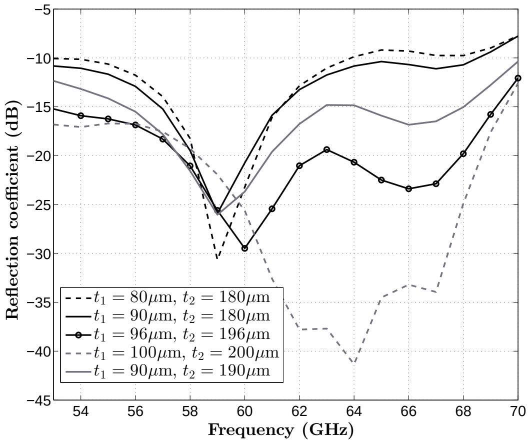

(a)

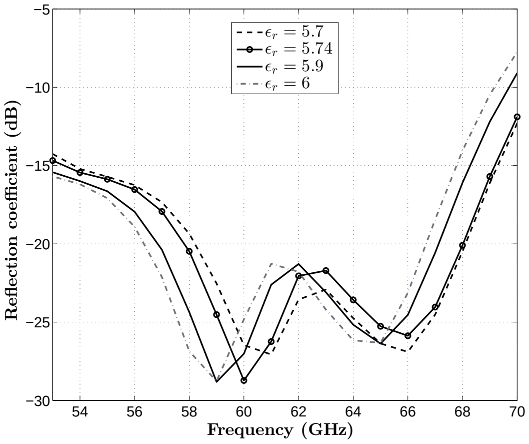

(b)

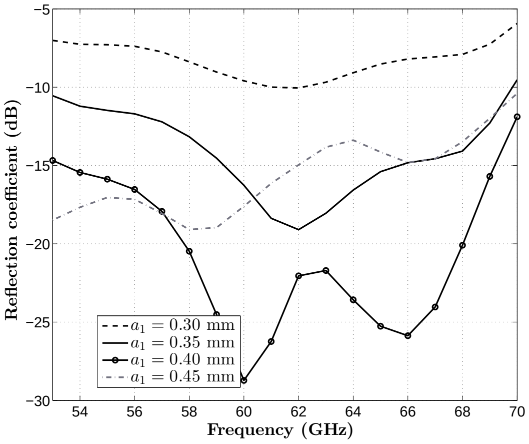

(c)

Figure 5.20: Sensitivity analysis on the reflection coefficient, relative to beam B0, at the reference plane AA' (see Fig. 5.17b) for deviations from the nominal values of: (a) the tape thicknesses t_1, t_2; (b) the relative permittivity ϵ_r; (c) the width a_1.

An increase of the value of ϵ_r shifts the resonances to lower frequencies but does not affect the bandwidth. The impact of some critical design features was investigated as well. The reflection coefficient was found to be particularly sensitive to variations of a_1, as illustrated in Fig. 5.20c. Indeed, a_1 determines the reactance of the step that matches the active impedance of the array to the desired impedance level. The parametric analysis demonstrates that a proper operation of the array is achieved if the deviation of a_1 from the nominal value are in the range $\pm$ 50μm. The sensitivity of the input matching to other design parameters was evaluated. In conclusion, the design of the radiating sections of the switched-beam antenna is robust to variations of the design features of about $\pm$ 50μm. The expected fabrication errors are within the latter range.

5.4.5 Design of the switch network

The switch network consists of three LTCC tapes (L1-L3), each of nominal thickness 196 μm and four metal layers (M1-M4), blind and buried vias, as illustrated in Fig. 5.21. It comprises four RF ports that are excited one at a time by coaxial end-launch connectors [111], four SP3Ts and two DC connectors that are used to feed 12 bias lines (6 each). The pads of the DC connectors are routed to the bias pads of the switch lines using the metal layer M4 and stacked vias in the three tapes (L1-L3). With this choice, the GCPW and SIW structure that guide the RF signal are not perturbed by the bias lines. The layout (top view) of metal layer M1 is shown in Fig. 5.21b.

The network is based on GCPW lines that minimizes ohmic and radiation loss in this frequency range, as compared to other planar transmission lines. The distance between the signal line (on M1) and the ground plane (on M3) of the GCPW is $h_w = 0.392$ mm $\approx \lambda_g/5$, where λ_g is the guided wavelength at 60 GHz.

The GCPW lines were designed in order to minimize the overall losses. The width of the gaps of the metal strips are reduced to ease the interconnection with the SP3Ts and minimize the radiation losses of the 90° bends.

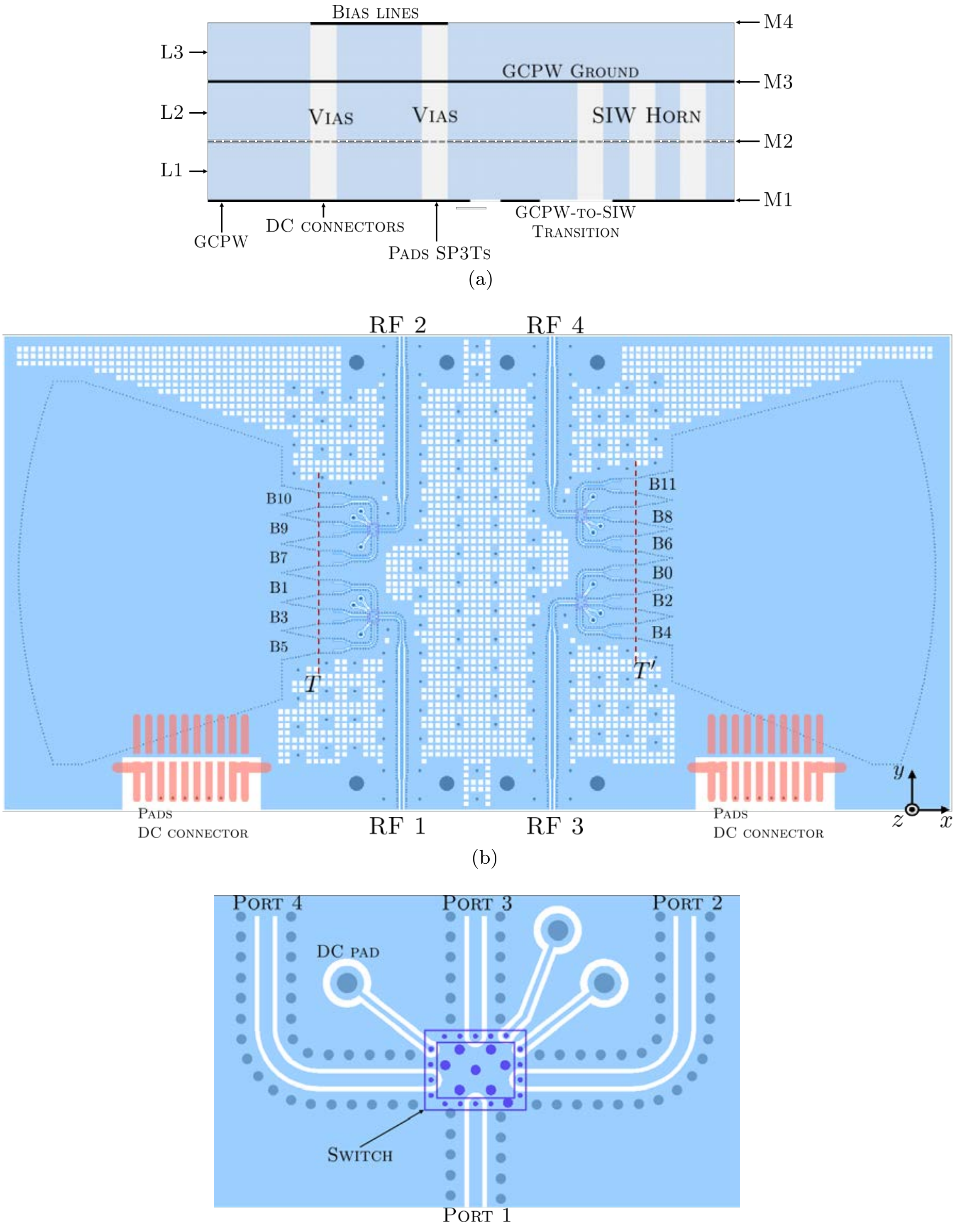

(a)

(b)

(c)

Figure 5.21: (a) Schematic cross section of the switch network and DC bias routing. (b) Top view of the metal layer M1 of the switch network (see Fig. 5.21a). Some areas of the ground plane are meshed. (c) Detail of the layout: land pattern for a switch and reference planes for the S-parameters shown in Fig. 5.22.

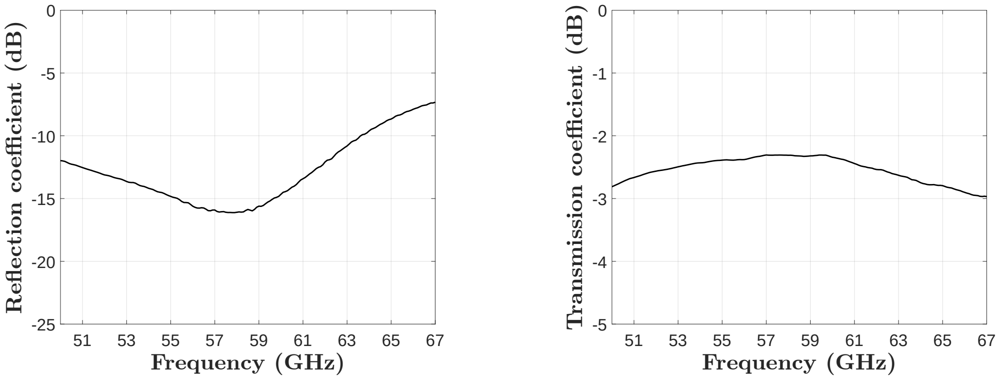

(a) (b)

Figure 5.22: (a) Reflection coefficient at Port 1 and (b) transmission coefficient from Port 1 to Port 3, for the structure in Fig. 5.21c.

The network was designed by assuming, for the S-parameters of the switches, the values extracted from measured test structures [121] on a substrate with thickness 96 μm.

The reflection coefficient at Port 1 and the transmission coefficient from Port 1 to Port 3, for the structure of Fig. 5.21c, are shown in Fig. 5.22. The return loss does not exceed 16 dB and is less than 10 dB for frequencies higher than 64 GHz, while the insertion loss is less than 2.5 dB in the band of interest. Similar results are obtained for the paths form Port 1 to Port 2 and from Port 1 to Port 4. It is worth to remark that the distance between each switch and the closest ground plane is $h_w = 0.392$ mm, while the data assumed for the design are derived from measurements on a substrate of thickness 96μm. This may determine some discrepancies between simulations and the actual matching performance. The reflection coefficients at the input connectors and the insertion losses from each connector to each integrated horn, at the reference planes T and T' in Fig. 5.21b, were evaluated by combining full-wave simulations and the measured scattering parameters of the switches. The mismatch due to the antenna and quasi-optical beamformer was considered negligible. Thus, the outputs at sections T and T' are assumed perfectly matched. The results obtained for the four paths from one of the input connectors to the horn fed by the central output line (Port 3 in Fig. 5.21c) of the corresponding switch are shown in Fig. 5.23. The input matching degrades with increasing frequency. The insertion losses at 61.5 GHz are between 8.3 dB and 8.7 dB, depending on the considered path.

The simulated results relative to the paths from the connectors that include the lateral output lines of the switches are presented in Fig. 5.24. The insertion losses range between 9.5 dB and 9.7 dB at 61.5 GHz. They are about 1 dB higher than those observed in the previous case, due to longer signal paths. The amplitude imbalance of the switch network

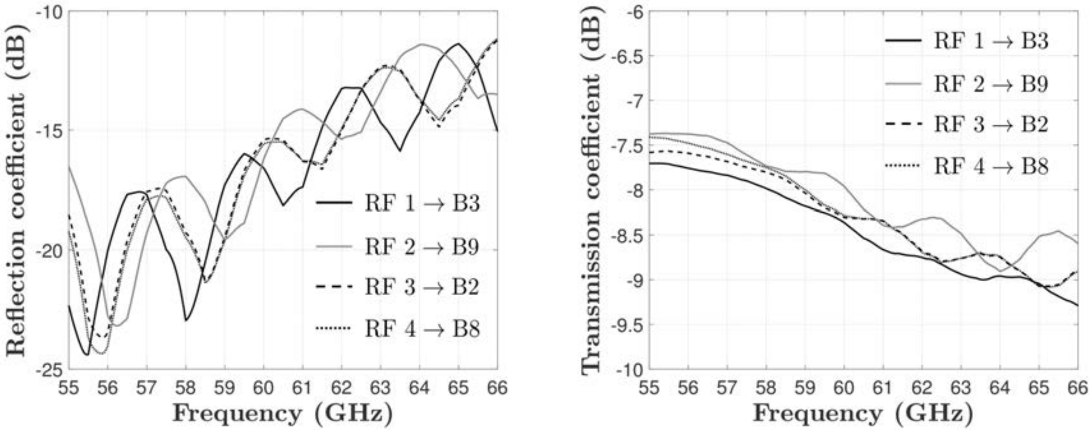

(a) (b)

Figure 5.23: Simulated (a) reflection and (b) transmission coefficients, relative to the paths from the connectors to the horns fed by the central outputs of the switches (see Fig. 5.21).

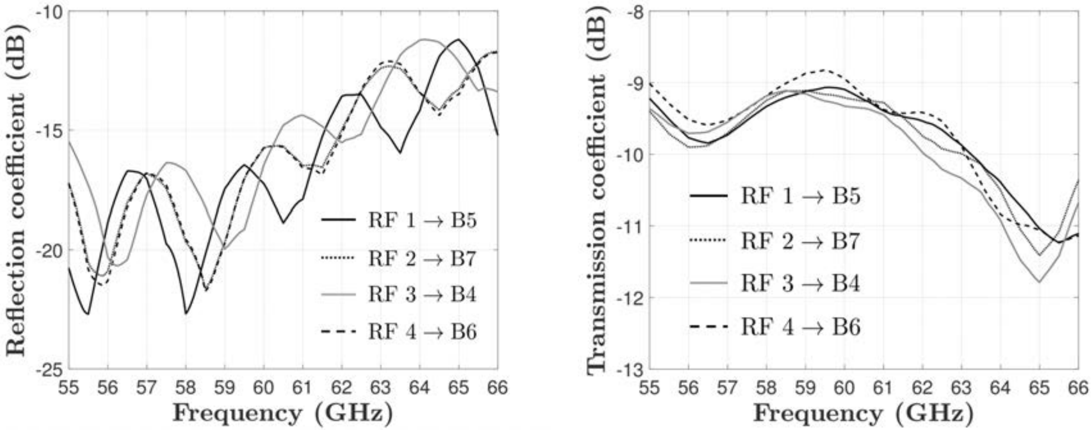

(a) (b)

Figure 5.24: Simulated (a) reflection and (b) transmission coefficients, relative to the paths from the connectors to the horns fed by the lateral outputs of the switches (see Fig. 5.21).

must be considered in order to fairly compare the gain of different radiated beams.

5.4.6 Prototypes and assembly

The antenna was fabricated and assembled at the Technical Research Centre of Finland (VTT). The fabrication process is similar to that employed for the fixed-beam antenna described in Section 5.3. However, an improved version (Ferro A6M-E [108]) of the tape system was used, that provides higher strength and toughness. The estimated thicknesses of the LTCC tapes after co-firing are 186 μm and 92 μm, whereas the values assumed in the

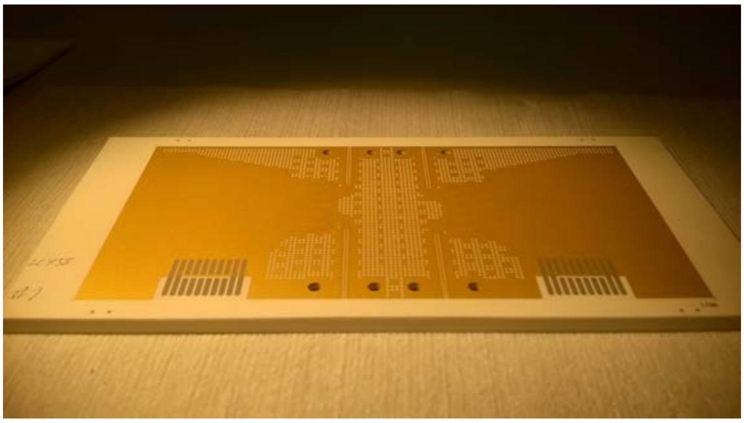

Figure 5.25: Photo of the LTCC module before the assembly of connectors and switches.

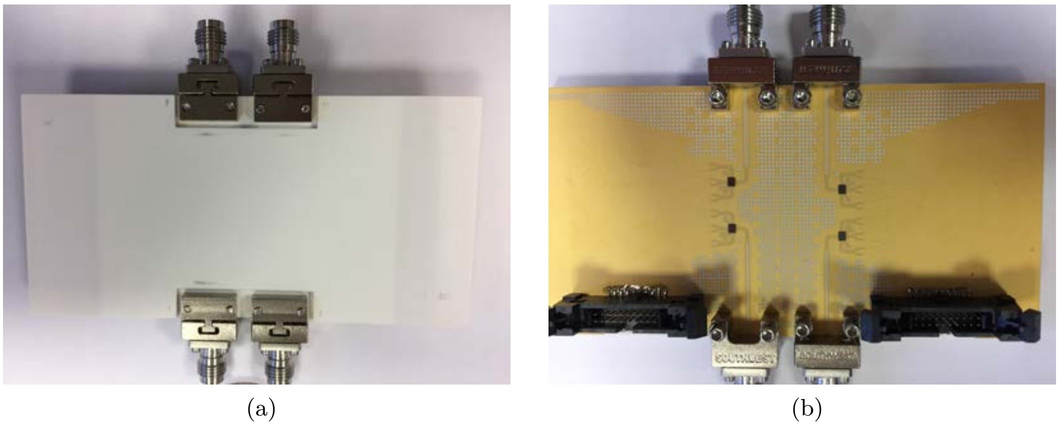

(a)

(b)

Figure 5.26: Photos of the switched-beam antenna: (a) top and (b) bottom view.

design are 196 μm and 96 μm, respectively.

A picture of the processed substrate, before the assembly of connectors and switches, is shown in Fig. 5.25. The bottom metal layer of the module (M1) is visible. Some areas of the ground plane were meshed, without altering the RF performance, to reduce the content of gold paste that, when excessively high, may lead to substrate shrinkage and deformation. The pads for the DC bias connectors and the screw holes to accommodate the RF connector can be recognized. The DC connectors were soldered on the pads and some epoxy glue was applied to improve the mechanical stability and to mitigate the danger of copper peeling-off. Two cavities were laser machined, in the top LTCC tapes, to mount the RF connectors. The SP3T switches were flip-chipped on the bottom metal layer. The top and bottom views of the final prototype are shown in Fig. 5.26. The radiating apertures can be barely distinguished in Fig. 5.26a, on the lateral edges of the modules, since they are covered by two matching LTCC tapes.

In order to control the switches and test the antenna module, a custom bias board and

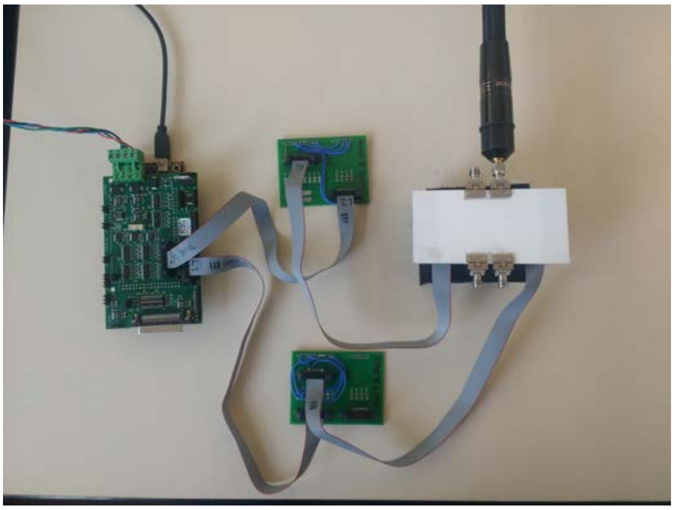

Figure 5.27: Setup for the measurement of the input reflection coefficient.

two interposer cards, one for each DC connector, were developed by VTT. The board is connected to a computer through a USB cable. The states of the switches, and thus the radiated beam, can be set using a terminal program. Figure 5.27 shows the setup for the measurements of the input reflection coefficients. A single RF connector is fed by the vector network analyzer, using a precision cable. The other connectors are left open, since a high isolation among them is expected. The electrical connections among bias board, interposer cards and antenna under test can be appreciated.

5.4.7 Simulation results and measurements

The complexity and the size of the complete antenna system, and the large number of vias make prohibitive, in terms of memory and time resources, a full-wave simulations of the overall structure. The radiation characteristics and the input reflection coefficients are evaluated by performing separate simulations of the two CTS subsystems, as done in [32]. The simulation results presented in this section are obtained by exciting each subsystem at the input ports of the horns in the corresponding beamformer. Each input horn is associated to a radiated beam, denoted with symbols B0-B5 for non-negative scan angles in the H-plane and with B6-B10 for negative ones, as illustrated in Fig. 5.14. The simulations account for material losses ($\tan\delta = 0.0023$, $\sigma = 7 \times 10^6$ S/m), unless explicitly stated otherwise.

5.4.7.1 Input matching

The simulated reflection coefficients relative at the input of the feed horns (see planes T and T' in Fig. 5.21b), relative to three beams (B0, B1 and B5), are shown in Fig. 5.28. All

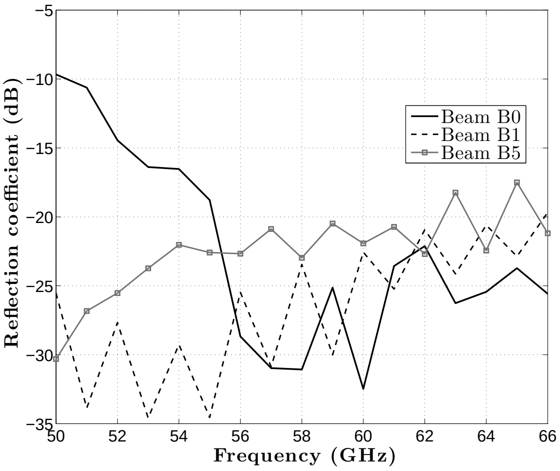

Figure 5.28: Simulated reflection coefficients relative to beams B0, B1, B5, at the corresponding input horns of the quasi-optical systems.

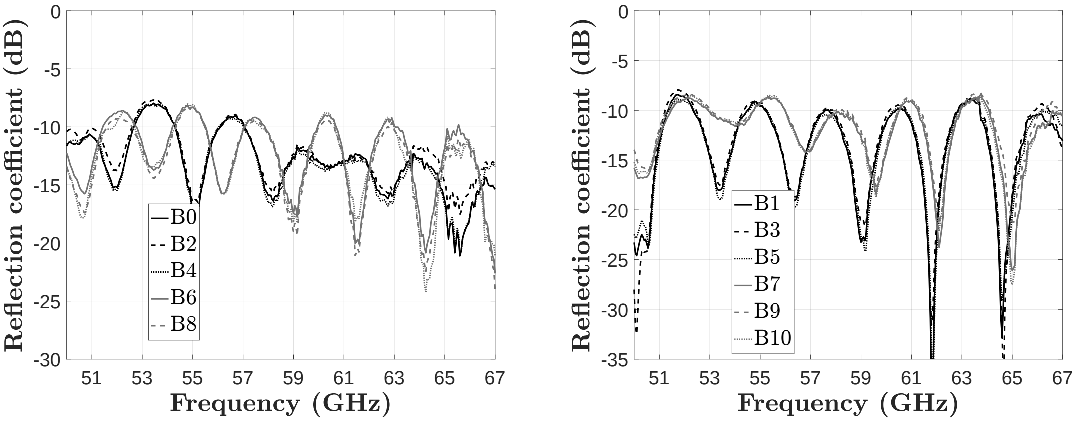

(a)

(b)

Figure 5.29: Measured reflection coefficients at the input connectors: (a) RF1, RF2 (first beamformer) and (b) RF3, RF4 (second beamformer).

reflection coefficients are less than -17.5 dB between 56 GHz and 66 GHz. For the beam B0, that points at boresight, the reflection coefficient tightly resembles the one simulated at the input section AA' of the CTS array for normal incidence. When the antenna beam is steered, the reflection coefficient is generally lower, except for the furthermost horn corresponding to beam B5. Given the good matching at the inputs of the quasi-optical system and the performance of the switch network (see Section 5.4.5), the reflection coefficient at the input connectors was expected lower than -10 dB, in the entire band.

The reflection coefficient at the input connectors was measured, for each beam, by exciting only a single RF connector. All switches were set in the off-state, except the one relative to the beam under measurement. The measured results are shown, for all beams, in Fig. 5.29a and in Fig. 5.29b, respectively. The input reflection coefficient is less than -8.5 dB, for all beams, in the $57 - 66$ GHz band. The peaks that exceed -10 dB can be attributed to reflections from the switches. It is worth noting that the design and simulations where performed assuming for the switches the S-parameters measured on an LTCC substrate of thickness $96\,\mu$m. This value is about a quarter of the distance between the switch and the ground plane in the prototype. Therefore, the input matching can be improved by considering more accurate data for the switches and by designing dedicated matching structures.

Finally, we observe that the results for the three beams associated to each switch are very similar. This confirms that the performance in reflection of the switches does not depend on the activated RF path and that the same matching structure can be used at the output ports of the each switch in a future design.

5.4.7.2 Radiation patterns

Full-wave simulations and preliminary measurements are presented in this section to evaluate the radiation performance of the antenna. The simulated results are obtained by exciting each CTS subsystem at the input ports of the feed horns. Figure 5.30 reports the simulated directivity patterns in the H-plane. The beams generated by both the CTS apertures are combined to analyze the radiation characteristics of the overall switched-beam antenna. By virtue of symmetry, only the beams pointing at non-negative scan angles (B0-B5) are shown.

A field of view of about ±38° is covered, with a low directivity drop in scanning. The scan losses relative to beam B5 are higher, up to a maximum 2.6 dB in the band, but still less than the targeted 3 dB. The HPBW ranges from 7.4° to 7.7° in the frequency band for the broadside beam B0. However, it increases with the scan angle, up to 10.5° for beam B5.

The split aperture decoupling technique effectively solves the trade-off between beam overlap level and SLLs. The values of the first SLLs are shown in Fig. 5.31a, as a function of frequency. As required by the specifications, they are less than -20 dB for the broadside beam (B0), in the entire band. An increase of the SLLs is observed when the beam is steered, due to the off-focus illumination of the quasi-optical systems. For the beam B5, that points at about 38°, an average SLL of about -12 dB is achieved. The crossing level between beams B0 and B1 is higher than -3 dB in the entire band, as shown in Fig. 5.31b. Similar values are obtained for all pairs of adjacent beams.

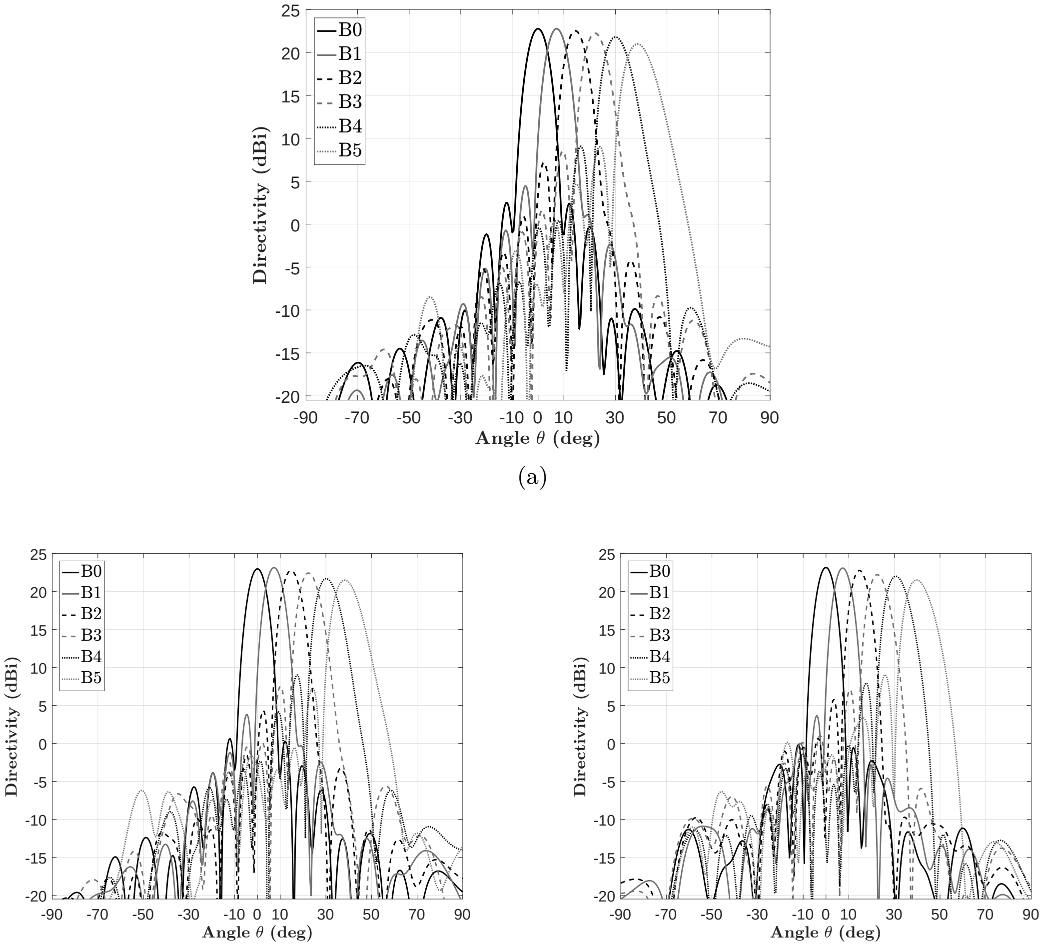

(a)

(b)

(c)

Figure 5.30: Simulated directivity patterns in the H-plane, relative to beams with a positive scan angle, at (a) 61.5 GHz, (b) 57 GHz, (c) 66 GHz. The beams radiated by the first and the second CTS aperture are shown in black and in grey, respectively.

The stability of the beam pointing directions, that vary of less than 1.5° in the $57-66$ GHz band, confirms the wideband performance of the system.

The gain performance is one of the main requirements for the switched-beam antenna system, that motivated the increase of the number of radiating slots, as compared to the design discussed in Section 5.3. The simulated directivity and realized gain are shown in Fig. 5.32 for three beams. The gain does not account for the insertion loss of the switch network antenna. The directivity of the broadside beam at 61.5 GHz is 23.1 dBi which is not far from the value of 24.2 dBi obtained from the preliminary analysis presented in Section 5.4.3. At the same frequency, the realized gain is 20.2 dBi. The frequency behaviour of the gain is stable over a wide frequency range. The realized gain of each beam varies less than 0.7 dB between 57 GHz and 66 GHz. The realized gain is higher than 17.4 dBi, that

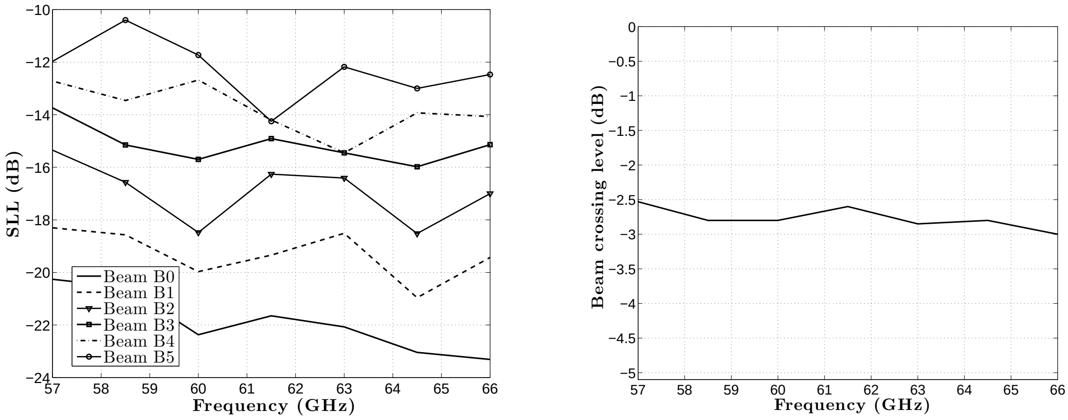

(a) (b)

Figure 5.31: (a) Simulated first side lobe levels for beams B0-B5 and (b) beam overlap level, between B0 and B1, as a function of frequency.

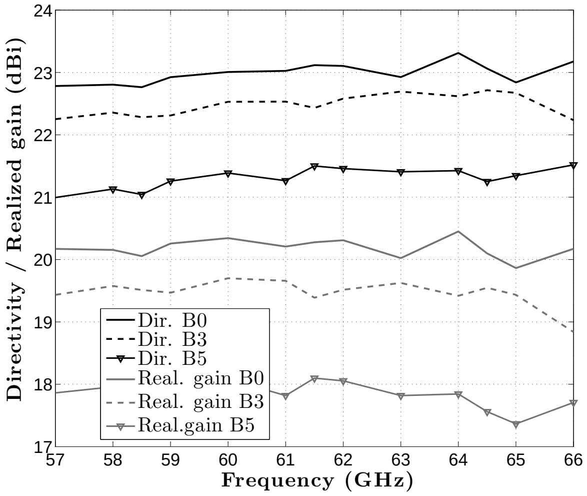

Figure 5.32: Simulated directivity (in black) and simulated realized gain (in grey) against frequency, for several beams.

is the minimum value achieved by beam B5. These values fulfill the initial specifications. For all beams, the estimated antenna efficiency is greater than 40% in the targeted band, and reaches a maximum of 55% at 61.5 GHz for the beam B0. These values are in line with the efficiency evaluated for the fixed-beam prototype (see Section 5.3).

An analysis of the scan losses is reported to assess the scanning capabilities of the antenna module. The gain drop with respect to the broadside beam is computed for each beam and shown in solid lines in Fig. 5.33. These values are compared to the ideal scan losses (in dashed lines), due to the bare reduction of the effective radiating aperture, that

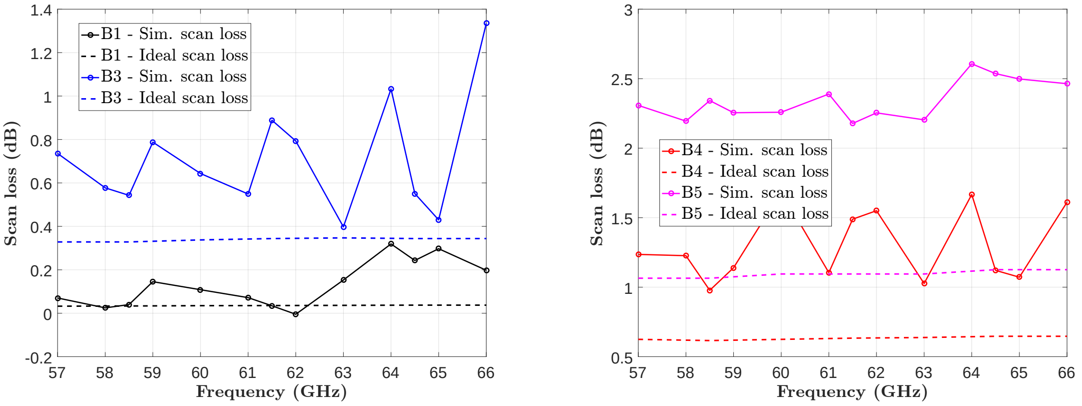

(a) (b)

Figure 5.33: Simulated scan losses of the switched-beam antenna for beams: (a) B1 and B3; (b) B4 and B5. For each beam, the ideal scan loss is computed as the cosine of the scan angle and is shown in dashed line.

is assumed equal to the cosine of the scan angle. The spread between ideal and simulated values increases with the scan angle. This is attributed to aberration phenomena in the quasi-optical systems and to the impact of the material losses. The latter becomes more relevant for large scan angles, due to the increase of the effective path of the waves that propagate in the structure. However, the scan losses are still limited up to ±30° and, for all beams, lower than 3 dB, as required by the specifications.

At the time of writing, the measurements of the radiation patterns are in progress. The

(a) (b)

Figure 5.34: Measurement setup in the compact antenna test range (CATR) facility of IETR. (a) Overview. (b) Detail of the prototype, within the plastic holder.

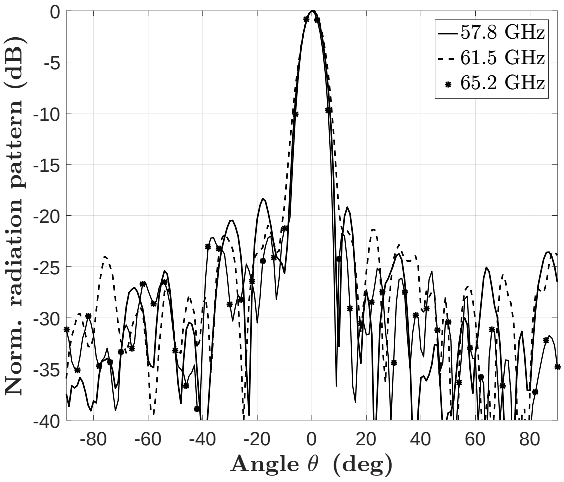

Figure 5.35: Measured normalized radiation patterns in the H-plane for the beam B0 at 57.8 GHz, 61.5 GHz and 65.2 GHz.

prototype is being characterized using the mm-wave compact antenna test range (CATR) facility of IETR [122]. The measurement setup is shown in Fig. 5.34. In order to improve the mechanical robustness under test, the antenna has been located in a plastic holder, designed to minimize its impact on the electrical performance. The computer and the voltage generator visible in Fig. 5.34a are used to select the radiated beam.

Figure 5.35 shows the normalized radiation patterns in the H-plane, relative to the beam B0, at three frequencies in the design band. As expected from simulations, the measured HPBW is about 7.5°. The SLLs are less than -18.3 dB between 57 GHz and 66 GHz, whereas the simulations of the bare CTS arrays predicted a maximum SLL of -20 dB.

The realized gain patterns, relative to beams B0-B10, are shown in Fig. 5.36 as functions of the elevation angle in the H-plane. The antenna covers a field of view of about 80° and achieves a high beam overlap level, in the order of -3 dB, for all pairs of adjacent beams. The differences of the maximum realized gain of the beams are due to the amplitude imbalance of the switch network (see Section 5.4.5) and to the different reflection coefficients at the input connectors (see Section 5.4.7.1). For each beam, the peak gain varies less than 3 dB between 57 GHz and 66 GHz. The maximum values of the realized gain, measured at the input connectors, are between 9.4 dBi and 14.7 dBi, depending on the beam considered. Similar results are obtained by subtracting the simulated insertion losses of the switch network from the simulated gain values presented in Fig 5.32. More precise comparisons will be performed when all measured results are available.

Since the insertion loss of the switch network varies for different beams, the scan losses cannot be directly evaluated from the measured realized gain. They will be estimated from

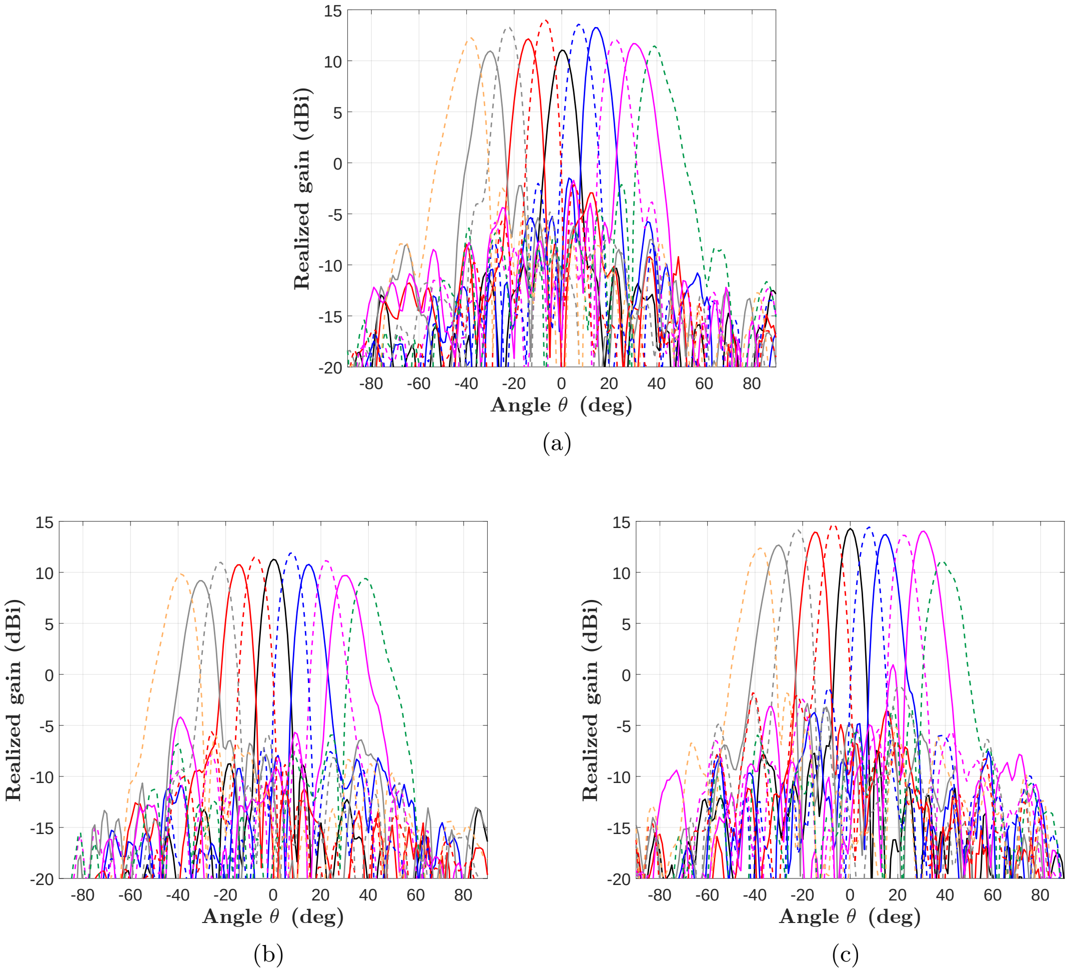

(a)

(b)

(c)

Figure 5.36: Measured realized gain patterns in the H-plane for beams B0-B10 at: (a) 61.5 GHz; (b) 57.8 GHz; (c) 65.2 GHz.

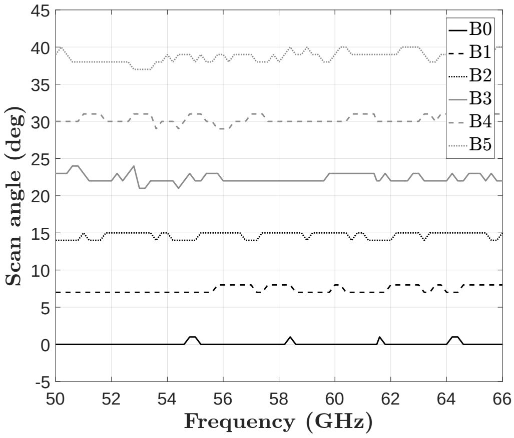

Figure 5.37: Measured scan angles for beams B0-B5, between 50 GHz and 66 GHz.

the variation with frequency of the HPBW of each beam. New measurements with finer angular resolution are being completed to accurately evaluate the HPBW.

The measured beam pointing directions match the design values. The scan angles for beams B0-B5 are plotted against frequency in Fig. 5.37. Their stability confirms the broadband behaviour of the antenna. The maximum variation observed between 57 GHz and 66 GHz is 2° for the beam B5, pointing at about 39°.

5.5 Conclusion

In this chapter, novel technical solutions have been proposed to integrate CTS antennas in multilayer dielectric substrates and to realize efficient mm-wave SiPs with beam steering capabilities. A new waveguide structure, i.e. the substrate integrated parallel plate waveguide, that supports the propagation of a quasi-TEM mode along the vertical axis of the substrate has been demonstrated. The SI-PPW is based on parallel rows of vias, stacked and aligned on several layers, that act as the solid metal plates of a standard PPW. This waveguide achieves the low-dispersive behaviour that is necessary for the broadband operation of CTS arrays.

The proposed antenna concept has been implemented in LTCC technology, that was recognized as the most reliable for the realization of the complex 3-D multilayer structures of a CTS antenna.

First, a broadside CTS array with four radiating slots has been fabricated and characterized to test the accuracy of the process and to prove the concept. Simulated and measured results tightly agree, thus demonstrating the robustness of the design to fabrication errors. The antenna achieves broadband performance. In the $50 - 66$ GHz band, the measured reflection coefficient is less than 9.3 dB, the SLLs in the H-plane are less than -17.5 dB and the average radiation efficiency is 46%. The maximum gain is 14.25 dBi and the relative -3 dB gain bandwidth is about 20%.

Based on these promising results, a switched-beam antenna has been design and fully integrated in an LTCC module, with applications to 5G access points. In order to solve the trade-off between beam overlap levels and SLLs, the system has been realized using two specular CTS antennas, each with eight slots, that differ only for the positions of the feed horns. They generate two sets of interleaved beams so that the overall antenna covers a wide field of view (±38°) with high radiation performance and beam crossing levels. Only one of the two CTS systems and a single feed of the corresponding quasi-optical beamformer is excited to radiate each beam. A switch network, integrated in the LTCC module, controls the RF signal and the excitation of the proper feed.

The correct operation of the switches was experimentally verified. The measured input reflection coefficients are less than -8.5 dB between 57 and 66 GHz. This mismatch is attributed to the lack of experimental data for the S-parameters of the switches. Indeed, they were characterized on a substrate with a thickness different from that of the final design. As per simulations, for the broadside beam, the simulated gain at 61.5 GHz is 20.15 dBi, with SLLs lower than -20 dB in the 57-66 GHz band. The maximum scan loss is about 2.6 dB for the beams pointing at $\pm 38°$ and less than 1.75 dB for those with a scan angle of $\pm 30°$. A beam crossing level of about -3 dB is achieved for all beams. The measurements of the radiation patterns are currently in progress. The preliminary measured results demonstrated the beam-switching capabilities of the antenna system. The beam pointing directions, the SLLs and the HPBW of the beams are in good agreement with the simulated values.

Chapter 6

A wideband solution to achieve circular polarization

Circular polarization offers higher link reliability for long-range wireless communications, since it is more robust to signal degradation due to atmospheric conditions. Modern Satcom systems exploit circularly polarized antennas to mitigate multipath fading and the effects of alignment errors between transmitting and receiving units [7, 8]. The use of circular polarization (CP) has been also proposed for future 5G networks operating at millimeter-waves, along with highly-directive receiving antennas to suppress multipath reflections [123]. The realization of a circularly-polarized CTS antenna that preservers the key characteristics of parallel-fed CTS arrays (e.g. wideband operation, high scanning performance, passive beamforming and low-profile) would represent a disruptive technology for satellite and mobile applications. Cross-connected CTS antennas [34] and CTS antennas with subarrays of two slots excited by orthogonally-polarized fields [124] were proposed to achieve circular polarization. However, all these modifications to the parallel-fed CTS architecture result in a degradation of the antenna performance. Therefore, the combination of a CTS antenna with a flat linear-to-circular polarization (LP-to-CP) converter, placed in proximity to the radiating aperture, can offer the best trade-off between antenna performance, size and design complexity. In order to attain the performance of standard LP CTS arrays, the LP-to-CP converter should properly work and exhibit low insertion loss over a wide frequency range and for large incident angles [35, 49]. As discussed in Section 6.1, wideband LP-to-CP converters are typically based on stacks of several anisotropic sheets, i.e. dielectric layers with printed metal patterns that differently affect the propagation of orthogonal field components. The thickness of these polarizers and their distance from the radiating aperture have to be minimized since strict constraints on the height and on the weight of the antenna are required for many applications, and in particular for satellite communications on the move.

The bandwidth of state-of-the-art, thin polarizers rarely exceeds 40% for normal incidence and 25% for incident angles of about 30°. Moreover, their design heavily relies on multiparameter optimization and full-wave simulations. In Section 6.2, a novel high-pass unit cell that can be exploited in the design of wideband LP-to-CP converters is studied. The proposed configuration consists of three anisotropic inductive sheets, separated by two dielectric spacers. A systematic design procedure is described in Section 6.3. The dispersion curves for the two orthogonal components of the incident field are engineered to achieve a broadband, linear phase response. The design procedure maximizes the differential phase bandwidth. The parameters of the circuit models are derived using simple design equations. A design example with applications to Ka-band Satcom terminals is discussed in Section 6.4. First, the equivalent circuits are designed following the steps of the procedure outlined in Section 6.2. Then, a possible physical design of the polarizer, suitable for implementation in standard PCB technology, is presented and numerically validated. Fractional bandwidths larger than 48.5%, for incident angles up to 30°, are achieved. Conclusions are drawn in Section 6.5.

The work presented in this chapter was carried out in collaboration with Prof. A. Grbic at the University of Michigan.

6.1 Review of linear-to-circular polarization converters

An ideal LP-to-CP converter works as a quarter-wave plate [79], which shifts of 90° the phases of two perpendicular field components, without altering their amplitudes. The LP-to-CP converter can be modeled as an anisotropic slab with two orthogonal principal axes, namely x and y. The x- and y component of any incident electric field undergo different phase delays. Let us assume that the incident electric field $\mathbf{E^i}$ is linearly polarized in the xy-plane and forms a 45° angle with the x-axis of the converter, i.e.

$$\mathbf{E^i} = \frac{E_0^i}{\sqrt{2}}\,(\hat{x} + \hat{y}) \tag{6.1}$$

Assuming that the converter does not couple the field components parallel to the principal axes, the transmitted field at the output of the polarizer is given by

$$\mathbf{E^t} = E_x^t\,\hat{x} + E_y^t\,\hat{y} = \frac{E_0^i}{\sqrt{2}}\,(S_{21}^x\,\hat{x} + S_{21}^y\,\hat{y}) \tag{6.2}$$

where S_{21}^x and S_{21}^y are the transmission coefficients for the x- and the y-component of the incident field, respectively. A perfect LP-to-CP conversion is achieved if the output field fulfills the following conditions

$$|E_x^t| = |E_y^t| \tag{6.3}$$

$$|\angle E_x^t - \angle E_y^t| = \pi/2 \tag{6.4}$$

A useful figure of merit to evaluate the purity of the circular polarization of the output field is the axial ratio. It is defined as the ratio of the lengths of the major and minor axes of the polarization ellipse of $\mathbf{E^t}$ and can be expressed as [64]

$$AR = \frac{|E_x^t|^2 + |E_y^t|^2 + \sqrt{\gamma}}{|E_x^t|^2 + |E_y^t|^2 - \sqrt{\gamma}} \tag{6.5}$$

where the parameter γ is

$$\gamma = |E_x^t|^4 + |E_y^t|^4 + 2\,|E_x^t|^2\,|E_y^t|^2 \cos\left[2(\angle E_x^t - \angle E_y^t)\right] \tag{6.6}$$

For an ideal CP-wave, $AR = 1$. In general, a wave is considered circularly polarized when its axial ratio is less than 3 dB. However, values lower than 1 dB are often required for satellite communications. In order to assess the insertion loss, the global transmission coefficient T of the LP-to-CP converter is introduced

$$\mathrm{T} \equiv \frac{|\mathbf{E^t}|}{|\mathbf{E^i}|} = \frac{\sqrt{|S_{21}^x|^2 + |S_{21}^y|^2}}{\sqrt{2}} \tag{6.7}$$

In this context, the bandwidth of the polarizer is defined as the frequency range where the axial ratio is less than 3 dB and the magnitude of the transmission coefficient T is greater than −1 dB.

We focus on a specific class of LP-to-CP converters that can be integrated on the CTS antenna aperture with minimum encumbrance. These polarizers operate in transmission and have a planar multilayer structure, as illustrated in Fig. 6.1. The anisotropy required for the polarization conversion is achieved by realizing patterned metal layers on one or both sides of the dielectric substrates, using standard PCB processes. The building block of this converter is a dielectric slab with one or two anisotropic metal sheets. These sections can be bonded together, using adhesive layers.

LP-to-CP converters based on the configuration of Fig. 6.1 have been extensively studied [125–130]. A synthetic comparison of state-of-the-art devices is presented in Table 6.1. The designs achieving the widest 3-dB axial ratio bandwidths (about 50%) [125, 126] are electrically thick. Their thickness is often in the order of half the free-space wavelength (λ_0) at the central frequency [126, 131]. Thick profiles lead to an increase of the volume of the system which may be unacceptable for the applications, such as for ground terminals on trains. Moreover, the performance of a polarizer under oblique incidence, crucial for

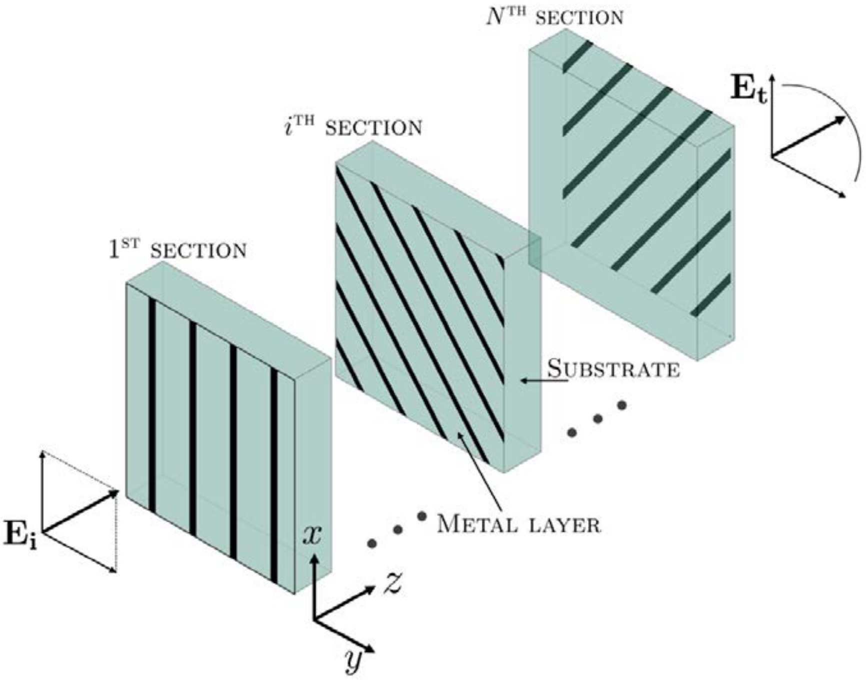

Figure 6.1: Exploded view of a multilayer LP-to-CP converter, with N sections. Each section comprises a substrate layer and one or two patterned metal layers.

Table 6.1: Comparison of state-of-the-art LP-to-CP converters.

Ref.	Central frequency	Thickness	Bandwidth ($AR < 3$dB, $\lvert\mathrm{T}\rvert > -1$ dB)	Oblique performance
[125]	Not available	$0.35\,\lambda_0$	46% ($AR < 2$ dB)	Not available
[126]	23.0 GHz	$0.50\,\lambda_0$	40% ($AR < 1.5$ dB)	Not available
[127]	88.5 GHz	$0.12\,\lambda_0$	26%	±30°
[128]	19.0 GHz	$0.25\,\lambda_0$	30%	±45°
[129]	9.5 GHz	$0.17\,\lambda_0$	32%	±30°

beam scanning systems, generally degrades with the thickness of the device. The fractional bandwidths reported for thinner polarizers [127–129] do not exceed 35%. A single-layer polarizer with a thickness of $0.02\lambda_0$ has been recently presented in [132], but it introduces an insertion loss greater than 2.5 dB in the operating band. The achieved axial ratio is between 1 dB and 3 dB in a 43%-relative bandwidth.

The design procedures are heavily based on multiparameter optimizations targeting the minimization of the insertion loss and of the axial ratio in given frequency ranges [130, 132]. The patterned metal sheets are often designed using meander lines, which exhibit inductive and capacitive behavior, respectively, for the two orthogonal components of the incident field. Compact, symmetrical structures with three sheets are proposed in [127] and [128].

First-order equivalent circuits are used in the design. Perfect transmission and a 90° phase shift between the field components are stipulated at the design frequency. However, the final susceptances and the phase delay experienced by each field component are not derived in closed form, but are determined through parametric studies.

A broadband converter realized with a miniaturized frequency selective surface (MFSS) is presented in [129]. The circuit models for the two orthogonal incident fields have the same topology. Their bandpass responses are shifted in frequency and are engineered to achieve wideband operation in the band where they overlap. The order of the response of the MFSS and the initial values of the circuit models are determined using filter theory. However, the 90° differential phase shift is achieved by tuning all elements with an optimization procedure.

This brief review of the state of the art reveals two main limitations in the design of LP-to-CP polarizer. First, the relative bandwidth of LP-to-CP converters with moderate thickness (about $0.25\,\lambda_0$) does not exceed 32% in a scan range of ±30°. Second, most design approaches rely on optimization routines that do no provide the physical insight needed to improve the performance. A novel configuration of LP-to-CP polarizers and a systematic design procedure are discussed in the next section to overcome both these issues.

6.2 A novel design concept for broadband, low-profile converters

An LP-to-CP converter has different frequency responses for the horizontal and vertical components of the incident wave. It can be modeled as the combination of two phase shifters, one for each field component, which provide two distinct delays. To a first approximation, these two circuits can be considered uncoupled. A proper design of the patterned metal sheets (see Fig. 6.1) can make reasonable this assumption. The approach here proposed seeks to manipulate the dispersion properties of the two equivalent phase shifters and achieve a wideband operation with a limited insertion loss.

An ultrawideband passive phase shifter design has been presented in [133,134]. It is based on an artificial negative refractive (NRI) index medium [135], realized by periodically loading a conventional transmission line (a microstrip line) with lumped series capacitors and shunt inductors. The unit cell of this metamaterial phase shifter is shown in Fig. 6.2. It has a high-pass response. The parameters of this unit cell can be designed so that the first stopband of its dispersion diagram is closed. In particular, the following relation must be fulfilled

$$Z_0 = \sqrt{\frac{L_0}{C_0}} \tag{6.8}$$

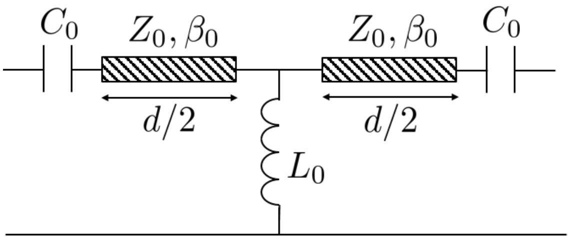

Figure 6.2: Unit cell of the passive phase shifter presented in [133].

where Z_0 is the characteristic impedance of the transmission line and L_0 and C_0 are, respectively, the inductance and capacitance of the lumped elements. When this condition is satisfied, the first and the second band of the dispersion diagram are continuous and a linear phase response can be achieved over a large bandwidth around the design frequency. The topology of Fig. 6.2 cannot be easily implemented using cascaded anisotropic impedance sheets. In particularly, it is hard to synthesize the series capacitances using the planar multilayer structure of Fig. 6.1.

A different high-pass configuration is thus investigated, which comprises only shunt elements. We focus on a class of polarizers whose unit cell can be modeled, under normal incidence, with the equivalent circuits shown in Fig. 6.3, for the two orthogonal components (E_x^i and E_y^i) of the incident field. This circuit can be realized using three inductive sheets separated by two dielectric layers, each of thickness $d/2$, as illustrated in Fig. 6.4. The sheet inductances seen by the x-component of the field are L_1^x and L_2^x, whereas the values seen by y-component are L_1^y and L_2^y. The network is symmetrical, so that the outer sheets

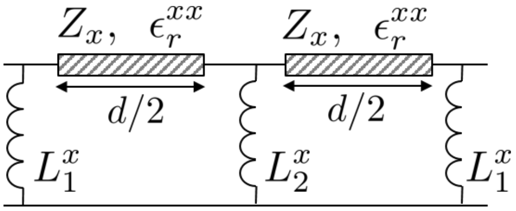

(a)

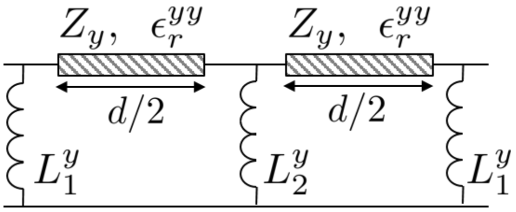

(b)

Figure 6.3: Circuit models for the design of the LP-to-CP converter under analysis, with three inductive sheets, for (a) an incident field polarized along the x-axis and (b) an incident field polarized along the y-axis.

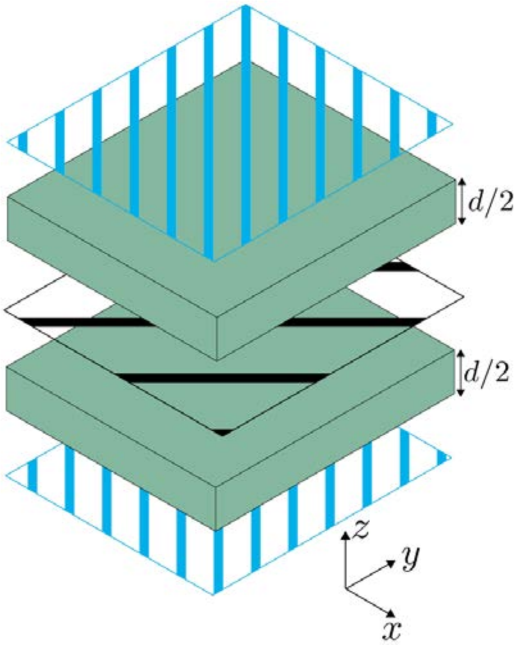

Figure 6.4: Proposed structure for the physical realization of the LP-to-CP polarizer described by the circuit models of Fig. 6.3. Three anisotropic sheets are interleaved by two dielectric spacers, each of thickness $d/2$ and with a relative permittivity ϵ_r. The outer sheets are identical.

are identical. The transmission lines are realized using dielectric slabs. However, different values of effective permittivity, ϵ_r^{xx} and ϵ_r^{yy}, are assumed for the two equivalent circuits. A method to achieve $\epsilon_r^{xx} \neq \epsilon_r^{yy}$ using isotropic dielectric spacers is presented in Section 6.3.

The transmission matrices of unit cells of Fig. 6.3, analyzed as a two-port networks, are computed in order to derive the dispersion relations of the polarizer. Since these circuits are topologically equal and differ only for the values of their parameters, we calculate the transmission matrix with reference to generic inductances L_1, L_2 and considering transmission lines with characteristic impedance Z_c and effective permittivity ϵ_r.

The network is lossless, reciprocal and symmetrical with respect to the central shunt inductor of inductance L_2. Therefore, the $ABCD$ parameters of the overall network can be computed using the transmission matrix of the series branch on the left, that comprises the shunt inductor (L_1) and the series transmission line section. In particular, the following relation holds [136]

$$\begin{bmatrix} A & B \\ C & D \end{bmatrix} = \begin{bmatrix} A_1 & B_1 \\ C_1 & D_1 \end{bmatrix} \begin{bmatrix} 1 & 0 \\ \dfrac{1}{j\omega L_2} & 0 \end{bmatrix} \begin{bmatrix} D_1 & B_1 \\ C_1 & A_1 \end{bmatrix} \tag{6.9}$$

where A_1, B_1, C_1, D_1 are the elements of the transmission matrix of the series branch, calculated below

$$\begin{aligned}\begin{bmatrix} A_1 & B_1 \\ C_1 & D_1 \end{bmatrix} &= \begin{bmatrix} 1 & 0 \\ \dfrac{1}{j\omega L_1} & 1 \end{bmatrix} \begin{bmatrix} \cos\left(\theta/2\right) & j\,Z_c\,\sin\left(\theta/2\right) \\ j\,\dfrac{1}{Z_c}\,\sin\left(\theta/2\right) & \cos\left(\theta/2\right) \end{bmatrix} \\ &= \begin{bmatrix} \cos\left(\theta/2\right) & j\,Z_c\,\sin\left(\theta/2\right) \\ -j\,\dfrac{\cos\left(\theta/2\right)}{\omega L_1} + j\,\dfrac{\sin\left(\theta/2\right)}{Z_c} & \dfrac{Z_c}{\omega\,L_1}\sin\left(\theta/2\right) + \cos\left(\theta/2\right) \end{bmatrix}\end{aligned} \tag{6.10}$$

where $\theta = \beta d$ is the electrical length of the unit cell and β is the propagation constant of the transmission lines. The overall transmission matrix is computed by substituting (6.9) into (6.10).

Assuming an infinitely periodic structure, the phase delay ϕ of the unit cell is given by [53]

$$\cos\phi = \frac{A + D}{2} \tag{6.11}$$

This relation also represents the dispersion equation of the structure. It further simplifies when the unit cell is symmetric ($A = D$), as in the case under analysis, yielding

$$\cos\phi = \cos\left(kd\right) = A \tag{6.12}$$

where k is commonly referred to as the Bloch wavenumber.

Given the symmetry of the unit cell, the dispersion relation can be derived without explicitly computing the value of A, using the formula [136]

$$\sin^2\left(\frac{\phi}{2}\right) = -B_1\left(C_1 + \frac{D_1\,Y}{2j\omega L_2}\right) \tag{6.13}$$

After substituting in (6.13) the matrix elements calculated in (6.10), the following dispersion equation is found

$$\sin^2\left(\frac{\phi}{2}\right) = -\frac{Z_c}{\omega}\left(\frac{1}{L_1} + \frac{1}{2\,L_2}\right)\sin\left(\frac{\theta}{2}\right)\cos\left(\frac{\theta}{2}\right) + \left(1 - \frac{Z_0^2}{2\omega^2 L_1 L_2}\right)\sin^2\left(\frac{\theta}{2}\right) \tag{6.14}$$

The dispersion diagram relative to a specific case is plotted in Fig. 6.5a. The values of the circuit parameters are listed in the caption. In general, a frequency stopband is observed for $\phi = \pi + 2l\pi$, with $l \in \mathbb{N}_0$. The cut-off angular frequencies $\overline{\omega_1}$ and $\overline{\omega_2}$, associated to this stopband, are found by analyzing the dispersion relation for $\phi = \pi + 2l\pi$. For these values of phase delay, (6.14) becomes

$$\cos^2\left(\frac{\theta}{2}\right) + \frac{Z_c}{\omega}\left(\frac{1}{L_1} + \frac{1}{2\,L_2}\right)\sin\left(\frac{\theta}{2}\right)\cos\left(\frac{\theta}{2}\right) + \frac{Z_0^2\,\sin^2\left(\frac{\theta}{2}\right)}{2\omega^2 L_1 L_2} = 0 \tag{6.15}$$

It is convenient to recast (6.15) by factorizing the left hand side in two terms

$$\left[\cos\frac{\theta}{2} + \frac{Z_c\,\sin(\theta/2)}{2\,L_2\,\omega}\right]\left[\cos\frac{\theta}{2} + \frac{Z_c\,\sin(\theta/2)}{\omega\,L_1}\right] = 0 \tag{6.16}$$

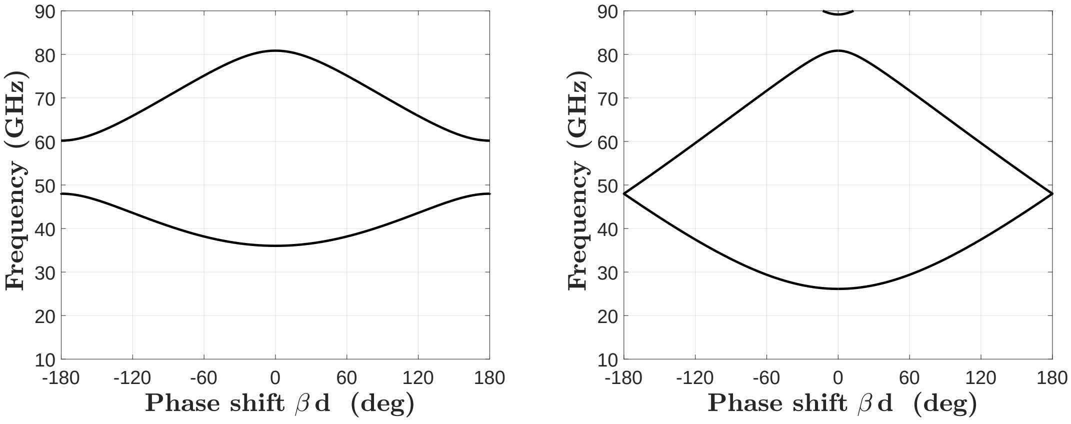

(a)

(b)

Figure 6.5: Dispersion diagram for a periodic structure with the unit cell of Fig. 6.3a and the following circuit parameters: $L_2^x = 1.39$ nH, $\epsilon_r = 2.2$ and (a) $L_1^x = 0.5\,L_2^x$ (a stopband appears for $\phi = \pi$); (b) $L_1^x = 2\,L_2^x$ (the stopband is closed).

The stopband disappears if the two factors admit the same zeros. In this case, the cut-off frequencies at $\phi = \pi + 2l\pi$ coincide. It is clear from (6.16) that the two factors and thus their zeros are equal if and only if the following condition is satisfied

$$L_1 = 2\,L_2 \tag{6.17}$$

The dispersion equation under this matching condition simplifies as follows

$$\cos^2\left(\frac{\phi}{2}\right) = \left[\cos\left(\frac{\theta}{2}\right) + \frac{Z_c}{2\,\omega\,L_2}\sin\left(\frac{\theta}{2}\right)\right]^2 \tag{6.18}$$

Figure 6.5b shows the dispersion diagram of a unit cell that fulfills (6.17). As for glide-symmetric structures [137,138], the closure of the stopband results in a potential linear phase response and wideband operation. Equation (6.17) also represents a matching condition for the unit cells of Fig. 6.3. Indeed, it can be easily demonstrated that when one port of the circuit is terminated on the characteristic impedance Z_c of the transmission line and the other port is excited by a generator with series impedance Z_c, the input reflection coefficient is null at the frequency ϖ for which the phase delay is π.

6.3 Design procedure

It has been shown that the dispersion curves of the high-pass cells of Fig. 6.3 can be engineered to eliminate the first stopband and achieve broadband operation. A rigorous procedure for the design of the equivalent circuits of the polarizer, for the two orthogonal components of the incident field, is outlined and discussed in this section. The dispersion curves are shaped by enforcing simple conditions, derived from physical arguments, in order to maximize the bandwidth, in terms of axial ratio and transmission coefficient. The procedure to determine the circuit parameters does not resort to optimization methods. It consists of the following steps:

1. the central frequency ω_0, the effective permittivity ϵ_r and the overall thickness d of the polarizer are arbitrarily set.
2. The condition 6.17 for the closure of the first stopband is enforced for both the equivalent circuits of Fig. 6.3, yielding
$$L_1^x = 2\,L_2^x \tag{6.19}$$
$$L_1^y = 2\,L_2^y \tag{6.20}$$
3. The matching condition for the circuit of Fig. 6.3b is stipulated at ω_0. At the same frequency, the differential phase shift $\phi_x - \phi_y$ between the two output field components circuits is set to $\pm\pi/2$ to get a right-handed or a left-handed circularly polarized wave, respectively. A $-\pi/2$-phase shift is here considered, yielding
$$\phi_x(\omega_0) = \pi/2 \tag{6.21}$$
$$\phi_y(\omega_0) = \pi \tag{6.22}$$
4. The slopes of the phase responses of the two circuits are equated at ω_0
$$\left.\frac{\partial \phi_x}{\partial \omega}\right|_{\omega_0} = \left.\frac{\partial \phi_y}{\partial \omega}\right|_{\omega_0} \tag{6.23}$$

Relations (6.19) and (6.20) are essential for achieving a wideband operation. A 90° differential phase shift between the orthogonal field components at the output of the polarizer is also necessary to attain the LP-to-CP conversion and is enforced by (6.21)-(6.22). However, the phase delays experienced by each field component can be arbitrarily chosen, provided that the absolute value of their difference is 90°. A 90° phase shift is stipulated by (6.21) for the x-polarized field component, which eases the derivation of an explicit expression for L_2^x. Indeed, equations (6.18) and (6.21) yield

$$L_2^x = \frac{1}{2\,\omega_0} \frac{Z_x \sin(\theta_x/2)}{\cos(\pi/4) - \cos(\theta_x/2)} \tag{6.24}$$

where $\theta_x = (\omega_0 \sqrt{\epsilon_r^{xx}}\, d)/c$. Condition (6.22) implies that a y-polarized field is perfectly transmitted through the LP-to-CP converter at the design frequency. By substituting (6.22) in (6.18) the following expression for L_2^y is found

$$L_2^y = -\frac{Z_y}{2\,\omega_0} \tan(\theta_y/2) \tag{6.25}$$

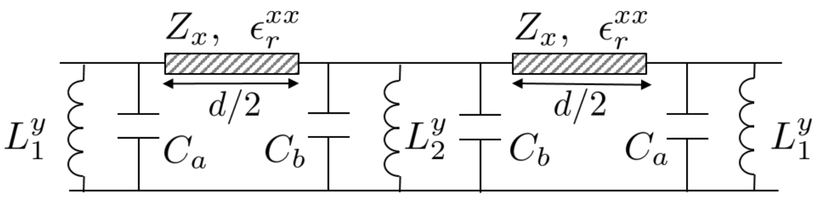

Figure 6.6: Modified equivalent circuit of the polarizer for incident y-polarized waves. The TLs of the model of Fig. 6.3b are replaced by TLs with characteristic impedances Z_x, loaded by the capacitances C_a and C_b.

where $\theta_y = (\omega_0 \sqrt{\epsilon_r^{yy}}\, d)/c$.

Equation (6.23) imposes that the slopes of the phase frequency responses are equal at the design frequency. In this way, the differential phase shift experiences small variations around 90°, i.e. the value specified at ω_0, in a wide band centered at the design frequency.

The five unknowns $L_1^x, L_2^x, L_1^y, L_2^y$ and ϵ_r^{yy} are determined using the five equations (6.19)-(6.23). In particular, once the input parameters of procedure (ω_0, ϵ_{rx} and d) are set, the value L_2^x is found. Note that equation (6.25) sets a minimum for the overall electrical thickness of polarizer. Indeed, the inductance L_2^y is positive and can be thus physically realized only if $\tan(\theta_y/2) < 0$. Therefore, the thickness d must be greater than half the wavelength in the dielectric of permittivity ϵ_r^{yy}, i.e.

$$d > \frac{\lambda_0}{2\sqrt{\epsilon_r^{yy}}} \tag{6.26}$$

The derivatives in (6.23) are easily found from (6.18). The derivative at the right hand side of (6.23) is a function of the relative permittivity ϵ_r^{yy}, while the right hand side is a scalar value. The value of ϵ_r^{yy} is determined by numerically solving (6.23). The inductance L_2^y is thus computed using (6.25). The values of L_1^x and L_1^y are calculated from (6.19) and (6.20).

Finally, one of the equivalent circuits of Fig. 6.3 must be modified in order to realize the converter using isotropic dielectric substrates, with the same relative permittivity along both x- and y-axis ($\epsilon_r = \epsilon_r^{xx} = \epsilon_r^{yy}$). Without loss of generality, let ϵ_r^{xx} be less than ϵ_r^{yy}. The transmission lines with higher relative effective permittivity ϵ_r^{yy} in the circuit of Fig. 6.3b can be replaced by transmission lines of the same length ($d/2$) and lower relative dielectric constant ϵ_r^{xx}, loaded by shunt capacitors C_a and C_b. Indeed, the additional capacitances increase the effective dielectric constant of the transmission lines and can be tuned to achieve a value close the original one, i.e. ϵ_r^{yy}. The final circuit model of the LP-to-CP converter for a y-polarized incident field is illustrated in Fig. 6.6.

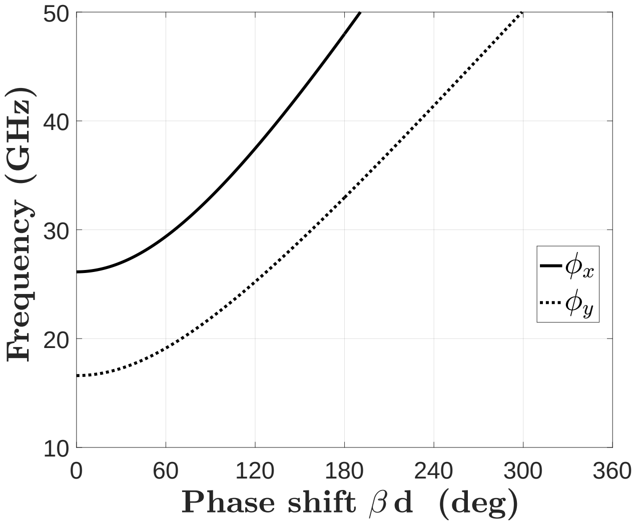

Figure 6.7: Dispersion diagrams of the unit cells of Fig. 6.3, relative to the proposed polarizer. The circuit parameters are: $d = 2.5$ mm, $\epsilon_r^{xx} = 2.2$, $\epsilon_r^{yy} = 4.41$, $L_1^x = 2.78$ nH, $L_1^y = 3.50$ nH, $L_2^x = 1.39$ nH, and $L_2^y = 1.75$ nH.

6.4 A wideband design for Ka-band applications

A design example is discussed to demonstrate the effectiveness of the models and of the design procedure described in the previous sections. The objective is the design of an LP-to-CP converter that achieves low insertion loss (< 1 dB) and high CP purity (< 3 dB) in the entire Ka-band (26.5-40 GHz). First, the parameters of the circuit models of Fig. 6.3a and Fig. 6.6 are determined. The performance of the polarizer based on this preliminary circuit design are evaluated. Then, a physical implementation of these models is presented. The proposed structure comprises three anisotropic sheets, separated by two isotropic dielectric slabs (see Fig. 6.4).

6.4.1 Preliminary design based on circuit models

As a first step of the design procedure outlined in Section 6.3, the input parameters of the design procedure are set. The design frequency is $f_0 = 33$ GHz. The relative dielectric constant of the substrate selected for the implementation of the polarizer is $\epsilon_r = \epsilon_r^{xx} = 2.2$, where ϵ_r^{xx} is the effective relative permittivity seen by the x-component of the incident field (see Fig. 6.3a). An overall thickness $d = 2.5$ mm $= 0.275\,\lambda_0$, being λ_0 the free-space wavelength at f_0, is chosen. The values $L_1^x = 2.78$ nH and $L_2^x = 1.39$ nH are obtained from (6.19) and (6.24). By solving (6.23), subject to conditions (6.19)-(6.22), the effective relative permittivity $\epsilon_r^{yy} = 4.41$ is found for the equivalent circuit associated of Fig. 6.3b. The inductances $L_1^y = 3.50$ nH and $L_2^y = 1.75$ nH are determined using (6.20) and (6.22).

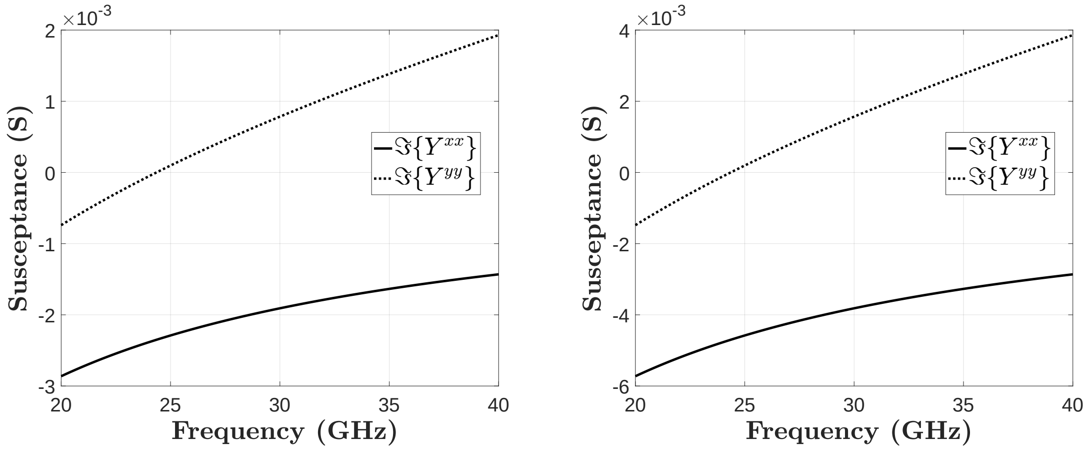

(a)

(b)

Figure 6.8: Admittance parameters of (a) the outer sheets and (b) the inner sheet, derived from the equivalent circuits of Fig 6.3a and Fig 6.6. The off-diagonal terms of the admittance matrices of the sheets are assumed nulls.

The dispersion relations of the equivalent circuits obtained for each polarization are shown in Fig. 6.7. The cut-off frequencies of these high-pass configurations are 26.6 GHz (circuit of Fig. 6.3a) and 16.6 GHz (circuit of Fig. 6.3b). In both cases, the first stopbands are closed. At the design frequency, the phase shit of the x and y components of the output field are $\pi/2$ and π, respectively, as prescribed by (6.21)-(6.22). The dispersion curves are quasi-linear, with similar slopes, in a wide frequency range centered at 33 GHz.

The designed of the final circuit model of Fig. 6.6, for an incident y-polarized field, is based on the parameters derived for the circuit of Fig. 6.3b. The capacitances are tuned in order to get a response as close as possible to that of the circuit in Fig. 6.3b, yielding $C_a = C_b = 12.2$ fF. The admittance parameters of the final anisotropic sheets are shown in Fig. 6.8. The sheets are purely inductive, as seen by an incident x-polarized field, whereas they are capacitive when shined by a y-polarized field, except at low frequencies, where the inductances dominate in the LC-tanks of Fig. 6.6. The frequency responses of the equivalent circuits relative to the x- and y-polarized components of the incident field are shown in Fig. 6.9 and in Fig. 6.10, respectively. The insertion losses of both circuits are less than 2 dB between 25 GHz and 40 GHz and are almost null around the central frequency. The cut-off frequency determines the drop of the amplitude of the transmission coefficient, relative to an x-polarized field (see Fig. 6.9a), at low frequencies. Figure 6.10 compares the frequency responses of the circuit featuring only shunt inductors (see Fig 6.3b) with that of the final circuit (see Fig. 6.6). The phase responses (see Fig. 6.10b) are almost identical between 20 GHz and 40 GHz. The final circuit exhibits a lower insertion loss.

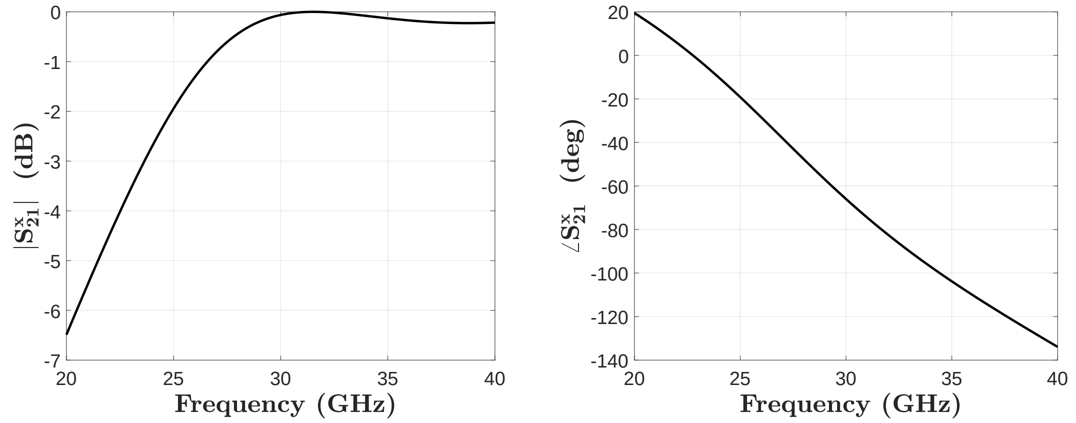

(a) (b)

Figure 6.9: Frequency response of the polarizer under analysis for an incident x-polarized field: (a) magnitude and (b) phase.

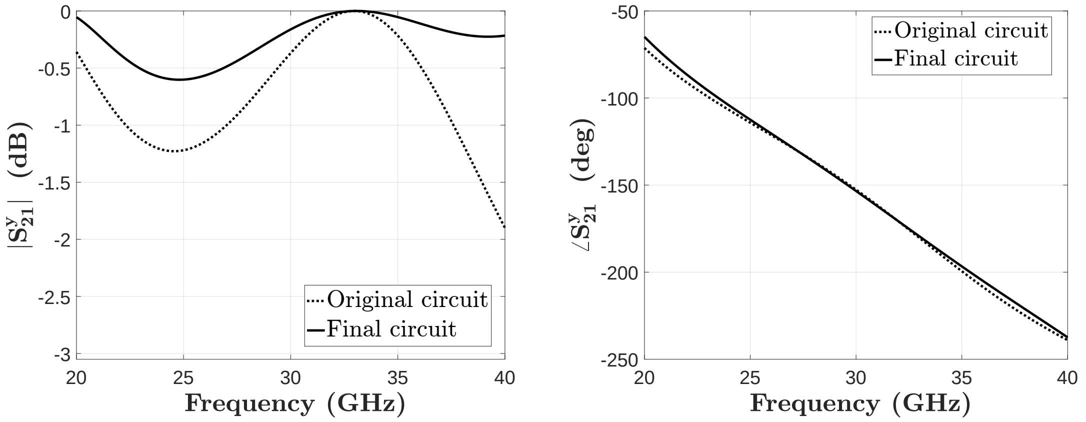

(a) (b)

Figure 6.10: Frequency response of the polarizer under analysis for an incident y-polarized field: (a) magnitude and (b) phase. The results obtained considering both the original circuit of Fig. 6.3b and the actual model of Fig. 6.6 are shown.

The purity of the CP is particularly sensitive to variations of the differential phase shift of the field components from $\pi/2$. The maximum deviation from this value is 9° for the final design, in the entire frequency range considered.

The transmission coefficient of the LP-to-CP converter is computed using (6.7) and plotted in Fig. 6.11. The values obtained by considering for the y-polarized field component the original circuit (see Fig. 6.3b) and the actual model (see Fig. 6.6) are shown. These results are very close between 20 GHz and 40 GHz. The actual insertion loss is less than 1 dB for frequencies greater than 25.7 GHz.

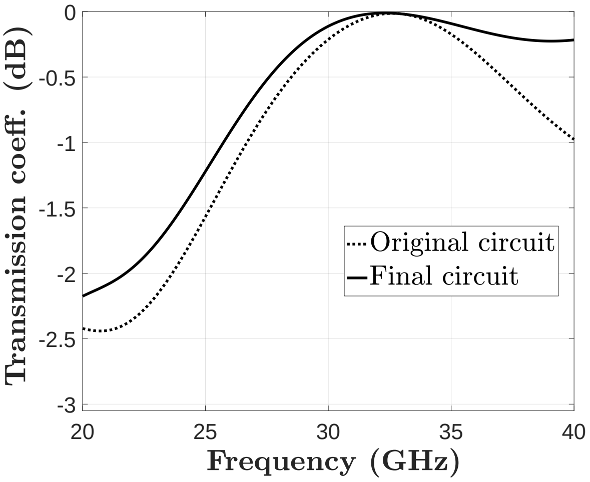

Figure 6.11: Transmission coefficient of the designed LP-to-CP converter. The input field is polarized along the direction $\hat{r} = \hat{x} + \hat{y}$ (see Fig. 6.4). The actual results are compared with those obtained when the circuit of Fig. 6.3b is considered for the y-polarized field component.

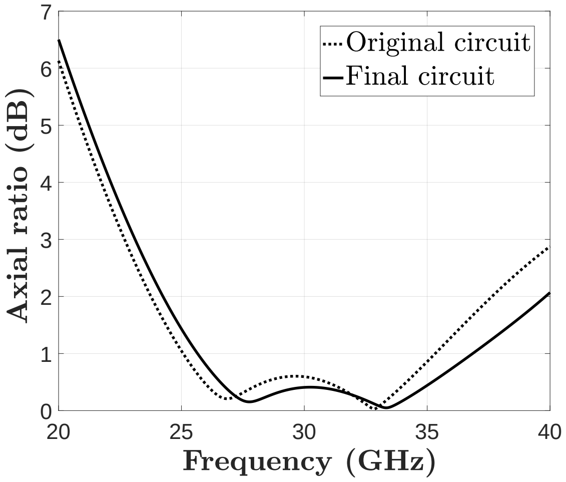

Figure 6.12: Axial ratio of the electric field at the output of the polarizer, as a function of frequency, for an incident field polarized along $\hat{r} = \hat{x} + \hat{y}$ (see Fig. 6.4). The final results are compared with those obtained when the circuit of Fig. 6.3b is considered for the y-polarized field component.

The axial ratios computed for the original and the final design are plotted versus frequency in Fig. 6.12. For the final design, the axial ratio is less than 3 dB between 22.7 GHz and 40 GHz, i.e. over a fractional bandwidth that exceeds 55%. Moreover, the axial ratio is less than 1 dB, as typically required for satellite communications, over a relative bandwidth of 34.2% (25 GHz - 35.3 GHz). It is worth to recall that the results presented so far are based on the circuit models and do not account for possible cross-polarization

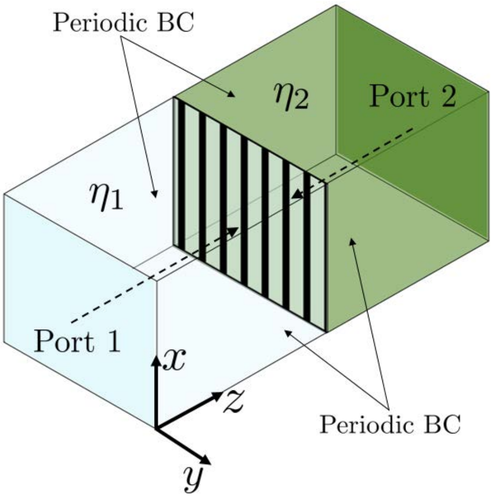

Figure 6.13: Simulation setup for the extraction of the sheet admittance parameters. The sheet is located between two media with wave impedances η_1 and η_2. Floquet ports, de-embedded to the positions of the sheets, excite normally incident waves.

effects. Nevertheless, they demonstrate a significant improvement over the state-of-the-art, for devices with thickness in the order of a quarter of the free-space wavelength.

Finally, note that better results are obtained using the modified circuit for the y-polarization, as compared to the original model with three shunt inductors. Indeed, the initial circuit models and the design procedure provide a systematic method to achieve a high performance, that can be, however, further improved by means of optimizations.

6.4.2 Physical design and simulation results

This section discusses possible ways to implement, at the physical level, the LP-to-CP converter designed in Section 6.4 using the proposed circuit approach. The first stack-up considered is similar to the one shown in Fig. 6.4. It ccomprises two dielectric substrates (Taconic TLY-5), each of thickness $d/2 = 1.27$ mm, relative permittivity $\epsilon_r = 2.2$ and loss tangent $\tan\delta = 9\times10^{-4}$. The first substrate has patterned metal layers on both sides, while the third sheet is realized on one side of the second substrate. An adhesive layer (Taconic Fast-Rise 27, $\epsilon_{rp} = 2.7$, $\tan\delta_p = 1.7\times10^{-3}$) of thickness $t = 0.08$ mm is employed to bond the two substrates. The overall thickness of the polarizer is 2.62 mm $\approx 0.28\lambda_0$. Copper metal sheets are considered, with conductivity $\sigma = 5.8\times10^7$ S.

The metal patterns of the sheets were designed to fit the values of the shunt admittances of both the equivalent circuits, under normal incidence, between 25 GHz and 40 GHz. The shapes and the geometrical parameters of the sheets were determined by means of full-wave simulations in Ansys HFSS. The unit cell of each anisotropic sheet was excited using the simulation setup illustrated in Fig. 6.13. Periodic boundary conditions were assumed at the

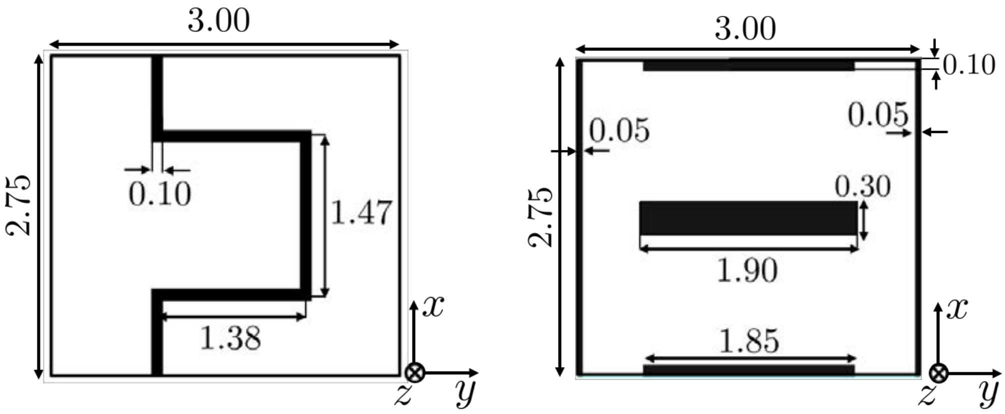

(a) (b)

Figure 6.14: Geometry of the unit cell of (a) the outer sheets and of (b) the inner sheet of the designed circular polarizer. Dimensions are in millimeters.

sides of the unit cell. The admittance matrix $\underline{\underline{Y_s}}$ of the sheet is obtained from the scattering parameters, using the following formula [139]

$$\begin{aligned}\underline{\underline{Y_s}} &= \left[\frac{1}{\eta_1}\left(\underline{\underline{I}} - \underline{\underline{S_{11}}}\right) - \frac{1}{\eta_2}\left(\underline{\underline{I}} + \underline{\underline{S_{11}}}\right)\right]\left(\underline{\underline{I}} + \underline{\underline{S_{11}}}\right)^{-1} \\ &= \left[\frac{1}{\eta_2}\left(\underline{\underline{I}} - \underline{\underline{S_{22}}}\right) - \frac{1}{\eta_1}\left(\underline{\underline{I}} + \underline{\underline{S_{22}}}\right)\right]\left(\underline{\underline{I}} + \underline{\underline{S_{22}}}\right)^{-1}\end{aligned} \tag{6.27}$$

where $\underline{\underline{I}}$ is the identity matrix, $\underline{\underline{S_{11}}}$ and $\underline{\underline{S_{22}}}$ are the matrices of the reflection coefficients at the two ports, η_1 and η_2 are the wave impedances of the media in the two half-spaces delimited by the sheet.

According to the circuit models of Fig. 6.3, a shunt inductance along the x-axis and an LC-tank along the y-axis must be implemented. However, this inevitably leads to crossing metal patterns. It was observed that crossing metal lines, and in particular crossing inductances, introduce non-negligible coupling effects between the two field components, that are not accounted by the circuit model. Moreover, crossing lines may define, under oblique incidence, electrically long paths for the currents which can cause resonant phenomena, limiting the scanning performance of the LP-to-CP converter. Therefore, the sheets were designed avoiding intersections among the metal lines. As a result, the equivalent circuits of the actual sheets are slightly different from the models used in the circuit design. The unit cells of outer and inner sheets are shown in Fig. 6.14. The size of the unit cell is 3.00 mm × 2.75 mm, i.e. $0.32\,\lambda_0 \times 0.28\,\lambda_0$, where λ_0 is the free-space wavelength at the design frequency. The outer sheets can be modeled as an inductance along the x-axis and a shunt admittance comprising a capacitance and an inductance in series, along the y-axis. The inner sheet act as an LC-tank for x-polarized fields and as a parallel of LC series resonators for y-polarized fields. The patterns were optimized to achieve the best match of

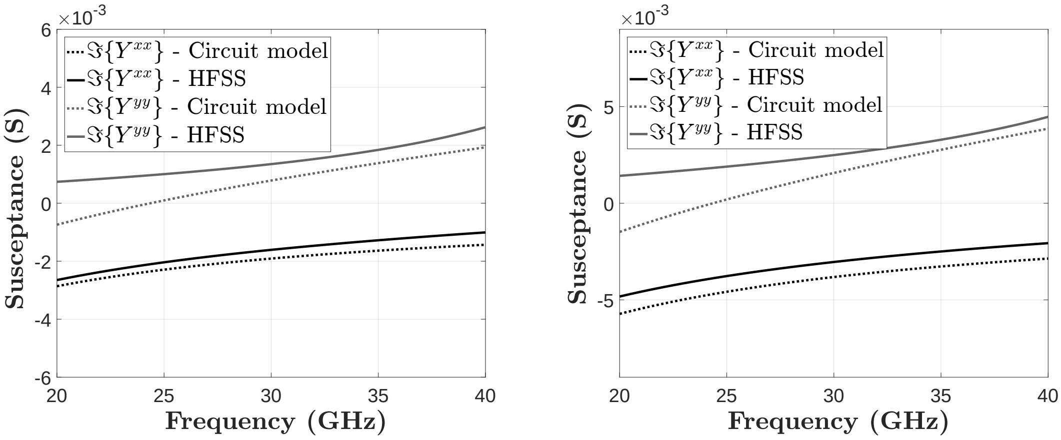

(a) (b)

Figure 6.15: Admittance parameters, along the principal axes, of (a) the outer sheets and of (b) the inner sheet, under normal incidence. The results obtained for the actual patterned sheets are compared with the targeted values, determined using the circuit-based design procedure.

their frequency responses with the targeted ones. The admittances of the patterned metal sheets, along both principal axes, are shown in Fig. 6.14 under normal incidence. They are compared with the reference values derived from the design procedure. The sheet admittances are close to the targeted inductances when an incident x-polarized field is considered (see the values of Y^{xx} in Fig. 6.15). By contrast, the sheet admittances along the y-axis do not correctly map the desired circuit parameters for frequencies lower than 26 GHz. Nevertheless, the frequency behaviours of the designed sheets are in reasonable agreement with those targeted, between 26 GHz and 40 GHz.

The 2 × 2 transmission matrix $\underline{\underline{S_{21}}}$ of the polarizer, for a incident wave polarized in the xy-plane, can be written in the following form

$$\underline{\underline{S_{21}}} = \begin{bmatrix} S_{21}^{xx} & S_{21}^{xy} \\ S_{21}^{yx} & S_{21}^{yy} \end{bmatrix} \tag{6.28}$$

This matrix was extracted from a full-wave simulation of the unit cell of the overall designed structure, comprising three sheets, two substrates and an adhesive layer. In particular, the off-diagonal elements S_{21}^{xy} and S_{21}^{yx} could be evaluated. They quantify the coupling effects between the orthogonal components of the incident field. Due to the design of the patterned sheets, they are much lower, in amplitude, than the diagonal terms and thus have a limited impact on the performance. Nevertheless, the full matrix was used to compute

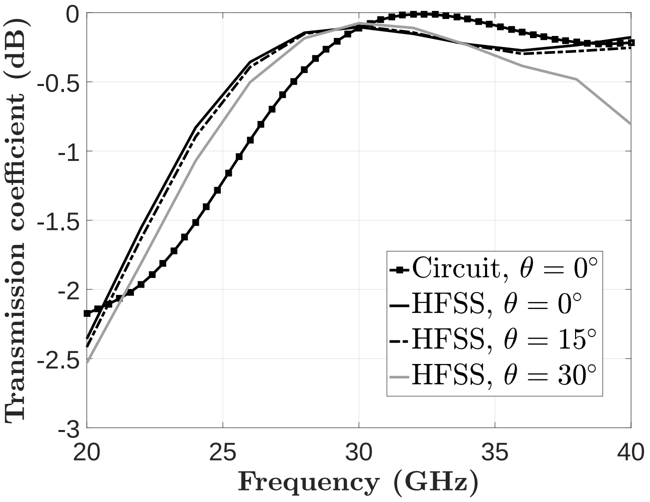

Figure 6.16: Magnitude of the simulated transmission coefficient of the designed LP-to-CP converter, when shined by an electric field polarized along the direction $\hat{r} = \hat{x} + \hat{y}$ (see Fig. 6.14). Several angles θ of incidence in the rz-plane are considered. The values obtained from the circuit design for normal incidence are shown as well.

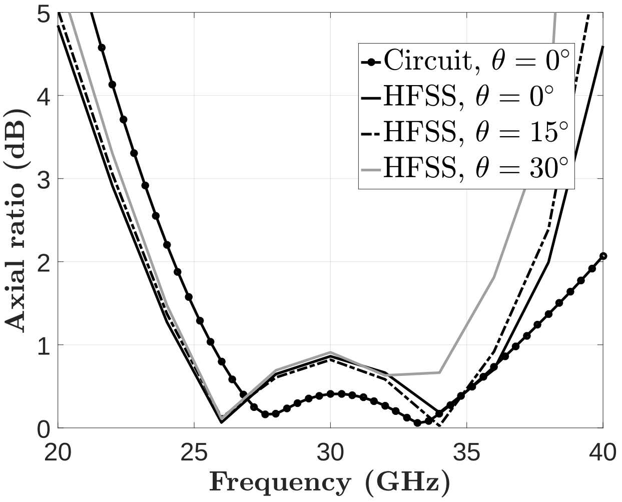

Figure 6.17: Simulated axial ratio when the designed LP-to-CP converted is shined by an electric field polarized along the direction $\hat{r} = \hat{x} + \hat{y}$ (see Fig. 6.14). Several angles θ of incidence in the rz-plane are considered. The axial ratio obtained from the circuit design for normal incidence is shown as well.

the transmitted $\mathbf{E_t}$ field that is given by

$$\begin{aligned} \mathbf{E_t} &= \underline{\underline{S_{21}}}\mathbf{E_i} = \frac{E_0}{\sqrt{2}}\,\underline{\underline{S_{21}}}\,(\hat{x} + \hat{y}) \\ &= \frac{E_0}{\sqrt{2}}\,\left[\left(S_{21}^{xx} + S_{21}^{xy}\right)\hat{x} + \left(S_{21}^{yy} + S_{21}^{yx}\right)\hat{y}\right] \end{aligned} \tag{6.29}$$

The axial ratio of the output field and the transmission coefficient were calculated using the definitions in (6.5)-(6.7), based on the expression of the transmitted field given in (6.29). The computed transmission coefficient of the LP-to-CP converter is shown in Fig. 6.16 for an incident electric field polarized along the direction $\hat{r} = \hat{x} + \hat{y}$ (see Fig. 6.14). Several angles of incidence θ in the rz-plane are considered. The insertion loss is less than 1 dB from 24 GHz to 40 GHz, for incident angles up to $\theta = 30°$.
The axial ratio of the output field is plotted in Fig. 6.17, considering the same input field and the same incident angles assumed for the evaluation of the transmission coefficient. The simulated 3-dB axial ratio bandwidth, under normal incidence, spans from 21.5 GHz to 39 GHz, which corresponds to a 57.85%-fractional bandwidth. The performance is rather stable under oblique incidence: the relative bandwidth for $\theta = 30°$ is 48.5%. These results demonstrate the effectiveness of the proposed circuit models and of the simple design procedure outlined in Section 6.3 to achieve a broadband operation and low losses.

The final results exhibit some differences with those targeted in the design procedure (see dotted lines in Fig. 6.16 and Fig. 6.17), such as a shift of the central frequency of about 2 GHz. These discrepancies do not affect the validity of the design procedure and the achievement of wideband performance. They can be significantly reduced by increasing the accuracy of the synthesis of the circuit parameters. The choice of avoiding intersecting lines in the design of the sheet patterns reduces the cross-coupling and prevents the onset of resonances. However, it hinders the achievement of the desired circuit parameters.

The accuracy of the synthesis can be improved without resorting to complex sheet designs by patterning both the top and the bottom face of an electrically thin substrate. In this way, the circuit elements required for the two orthogonal polarizations can be decoupled and realized in separate metal layers. Being thin, the dielectric substrate interposed between the two metal layers does not significantly affect the performance. Based on this concept, an alternative stack-up for the designed LP-to-CP converter is presented in Fig. 6.18. Each anisotropic sheet is realized using two patterned metal layers and a substrate layer of thickness ($h \ll \lambda_0/\sqrt{\epsilon_r}$). For each sheet, the inductances along the principal axes are implemented on different metal layers, so that there are no intersecting lines. As compared to the previous structure, two additional substrate layers of thickness h and two more adhesive layers of thickness t are needed. The constraints on t and h can be met, for designs in Ka-band, using commercially available materials. In particular, 0.127 mm-thick Taconic TLY-5 panels can be used for the additional substrates, so that $h = d/20$, along with adhesive layer Taconic FastRise 27, of thickness 0.08 mm. The total thickness of the LP-to-CP converter, based on the stack-up of Fig. 6.18 and on these parameters is about 3 mm, i.e. a third of the free-space wavelength at the design frequency. The implementation

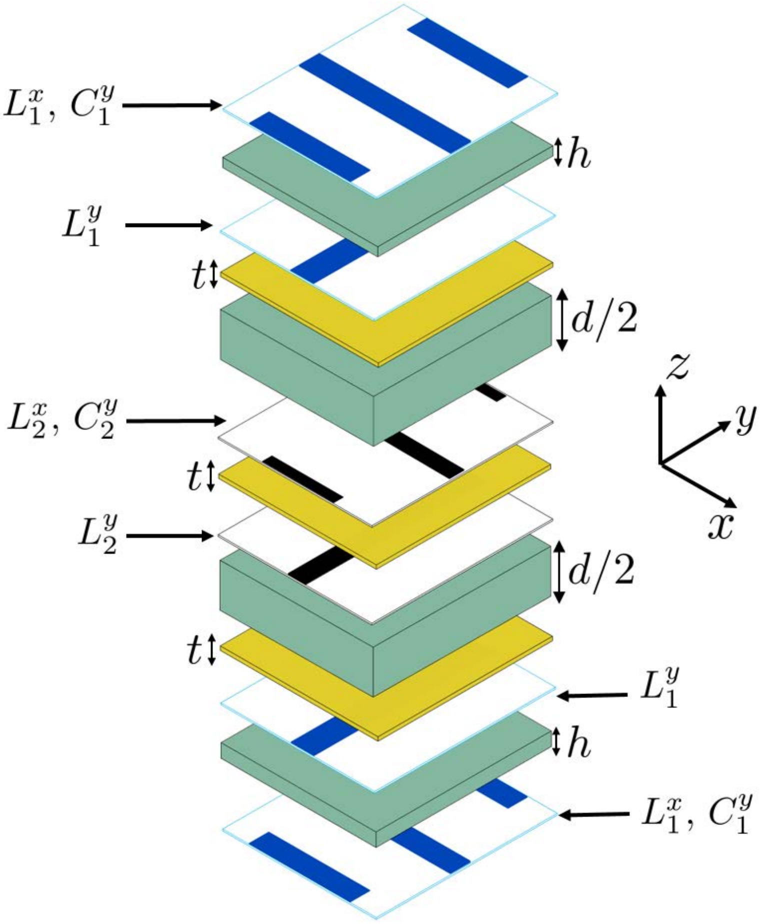

Figure 6.18: Alternative stack-up for the LP-to-CP converter. Each anisotropic sheet is realized with two metal layers and an electrically thin substrate ($h \ll \lambda_0/\sqrt{\epsilon_r}$). Thin adhesive layers are used to bond the substrate layers.

and characterization of a polarizer with the stack-up shown in Fig. 6.18 may be a subject of future work.

6.5 Conclusion

The combination of standard CTS arrays and planar multilayer LP-to-CP converters, placed in proximity to the radiating aperture, have been proposed as a simple and effective solution to realize circularly-polarized CTS antennas, with the minimum design effort. The overall system should preserve the wideband, wide-angle scanning performance of linearly-polarized CTS array. To this end, a novel approach for the design of low-profile LP-to-CP converters, with operating bandwidths in the order of 50% and stable performance under oblique incidence, has been presented. Polarizers based on three anisotropic sheets, interleaved by two dielectric spacers, have been considered to minimize the encumbrance. Novel high-pass phase-shifting cells are introduced to model the frequency responses of the polarizer to the orthogonal components of an incident field. A systematic design procedure has been presented to determine the parameters of the equivalent circuits. Broadband differential phase bandwidths are achieved by closing the stopband of the dispersion diagrams of the circuit models and equating the phase slopes at the design frequency. A physical structure that can be easily realized in PCB technology has been proposed to implement the preliminary circuit-based, targeting Ka-band applications. As per simulations, the insertion loss is less than 1 dB and, at the same time, the axial ratio of the transmitted field is less than 3 dB over a 50% relative bandwidth (24-40 GHz). Bandwidths larger than 48.5% are achieved for incident angles up to 30°. The overall thickness of the device is about 0.28 λ_0, where λ_0 is the free-space wavelength at the central frequency. The achieved performance represents a significant advance over state-of-the-art devices. Moreover, the proposed design procedure is innovative and efficient, as compared to the approaches presented in the literature, which heavily rely on optimization techniques.

Chapter 7

Conclusions

The main results and the novel contributions presented in this work are summarized in this chapter. Some topics requiring further investigation are highlighted. Finally, possible directions for future researches are outlined.

7.1 Summary and novel contributions

The main objective of this thesis was to propose and investigate a compact antenna solution that could achieve a broadband, wide-angle scanning performance at millimeter waves, enabling massive and high-speed data transfer for satellite and mobile communications. In particular, multibeam antennas based on passive beamformers were targeted in order to avoid the complexity and the power consumption of phased arrays. Parallel-fed continuous transverse stub (CTS) arrays were considered since their active impedances can be designed to be nearly frequency-independent over a multioctave bandwidth and stable over a wide field of view in the H-plane. Moreover, these arrays have a planar structure, robust to fabrication tolerances. As opposed to competing planar array antennas, they comprise a one-dimensional array of long slots which result in a simpler feed network. The reference architecture studied and developed in this work is based on the design of the multibeam CTS antenna for Ka-band Satcom applications, presented in Chapter 2. It comprises an array of long slots fed by a nearly non-dispersive corporate feed network, realized with PPWs, and a quasi-optical beamformer which includes a pillbox coupler, illuminated by an integrated horn.

7.1.1 Methods for the analysis and design of the proposed CTS antenna

Since most CTS antennas are protected by patents, only a few details about their design and the techniques used for their analysis are available. This work proposed novel numerical models that enable a fast evaluation of the antenna performance.

A mode matching procedure, based on a spectral Green's function approach, was proposed in Chapter 3 to compute the active impedance of the radiating slots, in an infinite array environment, in presence of a planar layered dielectric medium above the antenna aperture. This procedure is fast converging and accurate for any scan angle in the principal planes and for all frequencies that ensure a pure TEM excitation of the slots. A circuit representation of the array was derived from the expression obtained for the active impedance. This expression was expanded in several terms and a specific physical meaning was attributed to each of them. A method to evaluate the radiation patterns of the array in the principal planes, neglecting the impact of the corporate feed network, was proposed. It relies on the computation of the field at the output of the pillbox coupler, which is performed using tools of geometrical and physical optics, developed for the analysis of the quasi-optical system.

Scan blindness phenomena were investigated using the procedure for the computation of the active impedance. This analysis had as objective the assessment of the relations between the array parameters and the onset of radiation nulls. It emerges that if the array spacing d is equal to the free-space wavelength λ_0, a radiation null appears at broadside and moves to larger scan angles in the H-plane as the frequency increases or for larger values of d. A configuration with a single-layer dielectric cover above the slots was extensively studied, since it models CTS antennas loaded by matching layers or polarization converters. When the thickness of the cover is about a quarter of the dielectric wavelength, blind angles can appear for $\lambda_0/2 < d < \lambda_0$. A correlation between the radiation nulls and the radiation angles of leaky-waves supported by the array structure was demonstrated.

Numerical methods for the analysis of the corporate feed network and for the evaluation of the input reflection coefficient, when the CTS array radiates at broadside, were presented in Chapter 4. The building blocks of the PPW networks, e.g. T-junctions, bends and steps, were modeled using equivalent circuits reported in the literature and novel *ad-hoc* numerical procedures. In particular, a mode matching analysis of a 90° PPW E-plane bend with a square step was proposed. A numerical code for the evaluation of the scattering parameters of a 1-to-N feed network, for any N, was developed, by properly cascading the transmission matrices computed for each building block. This code has been effectively combined with the procedure for the computation of the active impedance of the array, presented in Chapter 3, to predict the input reflection coefficient of a broadside CTS array.

A software tool embedding the proposed numerical procedures was developed for the French Space Agency (CNES). It allows the user to define the geometry of a parallel-fed CTS array and to analyze the matching and radiation performance.

7.1.2 Substrate integrated CTS antennas in LTCC technology

A key objective of this work was the development of technological solutions to realize flat CTS antennas, with high scanning performance, suitable for highly-integrated systems-in-package at mm-waves. The results of this research axis were reported in Chapter 5. Novel design and fabrication approaches were proposed to make feasible and effective the integration of parallel-fed CTS antennas in multilayer dielectric substrates. A quasi-TEM waveguide, realized by means of parallel rows of vias, distributed in one or several layers, was introduced to replace vertical PPWs with continuous metal plates, whose implementation is prohibitive using planar technologies.

Two CTS antenna systems, operating at 60 GHz, were fabricated using LTCC technology, which was selected as the most mature for manufacturing complex multilayer structures. First, a fixed beam CTS antenna, with 4 radiating slots, comprising 18 LTCC tapes, was presented to validate the design and the technology. The measured impedance bandwidth exceeds 25%, the peak gain is 14.25 dB. Side lobe levels lower than -17.5 dB and an average antenna efficiency of 46% were achieved between 50 GHz and 66 GHz.

Based on the same technology, an integrated switched-beam antenna for 5G access points was developed. The main design goal was the simultaneous achievement of low SLLs and high beam overlap levels over a scan range wider than ±30°. This objective was accomplished by co-integrating two CTS arrays, each of 8 slots, that generate interleaved beams and are activated, one at a time, by a switch network, designed on the bottom of the LTCC module. The antenna covers a field of view of ±38° using 11 beams, with measured crossing levels of about -3 dB and SLLs lower than -17 dB between 57 GHz and 66 GHz. The scan losses are always less than 3 dB. Neglecting the losses of the switch network, the simulated peak gain is 20.15 dBi. The antenna has a thickness of about 3 mm and comprises 16 LTCC tapes.

7.1.3 Low-profile, wideband linear-to-circular polarization converters

The combination of a standard, linearly-polarized CTS antenna and a planar linear-to-circular polarization converters was proposed to achieve a low-profile circularly-polarized CTS antenna. The frequency behaviour and the scanning performance of the overall system mainly depends on the polarizer, which is usually the component with the narrowest bandwidth. A novel approach for the design of compact polarizers achieving high performance over a relative bandwidth of 50% was presented in Chapter 6. A structure based on three anisotropic sheets and two dielectric slabs was proposed. The design procedure engineers the dispersion properties of two simple high-pass cells, modeling the polarizer when shined by orthogonal linearly-polarized fields, so that a broadband polarization conversion and low insertion losses are achieved. A practical design for Ka-band applications that can be easily implemented in PCB technology was presented. Its thickness is about a quarter of the free-space wavelength. As per simulations, the axial ratio of the field at the output of the device is less than 3 dB and the insertion loss is less than 1 dB over a bandwidth of 48.5%, for incident angles up to 30° . The polarizer is suitable for integration with the Ka-band CTS antenna presented in Chapter 2.

7.2 Future work

In this section, we point out some aspects of this work that could be strengthened or further developed in future researches.

The active impedance of the slot array was computed in Chapter 3 under the hypotheses of infinite array and infinite length of the slots. It has been observed through the thesis that this approach provides accurate results when the array comprises eight or more slots, of length greater than five times the free-space wavelength. It has been also noted that negligible edge effects are observed in the proposed CTS antenna, due to the tapered excitation in the H-plane. However, a rigorous model for the analysis of finite CTS arrays could provide a quantitative insight on these effects and a useful tool for the design of small arrays.

The study of the scan blindness and of the effects of the array parameters on the onset of blind angles, presented in Chapter 3, were based on the computation of the active reflection coefficient. Rigorous or approximated formulas that express the position of the radiation null as a function of the array parameters can enable an *a-priori* estimation of the blind angles. A more in-depth analysis of the physics behind the scan blindness in the H-plane could ease the derivation of these formulas.

The numerical tools for the analysis of the corporate feed network (see Chapter 4) were developed assuming a normal wavefront impinging on the network, i.e. for a broadside radiation. These models can be easily extended to the case of tilted incident waves, in order to estimate the input reflection coefficient when the antenna beam is steered.

The design and implementation of substrate integrated CTS antennas are fields yet to be investigated, even though significant advances were presented in this thesis. First, a systematic study of the proposed substrate integrated parallel-plate waveguide (SI-PPW) is necessary to optimize the design. The dispersion characteristics and the losses of a SI-PPW should be derived as functions of the geometrical and electromagnetic parameters. In particular, the impact of the vias spacing should be assessed in order to reduce the number of vias employed.

The limits of the LTCC technology for the fabrication of CTS arrays could be further investigated. In particular, the yield of the process as a function of the number of stacked tapes should be determined, in order to design larger arrays and achieve higher gain values. The suitability of LTCC technology for designs at higher frequencies, e.g. in the E- and W-band, should be experimentally confirmed.

The assembly technique proposed in [50] could enable an effective realization of parallel-fed CTS arrays in multilayer PCB technology, using substrates with low dielectric constants. The antenna performance that can be achieved with this solution and the fabrication costs should be assessed and compared to the results presented in this thesis, relative to implementations in LTCC technology.

The switched-beam antenna described in Chapter 5 could be re-designed to achieve a higher realized gain, to improve the input matching and to reduce the amplitude imbalance of the switch network. In particular, a more accurate design of the switch network is required and amplifiers should be integrated to compensate the losses of the switches. Optimized designs of the reflectors of the pillbox systems could be used to shape the radiated beams.

Finally, the wideband linear-to-circular polarization converter discussed in Chapter 6 must be fabricated and characterized to validate the proposed design procedure. The approach presented to avoid resonances under oblique incidence should be followed for the final design.

The polarizer should be first characterized as a self-standing device and then associated to a linearly-polarized CTS array in Ka-band, e.g. the one presented in Chapter 2 and in [47], to verify the performance of the overall system. The circuit models developed for the linearly-polarized CTS antenna and for the polarizer could be combined to allow for a fast and efficient co-design of circularly-polarized CTS antennas. In this perspective, the impact of the distance between the radiating aperture and the polarizer on the accuracy of the models must be assessed.

Appendices

Appendix A

Complements on the analysis of the array of slots

This appendix includes additional details about the mathematical derivations relative to the numerical model presented in Section 3.1.1 for the analysis of the slot array.

A.1 Coefficients in the general expressions of the guided fields in a PPW

The mathematical expressions of the transverse component of the electric and magnetic fields guided in a PPW are given, respectively, in (3.4) and (3.5). The scalar coefficients b_m^{TE}, b_m^{TM}, c_m^{TE} and c_m^{TM}, for $m \in \mathbb{N}_0$, can be written as follows

$$b_m^{TE} = \frac{\sqrt{\nu_m} j k_{y0}\, Y_m^{TE}}{\sqrt{a}\sqrt{k_{y0}^2 + (m\pi/a)^2}}, \tag{A.1}$$

$$b_m^{TM} = \frac{\sqrt{\nu_m} m\pi/a\, Y_m^{TM}}{\sqrt{a}\sqrt{k_{y0}^2 + (m\pi/a)^2}} \tag{A.2}$$

$$c_m^{TE} = \frac{\sqrt{\nu_m} m\pi/a\, Y_m^{TE}}{\sqrt{a}\sqrt{k_{y0}^2 + (m\pi/a)^2}}, \tag{A.3}$$

$$c_m^{TM} = \frac{\sqrt{\nu_m} j k_{y0}\, Y_m^{TM}}{\sqrt{a}\sqrt{k_{y0}^2 + (m\pi/a)^2}} \tag{A.4}$$

A.2 Derivation of the transmitted magnetic field $\mathbf{H}^{\mathbf{t}}$

The transverse component $\mathbf{H}^{\mathbf{t}}$ of the magnetic field on the aperture plane $z = 0$ is found by solving the convolution integral (3.13). The expression of the magnetic current $\mathbf{M}_{\mathbf{n}}$ in the spatial domain is found by substituting (3.4) into (3.11)-(3.12), yielding

$$\begin{aligned}\mathbf{M_n}(x,y,0) = &\sum_{m=0}^{+\infty}\sum_{n=-\infty}^{+\infty}\sqrt{\frac{\nu_m}{a}}\frac{m\pi/aV_m^{TM} - jk_{y0}V_m^{TE}}{\sqrt{k_{y0}^2+(m\pi/a)^2}}\cdot\\ &\times\cos\left[\frac{m\pi}{a}(x-nd)\right]\operatorname{rect}\left[\frac{x-a/2-nd}{a}\right]e^{-jk_{x0}nd}e^{-jk_{y0}y}\,\hat{y}\\ &+\sqrt{\frac{2}{a}}\sum_{m=0}^{+\infty}\sum_{n=-\infty}^{+\infty}\frac{jk_{y0}V_m^{TM} - m\pi/aV_m^{TE}}{\sqrt{k_{y0}^2+(m\pi/a)^2}}\cdot\\ &\times\sin\left[\frac{m\pi}{a}(x-nd)\right]\operatorname{rect}\left[\frac{x-a/2-nd}{a}\right]e^{-jk_{x0}nd}e^{-jk_{y0}y}\hat{x}\end{aligned} \tag{A.5}$$

The Fourier transforms $\tilde{M}_x$ and $\tilde{M}_y$ of the x and the y components of the magnetic current $\mathbf{M_n}$ are given by

$$\begin{aligned}\tilde{M}_x(k_x,k_y) = &\frac{4\pi^2}{d}\delta(k_y-k_{y0})\sqrt{\frac{2}{a}}\sum_{m=0}^{+\infty}\frac{jk_{y0}V_m^{TM} - m\pi/aV_m^{TE}}{\sqrt{k_{y0}^2+(m\pi/a)^2}}\\ &\times\sum_{n=-\infty}^{+\infty}\delta(k_x-k_{xn})\Gamma(k_{xn},m)\end{aligned} \tag{A.6}$$

$$\begin{aligned}\tilde{M}_y(k_x,k_y) = &\frac{4\pi^2}{d}\delta(k_y-k_{y0})\sum_{m=0}^{+\infty}\sqrt{\frac{\nu_m}{a}}\frac{-jk_{y0}V_m^{TE} + m\pi/aV_m^{TM}}{\sqrt{k_{y0}^2+(m\pi/a)^2}}\\ &\sum_{n=-\infty}^{+\infty}\delta(k_x-k_{xn})\Lambda(k_{xn},m)\end{aligned} \tag{A.7}$$

In order to derive these expressions from (A.5), the Poisson's summation formula

$$\sum_{n=-\infty}^{\infty}e^{jk_xnd} = \frac{2\pi}{d}\sum_{n=-\infty}^{\infty}\delta\left(k_x-\frac{2\pi n}{d}\right) \tag{A.8}$$

has been used.

By taking the Fourier transform of both sides of (3.13), the two following scalar equations may be obtained, for each the x and y components of the magnetic field

$$\tilde{H}_x^t(k_x,k_y) = \tilde{G}_{xx}^{HM}\tilde{M}_x + \tilde{G}_{xy}^{HM}\tilde{M}_y \tag{A.9}$$

$$\tilde{H}_y^t(k_x,k_y) = \tilde{G}_{yx}^{HM}\tilde{M}_x + \tilde{G}_{yy}^{HM}\tilde{M}_y \tag{A.10}$$

where $\tilde{G}_{xx}^{HM}$, $\tilde{G}_{xy}^{HM} = \tilde{G}_{yx}^{HM}$, and $\tilde{G}_{xx}^{HM}$ are entries of the spectral Green's dyad $\underline{\underline{G}}^{HM}$ for the half space $z > 0$, whose expression are given in [59].

Finally, the expressions for H_x and H_y, given in (3.14) and (3.14), respectively, are found using (A.6)-(A.7) and taking the inverse Fourier transform of both sides of (A.9) and (A.10). In this context, the inverse Fourier transform $g(x,y)$ of a function $\tilde{g}(k_x,k_y)$ is defined as

$$g(x,y) = \frac{1}{4\pi^2}\int_{\mathbb{R}^2}\tilde{g}(k_x,k_y)e^{-jk_xx}\,e^{-jk_yy}\,dk_xdk_y. \tag{A.11}$$

A.3 Elements of the matrices in (3.23)

The unknown expansion coefficients V_p^{TE}, with $p = 0, 1, \dots, M-1$ and V_q^{TM}, with $q = 1, \dots, M-1$, are found by solving the matrix equation (3.23). Explicit expressions for the elements of the block matrices that appear in (3.23) are here reported.

The elements of the $M \times M$ matrix $\underline{\underline{Y}}^{TE,TE}$ are

$$\begin{aligned} Y_{ij}^{TE,TE} &= -\frac{b_j^{TE}}{Y_j^{TE} d} \sum_{n=-N_f}^{N_f} \Lambda_j(k_{xn}) \Lambda_i(-k_{xn}) \tilde{G}_{yy}^{HM}(k_{xn}, k_{y0}) \\ &- \frac{c_j^{TE}}{Y_j^{TE} d} \sum_{n=-N_f}^{N_f} \Gamma_j(k_{xn}) \Lambda_i(-k_{xn}) \tilde{G}_{yx}^{HM}(k_{xn}, k_{y0}) + \frac{a}{\nu_j} b_j^{TE} \delta_{ij} \end{aligned} \tag{A.12}$$

for $i = 0, 1, \dots M-1$, $j = 0, 1, \dots M-1$.

The elements of the $M \times M-1$ matrix $\underline{\underline{Y}}^{TE,TM}$ can be written as

$$\begin{aligned} Y_{ij}^{TE,TM} &= \frac{b_j^{TM}}{Y_j^{TM} d} \sum_{n=-N_f}^{N_f} \Lambda_j(k_{xn}) \Lambda_i(-k_{xn}) \tilde{G}_{yy}^{HM}(k_{xn}, k_{y0}) \\ &- \frac{a}{2} b_j^{TM} \delta_{ij} + \frac{c_j^{TM}}{Y_j^{TM} d} \sum_{n=-N_f}^{N_f} \Gamma_j(k_{xn}) \Lambda_i(-k_{xn}) \tilde{G}_{yx}^{HM}(k_{xn}, k_{y0}) \end{aligned} \tag{A.13}$$

for $i = 0, 1, \dots M-1$, $j = 1, 2 \dots M-1$.

The elements of the $M-1 \times M$ matrix $\underline{\underline{Y}}^{TM,TE}$ are given by

$$\begin{aligned} Y_{ij}^{TM,TE} &= -\frac{c_j^{TE}}{Y_j^{TE} d} \sum_{n=-N_f}^{N_f} \Gamma_j(k_{xn}) \Gamma_i(-k_{xn}) \tilde{G}_{xx}^{HM}(k_{xn}, k_{y0}) \\ &- \frac{b_j^{TE}}{Y_j^{TE} d} \sum_{n=-N_f}^{N_f} \Lambda_j(k_{xn}) \Gamma_i(-k_{xn}) \tilde{G}_{xy}^{HM}(k_{xn}, k_{y0}) + \frac{a}{2} c_j^{TE} \delta_{ij} \end{aligned} \tag{A.14}$$

for $i = 1, 2 \dots M-1$, $j = 0, 1, \dots M-1$. Finally, the elements of the $M-1 \times M-1$ matrix $\underline{\underline{Y}}^{TM,TM}$ are

$$\begin{aligned} Y_{ij}^{TM,TM} &= \frac{b_j^{TM}}{Y_j^{TM} d} \sum_{n=-N_f}^{N_f} \Lambda_j(k_{xn}) \Gamma_i(-k_{xn}) \tilde{G}_{xy}^{HM}(k_{xn}, k_{y0}) \\ &- \frac{a}{2} \delta_{ij} c_i^{TM} + \frac{c_j^{TM}}{d Y_j^{TM}} \sum_{n=-N_f}^{N_f} \Gamma_j(k_{xn}) \Gamma_i(-k_{xn}) \tilde{G}_{xx}^{HM}(k_{xn}, k_{y0}) \end{aligned} \tag{A.15}$$

for $i = 1, 2 \dots M-1$, $j = 1, 2 \dots M-1$.

In the previous formulas, δ_{ij} indicates the Kronecker delta function, that is 1 for $i = j$ and is null elsewhere.

Appendix B

Complements on the analysis of the compensated right-angle bend

In this appendix, the expressions of the TM eigenmodes of a parallel plate region bounded by a PEC and a PMC plate are rigorously derived. These modes are used as basis functions to expand the fields in Region 2 of the structure of Fig. 4.14b. Moreover, explicit expressions for the elements of the matrices $\underline{\underline{M}}^{\mathrm{I,II}}$ in (4.25) are given.

B.1 TM modes in a parallel plate region delimited by a PEC and a PMC

We rigorously derive the expressions of the TM eigenmodes in an infinite region delimited by two parallel planes: one is a PEC, the other a PMC. The cross section of this structure is uniform and is shown in Fig. B.1. It includes a PEC plate on the plane $y = 0$ and a PMC plate on the plane $z = h$. The direction of propagation is x.

Maxwell's equations can be transversalized with respect to the x-axis, using Marcuvitz-Schwinger's formulation [59]. By doing so, the TM fields supported by the structure can be found as solutions of the following scalar eigenvalue problem with Dirichlet boundary conditions

$$\nabla_t^2 \phi + k_t^2 \phi = 0 \tag{B.1}$$

$$\phi|_{y=0} = 0 \tag{B.2}$$

$$(\hat{y} \times \nabla_t \phi)\Big|_{y=h} = 0; \tag{B.3}$$

where ϕ is the scalar potential, $k_t = \sqrt{k_y^2 + k_z^2}$ is the transverse wavenumber and the operator $\nabla_t = \nabla - \frac{\partial}{\partial z}\hat{x}$ has been introduced. Relations (B.2) and (B.3) stipulate, respectively, that the tangential component of electric field is null on the plane $y = 0$, and that the tangential magnetic field vanishes for $y = h$. If only the discrete spectrum of the operator

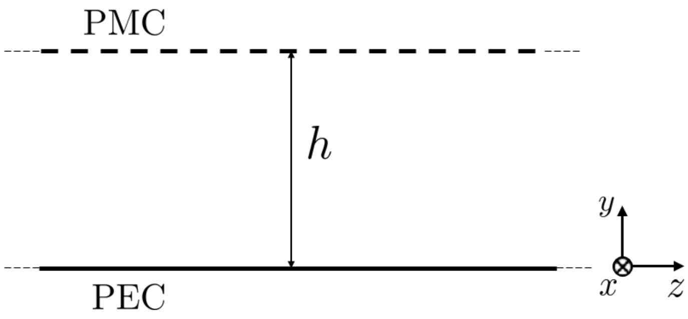

Figure B.1: Cross section of the waveguide under analysis and reference system.

$\nabla_t + k_t^2$ is considered, it can be assumed that the potential is a function of the only variable y, i.e. the scalar function $\phi(y,z) = \phi(z)$ and $k_t = k_y$. The general solution of (B.1), under these hypotheses is

$$\phi(y) = c_1 \cos k_y y + c_2 \sin k_y y \tag{B.4}$$

where $c_1, c_2 \in \mathbb{C}$. Conditions (B.2) and (B.3) yield, respectively

$$c_1 = 0 \tag{B.5}$$

$$k_{yn} = \frac{\pi(2n+1)}{2h}, \qquad n \in \mathbb{N}_0 \tag{B.6}$$

Therefore, the transverse mode functions [59] $\mathbf{e_n}$ and $\mathbf{h_n}$, for electric and magnetic field are

$$\mathbf{e_n}(y) = -\frac{1}{k_t}\nabla_t\phi = a_n \cos\left[\frac{\pi(2n+1)}{2h}y\right]\hat{y} \tag{B.7}$$

$$\mathbf{h_n}(y) = \hat{x} \times \mathbf{e_n} = a_n \cos\left[\frac{\pi(2n+1)}{2h}y\right]\hat{z} \tag{B.8}$$

where $a_n = -c_{2n}k_{yn}$, with $n \in \mathbb{N}_0$. The constants a_n can be determined by enforcing the orthornormality of the eigenfunctions $\mathbf{e_n}$ and $\mathbf{h_n}$.

Finally, the complete expression for the transverse components of the TM electric and magnetic fields can be written as follows

$$\mathbf{E_t} = \sum_{n=0}^{+\infty} V_n(x)\,\mathbf{e_n}\,e^{-jk_{xn}x} = \sum_{n=0}^{+\infty} V_n(x)\cos\left[\frac{\pi(2n+1)}{2h}y\right]\,e^{-jk_{xn}x}\;\hat{y} \tag{B.9}$$

$$\mathbf{H_t} = \sum_{n=0}^{+\infty} I_n(x)\,\mathbf{h_n}\,e^{-jk_{xn}x} = \sum_{n=0}^{+\infty} I_n(x)\cos\left[\frac{\pi(2n+1)}{2h}y\right]\,e^{-jk_{xn}x}\;\hat{z} \tag{B.10}$$

where V_n and I_n are the scalar mode functions [59].

B.2 Explicit expressions of the matrices in (4.25)

The elements of the $2N_1 \times 2N_1$-matrix $\underline{\underline{M}}^{\mathrm{I}}$ in the system of differential equations (4.25), that models the auxiliary problem defined in Fig 4.14a, are found using (4.21) and (4.22).

This matrix can be written in block form, as follows

$$\underline{\underline{M}}^{\mathrm{I}} = \begin{pmatrix} \underline{\underline{A}}^{\mathrm{I}} & \underline{\underline{B}}^{\mathrm{I}} \\ \\ \underline{\underline{C}}^{\mathrm{I}} & \underline{\underline{D}}^{\mathrm{I}} \end{pmatrix} \tag{B.11}$$

The expressions of the elements of the $N_1 \times N_1$-matrices $\underline{\underline{A}}^{\mathrm{I}}$ and $\underline{\underline{B}}^{\mathrm{I}}$ are derived from (4.21), yielding

$$A^{\mathrm{I}}_{11} = \frac{1}{h(x)} \tag{B.12}$$

$$A^{\mathrm{I}}_{1n} = 0, \quad n = 2, 3, \ldots, N_1 \tag{B.13}$$

$$A^{\mathrm{I}}_{m1} = (-1)^{m-1} \frac{2}{h(x)}, \quad m = 2, 3, \ldots, N_1 \tag{B.14}$$

$$A^{\mathrm{I}}_{mm} = \frac{3}{2h(x)}, \quad m = 2, 3, \ldots, N_1 \tag{B.15}$$

$$A^{\mathrm{I}}_{mn} = -\frac{2\,(-1)^{m+n-2}\,(m-1)^2}{\left[(n-1)^2 - (m-1)^2\right] h(x)}, \quad m \neq n,\; m, n = 2, 3, \ldots, N_1 \tag{B.16}$$

$$B^{\mathrm{I}}_{mm} = -j\omega\mu \left[1 - \frac{(m-1)^2\,\pi^2}{k^2 h^2(x)}\right], \quad m = 1, 2, \ldots, N_1 \tag{B.17}$$

$$B^{\mathrm{I}}_{mn} = 0 \quad m \neq n,\; m, n = 2, 3, \ldots, N_1 \tag{B.18}$$

The $N_1 \times N_1$ diagonal matrix $\underline{\underline{C}}^{\mathrm{I}}$ is found using (4.22) and can be written as

$$\underline{\underline{C}}^{\mathrm{I}} = -j\omega\epsilon\, \underline{\underline{I}}_{N_1} \tag{B.19}$$

where $\underline{\underline{I}}_{N_1}$ is the $N_1 \times N_1$ identity matrix.
The elements of the $N_1 \times N_1$-matrix $\underline{\underline{D}}^{\mathrm{I}}$ are derived from (4.22) and can be expressed as

$$D^{\mathrm{I}}_{m,1} = 0, \quad m = 1, 2, \ldots, N_1 \tag{B.20}$$

$$D^{\mathrm{I}}_{1,n} = \frac{(-1)^n}{h(x)} \quad n = 2, 3, \ldots, N_1 \tag{B.21}$$

$$D^{\mathrm{I}}_{m,m} = -\frac{1}{2h(x)} \quad m = 2, 3, \ldots, N_1 \tag{B.22}$$

$$D^{\mathrm{I}}_{m,n} = -2\,\frac{(-1)^{n+m}}{h(x)}\,\frac{(n-1)^2}{(n-1)^2 - (m-1)^2}, \quad m \neq n,\; m, n = 2, 3, \ldots, N_1 \tag{B.23}$$

The $2N_2 \times 2N_2$-matrix $\underline{\underline{M}}^{\mathrm{II}}$ in the system of differential equations (4.25), for the auxiliary problem defined in Fig 4.14b, are derived from (4.21) and (4.22) and can be written in block form, as follows

$$\underline{\underline{M}}^{\mathrm{II}} = \begin{pmatrix} \underline{\underline{A}}^{\mathrm{II}} & \underline{\underline{B}}^{\mathrm{II}} \\ \\ \underline{\underline{C}}^{\mathrm{II}} & \underline{\underline{D}}^{\mathrm{II}} \end{pmatrix} \tag{B.24}$$

The expressions of the elements of the $N_2 \times N_2$-matrices $\underline{\underline{A}}^{\mathrm{II}}$ and $\underline{\underline{B}}^{\mathrm{II}}$ are found from (4.23) and can be written as follows

$$A^{\mathrm{II}}_{mm} = \frac{1}{2h(x)}, \quad m = 1, 2, \ldots, N_2 \tag{B.25}$$

$$A^{\mathrm{II}}_{mn} = \frac{(-1)^{m+n}\,(2n-1)}{2(m+n-1)\,h(x)} - \frac{(-1)^{n-m}\,(2n-1)}{2(n-m)\,h(x)}, \quad m \neq n,\ m, n = 1, 2, \ldots, N_2 \tag{B.26}$$

$$B^{\mathrm{II}}_{mm} = -j\omega\mu \left[1 - \frac{(2m-1)^2\,\pi^2}{k^2 h^2(x)}\right], \quad m = 1, 2, \ldots, N_2 \tag{B.27}$$

$$B^{\mathrm{II}}_{mn} = 0 \quad m \neq n,\ m, n = 1, 2, \ldots, N_2 \tag{B.28}$$

The $N_2 \times N_2$ diagonal matrix $\underline{\underline{C}}^{\mathrm{II}}$ is found from (4.22) and is given by

$$\underline{\underline{C}}^{\mathrm{II}} = -j\omega\epsilon\,\underline{\underline{I}}_{N_2} \tag{B.29}$$

where $\underline{\underline{I}}_{N_2}$ is the $N_2 \times N_2$ identity matrix.

The $N_2 \times N_2$-matrix $\underline{\underline{D}}^{\mathrm{II}}$ is derived from (4.24) and its elements can be written as follows

$$D^{\mathrm{II}}_{mm} = \frac{1}{h(x)}, \quad m = 1, 2, \ldots, N_2 \tag{B.30}$$

$$D^{\mathrm{II}}_{mn} = -\frac{(-1)^{m+n}\,(2n-1)\,(2m-1)}{2\,(m+n-1)\,(n-m)\,h(x)}, \quad m \neq n,\ m, n = 1, 2, \ldots, N_2 \tag{B.31}$$

Bibliography

[1] T. Rossi, M. De Sanctis, M. Ruggieri, C. Riva, L. Luini, G. Codispoti, E. Russo, and G. Parca, "Satellite communication and propagation experiments through the Alphasat Q/V band Aldo Paraboni technology demonstration payload," *IEEE Aerosp. Electron. Syst. Mag.*, vol. 31, no. 3, pp. 18–27, Mar. 2016.

[2] C. Dehos, J. L. González, A. De Domenico, D. Kténas, and L. Dussopt, "Millimeter-wave access and backhauling: the solution to the exponential data traffic increase in 5G mobile communications systems?" *IEEE Commun. Mag.*, vol. 52, no. 9, pp. 88–95, Sept. 2014.

[3] European Union Seventh Framework Programme "MiWaveS". Beyond 2020 heterogeneous wireless network with mmw small cells. [Online]. Available: http://www.miwaves.eu

[4] M. Pierpoint and G. M. Rebeiz, "Paving the way for 5G realization and mmWave communication systems," *Microw. J.*, vol. 59, no. 4, pp. 106–112, Apr. 2016.

[5] D. H. Schaubert, A. O. Boryssenko, A. van Ardenne, J. G. B. de Vaate, and C. Craeye, "The Square Kilometer Array (SKA) antenna," in *Proc. IEEE Int. Symp. Phased Array Syst. Technol.*, Oct. 2003, pp. 351–358.

[6] T. Nakagawa, "Observations of the universe in the terahertz range: from AKARI to SPICA," *IEEE Trans. Terahertz Sci. Technol.*, vol. 5, no. 6, pp. 1133–1139, Nov. 2015.

[7] R. Dybdal, *Communication satellite antennas: system architecture, technology, and evaluation.* McGraw-Hill, 2009.

[8] H. Bayer, A. Krauss, T. Zaiczek, R. Stephan, O. Enge-Rosenblatt, and M. A. Hein, "Ka-band user terminal antennas for satellite communications," *IEEE Antennas Propagat. Mag.*, vol. 58, no. 1, pp. 76–88, Feb. 2016.

[9] S. Reynolds, A. Valdes-Garcia, B. Floyd, T. Beukema, B. Gaucher, D. Liu, N. Hoivik, and B. Orner, “Second generation 60-GHz transceiver chipset supporting multiple modulations at Gb/s data rates,” in *Proc. IEEE Bipolar/BiCMOS Circ. and Techn. Meeting*, Sept. 2007, pp. 192–197.

[10] J. M. Gilbert, C. H. Doan, S. Emami, and C. B. Shung, “A 4-Gbps uncompressed wireless HD A/V transceiver chipset,” *IEEE Micro*, vol. 28, no. 2, pp. 56–64, Mar. 2008.

[11] D. H. Schaubert, “Radiation characteristics of linearly tapered slot antennas,” in *Proc. IEEE Antennas Propag. Soc. Int. Symp.*, June 1989, pp. 1324–1327.

[12] D. T. McGrath, N. Schuneman, T. H. Shively, and J. Irion, “Polarization properties of scanning arrays,” in *Proc. IEEE Int. Symp. Phased Array Syst. Technol.*, Oct. 2003, pp. 295–299.

[13] L. Diamond, “Ka-band user terminal antennas,” in *34th ESA Antenna Workshop and 2nd Evolutions Satellite Telecommun. Ground Segments Workshop on Satcom User Terminal Antennas*, Oct. 2012.

[14] H. Bayer, A. Krauss, R. Stephan, and M. A. Hein, “Compact Ka-band Cassegrain antenna with multimode monopulse tracking feed for Satcom-on-the-move applications,” in *Proc. 10th Eur. Conf. Antennas Propag.*, Apr. 2016, pp. 1–5.

[15] C. Hua, X. Wu, N. Yang, and W. Wu, “Air-filled parallel-plate cylindrical modified Luneberg lens antenna for multiple-beam scanning at millimeter-wave frequencies,” *IEEE Trans. Microw. Theory Techn.*, vol. 61, no. 1, pp. 436–443, Jan. 2013.

[16] N. T. Nguyen, A. V. Boriskin, L. Le Coq, and R. Sauleau, “Improvement of the scanning performance of the extended hemispherical integrated lens antenna using a double lens focusing system,” *IEEE Trans. Antennas Propag.*, vol. 64, no. 8, pp. 3698–3702, Aug. 2016.

[17] A. Artemenko, A. Mozharovskiy, A. Maltsev, R. Maslennikov, A. Sevastyanov, and V. Ssorin, “Experimental characterization of E-band two-dimensional electronically beam-steerable integrated lens antennas,” *IEEE Antennas Wireless Propag. Lett.*, vol. 12, pp. 1188–1191, 2013.

[18] R. B. Waterhouse, “Design and performance of large phased arrays of aperture stacked patches,” *IEEE Trans. Antennas Propag.*, vol. 49, no. 2, pp. 292–297, Feb. 2001.

[19] L. Infante, S. Mosca, and M. Teglia, “Low-profile wide-band wide-angle-scan antenna array element,” in *Proc. 6th Eur. Conf. Antennas Propag.*, Mar. 2012, pp. 638–642.

[20] M. H. Awida, A. H. Kamel, and A. E. Fathy, “Analysis and design of wide-scan angle wide-band phased arrays of substrate-integrated cavity-backed patches,” *IEEE Trans. Antennas Propag.*, vol. 61, no. 6, pp. 3034–3041, June 2013.

[21] R. C. Hansen, “Linear connected arrays,” *IEEE Antennas Wireless Propag. Lett.*, vol. 3, no. 1, pp. 154–156, Dec. 2004.

[22] A. Neto and J. J. Lee, “Ultrawide-band properties of long slot arrays,” *IEEE Trans. Antennas Propag.*, vol. 54, no. 2, pp. 534–543, Feb. 2006.

[23] D. Cavallo, “Connected array antennas,” Ph.D. dissertation, Eindhoven University of Technology, Eindhoven, The Netherlands, 2011.

[24] J. P. Doane, K. Sertel, and J. L. Volakis, “A wideband, wide scanning tightly coupled dipole array with integrated balun (TCDA-IB),” *IEEE Trans. Antennas Propag.*, vol. 61, no. 9, pp. 4538–4548, Sept. 2013.

[25] H. Moody, “The systematic design of the Butler matrix,” *IEEE Trans. Antennas Propag.*, vol. 12, no. 6, pp. 786–788, Nov. 1964.

[26] W. Rotman, “Wide-angle scanning with microwave double-layer pillboxes,” *IRE Trans. Antennas Propag.*, vol. 6, no. 1, pp. 96–105, January 1958.

[27] V. Mazzola and J. E. Becker, “Coupler-type bend for pillbox antennas,” *IEEE Trans. Microw. Theory Techn.*, vol. 15, no. 8, pp. 462–468, Aug. 1967.

[28] R. V. Gatti, L. Marcaccioli, E. Sbarra, and R. Sorrentino, “Flat array antenna for Ku-band mobile satellite terminals,” in *Proc. 5th Eur. Conf. Antennas Propag.*, Apr. 2011, pp. 2618–2622.

[29] M. Tripodi, F. D. Marca, T. Cadili, C. Mollura, F. D. Maggio, and M. Russo, “Ka band active phased array antenna system for satellite communication on the move terminal,” in *Proc. 5th Eur. Conf. Antennas Propag.*, Apr. 2011, pp. 2628–2630.

[30] K. Tekkouk, J. Hirokawa, R. Sauleau, M. Ettorre, M. Sano, and M. Ando, “Dual-layer ridged waveguide slot array fed by a Butler matrix with sidelobe control in the 60-GHz band,” *IEEE Trans. Antennas Propag.*, vol. 63, no. 9, pp. 3857–3867, Sept. 2015.

[31] Y. J. Cheng, W. Hong, K. Wu, Z. Q. Kuai, C. Yu, J. X. Chen, J. Y. Zhou, and H. J. Tang, “Substrate integrated waveguide (SIW) Rotman lens and its Ka-band multibeam array antenna applications,” *IEEE Trans. Antennas Propag.*, vol. 56, no. 8, pp. 2504–2513, Aug. 2008.

[32] K. Tekkouk, M. Ettorre, E. Gandini, and R. Sauleau, “Multibeam pillbox antenna with low sidelobe level and high-beam crossover in SIW technology using the split aperture decoupling method,” *IEEE Trans. Antennas Propag.*, vol. 63, no. 11, pp. 5209–5215, Nov. 2015.

[33] W. W. Milroy, “The continuous transverse stub (CTS) array: basic theory, experiment, and application,” in *Proc. Antenna Appl. Symp.*, vol. 2, Sept. 1991, pp. 253–283.

[34] ——, “Continuous transverse stub element devices and methods of making same,” U.S. Patent 5 266 961, 11 30, 1993.

[35] W. H. Henderson and W. W. Milroy, “Wireless communication applications of the continuous transverse stub (CTS) array at microwave and millimeter wave frequencies,” in *IEEE/ACES Int. Conf. Wireless Commun. Appl. Computational Electromagnetics*, Apr. 2005, pp. 253–256.

[36] A. Lemons, R. Lewis, W. Milroy, R. Robertson, S. Coppedge, and T. Kastle, “W-band CTS planar array,” in *Proc. IEEE MTT-S Int. Microw. Symp. Dig.*, vol. 2, June 1999, pp. 651–654 vol.2.

[37] E. L. Holzman, “Pillbox antenna design for millimeter-wave base-station applications,” *IEEE Antennas Propagat. Mag.*, vol. 45, no. 1, pp. 27–37, Feb. 2003.

[38] W. W. Milroy, “Compact, ultra-wideband, antenna feed architecture comprising a multistage, multilevel network of constant reflection-coefficient components,” U.S. Patent 6 075 494, June 13, 2000.

[39] H. Choe and S. Lim, “Millimeter-wave continuous transverse stub (CTS) antenna array using substrate integrated waveguide (SIW) technology,” *IEEE Trans. Antennas Propag.*, vol. 62, no. 11, pp. 5497–5503, Nov. 2014.

[40] M. F. Iskander, Z. Yun, Z. Zhang, R. Jensen, and S. Redd, “Design of a low-cost 2-D beam-steering antenna using ferroelectric material and CTS technology,” *IEEE Trans. Microw. Theory Techn.*, vol. 49, no. 5, pp. 1000–1003, May 2001.

[41] A. Hessel, “General characteristics of traveling-wave antennas,” in *Antenna Theory*, R. E. Collin and F. J. Zucker, Eds. New York: McGraw-Hill, 1969, ch. 19.

[42] D. M. Pozar, "A relation between the active input impedance and the active element pattern of a phased array," *IEEE Trans. Antennas Propag.*, vol. 51, no. 9, pp. 2486–2489, Sep 2003.

[43] D. Cavallo and A. Neto, "A connected array of slots supporting broadband leaky waves," *IEEE Trans. Antennas Propag.*, vol. 61, no. 4, pp. 1986–1994, Apr. 2013.

[44] W. W. Milroy, "Planar antenna radiating structure having quasi-scan frequency-independent driving point impedance," U.S. Patent 5 995 055, Nov. 30, 1999.

[45] W. W. Milroy, S. B. Coppedge, A. Ekmekji, S. Hashemi-Yeganeh, and S. G. Buczek, "True-time-delay feed network for CTS array," Patent US 7 432 871, Oct. 7, 2008.

[46] Y. Xu, H. Dong, Y. Liu, and P. Zhang, "Continuous transverse stub (CTS) array antenna," in *Proc. Int. Symp. Antennas Propag. (ISAP)*, Oct. 2012, pp. 1083–1086.

[47] M. Ettorre, F. Foglia Manzillo, M. Casaletti, R. Sauleau, L. Le Coq, and N. Capet, "Continuous transverse stub array for Ka-band applications," *IEEE Trans. Antennas Propag.*, vol. 63, no. 11, pp. 4792–4800, Nov. 2015.

[48] N. E. Lindenblad and P. Jefferson, "Multiple slot antenna," U.S. Patent 2 628 311, Feb. 10, 1953.

[49] J. Vazquez, M. Shelley, and D. Moore, "Advanced flat panel antennas for small satcom terminals," in *34th ESA Antenna Workshop*, Oct. 2012, pp. 1–6.

[50] N. Capet, F. Foglia Manzillo, K. Tekkouk, R. Sauleau, and M. Ettorre, "Guide d'onde multicouche comprenant au moins un dispositif de transition entre des couches de ce guide d'onde multicouche," French Patent Application, 10 21, 2016.

[51] T. Teshirogi, Y. Kawahara, A. Yamamoto, Y. Sekine, N. Baba, and M. Kobayashi, "Dielectric slab based leaky-wave antennas for millimeter-wave applications," in *Proc. IEEE Antennas Propag. Soc. Int. Symp.*, vol. 1, July 2001, pp. 346–349.

[52] M. Ettorre, R. Sauleau, and L. Le Coq, "Multi-beam multi-layer leaky-wave SIW pillbox antenna for millimeter-wave applications," *IEEE Trans. Antennas Propag.*, vol. 59, no. 4, pp. 1093–1100, Apr. 2011.

[53] D. M. Pozar, *Microwave engineering.* John Wiley & Sons, 2012.

[54] G. L. Matthaei, E. M. T. Jones, and L. Young, *Microwave filters, impedance-matching networks, and coupling structures.* New York, USA: McGraw-Hill, 1964.

[55] W. W. Milroy, “Compact, ultra-wideband matched E-plane power divider,” U.S. Patent 5 926 077, July 20, 1999.

[56] R. Wolfson, W. W. Milroy, and S. Coppedge, “Methods of fabricating true-time delay continuous transverse stub array,” U.S. Patent 5 995 055, Aug. 13, 2002.

[57] R. J. Mailloux, *Phased Array Antenna Handbook.* Artech House, 1994.

[58] G. Floquet, “Sur les équations différentielles linéaires à coefficients périodiques,” *Annales de l’Ecole Normale Supérieure*, vol. 12, p. 47–88, 1883.

[59] L. B. Felsen and N. Marcuvitz, *Radiation and Scattering of Waves.* New York, USA: Wiley-IEEE Press, 1994.

[60] N. Amitay, V. Galindo, and C. Wu, *Theory and analysis of phased array antennas.* New York, USA: Wiley, 1972.

[61] A. Neto, D. Cavallo, G. Gerini, and G. Toso, “Scanning performances of wideband connected arrays in the presence of a backing reflector,” *IEEE Trans. Antennas Propag.*, vol. 57, no. 10, pp. 3092–3102, Oct. 2009.

[62] E. Magill and H. Wheeler, “Wide-angle impedance matching of a planar array antenna by a dielectric sheet,” *IEEE Trans. Antennas Propag.*, vol. 14, no. 1, pp. 49–53, Jan. 1966.

[63] D. Cavallo, A. Neto, and G. Gerini, “Green’s function based equivalent circuits for connected arrays in transmission and in reception,” *IEEE Trans. Antennas Propag.*, vol. 59, no. 5, pp. 1535–1545, May 2011.

[64] C. A. Balanis, *Antenna Theory: Analysis and Design.* Wiley-Interscience, 2005.

[65] G. H. Knittel, A. Hessel, and A. A. Oliner, “Element pattern nulls in phased arrays and their relation to guided waves,” *Proc. IEEE*, vol. 56, no. 11, pp. 1822–1836, Nov. 1968.

[66] D. Pozar and D. Schaubert, “Scan blindness in infinite phased arrays of printed dipoles,” *IEEE Trans. Antennas Propag.*, vol. 32, no. 6, pp. 602–610, June 1984.

[67] D. Jackson and N. Alexopoulos, “Gain enhancement methods for printed circuit antennas,” *IEEE Trans. Antennas Propag.*, vol. 33, no. 9, pp. 976–987, Sep 1985.

[68] L. Stark, “Microwave theory of phased-array antennas: a review,” *Proc. the IEEE*, vol. 62, no. 12, pp. 1661–1701, Dec. 1974.

[69] C. P. Wu and V. Galindo, “Surface-wave effects on dielectric sheathed phased arrays of rectangular waveguides,” *Bell Syst. Tech. J.*, vol. 47, no. 1, pp. 117–142, Jan. 1968.

[70] F. Foglia Manzillo, M. Ettorre, M. S. Lahti, K. T. Kautio, D. Lelaidier, E. Seguenot, and R. Sauleau, “A multilayer LTCC solution for integrating 5G access point antenna modules,” *IEEE Trans. Microw. Theory Techn.*, vol. 64, no. 7, pp. 2272–2283, July 2016.

[71] J. L. Allen, “A theoretical limitation on the formation of lossless multiple beams in linear arrays,” *IRE Trans. Antennas Propag.*, vol. 9, no. 4, pp. 350–352, July 1961.

[72] G. Farrell and D. Kuhn, “Mutual coupling effects of triangular-grid arrays by modal analysis,” *IEEE Trans. Antennas Propag.*, vol. 14, no. 5, pp. 652–654, Sep 1966.

[73] B. Diamond, “Resonance phenomena in waveguide arrays,” in *Proc. IEEE Antennas Propag. Soc. Int. Symp.*, vol. 5, Oct. 1967, pp. 110–115.

[74] V. Galdi and I. M. Pinto, “A simple algorithm for accurate location of leaky-wave poles for grounded inhomogeneous dielectric slabs,” *Microw. Opt. Technol. Lett.*, vol. 24, no. 2, pp. 135–140, Jan. 2000.

[75] T. Tamir, “Leaky wave antennas,” in *Antenna Theory*, R. E. Collin and F. J. Zucker, Eds. New York: McGraw-Hill, 1969, ch. 20.

[76] D. R. Jackson and A. A. Oliner, “Leaky-wave antennas,” in *Modern antenna handbook*, C. Balanis, Ed. New York, NY, USA: Wiley, 2008.

[77] D. M. Pozar, “The active element pattern,” *IEEE Trans. Antennas Propag.*, vol. 42, no. 8, pp. 1176–1178, Aug. 1994.

[78] A. Ishimaru, R. Coe, G. Miller, and W. Geren, “Finite periodic structure approach to large scanning array problems,” *IEEE Trans. Antennas Propag.*, vol. 33, no. 11, pp. 1213–1220, Nov. 1985.

[79] M. Born and E. Wolf, *Principles of Optics*, 7th ed. Cambridge University Press, 1999.

[80] E. Girard, G. Valerio, M. Ettorre, R. Sauleau, and H. Legay, “Physical-optics analysis and design of a beam-forming network coupled to an imaging-system configuration for Ka-band satellite applications,” in *Proc. 9th Eur. Conf. Antennas Propag.*, May 2015, pp. 1–5.

[81] A. Ludwig, “The definition of cross polarization,” *IEEE Trans. Antennas Propag.*, vol. 21, no. 1, pp. 116–119, Jan. 1973.

[82] N. Marcuvitz, *Waveguide handbook*, 3rd ed. McGraw-Hill, 1951.

[83] B. Gimeno and M. Guglielmi, “Multimode equivalent network representation for H- and E-plane uniform bends in rectangular waveguide,” *IEEE Trans. Microw. Theory Techn.*, vol. 44, no. 10, pp. 1679–1687, Oct. 1996.

[84] J. J. Campbell and W. R. Jones, “Symmetrically truncated right-angle corners in parallel-plate and rectangular waveguides,” *IEEE Trans. Microw. Theory Techn.*, vol. 16, no. 8, pp. 517–529, Aug. 1968.

[85] V. A. Labay and J. Bornemann, “Generalized scattering matrix of waveguide corners distorted by discontinuities in the resonator region,” in *Proc. IEEE MTT-S Int. Microw. Symp.*, May 1995, pp. 269–272 vol.1.

[86] P. Carle, “Right-angle junction for rectangular waveguides,” in *21st Eur. Microw. Conf.*, vol. 1, Sept. 1991, pp. 711–715.

[87] Y. Zhang and D. Liu, “Antenna-on-chip and antenna-in-package solutions to highly-integrated millimeter-wave devices for wireless communications,” *IEEE Trans. Compon. Packag. Manuf. Technol.*, vol. 57, no. 10, pp. 2830–2841, Oct. 2009.

[88] E. Cohen, M. Ruberto, M. Cohen, O. Degani, S. Ravid, and D. Ritter, “A CMOS bidirectional 32-element phased-array transceiver at 60 GHz with LTCC antenna,” *IEEE Trans. Microw. Theory Techn.*, vol. 61, no. 3, pp. 1359–1375, Mar. 2013.

[89] M. F. Karim, Y. X. Guo, M. Sun, J. Brinkhoff, L. C. Ong, K. Kang, and F. Lin, “Integration of SiP-based 60-GHz 4 × 4 antenna array with CMOS OOK transmitter and LNA,” *IEEE Trans. Microw. Theory Techn.*, vol. 59, no. 7, pp. 1869–1878, July 2011.

[90] P. Pursula, T. Karttaavi, M. Kantanen, A. Lamminen, J. Holmberg, M. Lahdes, I. Marttila, M. Lahti, A. Luukanen, and T. Vähä-Heikkilä, “60-GHz millimeter-wave identification reader on 90-nm CMOS and LTCC,” *IEEE Trans. Microw. Theory Techn.*, vol. 59, no. 4, pp. 1166–1173, Apr. 2011.

[91] R. A. Alhalabi, Y. C. Chiou, and G. M. Rebeiz, “Self-shielded high-efficiency yagi-uda antennas for 60 GHz communications,” *IEEE Trans. Antennas Propag.*, vol. 59, no. 3, pp. 742–750, Mar. 2011.

[92] T. Zwick, D. Liu, and B. P. Gaucher, “Broadband planar superstrate antenna for integrated millimeter-wave transceivers,” *IEEE Trans. Antennas Propag.*, vol. 54, no. 10, pp. 2790–2796, Oct. 2006.

[93] F. Foglia Manzillo, R. Nastri, M. Spella, G. Gentile, and M. Spirito, “A 60-GHz passive broadband multibeam antenna system in fused silica technology,” *IEEE Antennas Wireless Propag. Lett.*, vol. 12, pp. 1376–1379, 2013.

[94] C. E. Patterson, W. T. Khan, G. E. Ponchak, G. S. May, and J. Papapolymerou, “A 60-GHz active receiving switched-beam antenna array with integrated Butler matrix and GaAs amplifiers,” *IEEE Trans. Microw. Theory Techn.*, vol. 60, no. 11, pp. 3599–3607, Nov. 2012.

[95] B. Zhang, C. Kärnfelt, H. Gulan, T. Zwick, and H. Zirath, “A D-band packaged antenna on organic substrate with high fault tolerance for mass production,” *IEEE Trans. Compon. Packag. Manuf. Technol.*, vol. 6, no. 3, pp. 359–365, Mar. 2016.

[96] W. Liu, Z. N. Chen, and X. Qing, “60-GHz thin broadband high-gain LTCC metamaterial-mushroom antenna array,” *IEEE Trans. Antennas Propag.*, vol. 62, no. 9, pp. 4592–4601, Sept. 2014.

[97] L. Wang, Y. X. Guo, and W. X. Sheng, “Wideband high-gain 60-GHz LTCC L-probe patch antenna array with a soft surface,” *IEEE Trans. Antennas Propag.*, vol. 61, no. 4, pp. 1802–1809, Apr. 2013.

[98] U. Ullah, N. Mahyuddin, Z. Arifin, M. Z. Abdullah, and A. Marzuki, “Antenna in LTCC technologies: a review and the current state of the art,” *IEEE Antennas Propagat. Mag.*, vol. 57, no. 2, pp. 241–260, Apr. 2015.

[99] R. Kulku, M. Rittweger, P. Uhlig, and C. Günner. LTCC - Multilayer ceramic for wireless and sensor applications. [Online]. Available: http://www.ltcc.de/downloads/rd/pub/10-doc-plus-engl-2001.pdf

[100] M. Lahti, K. Kautio, V. Kondratyev, M. Kaunisto, and T. Vähä-Heikkilä, “LTCC packaging from RF to millimeter waves,” in *IMAPS Nordic Conf.*, June 2011, pp. 96–101.

[101] A. E. I. Lamminen, J. Saily, and A. R. Vimpari, “60-GHz patch antennas and arrays on LTCC with embedded-cavity substrates,” *IEEE Trans. Antennas Propag.*, vol. 56, no. 9, pp. 2865–2874, Sept. 2008.

[102] B. Zhang and Y. P. Zhang, “Grid array antennas with subarrays and multiple feeds for 60-GHz radios,” *IEEE Trans. Antennas Propag.*, vol. 60, no. 5, pp. 2270–2275, May 2012.

[103] F. Bauer and W. Menzel, “A 79-GHz planar antenna array using ceramic-filled cavity resonators in LTCC,” *IEEE Antennas Wireless Propag. Lett.*, vol. 12, pp. 910–913, 2013.

[104] Y. She, R. Fujino, J. Hirokawa, M. Ando, D. Hanatani, and M. Fujimoto, “LTCC oversized rectangular waveguide slot array antenna with air-layer in the radiating part in the millimeter-wave band,” *IEEE Trans. Antennas Propag.*, vol. 61, no. 4, pp. 1777–1783, Apr. 2013.

[105] J. Xu, Z. N. Chen, X. Qing, and W. Hong, “140-GHz TE_{20}-mode dielectric-loaded SIW slot antenna array in LTCC,” *IEEE Trans. Antennas Propag.*, vol. 61, no. 4, pp. 1784–1793, Apr. 2013.

[106] T. Tick, “Fabrication of advanced LTCC structures for microwave devices,” Ph.D. dissertation, University of Oulu, Oulu, Finland, 2009.

[107] H. Chu, J. X. Chen, and Y. X. Guo, “An efficient gain enhancement approach for 60-GHz antenna using fully integrated vertical metallic walls in LTCC,” *IEEE Trans. Antennas Propag.*, vol. 64, no. 10, pp. 4513–4518, Oct. 2016.

[108] *A6M/A6M-E High Frequency LTCC Tape System*, Ferro, 11 2015.

[109] D. Deslandes and K. Wu, “Accurate modeling, wave mechanisms, and design considerations of a substrate integrated waveguide,” *IEEE Trans. Microw. Theory Techn.*, vol. 54, no. 6, pp. 2516–2526, June 2006.

[110] T. Tajima, H. J. Song, K. Ajito, M. Yaita, and N. Kukutsu, “300-GHz step-profiled corrugated horn antennas integrated in LTCC,” *IEEE Trans. Antennas Propag.*, vol. 62, no. 11, pp. 5437–5444, Nov. 2014.

[111] Southwest Microwave. 1.85 mm jack end launch connector low profile. [Online]. Available: http://mpd.southwestmicrowave.com/showImage.php?image=762&name=1892-03A-6.pdf

[112] K. Tekkouk, M. Ettorre, L. Le Coq, and R. Sauleau, “Multibeam SIW slotted waveguide antenna system fed by a compact dual-layer Rotman lens,” *IEEE Trans. Antennas Propag.*, vol. 64, no. 2, pp. 504–514, Feb. 2016.

[113] Y. Rahmat-Samii, “Reflector antennas,” in *Antenna Handbook*, Y. Lo and S. W. Lee, Eds. New York: Van Nostrand Reinhold, 1988.

[114] F. Foglia Manzillo, M. Ettorre, M. Casaletti, N. Capet, and R. Sauleau, “Active impedance of infinite parallel-fed continuous transverse stub arrays,” *IEEE Trans. Antennas Propag.*, vol. 63, no. 7, pp. 3291–3297, July 2015.

[115] J. Xu, Z. N. Chen, X. Qing, and W. Hong, “Bandwidth enhancement for a 60 GHz substrate integrated waveguide fed cavity array antenna on LTCC,” *IEEE Trans. Antennas Propag.*, vol. 59, no. 3, pp. 826–832, Mar. 2011.

[116] *60-90 GHz SP3T Switch Flip Chip*, TriQuint Semiconductor, 1 2014, rev. C.

[117] W. D. White, “Pattern limitations in multiple-beam antennas,” *IRE Trans. Antennas Propag.*, vol. 10, no. 4, pp. 430–436, July 1962.

[118] S. Stein, “On cross coupling in multiple-beam antennas,” *IRE Trans. Antennas Propag.*, vol. 10, no. 5, pp. 548–557, Sept. 1962.

[119] M. Romier, R. Contreres, and B. Palacin, “Overlapping efficiency of multiple feed per beam concepts including orthogonality constraints,” in *Proc. 10th Eur. Conf. Antennas Propag.*, Apr. 2016, pp. 1–5.

[120] C. Leclerc, M. Romier, H. Aubert, and A. Annabi, “Ka-band multiple feed per beam focal array using interleaved couplers,” *IEEE Trans. Microw. Theory Techn.*, vol. 62, no. 6, pp. 1322–1329, June 2014.

[121] MiWaveS Consortium, “Deliverable 4.3: antenna designs for mmW access and backhaul communications ,” Tech. Rep., Sept. 2015.

[122] L. Le Coq, B. Fuchs, T. Kozan, S. Burgos, and P. O. Iversen, “IETR millimeter-wave compact antenna test range implementation and validation,” in *Proc. 9th Eur. Conf. Antennas Propag.*, May 2015, pp. 1–5.

[123] T. Manabe, Y. Miura, and T. Ihara, “Effects of antenna directivity and polarization on indoor multipath propagation characteristics at 60 GHz,” *IEEE J. Sel. Areas Commun.*, vol. 14, no. 3, pp. 441–448, Apr. 1996.

[124] F. Foglia Manzillo, M. Ettorre, T. Potelon, M. Śmierzchalski, R. Sauleau, and N. Capet, “Wideband multibeam arrays of long slots fed by quasi-optical systems,” in *Proc. 11th Eur. Conf. Antennas Propag.*, Mar. 2017.

[125] D. Lerner, “A wave polarization converter for circular polarization,” *IEEE Trans. Antennas Propag.*, vol. 13, no. 1, pp. 3–7, Jan. 1965.

[126] L. Young, L. Robinson, and C. Hacking, “Meander-line polarizer,” *IEEE Trans. Antennas Propag.*, vol. 21, no. 3, pp. 376–378, May 1973.

[127] C. Pfeiffer and A. Grbic, “Millimeter-wave transmitarrays for wavefront and polarization control,” *IEEE Trans. Microw. Theory Techn.*, vol. 61, no. 12, pp. 4407–4417, Dec. 2013.

[128] M. A. Joyal and J.-J. Laurin, “Analysis and design of thin circular polarizers based on meander lines,” *IEEE Trans. Antennas Propag.*, vol. 60, no. 6, pp. 3007–3011, June 2012.

[129] S. M. A. Momeni Hasan Abadi and N. Behdad, “Wideband linear-to-circular polarization converters based on miniaturized-element frequency selective surfaces,” *IEEE Trans. Antennas Propag.*, vol. 64, no. 2, pp. 525–534, Feb. 2016.

[130] M. Letizia, B. Fuchs, C. Zorraquino, J.-F. Zürcher, and J. R. Mosig, “Oblique incidence design of meander-line polarizer for dielectric lens antennas,” *Prog. Electrom. Res. B.*, vol. 45, pp. 309–335, Feb. 2012.

[131] J. Epis, “Broadband antenna polarizer,” U.S. Patent 3 754 217, Aug. 21, 1973.

[132] P. Fei, Z. Shen, X. Wen, and F. Nian, “A single-layer circular polarizer based on hybrid meander line and loop configuration,” *IEEE Trans. Antennas Propag.*, vol. 63, no. 10, pp. 4609–4614, Oct. 2015.

[133] M. A. Antoniades and G. V. Eleftheriades, “Compact linear lead/lag metamaterial phase shifters for broadband applications,” *IEEE Antennas Wireless Propag. Lett.*, vol. 2, no. 1, pp. 103–106, 2003.

[134] ——, “A broadband Wilkinson balun using microstrip metamaterial lines,” *IEEE Antennas Wireless Propag. Lett.*, vol. 4, pp. 209–212, 2005.

[135] G. V. Eleftheriades, A. K. Iyer, and P. C. Kremer, “Planar negative refractive index media using periodically L-C loaded transmission lines,” *IEEE Trans. Microw. Theory Techn.*, vol. 50, no. 12, pp. 2702–2712, Dec. 2002.

[136] A. Grbic, “Super-resolving negative-refractive-index transmission-line lenses,” Ph.D. dissertation, University of Toronto, Toronto, Canada, 2006.

[137] A. Hessel, M. H. Chen, R. C. M. Li, and A. A. Oliner, “Propagation in periodically loaded waveguides with higher symmetries,” *Proc. IEEE*, vol. 61, no. 2, pp. 183–195, Feb. 1973.

[138] M. Ebrahimpouri, E. Rajo-Iglesias, Z. Sipus, and O. Quevedo-Teruel, “Low-cost metasurface using glide symmetry for integrated waveguides,” in *Proc. 10th Eur. Conf. Antennas Propag.*, Apr. 2016, pp. 1–2.

[139] C. Pfeiffer and A. Grbic, “Bianisotropic metasurfaces for optimal polarization control: analysis and synthesis,” *Phys. Rev. Applied*, vol. 2, p. 044011, Oct. 2014.

About the author

I was born on October 11, 1988. I grew up in Castellammare di Stabia, Italy.

I received the B.Sc. (*cum laude*) and M.Sc. (*cum laude*) degrees in electronic engineering from the University of Naples "Federico II", Naples, Italy, in 2010 and 2012, respectively.

I carried out my M.Sc. thesis project, from April to October 2012, in the Electronic Research Laboratory, Delft University of Technology, Delft, The Netherlands, in collaboration with NXP Semiconductors, Eindhoven, The Netherlands, where I was an intern from April to December 2012.

In 2013, I worked as an RF engineer at eWings s.r.l., Bologna, Italy.

In January 2014 I started working toward my Ph.D. in electrical engineering at the Institute of Electronics and Telecommunications of Rennes, University of Rennes 1, Rennes, France, under the supervision of Prof. R. Sauleau and Dr. M. Ettorre. I have been involved in the European collaborative project "MiWaveS" and in research and developments activities in collaboration with the French Space Agency (CNES).

From April to October 2016, I was a visiting Ph.D. student at the Radiation Laboratory, University of Michigan, Ann Arbor, MI, USA, supervised by Prof. A. Grbic.

My research interests include the analysis and design of wideband arrays, multibeam antennas, periodic structures, numerical modeling, and the integration of millimeter-wave systems.

List of publications

Patents

P-1. N. Capet, F. Foglia Manzillo, K. Tekkouk, R. Sauleau, M. Ettorre, “Guide d’onde multicouche comprenant au moins un dispositif de transition entre des couches de ce guide d’onde multicouche”, French Patent Application no. 1660249, 21 Oct. 2016.

Journal papers

J-1. F. Foglia Manzillo, R. Sauleau, N. Capet, and M. Ettorre, “Mode matching analysis of an E-plane 90° bend with a square step in parallel plate waveguide”, to be published in *IEEE Antennas Wireless Propag. Lett.*, 2017.

J-2. F. Foglia Manzillo, M. Ettorre, M. S. Lahti, K. T. Kautio, D. Lelaidier, E. Seguenot, and R. Sauleau, “A multilayer LTCC solution for integrating 5G access point antenna modules”, *IEEE Trans. Microw. Theory Tech.*, vol. 64, no. 7, pp. 2272-2283, July 2016.

J-3. M. Ettorre, F. Foglia Manzillo, M. Casaletti, R. Sauleau, L. Le Coq, and N. Capet, “Continuous transverse stub array for Ka-band applications”, *IEEE Trans. Antennas Propag.*, vol. 63, no. 11, pp. 3291-3297, Nov. 2015.

J-4. F. Foglia Manzillo, M. Ettorre, M. Casaletti, N. Capet, and R. Sauleau, “Active impedance of infinite parallel-fed continuous transverse stub arrays”, *IEEE Trans. Antennas Propag.*, vol. 63, no. 7, pp. 3291-3297, July 2015.

J-5. F. Foglia Manzillo, R. Nastri, M. Spella, G. Gentile, and M. Spirito, “A 60-GHz passive broadband multi-beam antenna system in fused silica technology”, *IEEE Antennas Wireless Propag. Lett.*, vol. 12, pp. 1376-1379, 2013.

J-. F. Foglia Manzillo, M. Ettorre, N. Capet, and R. Sauleau, “Analysis of scan blindness in arrays of long slots fed by parallel plate waveguides”, in preparation for submission to *IEEE Trans. Antennas Propag.*, 2017.

J-. F. Foglia Manzillo, M. Śmierzchalski, L. Le Coq, M. Ettorre, J. Aurinsalo, K.T. Kautio, M. S. Lahti, A. E. I. Lamminen, J. Säily, and R. Sauleau, “A switched-beam antenna

with high beam crossover level and wide field of view in LTCC technology", in preparation for submission to *IEEE Trans. Antennas Propag.*, 2017.

International conference papers

IC-1. F. Foglia Manzillo, M. Śmierzchalski, M. Ettorre, J. Aurinsalo, Kari T. Kautio, M. S. Lahti, A. E. I. Lamminen, J. Säily, and R. Sauleau, "An LTCC beam-switching antenna with high beam overlap for 60-GHz mobile access points", accepted for presentation at *IEEE Antennas Propag. Soc. Int. Symp.*, San Diego, CA, USA, 9-14 July 2017.

IC-2. F. Foglia Manzillo, M. Ettorre, T. Potelon, M. Śmierzchalski, R. Sauleau, N.Capet, "Wideband multibeam arrays of long slots fed by quasi-optical systems", accepted for presentation at *11th Eur. Conf. Antennas Propag.*, Paris, France, 19-24 Mar. 2017 (*Convened session*).

IC-3. F. Foglia Manzillo, M. Ettorre, R. Sauleau, A. Grbic, "Systematic design of a class of wideband circular polarizers using dispersion engineering", *accepted for presentation at 11th Eur. Conf. Antennas Propag.*, Paris, France, 19-24 Mar. 2017.

IC-4. K. Tekkouk, M. Ettorre, F. Foglia Manzillo, T. Potelon, M. Śmierzchalski, D. Blanco, L. Le Coq, R. Sauleau, "Recent and future research trends in planar multi-beam antennas in the millimeter wave range at IETR-France", in *Proc. Int. Symp. Antennas Propag.*, Okinawa, Japan, 24-28 Oct. 2016 (*Invited*).

IC-5. F. Foglia Manzillo, M. Ettorre, M. Śmierzchalski, M. S. Lahti, K. T. Kautio, D. Lelaidier, E. Seguenot, R. Sauleau, "A V-band antenna module based on vertical TEM waveguides fully integrated in LTCC", in *Proc. IEEE Antennas Propag. Soc. Int. Symp.*, Fajardo, Porto Rico, 26 June - 1 July 2016.

IC-6. F. Foglia Manzillo, M. Ettorre, R. Sauleau, N.Capet, "Equivalent circuit and scanning capabilities of long slot arrays with TEM parallel-feed excitation", in *Proc. 10th Eur. Conf. Antennas Propag.*, Davos, Switzerland, 10-15 Apr. 2016.

IC-7. F. Foglia Manzillo, M. Ettorre, M. S. Lahti, K. T. Kautio, D. Lelaidier, E. Seguenot, R. Sauleau, "A long slot array fed by a multilayer true-time delay network in LTCC for 60-GHz communications", in *Proc. 10th Eur. Conf. Antennas Propag.*, Davos, Switzerland, 10-15 Apr. 2016.

IC-8. M. Ettorre, F. Foglia Manzillo, M. Casaletti, R. Sauleau, N.Capet, "A compact and high-gain Ka-band multibeam continuous transverse stub antenna", in *Proc. IEEE Antennas Propag. Soc. Int. Symp.*, Vancouver, Canada, 19-24 July 2015, pp. 671-672.

IC-9. F. Foglia Manzillo, M. Ettorre, M. Casaletti, R. Sauleau, N.Capet, "Modeling and design of parallel-fed continuous transverse stub (CTS) arrays", in *Proc. 9th Eur. Conf. Antennas Propag.*, Lisbon, Portugal, 13-17 Apr. 2015.

National conference papers

NC-1. T. Potelon, F. Foglia Manzillo, M. Ettorre, L. Le Coq, M. S. Lahti, K. T. Kautio, T. Bateman, J. Francey, D. Lelaidier, E. Seguenot, and R. Sauleau, “Antennes CTS-pillbox large bande pour applications 5G,” submitted for presentation at $20^{émes}$ *Journées Nationales Micro-ondes*, Saint-Malo, France, May 2017.

NC-2. M. Ettorre, F. Foglia Manzillo, M. Casaletti, R. Sauleau, N.Capet, “Réseau d’antennes CTS pour applications satellitaires en bande Ka”, $19^{émes}$ *Journées Nationales Micro-ondes*, Bordeaux, France, June 2015.

Acknowledgments

All human actions and endeavors are influenced, directly or indirectly, by other human beings. This little book does not make an exception to this rule.

It is unfair to acknowledge in a few lines all the people who contributed to this work and life experience. I would like to express my gratitude to each of them and I will name here only a few.

First, I would like to thank my supervisors, whose dedication to work has been inspirational. I am grateful to Prof. Ronan Sauleau for his guidance, his confidence in me and the numerous opportunities he has given me during these years. Dr. Mauro Ettorre deserves equal thanks. He shared and transmitted to me his technical skills, he supported my research day-by-day and valorized my work.

I express my deep gratitude to Professor Anthony Grbic for accepting me in his research group at the University of Michigan as a visiting student and for broadening my knowledge of periodic structures. His research approach, the way he leads his group and his cordiality enriched me a lot.

I wish to acknowledge Prof. Andrea Neto and Prof. Thomas Zwick for reviewing my manuscript, as well as Dr. Romain Czarny and Dr. Giovanni Toso for accepting to be in my Ph.D. committee and for providing valuable comments.

I thank Dr. Nicolas Capet for attending my defense and for managing with high competence one of the two projects I have been involved in during my thesis. I acknowledge all participants in the FP7 *MiWaveS* project and in particular the engineers from VTT and from Orange I collaborated with for the realization and characterization of my prototypes.

I wish to thank the people who made pleasant my experience in IETR. I thank the technicians and the secretaries (Chantal, Martine, Nathalie and Noëlle). I thank Dr. Maxim Zhadobov, Dr. David González Ovejero, Prof. Franck Colombel, even though I will never join Les Républicains, and Dr. Laurent Le Coq who demonstrated to me that a Frenchman can have a sarcastic sense of humour. I acknowledge Karim for the fruitful technical discussions we had and Thomas for the constant collaboration through these years.

I thank my past and present officemates Artem, Josip, Walter, Tuyen and François (my teacher of French in IETR) who made shorter our long working days. I also thank the colleagues at the University of Michigan who welcomed me in their group, and Marthe and Giulio who hugely helped me to settle down in Ann Arbor.

I wish to heartily thank some friends who marked my life in Rennes. Francesco helped me a lot in the laboratory and outside since my first days. He definitely made me feel home in Brittany, despite always complaining about it. I thank him, Riccardo, Giovanni and Ana, Fabrizio and Ida, the first members of our Italian community, for the mutual support and the nice time we spent together. A huge thank goes to Yannis, without whom this experience would have been poorer. We shared side-by-side worries, hopes and ideas related to our theses. And we had fun together in the many social events and nights out he used to organize, even after long days in the laboratory. I thank Rosa for joining in those nights with her smile and openness. Being a Southern person as she is, I cannot promise I will be more open-minded. I want to acknowledge Benjamin for his human qualities which come before his talent as a researcher. I wish to thank María and Joris, always kind and stimulating. I will miss our discussions, never trivial, and the Saturday afternoons at L'Amaryllis. I wish to thank Maciek for the nice work we did together and for being always easy-going and humble. I thank Denys for his trust in me and for the discussions about such different topics we had. Un remerciement tout spécial va à Laura.

I cannot refrain from expressing my pride in my roots which made me the person I am. I am grateful to the professors and friends of my high school in Castellammare di Stabia and to the University of Naples Federico II. Hearty thanks go to my long-term friends, now spread all over Europe, who support me remotely and, whenever possible, find time for meeting as we never left.

Finally, I would like to dedicate this thesis to my parents and my brother.

ANNEXE 2 (Modèle dernière page de thèse)

VU :	VU :
Le Directeur de Thèse (Nom et Prénom)	**Le Responsable de l'École Doctorale**

VU pour autorisation de soutenance

Rennes, le

Le Président de l'Université de Rennes 1

David ALIS

VU après soutenance pour autorisation de publication :

Le Président de Jury,
(Nom et Prénom)